Structure and Bonding 160
Series Editor: D.M.P. Mingos

Daniel Rabinovich *Editor*

Molecular Design in Inorganic Biochemistry

Springer

160
Structure and Bonding

For further volumes:
http://www.springer.com/series/430

Aims and Scope

The series *Structure and Bonding* publishes critical reviews on topics of research concerned with chemical structure and bonding. The scope of the series spans the entire Periodic Table and addresses structure and bonding issues associated with all of the elements. It also focuses attention on new and developing areas of modern structural and theoretical chemistry such as nanostructures, molecular electronics, designed molecular solids, surfaces, metal clusters and supramolecular structures. Physical and spectroscopic techniques used to determine, examine and model structures fall within the purview of *Structure and Bonding* to the extent that the focus is on the scientific results obtained and not on specialist information concerning the techniques themselves. Issues associated with the development of bonding models and generalizations that illuminate the reactivity pathways and rates of chemical processes are also relevant

The individual volumes in the series are thematic. The goal of each volume is to give the reader, whether at a university or in industry, a comprehensive overview of an area where new insights are emerging that are of interest to a larger scientific audience. Thus each review within the volume critically surveys one aspect of that topic and places it within the context of the volume as a whole. The most significant developments of the last 5 to 10 years should be presented using selected examples to illustrate the principles discussed. A description of the physical basis of the experimental techniques that have been used to provide the primary data may also be appropriate, if it has not been covered in detail elsewhere. The coverage need not be exhaustive in data, but should rather be conceptual, concentrating on the new principles being developed that will allow the reader, who is not a specialist in the area covered, to understand the data presented. Discussion of possible future research directions in the area is welcomed.

Review articles for the individual volumes are invited by the volume editors.

In references *Structure and Bonding* is abbreviated *Struct Bond* and is cited as a journal.

Daniel Rabinovich
Editor

Molecular Design in Inorganic Biochemistry

With contributions by

N.A. Dixon • P.M. Gurubasavaraj • T.C. Harrop • P.L. Holland • M. Kumar • P.K. Mascharak • T.K. Paine • E.T. Papish • L. Que Jr • M.A. Rhine • B.C. Sanders • W. Yao

Springer

Editor
Daniel Rabinovich
Department of Chemistry
University of North Carolina
Charlotte
North Carolina
USA

ISSN 0081-5993 ISSN 1616-8550 (electronic)
ISBN 978-3-662-43598-4 ISBN 978-3-662-43599-1 (eBook)
DOI 10.1007/978-3-662-43599-1
Springer Heidelberg New York Dordrecht London

Library of Congress Control Number: 2014943448

Printed on acid-free paper

Springer is part of Springer Science+Business Media (www.springer.com)

Preface

The preparation and study of coordination complexes that mimic the structure and function of metallobiomolecules, the heart and soul of this volume of *Structure and Bonding*, is currently one of the most active areas of research in bioinorganic chemistry. The synthetic analogue approach, elegantly described by Ibers and Holm more than 30 years ago [1], is still today a valuable and versatile strategy to investigate the active sites of biological systems that rely on the use of metal ions as prosthetic groups. In this regard, major improvements in spectroscopic techniques and computational methods in recent years have enhanced the ability of "speculative" or "corroborative" model compounds to predict or substantiate the properties and structures of complex biomolecules [2, 3].

This book features five chapters written by recognized experts in their fields of study and, taken together, the reviews nicely illustrate the topical diversity in modern inorganic biochemistry. In this regard, it is worth noting that, even for a single element such as iron (i.e., the most abundant transition metal in the human body), four of the five chapters cover rather different aspects of its biological chemistry.

Iron–sulfur clusters, typically containing a combination of divalent and trivalent metal ions, are ubiquitous cofactors in biological electron-transfer processes and their redox and spectroscopic properties have been extensively studied. However, highly reduced iron–sulfur clusters featuring exclusively iron(II) ions are significantly less common. In the first chapter of the book, "All-Ferrous Iron–Sulfur Clusters", Yao, Gurubasavaraj and Holland present a systematic description of several all-ferrous multimetallic complexes, including selected examples of clusters found in biological systems and a range of synthetic derivatives based on thiolate, phosphine, cyanide, and *N*-heterocyclic carbene (NHC) ligands.

Paine and Que's review on chapter two, "Dioxygen Activation by Biomimetic Iron Complexes of α-Keto Acids and α-Hydroxy Acids", focuses on the synthesis and reactivity of well-defined mononuclear iron complexes designed as functional models for oxidase and oxygenase enzymes that mediate the oxidative decarboxylation of α-ketocarboxylate and α-hydroxycarboxylate substrates. Studies such as these provide invaluable information to better understand the role that iron(III) superoxo and iron(IV) oxo (i.e., ferryl) species play in the activation of dioxygen by nonheme iron enzymes.

The review by Sanders, Rhine and Harrop in chapter three, "Properties of $\{FeNO\}^8$ and $\{CoNO\}^9$ Metal Nitrosyls in Relation to Nitroxyl Coordination Chemistry", describes in detail synthetic, structural, spectroscopic, electrochemical, and theoretical studies pertaining to biologically relevant iron– and cobalt–NO complexes featuring the rare Enemark–Feltham notations $\{FeNO\}^8$ and $\{CoNO\}^9$. In particular, the biological role of the one-electron reduced analogue of nitric oxide, namely nitroxyl (HNO) or its conjugate base (NO^-), is discussed in the context of their iron and cobalt complexes and the potential development of new delivery agents for these species in the treatment of cardiovascular diseases.

Chapter four, "The Active Site of Nitrile Hydratase: An Assembly of Unusual Coordination Features by Nature" is dedicated to the enzyme nitrile hydratase (NHase), which catalyzes the hydration of organic nitriles to the corresponding amides and contains either a non-heme iron(III) or a non-corrinoid cobalt(III) center at the active site. In this regard, the review by Mascharak includes a description of several complexes supported by multidentate mixed-donor ligands that have been used to prepare structural or functional model compounds of NHase in recent years.

In the fifth and final chapter, "Biomimetic Chemistry with Tris(triazolyl) borate Ligands: Unique Structures and Reactivity via Interactions with the Remote Nitrogens", Papish, Dixon and Kumar survey the coordination chemistry of tris (triazolyl)borate (Ttz) and related ligands, with an emphasis on biomimetic applications. Although seemingly analogous to the popular tris(pyrazolyl)borate (Tp) ligands introduced by Trofimenko nearly 50 years ago, the presence of the additional nitrogen atom in the 4-position of the heterocyclic rings often leads to the binding of additional metal ions and the formation of extended structures. In addition, the triazolyl-based ligands (and their complexes) tend to exhibit enhanced solubility in water, an attractive feature for the preparation of synthetic analogues of metalloenzymes such as copper nitrite reductase and carbonic anhydrase.

The five chapters in the book evidently represent only a small fraction of the entire spectrum of research opportunities in contemporary bioinorganic chemistry. It is clear, however, that the design of reliable ligands and the preparation of synthetic analogues of metalloproteins and metalloenzymes can be both challenging and rewarding. In closing, my hope is that these chapters not only underscore the value of interdisciplinary research but also inspire many colleagues with similar interests to pursue new lines of research in synthetic bioinorganic chemistry.

April 2014 Daniel Rabinovich
Charlotte, NC, USA

References

1. Ibers JA, Holm RH (1980) Science 209:223
2. Karlin KD (1993) Science 261:701
3. Lee SC, Holm RH (2003) Proc Natl Acad Sci U S A 100:3595

Contents

Struct Bond (2014) 160: 1–38
DOI: 10.1007/430_2012_81

Published online: 8 December 2012

All-Ferrous Iron–Sulfur Clusters

Wenwen Yao, Prabhuodeyara M. Gurubasavaraj, and Patrick L. Holland

Abstract Iron–sulfur clusters are important biological cofactors that are used for electron transfer and also for reactivity. Though the iron atoms in these clusters are typically a mixture of ferrous iron(II) and ferric iron(III), there have been reports of biological iron–sulfur clusters in which all the iron atoms are reduced to the iron(II) oxidation state. These reports have inspired synthetic studies on all-ferrous iron–sulfur clusters. This chapter describes both the biological and synthetic work on all-iron(II) clusters, drawing comparisons and noting promising avenues for future research.

Keywords Iron-sulfur cluster · Synthetic model · Iron(II)

Contents

W. Yao, P.M. Gurubasavaraj, and P.L. Holland (✉)
Department of Chemistry, University of Rochester, Rochester, NY 14627, USA
e-mail: holland@chem.rochester.edu

1 Introduction

Iron–sulfur clusters have been an important topic of chemical research for several decades [1, 2]. As "clusters", they contain more than one iron atom held close to other iron atoms, and the number of iron atoms can vary from 2 to 16 or more. Some examples of iron–sulfur cluster types are shown in Fig. 1. The bridges between iron atoms in these clusters are sulfides (S^{2-}), which form strong bonds with Fe^{2+} and Fe^{3+} and often bridge multiple metal ions. Though the Fe–S bonds are thermodynamically stable, they are labile by virtue of (a) the weak ligand-field strength of sulfide, which leads to a high-spin electronic configuration of the iron atoms that places electrons in metal–ligand antibonding orbitals, and (b) the spherical charge density on the sulfide, which admits a range of bond angles and lengths and presumably gives low activation barriers for bond rearrangements.

Iron–sulfur clusters are naturally found in all known bacteria, plants, animals, and archaea [3, 4]. In biological systems, they are always part of metalloproteins, where they are covalently attached to thiolates from deprotonated cysteine amino acid sidechains. Because the cysteinates are anions and the sulfides are dianions, the overall charge on most biological iron–sulfur clusters is negative. This has

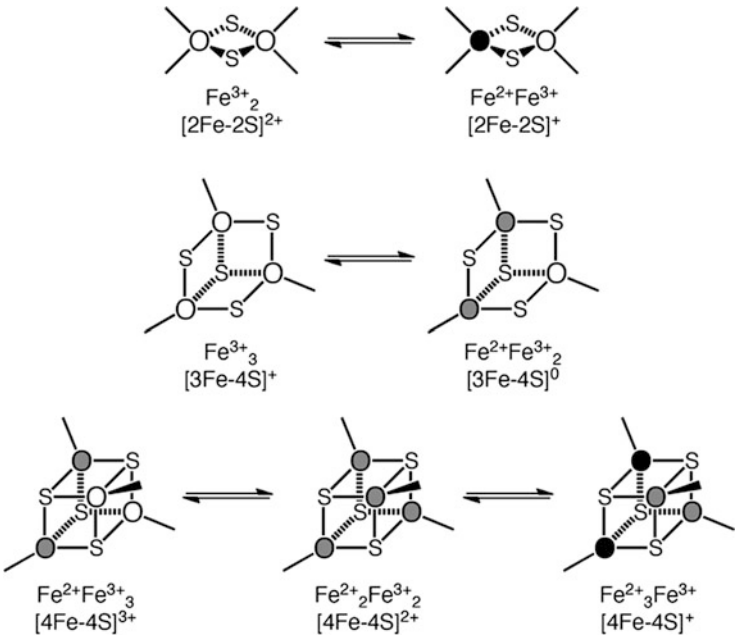

Fig. 1 The most common structures and oxidation levels of [2Fe–2S], [3Fe–4S], and [4Fe–4S] clusters. *White circles* represent Fe^{3+} ("ferric"), *black circles* represent Fe^{2+} ("ferrous"), and *grey circles* represent $Fe^{2.5+}$ (delocalized valence)

important consequences for their chemistry, especially that a more polar medium tends to stabilize the more reduced form (i.e., gives a less negative redox potential), because this form bears the greater charge. Often the biological clusters can be extracted intact from the protein environment, through exchange with exogenous thiolate donors [5].

Iron–sulfur clusters play many roles in biological systems [3, 6, 7]. Much recent attention has focused on sensory and transcriptional regulation roles [8, 9]. Nevertheless, one of the most important functions of iron–sulfur clusters in biological systems is to be a one-electron redox shuttle. Many metabolic processes use iron–sulfur enzymes (also denoted as "ferredoxins") as part of the electron transport chain. Though the proteins are generally air sensitive, they are used in both aerobic and anaerobic organisms. They are well adapted to electron-transfer roles because their structures change little between redox levels. From a coordination chemistry point of view, the structural invariance with redox changes arises from two factors: (a) the tetrahedral geometry at the iron atoms is similar for both Fe^{2+} and Fe^{3+}, and (b) the accessible states are often mixed valence, with delocalized charge. Because there is little reorganization energy associated with redox changes, rapid electron transfer is possible. A number of proteins have several iron–sulfur clusters of graded potential that act as electron conduits (for example, [10]).

Other iron–sulfur clusters are at the active sites of enzymes. The longest-known iron–sulfur enzyme is aconitase [11], which brings about a non-redox reaction within the tricarboxylic acid (TCA) cycle, but most iron–sulfur cluster enzymes accomplish redox reactions. Iron–sulfur clusters are especially common in enzymes that perform redox transformations of simple small molecules, such as H_2 (Fe-only and Fe–Ni hydrogenases), N_2 (nitrogenase), CO and CO_2 (Ni–Fe CO dehydrogenase) in bacteria and archaea. It is possible that the widespread role of FeS clusters in small-molecule transformations is a reflection of the conditions of early Earth: when these enzymes evolved, Earth's environment was anaerobic and sulfidic with a significant amount of dissolved Fe^{2+} [12]. It is notable that iron–sulfur clusters can self-assemble from dissolved iron, hydrosulfide, and thiolates [13], indicating that they could have been formed readily from available raw materials early in the history of life. Both iron–sulfur clusters and iron–sulfur minerals have even been postulated as key catalysts in primordial metabolism that led to the first life forms [14, 15].

The role of iron–sulfur clusters in the biological reduction of small molecules is paralleled by the catalytic ability of solid iron sulfides in small-molecule reactions of CO [15] and CO_2 [16]. In addition, solid iron sulfide has been observed to catalyze ammonia formation from N_2 [17]. Understanding soluble iron–sulfur clusters (in biological and abiological systems) may give insight into possible mechanisms at the surfaces of these solids.

Because of the redox activity of the clusters, there have been many studies on the redox potentials and spectroscopic features of FeS cluster-containing compounds in different oxidation states. The accumulated data have shown that the most common oxidation levels of iron–sulfur clusters have a mixture of Fe^{2+} (ferrous) and Fe^{3+} (ferric). Often iron atoms have delocalized valence, with some iron ions best

described as $Fe^{2.5+}$ because they share an electron equally with another iron site. In general, the Kramers states (those with an odd number of total electrons, corresponding to an odd number of iron(III) centers) are more easily detected and characterized because they show characteristic signals in perpendicular-mode electron paramagnetic resonance (EPR) spectra. Iron-57 Mössbauer spectroscopy is a useful technique, because it shows all iron ions, and the characteristic isomer shift (δ) and quadrupole splitting (ΔE_Q) often are used to specify the oxidation state of the iron. Other techniques, such as X-ray absorption, magnetic circular dichroism, and resonance Raman are also useful. The combination of these spectroscopic methods has shown that the common oxidation states are those shown in Fig. 1 [1, 2].

It is interesting that none of the common cluster states in Fig. 1 has all of the iron atoms as Fe^{2+} ("all-ferrous"). All-ferrous states are uncommon because the buildup of additional negative charge on the cluster is difficult, and could require a reducing agent outside the physiologically possible range. Despite these difficulties, a few teams of biochemists, chemists, and spectroscopists have been able to identify iron–sulfur clusters in biological and synthetic systems that are all ferrous. These rare and interesting systems are the focus of this review. They push the limits of chemistry for several reasons. First, they are usually very sensitive and difficult to isolate, because of the very negative redox potential at which they are formed, and because of oxygen sensitivity. Second, all-ferrous clusters are non-Kramers systems, and thus give little to no EPR signal, especially with the common X-band microwave frequency. Because of the muted EPR signature, it is possible that other all-ferrous clusters in biology have not yet been detected. Finally, they offer interesting spectroscopic challenges, which have been highlighted in a recent minireview [18].

This review describes the biological examples of all-ferrous clusters, followed by synthetic clusters. In order to limit the review to a reasonable size, we do not describe the large literature on nitrosyl, cyclopentadienyl, and carbonyl-containing clusters, which have been comprehensively reviewed [19]. We have also omitted other related clusters that have a low-spin electronic configuration at iron, in order to focus on the high-spin clusters that are most comparable to the biological systems. We do not include heteronuclear clusters that contain iron in addition to other transition metals (most often nickel or molybdenum), which have been included in larger reviews [7, 20–22].

It is our hope that this organized description of highly reduced iron–sulfur clusters will assist biological chemists who may encounter these clusters in new proteins and enzymes. In addition, we hope that this systematic review of the recent exciting developments is of use to synthetic chemists who desire to expand the range of known clusters. In order to facilitate comparisons between the biological and synthetic systems, all redox potentials in this review are given versus the hydrogen electrode (NHE), even though the synthetic clusters have been reported in the primary literature against a variety of different reference potentials.

2 Biological Examples of All-Ferrous Iron–Sulfur Clusters

One of the interesting aspects of the field of highly reduced iron–sulfur clusters is that the examples in biological molecules often preceded the synthetic examples. In several cases, no synthetic analogue exists. This may seem surprising, given that synthetic compounds and non-aqueous solvents offer more options for protecting sensitive, highly reducing metal centers. However, natural iron–sulfur clusters are held in protein environments that stabilize negative charges on the cluster. As a result, the same formal redox couple typically has a much more negative redox potential in synthetic clusters than in the analogous biological system with the same coordinating ligands. The synthetic clusters are accordingly more difficult to isolate in highly reduced forms, and recent progress (described below) has depended on the use of abiological ligand sets.

What makes the protein able to stabilize large negative charges on such highly reduced sites? As will become evident below, moderation of the redox potential in the biological systems often comes from interactions with protons: either the cluster may become protonated, or there may be hydrogen bonds to the rest of the protein. Hydrogen bonds to the coordinating cysteine thiolate residues are a ubiquitous feature of biological iron–sulfur sites. The electron-withdrawing influence of hydrogen bonds diffuses the buildup of charge density on the cluster, and acts to make the redox potential more positive [23, 24].

2.1 Two-Iron Clusters

The simplest type of iron–sulfur cluster in biological systems is the [2Fe–2S] cluster, which typically transfers a single electron to convert between the $[2Fe–2S]^{2+}$ (oxidized, with two Fe^{3+}) and $[2Fe–2S]^{+}$ (reduced, with mixed-valence $Fe^{2+}Fe^{3+}$) oxidation levels. However, a few situations have been identified in which both iron atoms may be reduced to the ferrous oxidation level, giving a $[2Fe–2S]^{0}$ cluster.

The first example is the reduction of plant [2Fe–2S] ferredoxins using chromium(II) 15-aneN_4 (Fig. 2) [25–27]. Interestingly, Cr^{2+} is the only reductant reported to perform this reaction, and NMR studies show that the reduced protein binds the Cr^{3+} ion. It is likely that this binding imparts extra energy that enables Cr^{2+} to achieve the difficult reduction. Because of the influence of chromium binding, a formal redox potential is not defined for this transition. Mössbauer studies have shown that the $[2Fe–2S]^{0}$ center in the protein is diamagnetic, resulting from strong ($|J| > 80$ cm^{-1}) anti-ferromagnetic coupling between high-spin ($S_{Fe} = 2$) sites to give an $S_{total} = 0$ ground state [28]. This diamagnetic all-ferrous state has also been produced in frozen glasses using radiolytic reduction by gamma rays [28].

Using electrochemical methods or europium(II) salts, certain Rieske proteins can be reduced beyond the usual mixed-valence $[2Fe–2S]^{+}$ form to give diamagnetic

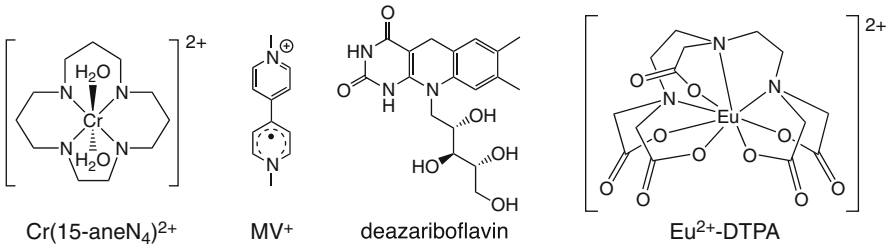

Fig. 2 Reducing agents that have been used to generate the all-ferrous redox level in biological iron–sulfur clusters

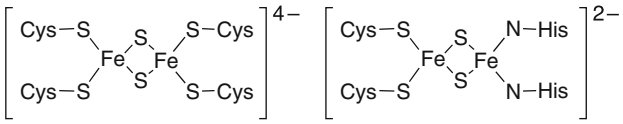

Fig. 3 There is more negative charge on a normal $[2Fe–2S]^0$ cluster (*left*) than on a Rieske $[2Fe–2S]^0$ cluster, and so the Rieske cluster is less difficult to reduce to the all-ferrous state

$[2Fe–2S]^0$ clusters [29, 30]. The iron–sulfur clusters in Rieske proteins are special because one of the iron atoms is coordinated by two histidine residues (Fig. 3). This change in coordination reduces the overall negative charge on the cluster, and makes all of the cluster redox potentials more positive by several tenths of a volt. Therefore, it is not surprising that these clusters are the least difficult to reduce to the unusual all-ferrous state. Despite this influence, the $[2Fe–2S]^{+/0}$ potentials remain quite cathodic, near −0.8 V. This potential is pH-dependent, which implies that the reduced form is protonated, most likely on a bridging sulfide [30].

2.2 *Three-Iron Clusters*

[3Fe–4S] clusters are typically observed in the $[3Fe–4S]^+$ (Fe_3^{3+}) and $[3Fe–4S]^0$ ($Fe^{2+}Fe_2^{3+}$) states, but protein film voltammetry at low potentials has shown a two-electron reduction of the $[3Fe–4S]^0$ form to the all-ferrous $[3Fe–4S]^{2-}$ oxidation level (Fig. 4) [31]. This phenomenon was observed in several different three-iron ferredoxins [32]. Bulk electrolysis yielded samples for UV–vis, EPR, and magnetic circular dichroism (MCD) characterization that were consistent with this formulation, although the data did not elucidate the ground spin state of the cluster. Though the standard potential for forming the highly reduced state is ca. −0.7 V, the potential is very pH-dependent. At pH 4, the potentials are close to −0.5 V.

This pH dependence also gives insight into the mechanism through which the protein stabilizes the significant negative charge on the cluster. The slope of the plot of pH vs. potential (the "Pourbaix diagram") gives information on the number of protons transferred in the process. Interestingly, two protons accompany the two

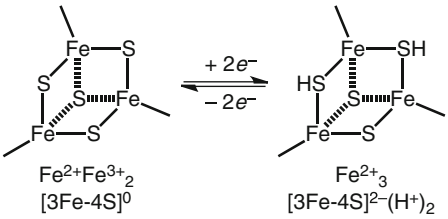

Fig. 4 In some [3Fe–4S] clusters, a two-electron reduction gives an all-ferrous state. Though protonation of the reduced form is evident from electrochemical data, the proton locations given here are speculative

electrons during reduction of $[3Fe–4S]^0$ to $[3Fe–4S]^{2–}$, neutralizing the added positive charge and moderating the reduction potential. The site of protonation is not yet known for the three-iron ferredoxins, but the protonation may be one factor that makes electron transfer relatively slow in this system [33].

2.3 Four-Iron and Larger Clusters

2.3.1 Introduction to Nitrogenase

Considering that nitrogenase reduces N_2, one of the most inert enzyme substrates in biological chemistry, it is not surprising that nitrogenase contains several examples of highly reduced iron–sulfur clusters. Because these clusters have been subjected to especially intense study, two sections below deal with the iron–sulfur clusters in nitrogenase. The molybdenum-dependent nitrogenase system has a total of three clusters that lie in two proteins: the Fe protein and the MoFe protein. The MoFe protein contains two eight-metal clusters, one of which is termed the "P cluster" and the other is called the "M cluster" or "FeMoco." The orientation of the clusters in the Fe protein–MoFe protein complex indicates that electrons flow from the Fe protein to the P cluster, and from the P cluster to the FeMoco. (As discussed below, there is controversy about the order of these events, and about the number of electrons transferred in each event.) Both the P cluster and the Fe protein cluster have been characterized in states that are all-ferrous. The P cluster of the MoFe protein will be described first, and then the four-iron cluster of the Fe protein. The discussion will be selective, focusing only on the highly-reduced (all-ferrous) forms of each cluster.

2.3.2 Nitrogenase P Cluster

The P cluster has eight iron atoms and seven sulfides. The X-ray crystal structures of both *Azotobacter vinelandii* and *Klebsiella pneumoniae* proteins have been obtained in the dithionite-reduced form (P^N). As indicated in Fig. 5, the reduced

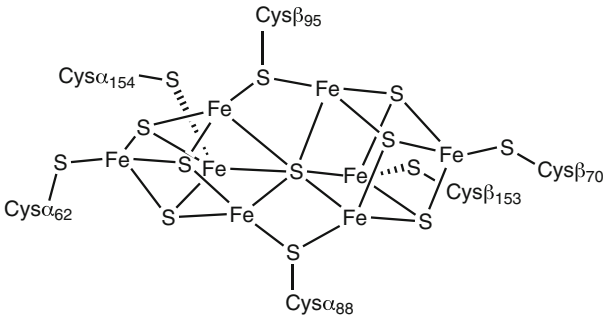

Fig. 5 The structure of the reduced P^N cluster, which has been crystallographically characterized in this likely all-ferrous state

cluster is a "double-cubane" structure of two [4Fe–4S] clusters joined at a common six-coordinate sulfide [34, 35]. The cluster lies at the interface of the α and β subunits of the MoFe protein, and is held by three cysteine residues from each subunit. Two cysteine sulfur atoms bridge the two cubes, and each iron atom is four-coordinate (pseudotetrahedral) in the P^N state.

The reduced P^N state is EPR silent and shows no magnetic splitting in its Mössbauer spectrum, indicating that it is diamagnetic [36]. Interestingly, it can be oxidized by two one-electron steps with potentials of −0.31 V (P^{1+}/P^N) and +0.08 V (P^{2+}/P^{1+}) [37]. Based on the isomer shifts in Mössbauer spectra, the P^N form is thought to be all-ferrous [38]. Although it is beyond the scope of this review, it is worth noting that the X-ray crystal structure of the P^{2+} form displays a structural change where the two cubanes move apart [35]. The coupling of conformational and redox changes suggests a potential gating role for electron flow into the FeMoco [39]. The redox changes also correlate with the number of surface-exposed water molecules [40].

The P cluster is likely to play a role in electron transfer, because it is situated about 15 Å from the site at which the Fe protein binds and about the same distance from the FeMoco. It has been difficult to find direct support for this idea, because the resting-state P^N form is EPR silent and thus difficult to follow spectroscopically. However, a Ser188Cys variant of the MoFe protein has a modified P cluster with a paramagnetic resting state, for which the EPR signal disappears during turnover and then reappears. This behavior is as expected for an electron relay [41, 42].

If the P cluster is indeed all ferrous and participates in electron transfer, it raises interesting issues that form the basis for continued research. First, the ferrous oxidation state is generally considered to the lowest possible oxidation state for biological iron (in the absence of strong-field donors like CO and CN^- found in hydrogenases). However, if the P cluster in its resting P^N (all-ferrous) state is to act as a typical relay by accepting an electron from the Fe protein and then passing it along to the FeMoco, it would need to be reduced to a state P^{1-} that would have at least one iron atom below the ferrous state (Fig. 6a). Alternatively, the P cluster would need to transfer an electron to the FeMoco *prior* to being reduced by the Fe

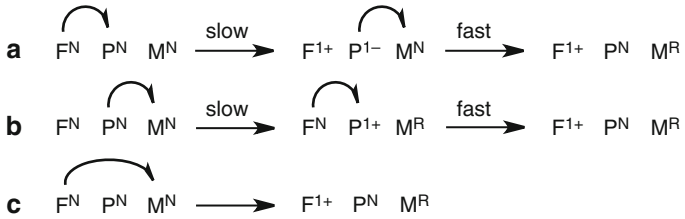

Fig. 6 Three models for electron transfer from the Fe protein (F^N in its reduced, resting state) to the FeMoco (M^N in its resting state; M^R in its reduced state) through the P cluster (P^N in its resting state). Mechanism (**a**) would require an unprecedented subferrous oxidation level. Mechanism (**b**) is termed the "deficit spending" model, where P → M electron transfer is followed by rapid backfilling by the Fe protein [43]. Mechanism (**c**) would skip the P cluster entirely, but seems unlikely given the spatial disposition of proteins and the influences of mutations near the P cluster on activity [42, 44]

protein. This model has been termed "deficit spending" [43]. Though the deficit spending model implies that P would become oxidized, EPR spectroscopy shows no sign of an oxidized P cluster under conditions of low electron flux [45]. Thus, the FeMoco would pull an electron out of the P cluster, which would then suck an electron out of the Fe protein rapidly enough that no significant concentration of oxidized P cluster builds up (Fig. 6b). Dean, Hoffman, and Seefeldt have recently shown using a S188C mutant (which substitutes one donor to the P cluster to shift its potential) that electron transfer from the Fe protein to the P cluster is much faster than from the P cluster to FeMoco, supporting the feasibility of the deficit spending model [43].

The deficit spending mechanism requires docking of Fe protein with MoFe protein *before* the rate-limiting electron transfer from the P cluster to the FeMoco. But how does the FeMoco sense whether the Fe protein is present? Association, dissociation, and movement of the Fe protein on the outside of the MoFe protein cause no obvious conformational change near the FeMoco [46]. It is not clear how this dilemma will be resolved: perhaps there is actually transient formation of P^{1-}; perhaps P^N is not actually all-ferrous but instead $Fe_6^{2+}Fe_2^{3+}$; or perhaps there is a "trigger" for electron flow that has not yet been discovered. One interesting possibility is that that Fe protein binding is coupled to coordination of S188 to the P cluster, lowering its potential and inducing electron transfer to FeMoco and then "backfilling" by the Fe protein [43].

Another issue is raised by the possibility of two-electron redox processes in both the Fe protein (see below) and the P cluster. This naturally raises the possibility of transferring two electrons at a time, which would make the enzyme more efficient. A two-electron transfer would explain why P is a "double cluster" and why all nitrogenase substrates are reduced by an even number of electrons. Two-electron transfers are rare because it would be difficult to balance the large amount of charge displacement; in nitrogenase, this charge balance could come from protonation of substrates at the FeMoco.

2.3.3 Nitrogenase Fe Protein

The Fe protein contains a single [4Fe–4S] cluster at the interface of two identical polypeptide chains. It may be reduced to a $[4Fe–4S]^{+}$ ($Fe_3^{2+}Fe^{3+}$) form by dithionite reduction. This reduced form, which has spectroscopic features typical of reduced [4Fe–4S] clusters, is essential for both the biosynthesis and the catalytic function of the nitrogenase system. Classic studies on the turnover mechanism by Thorneley and Lowe were understood in the context of the reduced Fe protein associating and dissociating from the catalytic MoFe protein once for each electron transferred [47]. This corresponded with the usual one-electron-transfer ability of iron–sulfur clusters. However, in 1994, Watt reported the reduction of the $[4Fe–4S]^{+}$ ($Fe_3^{2+}Fe^{3+}$) form of the Fe protein to a "super-reduced" form using two equivalents of reduced methylviologen (illustrated in Fig. 2b) at −0.46 V [48]. The reduced form was proposed to be all-ferrous $[4Fe–4S]^{0}$ based on the stoichiometry of reduction and reoxidation. The iron(II) was also extracted by 2,2′-bipyridine, giving >93% of the expected iron(II) concentration.

Subsequent studies have used a variety of strong reducing agents to generate super-reduced clusters in the nitrogenase Fe protein, and evidence exists for two different forms, one with a total spin $S = 4$ and another with $S = 0$. The reason why it is possible to generate two different forms at the same redox level is not clear. (The possibility that spent reducing agent binds to the protein has been ruled out in each case described below.) As will be seen, the $S = 4$ state has been characterized in much greater detail and by multiple research groups, and its formation is well established. The $S = 0$ state has been reported in only one paper, and is much more difficult to study due to the inability to use magnetic measurements.

The $S = 4$ state of the all-ferrous cluster can be generated using Ti(III) citrate, deazariboflavin, Eu^{2+}-DTPA [49], or Cr^{2+}(15-aneN_4), as well as by radiolytic reduction. Each of these reductants gives a characteristic $g_{\text{eff}} = 16$ signal in EPR spectra [50]. The first definitive spectroscopic characterization of the $S = 4$ form came from Ti(III) citrate reduced protein that was examined using Mössbauer spectroscopy and parallel-mode X-band EPR spectroscopy at 2 K [51]. Both the Mössbauer isomer shift of $\delta = 0.68$, and XAS studies showing the iron edge energy, indicate that all four sites have the Fe^{2+} oxidation state [51, 52]. The EPR transition at $g_{\text{eff}} = 16$ is characteristic of an integer-spin system. The EPR and variable-field Mössbauer spectra indicate the $S = 4$ ground state. A signature visible absorption band is present at $\lambda_{\max} = 520$ nm, and apparent *d–d* transitions can be detected using MCD [53].

The Mössbauer signal of the $S = 4$ cluster may be resolved into a 3:1 ratio of signals with different quadrupole splitting values, suggesting that the "cubane" structure is compressed along a body diagonal (C_3 axis) [50, 51]. EXAFS data suggest that the cluster has a longer (2.77 Å) and a shorter (2.53 Å) Fe–Fe distance [52]. X-ray crystallography shows that the cluster has identical coordination in the all-ferrous form as in the other oxidation states, but the resolution of the X-ray data

was not sufficient to clearly distinguish the bond lengths within the cluster [54]. Computational investigations indicate that all of these data can be reconciled within a model in which one of the high-spin iron atoms has its spin aligned opposite to the spin on the three other iron atoms [23].

Potentiometric titration with $Cr^{3+/2+}$-EDTA indicated that the redox potential of the $S = 4$ form is -0.79 V at pH 8 [55]. This is roughly 0.48 V more negative than the potential for the reduction of $[4Fe–4S]^{2+}$ to $[4Fe–4S]^{+}$. What stabilizes the very low oxidation state enough for its observation? The X-ray crystal structure indicates an unusually large number of NH-thiolate hydrogen bonds [54]. Hydrogen bonds are well known to modulate the redox potentials of iron–sulfur clusters [24]. Even though the super-reduced state is stable enough for isolation and characterization in vitro, the reduction is outside the range of typical physiological electron donors in vivo, raising questions about whether this form is relevant in living organisms.

An apparently different form of the all-ferrous Fe protein has been generated using flavodoxin [56]. A combination of UV–vis, EPR, stoichiometry of reduction and solution magnetic susceptibility indicated that this form has $S = 0$, because it lacks the EPR signal and visible UV–visible band. Flavodoxin is a physiological electron donor whose potential is -0.52 V. This implies that the $[4Fe–4S]^{+/0}$ potential is less negative than -0.52 V, and much less negative than the -0.79 V value measured for the $S = 4$ form. In the future, it would be valuable to pursue CD and/or X-ray diffraction studies to show if the protein conformation is different between these different forms.

If the results on the flavodoxin reduction are correct, it is not clear why dithionite, which has a nominal redox potential of -0.66 V, does not reduce the $[4Fe–4S]^{+}$ state to this $[4Fe–4S]^{0}$ state. This discrepancy has been attributed to a reaction between dithionite and the all-ferrous protein [48]. It is worth noting that dithionite does not have a simple reversible redox couple, and that dithionite purity can be problematic [57]. Titanium(III) citrate, the reductant used to form the $S = 4$ state, also has a complicated speciation in aqueous solution [58]. Further study is needed to understand the reason for the reductant-dependent generation of different all-ferrous species.

If a doubly-reduced Fe protein is involved in nitrogenase catalysis, it could in principle achieve a two-electron reduction of the MoFe protein. This idea found support in single-turnover experiments from two different labs showing that the all-ferrous state could be used productively for reduction of substrates (protons, acetylene, or N_2) [48, 53]. Spectroscopic studies also demonstrated nucleotide binding to the $[4Fe–4S]^{0}$ state, and binding to the MoFe protein. Watt has also shown that use of Ti(III) (which generates the $[4Fe–4S]^{0}$ state) eliminates the characteristic “lag phase” or induction period before substrate reduction [59]. The most direct evidence for two-electron transfer comes from experiments in which the turnover frequencies of ATP and substrate indicated that 2 ATPs were consumed per 2 electrons when using Ti(III) as the reductant [60]. Since 2 ATP molecules are hydrolyzed in the course of each Fe protein–MoFe protein dissociation cycle, this implies that *two* electrons are passed each time the all-ferrous Fe

protein binds to the MoFe protein. The product distributions were similar with the different reducing agents, suggesting that the FeMoco functions similarly despite the change in electron supply [60]. However, since Ti(III) produces the state of the cluster which apparently has a redox potential of −0.79 V, it is unclear whether this very reduced species is relevant in vivo.

2.3.4 Other Four-Iron Clusters

A second example of a protein that supports a $[4Fe–4S]^0$ cluster was identified more recently in HgdC, the activator protein for 2-hydroxyglutaryl-coenzyme A dehydratase (HgdAB) [61]. Each Hgd protein has a [4Fe–4S] cluster, and reduced cluster in the reduced activator transfers an electron to the iron–sulfur cluster of the enzyme. This electron transfer ultimately activates the enzyme for catalysis. When the reduced $[4Fe–4S]^+$ form of the activator protein is reduced with 10M equivalents of titanium(III) citrate, about 50% of it is converted to a super-reduced form that is spectroscopically similar to the $S = 4$ all-ferrous state of the nitrogenase Fe protein. Mössbauer and EPR studies were used for comparison and characterization. It is not clear why excess titanium(III) citrate is necessary: it may be that the redox potential is very negative, or that there is a distribution of cluster environments in the protein sample. In addition, the functional role (if any) of a doubly reduced cluster is not clear in this system, because one electron is sufficient to fulfill its activator role.

Both the nitrogenase Fe protein and HgdC have similar quaternary structures with the cluster at the interface of two identical peptides. This suggests that a [4Fe–4S]-bridged homodimer may be unusually adept at stabilizing the large negative charge of the super-reduced clusters. It also suggests that other proteins with clusters at solvent-exposed interfaces (which often couple nucleotide triphosphate hydrolysis to reduction) may provide additional examples of biological $[4Fe–4S]^0$ clusters.

3 Synthetic All-Ferrous Iron–Sulfur Clusters of Nuclearities Two and Three

3.1 Two-Iron Clusters [2Fe–2S]^0

In 1973, the first complex having a [2Fe–2S] core was isolated as the diiron(III) compound $[Fe_2S_2(o\text{-}(CH_2S)_2Ph)_2]^{2-}$, which has the structure shown as **6c** in Fig. 7 [62]. Cyclic voltammetry (CV) of this complex in DMF (dimethylformamide) or acetonitrile gave two well-separated one-electron cathodic peaks. This indicates the stepwise two-electron reduction of the Fe_2^{3+} core to a Fe_2^{2+} state (Eq. 1) [62, 63].

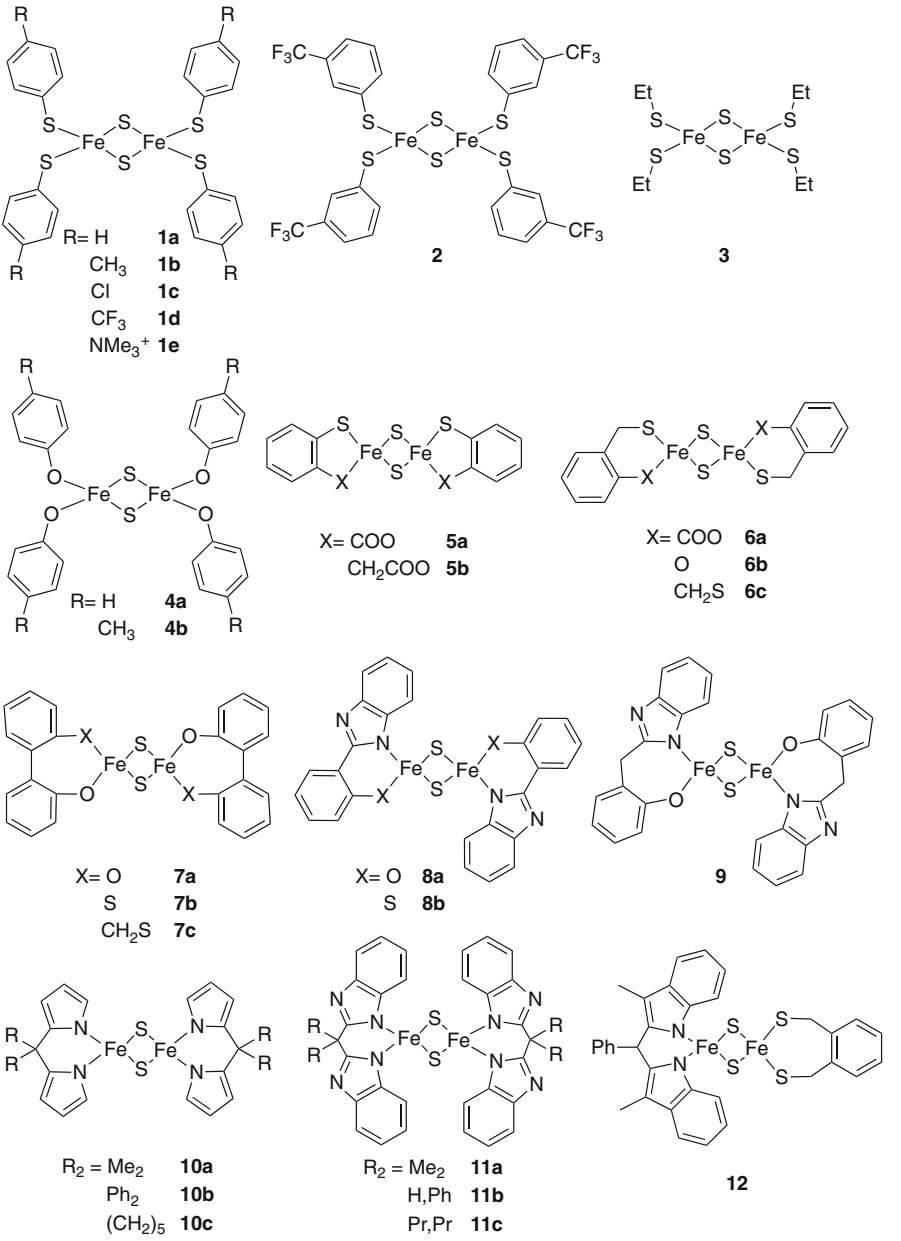

Fig. 7 Synthetic [2Fe–2S] complexes that can be reduced by two electrons from the $[2Fe–2S]^{2+}$ state, presumably generating all-ferrous clusters in solution. Charges are not shown for simplicity

Table 1 CV data for [2Fe–2S] complexes

	$E_{1/2}$ (V)[a,b]		
	$Fe^{3+}Fe^{3+}/Fe^{3+}Fe^{2+}$	$Fe^{3+}Fe^{2+}/Fe^{2+}Fe^{2+}$	Reference
1a	−0.85	−1.13	[64]
1b	−0.91	−1.17	[64]
1c	−0.73	−1.06	[64]
1d	−0.81?[c]	−1.19?[c]	[65]
1e	−0.59	~ −1.01	[64]
2	−0.92?[c]	−1.23?[c]	[65]
3	−1.20	−1.45?[c]	[69, 70]
4a	−1.08	−1.49?[c]	[71]
4b	−1.13	−1.54?[c]	[71]
5a	−0.78	−1.60?[c]	[70]
5b	−0.84	−1.42?[c]	[70]
6a	−0.91	−1.29?[c]	[70]
6b	−1.20	−1.52?[c]	[72]
6c[d]	−1.27	−1.57?[c]	[62]
7a	−1.12	−1.60?[c]	[71]
7b	−1.11	−1.59?[c]	[72]
7c	−1.23	−1.52?[c]	[72]
8a	−0.85	−1.73?[c]	[69, 73]
8b	−0.75	−1.63?[c]	[69, 73]
9	−0.89	−1.71?[c]	[69, 73]
10a[d]	−0.93	~ −1.8[e]	[74]
10b[d]	−0.99	~ −1.9[e]	[74]
10c[d]	−1.05	~ −2.0[e]	[74]
11a	−0.58	−1.57	[69, 73]
11b[f]	−0.50	−1.46	[75]
11c[f]	−0.58	−1.56	[76]
12[d]	−1.09	~ −1.8	[68]

[a]Potentials given versus NHE; unless otherwise indicated, they were converted from SCE reference (+0.24 V)
[b]$E_{1/2} = 0.5(E_{pc} + E_{pa})$
[c]E_{pc} only for an irreversible wave
[d]Potentials converted from $Cp^*_2Fe^+/Cp^*_2Fe$ reference (+0.26 V)
[e]Clusters can be further reduced in an irreversible wave; potentials were not reported
[f]Potentials converted from Cp_2Fe^+/Cp_2Fe reference (+0.64 V)

The second reduction, which leads to the all-ferrous $[2Fe–2S]^0$, has a very negative potential of $E_{1/2} = -1.81$ V and is quasireversible.

$$\underset{Fe^{3+}Fe^{3+}}{[Fe_2S_2(SR)_4]^{2-}} \xrightarrow{e^-} \underset{Fe^{3+}Fe^{2+}}{[Fe_2S_2(SR)_4]^{3-}} \xrightarrow{e^-} \underset{Fe^{2+}Fe^{2+}}{[Fe_2S_2(SR)_4]^{4-}} \quad (1)$$

In the years since then, numerous ligands have been used to construct complexes with the [2Fe–2S] core. Some of them are shown in Fig. 7 [62, 64–68].

All-thiolate terminated clusters were the first and most widely studied. Table 1 shows that arylthiolate complexes are more easily reduced than alkylthiolate

species. Within the arylthiolate series, the reduction potential becomes less negative as the electron-withdrawing power of the *para* substituent on the aryl group increases [64, 77]. Thus the choice of thiolate substituent can lead to a marked influence on the redox potential. Other complexes with chelating supporting ligands, for example a Rieske model with one NN-coordinated iron and one SS-coordinated iron, show an irreversible cathodic feature at a much more negative potential around −1.8 V [66, 67, 77].

Though these high spin $[2Fe–2S]^0$ clusters have been generated in solution by reducing $[2Fe–2S]^{2+}$ species in electrochemical experiments, they have not been isolated as solids. The instability can be attributed to two factors. First, most of the synthetic $[2Fe–2S]^0$ clusters are tetraanions, because they are supported by four anionic donors. As a result, the $[2Fe–2S]^{+/0}$ potentials for the synthetic compounds are usually more cathodic than −1.0 V, which is much more extreme than those for the proteins discussed in Sect. 2. It is likely that this difference is due to the lack of hydrogen bonds that withdraw charge density from the thiolate sulfur atoms. Therefore, it would be an interesting challenge in future research to append groups that can form hydrogen bonds to the coordinated sulfur atoms, to learn the effect on the redox potential. This may lead to isolable all-ferrous [2Fe–2S] compounds.

A second factor contributing to the difficulty in isolating all-ferrous [2Fe–2S] clusters is that the two-electron reduction of $[2Fe–2S]^{2+}$ clusters takes place through the intermediacy of $[2Fe–2S]^{+}$ clusters, which are often unstable themselves. Many $[2Fe–2S]^{+}$ clusters couple with loss of two terminal ligands to form $[4Fe–4S]^{2+}$ clusters, leaving the iron atoms in the same oxidation states (Eq. 2). This coupling is especially rapid in halide-ligated dinuclear complexes $[Fe_2S_2X_4]^{2-}$. In these systems, the initial cathodic CV features are associated with the 2−/3− couples of the dinuclear clusters, but the next wave appears at the same potential as the analogous four-iron clusters in the CV [78, 79]. This observation suggests that the second reduction is associated with four-iron clusters rather than two-iron clusters. However, since thiolate ligands are less labile than halides, the conversion to the four-iron cluster is not as fast in sulfur-ligated dinuclear complexes $[Fe_2S_2(SR)_4]^{2-}$, and thus a quasireversible reduction to $[2Fe–2S]^0$ can still be observed using CV [64].

$$2\,[Fe_2S_2(SR)_4]^{3-} \longrightarrow [Fe_4S_4(SR)_4]^{2-} + 4\,RS^{-}. \tag{2}$$

Singly reduced $[2Fe–2S]^{+}$ clusters can be stabilized by using chelating capping ligands, thus slowing the ligand loss that leads to dimerization. The combination of this strategy and the use of electron-withdrawing benzimidazole groups is evident in **11a**, which was the first reduced $[2Fe–2S]^{+}$ cluster to be isolable as a solid [69]. A close relative of this compound, **11b**, was crystallographically characterized recently [75]. Cyclic voltammetry studies on **11b** and another close relative, **11c** [76], show reversible reduction to the all-ferrous level at −1.46 V and −1.56 V, respectively. These observations suggest that the all-ferrous form might also have enhanced stability with these capping ligands.

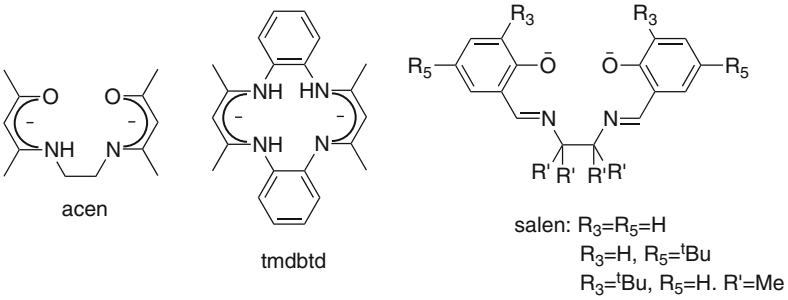

Fig. 8 Ligands used for $[2Fe–1S]^{4+}$ compounds, which could not be reduced to the all-ferrous $[2Fe–1S]^{2+}$ state

Since the formation of the all-ferrous clusters in synthetic systems has been observed only by CV, there are no spectroscopic data on the putative $[2Fe–2S]^{0}$ clusters. These data would be very useful to compare to the biological examples in Sect. 2, and future advances are eagerly awaited.

3.2 Two-Iron Clusters $[2Fe–1S]^{2+}$

Tetradentate ligands, such as acen [80], salen [81, 82] and tmdbtd [83] (H_2acacen = *N*,*N*′-ethylenebis(acetylacetoneiminate); H_2salen = 1,2-bis(salicylideneaminato) ethanediyl; H_2tmdbtd = 5H,14H-6,8,15,17-tetramethyldibenzo[*b*,*i*][1,4,8,11] tetraazacyclotetradecene) (Fig. 8), support sulfide-bridged diiron cores at the diiron (III) oxidation level ($[2Fe–1S]^{4+}$). No reduction to all-ferrous $[2Fe–1S]^{2+}$ clusters appears to be accessible using these ligand systems. For example, the CV of $[2Fe–1S]^{4+}$ clusters supported by salen ligands showed a reversible reduction to the mixed-valence $[2Fe–1S]^{3+}$ level, followed by a broad, irreversible reduction around −1.5 V. Fe–S bond cleavage apparently occurs during the electrochemical decomposition, because an iron(III) salen monomer is formed [82].

In 2004, a stable all-ferrous $[2Fe–1S]^{2+}$ cluster **13** was isolated, and it was stabilized by a very bulky β-diketiminate ligand (L^{Me} = C[C(Me)N(2,6-diisopropylphenyl)]$_2$)$^-$) that made each iron center three-coordinate [84]. Two novel methods have been reported for the synthesis of **13** (Fig. 9). One is the oxidation of a formally diiron(I) N_2 complex with elemental sulfur [84], and the other is heating a mixture of a phosphine sulfide and an iron(II) alkyl complex, a reaction that presumably proceeds by β-hydride elimination followed by reductive elimination of H_2 [85]. It remains to be seen whether these synthetic methods are general to other series of iron sulfides in which high-spin iron(I) precursors and high-spin iron (II) alkyl/hydride precursors are available.

The spins on the two Fe^{2+} ions in **13** antiferromagnetically couple to give a diamagnetic ground state, as shown by variable-field Mössbauer spectroscopy.

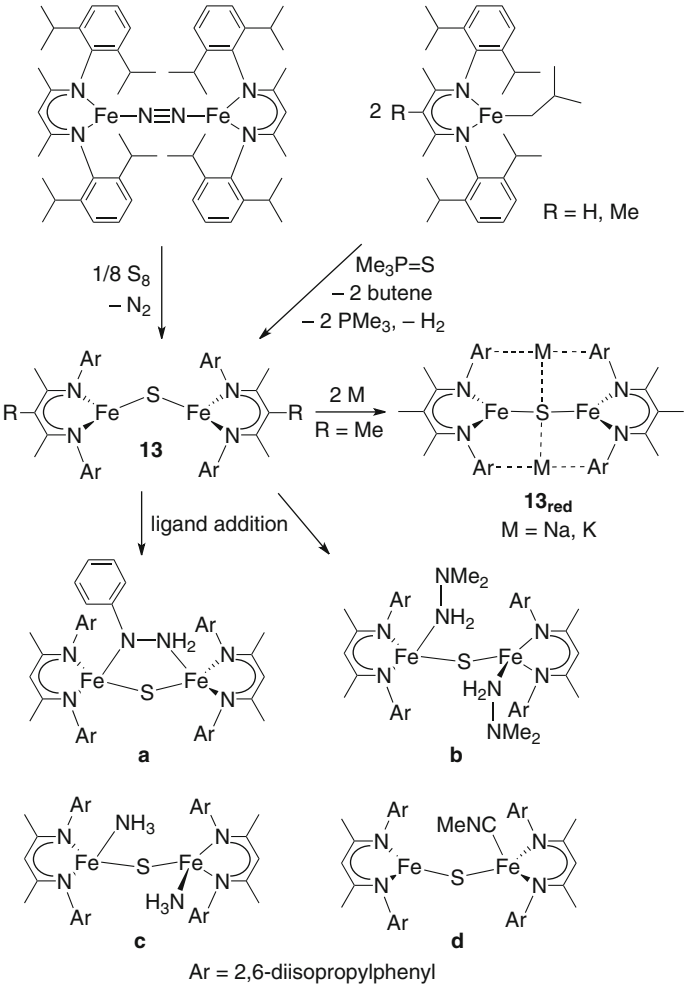

Fig. 9 Formation and reactions of the diiron(II) sulfido complex **13**, which is supported by bulky β-diketiminate ligands. It may also be reduced to the first iron(I)-containing iron-sulfido complexes $\mathbf{13_{red}}$, which feature alkali metals bound to the sulfur and the arene rings of the β-diketiminates

In contrast to the all-ferric $[2Fe–1S]^{4+}$ species with a diiron(III) core [80, 81, 83], the diiron(II) cluster **13** is quite bent at the bridging sulfur (Fe–S–Fe $< 120°$). Unfortunately, the exact bond angle is not known with precision because of disorder in X-ray crystal structures of the compound, and computational studies would be helpful in defining this angle and determining whether the lower oxidation state is the cause of the more acute angle (perhaps through a decrease in metal–sulfur π-bonding).

Compound **13** was the first iron–sulfur cluster to be structurally characterized to have three-coordinate iron atoms. This coordinative unsaturation enables **13** to

react with donor ligands that give the products pseudotetrahedral iron atoms [84]. An interesting example of cooperative reactivity is the reaction of **13** with phenylhydrazine ($PhNHNH_2$), which gives the mixed-valence iron(II)–iron(III) compound $(L^{Me}Fe)_2(\mu\text{-}S)(\mu\text{-}PhNNH_2)$ (Fig. 9a) [84]. The overall reaction is a two-electron reduction of the N–N bond of hydrazine by two of the diiron clusters (each cluster is oxidized by one electron). Other hydrazines were not reduced by **13**, with 2:1 adducts formed instead (Fig. 9b); similar adducts were characterized using nitrogen-based donors such as NH_3 and MeCN (Fig. 9c, d).

In recent work, addition of Na or K (as potassium graphite) to **13** was shown to give two-electron reduction to the diiron(I) complex $\mathbf{13_{red}}$ [85]. The iron atoms in both the sodium and potassium versions of $\mathbf{13_{red}}$ are again three coordinate. They have a high-spin d^7 configuration, as demonstrated by Mössbauer spectroscopy and density-functional calculations, and the iron(I) ions are antiferromagnetically coupled to give a diamagnetic ($S_{total} = 0$) ground state. The surprising ability to reduce these compounds to the Fe^{1+} (subferrous) oxidation level was attributed to the stabilizing effect of the main-group cations on the anionic core, as they are not stable without the alkali metals incorporated into the structure. It remains to be seen whether the presence of closely held cations will be more generally useful for the isolation of other highly reduced iron–sulfur clusters.

The open coordination sites on the three-coordinate iron atoms in these iron-sulfide compounds offer significant promise for modifying the coordination sphere. In particular, a second sulfide could be introduced into the ligand sphere to form a [2Fe–2S] cluster, or perhaps other iron–sulfur clusters could be incorporated to form larger structures. The ability to vary the substituents in the β-diketiminate also promises the ability to tune the redox potential and sterics of this unusual type of cluster.

3.3 Three-Iron Clusters

Despite the biological examples of $[3Fe\text{–}4S]^{2-}$ clusters (Sect. 2.2), there are not yet reports of generating this redox level in a synthetic cluster, even using electrochemistry. As described in Sect. 2.2, the highly reduced biological clusters are protonated during reduction, and this process of charge balancing is typically not observed in synthetic clusters. Therefore, it seems possible that mimicking the hydrogen-bond donors (or Brønsted acids) that stabilize the biological $[3Fe\text{–}4S]^{2-}$ clusters might render this goal a reality.

There are examples of all-ferrous $[3Fe\text{–}1S]^{4+}$ cores with all ferrous sites, in compounds of the type $[Fe_3S(S_2\text{-}o\text{-}xyl)_3]^{2-}$ [86, 87]. These have a μ_3-bridging sulfide, three μ_2-bridging thiolates, and three terminal thiolates, as shown in Fig. 10. No electrochemically reversible waves were seen in the CV responses of these compounds.

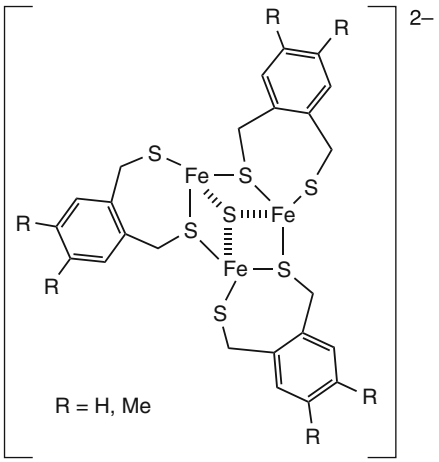

Fig. 10 All-ferrous three-iron sulfide clusters supported by chelating ligands

4 Synthetic All-Ferrous Iron–Sulfur Clusters of Nuclearity Four

4.1 Four-Iron Clusters [4Fe–4S]^0 with Thiolate and Phenoxide Ligands

Four-iron clusters at the [4Fe–4S]^0 oxidation level were first detected in electrochemical investigations of the thiolate-terminated clusters $[Fe_4S_4(SR)_4]^{2-}$ in aprotic solvents; because the starting material formally has two iron(II) and two iron(III), the second reduction of the cluster around −1.4 V was postulated to give the all-ferrous form [78, 88, 89]. Analogous reductions have been done with dithiolene-terminated clusters, but there are no thorough studies of their voltammetry at negative potentials [90]. Because the redox ambiguity of the dithiolene ligands makes it difficult to assign the oxidation state of the iron atoms in these clusters, the discussion here focuses on the thiolate-terminated clusters. The key reduction of $[Fe_4S_4(SR)_4]^{3-}$ to $[Fe_4S_4(SR)_4]^{4-}$ occurs at potentials more cathodic than −1.0 V (Table 2), and thus the reduced species are highly reducing and very sensitive.

Table 2 shows the potentials for a number of these clusters. In general, these follow the same trend as the 2−/3− potentials, with potentials more cathodic by 0.7 V. The potentials correlate with the Hammett parameter for aromatic substituents, with electron-withdrawing groups giving a less negative potential [78, 89]. The use of positively charged ammonium substituents gave a positive shift in the redox potential, but the amount of shift was consistent with the expected substituent effect, without any extra consideration for the change in charge [89]. The 3−/4− waves are quasireversible, implying that the all-ferrous species are unstable, except for the bulkiest thiolate substituents like R = *t*-butyl. Thus, they have not been isolated.

Table 2 Electrochemical generation of thiolate-terminated cuboidal all-ferrous species $[Fe_4S_4(SR)_4]_4^{4-}$ in DMF[a]

R	$E_{1/2}^{3-/4-}$ (V)	Reference
CH_3	−1.78	[78]
CH_2CH_3	−1.80	[78]
$CH(CH_3)_2$	−1.86	[78]
$CH_2C_6H_{11}$	−1.89	[78]
$C(CH_3)_3$	−1.92	[78]
$CH_2C_6H_5$	−1.72	[78]
m-$C_6H_4(CH_2)_2$	−1.79	[78]
C_6H_5	−1.51	[64, 78]
p-$C_6H_4CH_3$	−1.52	[64, 78]
p-$C_6H_4NMe_2$	−1.56	[78]
p-$C_6H_4NMe_3^+$	−1.12	[64, 78]
p-$C_6H_4NO_2$	−1.01	[78]
p-C_6H_4Cl	−1.39	[64]
m-$C_6H_4(CF_3)$	−1.49	[65]
p-$C_6H_4(CF_3)$	−1.32	[65]

[a]Potentials converted from SCE reference (+0.24 V)

The electrochemically generated all-ferrous clusters have been used for reduction of substrates. In research using $[Fe_4S_4(SR)_4]$ systems (R = benzyl, *t*-butyl or macrocycle), electrocatalytic reduction of CO_2 to formate proceeded from the all-ferrous cluster [91–93]. Likewise, the exchange of H_2 and D_2 to form HD occurs through the action of a $[4Fe–4S]^0$ cluster [94]. In these reports, the intermediacy of $[4Fe–4S]^0$ rather than $[4Fe–4S]^+$ was shown by the observation of cathodic electrocatalytic current only when the potential entered the range when $[4Fe–4S]^0$ is formed. In the case of acetylene reduction to ethylene, $[Fe_4S_4(SPh)_4]^{3-}$ is capable of catalysis, but $[Fe_4S_4(SPh)_4]^{4-}$ reduces the acetylene more quickly [95]. A wider range of electrocatalytic reductions has been achieved with mixed molybdenum/iron systems, which are beyond the scope of this review and have been reviewed [96]. Other reports use extremely strong chemical reducing agents (e.g. sodium sand) to generate the tetraanion, followed by treatment with the substrate. This treatment has given catalytic thiol addition to isocyanides [97]. In combination with a Mo–N_2 coordination complex, one of the dithiolene-appended clusters was reported to give small amounts of ammonia [98, 99]. However, given the short lifetimes of the reduced $[Fe_4S_4(SR)_4]^{4-}$ clusters (as demonstrated by CV), it is not clear whether the reactions that involve chemical reduction of the cluster are mediated by the all-ferrous cluster or by its decomposition products.

The halide-terminated clusters with X = Cl and Br give irreversible $[Fe_4S_4X_4]^{3-/4-}$ reductions with E_{pc} of −1.4 to −1.5 V [79]. Thus, the halide species are more easily reduced than the thiolate species, but the reductions give tetraanions that are not stable on the time scale of the CV experiment. On the other hand, the phenoxide-terminated clusters $[Fe_4S_4(OPh)_4]^{2-}$ have two electrochemically reversible reduction features at −1.6 V [100]. These potentials are somewhat more cathodic than the thiolate analogues, suggesting that the phenoxides do not support the buildup of negative

Table 3 Reduction of phosphine-ligated iron–sulfur cubanes $[Fe_4S_4(PR_3)_4]^+$ to the all-ferrous level[a]

Terminal ligands	Solvent	$E_{1/2}^{+/0}$ (V)	Reference
$(P^tBu_3)_3Cl$	1,2-Dichloroethane[a]	−1.2?[b]	[104]
$(P^tBu_3)_3Br$	1,2-Dichloroethane[a]	−1.2?[b]	[104]
$(P^tBu_3)_3I$	1,2-Dichloroethane[a]	−1.3?[b]	[104]
$(PCy_3)_3Cl$	CH_2Cl_2[c]	−0.83	[103]
$(PCy_3)_3(SPh)$	CH_2Cl_2[c]	−0.82	[103]
$(P^tBu_3)_4$	CH_2Cl_2[c]	−0.74	[103, 105]
$(PCy_3)_4$	CH_2Cl_2[c]	−0.82	[105]
$(P^iPr_3)_4$	CH_2Cl_2[c]	−0.75	[105]

[a]Potentials converted from Ag^+ reference (+0.01 V)
[b]E_{pc} only for an irreversible wave
[c]Potentials converted from SCE reference (+0.24 V)

charge as effectively as the thiolates (the opposite of the trend expected from the relative electronegativities). Again, the all-ferrous forms have been studied only transiently in solution using CV, and no spectroscopic studies have been reported.

4.2 *Four-Iron Clusters [4Fe–4S]^0 with Phosphine Ligands*

Because phosphines are neutral and have some π-accepting character, they ameliorate the problem of charge buildup in the most reduced forms. Initial attempts to obtain reduced [4Fe–4S] clusters with aliphatic, sterically unencumbered phosphines as terminal ligands were unsuccessful, because addition of small phosphines gave known $[Fe_6S_6(PR_3)_4Cl_2]$ basket clusters [101, 102]. Larger phosphines with isopropyl, cyclohexyl, or *tert*-butyl substituents cannot fit into the basket structure, and so the [4Fe–4S] cubane core structure is maintained [103–105]. Interestingly, phosphines can be introduced with concomitant reduction of the cluster: the synthesis begins from the halide-terminated $[4Fe–4S]^{2+}$ clusters $[Fe_4S_4X_4]^{2-}$, and addition of phosphine reduces them to the $[4Fe–4S]^+$ level in the neutral product $[Fe_4S_4(P^tBu_3)_3X]$. Some of the phosphine is oxidized to the phosphine sulfide [104]. These clusters give an irreversible reduction waves around −1.2 V, indicating that the all-ferrous $[Fe_4S_4(PBu^t_3)_3X]^-$ with mixed ligation are not stable [104]. However, using a slight excess of large tertiary phosphines, it is possible to substitute all four iron atoms to yield $[Fe_4S_4(PR_3)_4]^+$ (R = Bu^t, Cy, Pr^i) [103]. The four-phosphine clusters could be reduced to the all-ferrous $[Fe_4S_4(PR_3)_4]^0$ level reversibly using electrochemistry; the relevant redox potentials are given in Table 3. Alternatively, $[Fe_4S_4(PR_3)_4]^0$ can be prepared by chemical reduction of the monocation with a slight excess of sodium acenaphthalenide. Unlike their positively charged precursors, the neutral black cubane clusters are soluble in benzene and toluene.

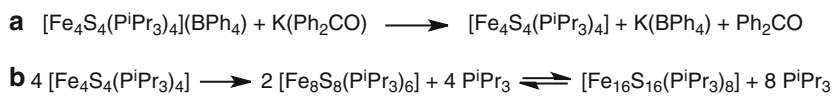

Fig. 11 (**a**) An example of the synthetic route that leads to all-ferrous $[Fe_4S_4(PR_3)_4]$ (R = ^{i}Pr, Cy, ^{t}Bu) in solution using potassium benzophenone. (**b**) Over days in solution, these decompose to stable, higher nuclearity edge-bridged clusters

These neutral clusters have higher stability than the anionic clusters in Sect. 4.1. They decompose only over days in solution; however, they are still very sensitive to oxidation, and they have not been isolated as pure solids or subjected to X-ray diffraction [103, 105]. Upon standing in solution, the neutral $[Fe_4S_4(PR_3)_4]$ clusters aggregate to form insoluble edge-bridged dicubane or tetracubane clusters $[Fe_8S_8(PCy_3)_6]$ and $[Fe_{16}S_{16}(PBu^{t})_8]$, in which one of the sulfur vertices forms a bond to a fourth iron center (Fig. 11; see Figs. 17 and 18 for structures) [103]. The Lewis basicity of the sulfur in the all-ferrous clusters is greater because of the relatively low oxidation level of the cluster; this apparently makes the sulfur a strong enough nucleophile to displace phosphine from an adjacent cluster. It will be interesting to learn whether the combination of cluster stability and sulfur nucleophilicity will lead to sulfur-based reactivity from these $[Fe_4S_4(PR_4)_4]$ clusters with substrates such as alkynes and CO_2.

4.3 Four-Iron Clusters [4Fe–4S]^0 with Cyanide Ligands

The studies in Sect. 4.2 point toward the use of terminal ligands that maintain the binding ability of an anionic donor but do not place as much electron density on the metal as a halide, aryloxide, or thiolate. Cyanide (CN^-) strikes a good balance, and reduction of a phosphine cluster in the presence of cyanide was effective (Fig. 12). This led to the first successful crystallographic characterization of an all-ferrous [4Fe–4S]^0 cluster [106]. The [4Fe–4S]$^{+/0}$ redox couple has $E_{1/2} = -1.18$ V, showing that cyanide falls between thiolate/halide (more electron donating) and phosphine (less electron-donating) in terms of its influence on the cluster potential.

The isolable $[Fe_4S_4(CN)_4]^{4-}$ species was characterized by visible absorption and Mössbauer spectroscopies as well as X-ray diffraction, which allowed comparison to the biological cubane clusters (see Sect. 2.3.3) [106]. It has a distinct red color in solution and an absorption band around 520 nm that is reminiscent of the protein-bound [4Fe–4S]^0 cluster. Like the biological examples, the isomer shifts in the Mössbauer spectrum are indicative of iron(II), but they are not split into the 3:1 ratio as seen in the protein (Table 4). This is probably because the synthetic cluster is more symmetrical, and accordingly the X-ray diffraction analysis reveals that the structure is very close to idealized D_{2d} symmetry. The mean Fe–Fe and Fe–S distances, as well as the core volumes, are close to those of the [4Fe–4S]^0 cluster of the fully reduced Fe–protein (Table 5).

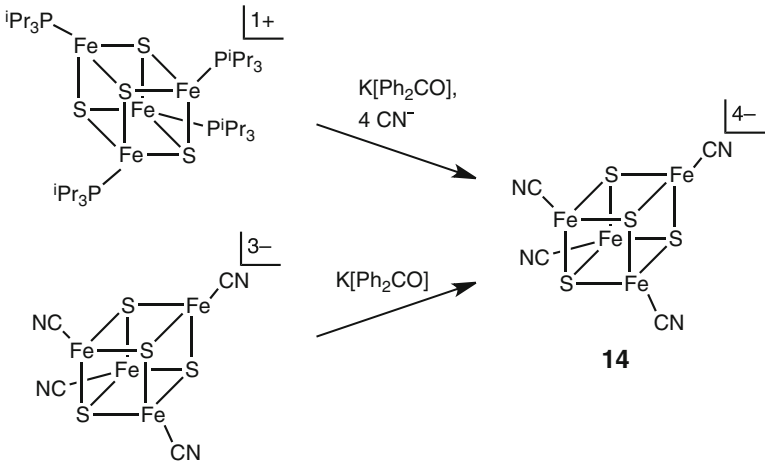

Fig. 12 Synthetic routes to the isolable all-ferrous cluster $[Fe_4S_4(CN)_4]^{4-}$

Table 4 Comparison of ^{57}Fe Mössbauer parameters for $[4Fe–4S]^0$ clusters

	T (K)	δ (mm/s)	ΔE_Q (mm/s)	%
$[Fe_4S_4(CN)_4]^{4-}$ [106]	77	0.65	2.00	50
		0.65	1.45	50
$[Fe_4S_4(NHC)_4]$ [107]	77	0.54	2.92	25
		0.62	1.54	75
A*v* Fe-protein [50, 51]	4.2	0.68	3.08	25
		0.68	1.72	25
		0.68	1.48	25
		0.68	1.24	25

NHC represents the *N*-heterocyclic carbene indicated in Fig. 13

Table 5 Metrical parameters of $[4Fe–4S]^0$ clusters

			A*v* Fe–protein	
	$[Fe_4S_4(CN)_4]^{4-}$ [106]	$[Fe_4S_4(NHC)_4]$[107]	X-ray [54]	XAS [52]
Fe–Fe (Å)	2.676(1), 2.696(1)	2.764(1), 2.675(1)	2.79, 2.67	2.77, 2.53
	2.683(1), 2.683(1)	2.719(1), 2.613(1)	2.69, 2.57	2.77, 2.53
	2.627(1), 2.676(1)	2.710(1), 2.603(1)	2.66, 2.54	2.53, 2.53
Average	2.67(2)	2.68(1)	2.65(9)	2.61(12)
Ave. Fe–S (Å)	2.33(2)	2.33(2)	2.33	4 at 2.52
				2 at 2.77
$V(Fe_4)$ (Å^3)	2.25	2.26	2.17	
$V(S_4)$ (Å^3)	6.21	6.14	6.21	
$V(Fe_4S_4)$ (Å^3)	9.48	9.47	9.23	

V indicates the cluster volume, *NHC* represents the *N*-heterocyclic carbene indicated in Fig. 13

Although $[Fe_4S_4(CN)_4]^{4-}$ was stable enough for solution and crystallographic studies, it could only be crystallized in the presence of excess of reductant [106]. As judged by the redox potentials (see above), the Fe^{2+} oxidation state is more stabilized by phosphine ligation. This suggests that neutral compounds have greater oxidative stability, and synthesis of neutral $[4Fe–4S]^0$ clusters requires neutral terminating ligands.

4.4 *Four-Iron Clusters $[4Fe–4S]^0$ with NHC Ligands*

The trends shown in the previous sections suggest that for isolation of highly reduced clusters that do not undergo aggregation, the ideal capping groups would be neutral ligands that bind very tightly to the iron center. The *N*-heterocyclic carbene (NHC) ligands have this combination of strong electron donating ability and lack of negative charge, which led to success [107]. In this work, the NHC ligand shown in the lower left of Fig. 13 was used. The all-ferrous cubane cluster **15** can be synthesized by displacement of phosphine from pre-formed clusters like **16**, or by self-assembly of a double-cubane NHC cluster **17** and subsequent cluster fission with additional NHC (Fig. 13). In contrast with phosphines (which are displaced by sulfides during the formation of cubane aggregates) [103], NHC ligands can break up the double and quadruple cubanes. They have much greater solution stability as well, and the cluster $[Fe_4S_4(NHC)_4]$ (**7**) can survive in aprotic solvents under anaerobic conditions for at least 3–4 days. The $[4Fe–4S]^{+/0}$ redox potential of cluster **15** is at −1.06 V, less negative than for clusters ligated by anions like CN^- or SR^- but more negative than the phosphine-terminated clusters.

Cluster **15** has been fully characterized by X-ray crystallography, as well as ^1H NMR, Mössbauer, and electronic absorption spectroscopies [107]. Because of its higher stability, it has been characterized in more detail than the previously discussed $[Fe_4S_4(CN)_4]^{4-}$ clusters, and the nature of the $[4Fe–4S]^0$ core is better understood. The average Fe–S bond distance and cluster volume in the NHC-terminated cluster are close to those of the cyanide-terminated cluster, and each is somewhat more symmetric than the reduced Fe protein (Table 5). An absorption band is again observed around 510 nm, which is very close to those seen in $[Fe_4S_4(CN)_4]^{4-}$ and the all-ferrous Fe protein of nitrogenase. The position of this band shows little dependence on the identity of the terminal ligands, indicating that this electronic transition is an intrinsic property of the $[4Fe–4S]^0$ core.

In order to obtain insight into the electronic structure of the $[4Fe–4S]^0$ core and to compare to the biological all-ferrous [4Fe–4S] clusters, detailed EPR and Mössbauer analysis have been carried out on **15** [108]. The parallel-mode X-band EPR spectrum of cluster **15** at 2 K exhibits a resonance with $g_{eff} = 16.1$ that originates from the $M_S = \pm 4$ doublet of an $S = 4$ ground state. The zero-field Mossbauer spectrum of cluster **15** at 100 K exhibits two doublets with a 3:1 intensity ratio, which is different from the cyanide-terminated cluster but in agreement with the data on the all-ferrous Fe protein of nitrogenase [50]. The average

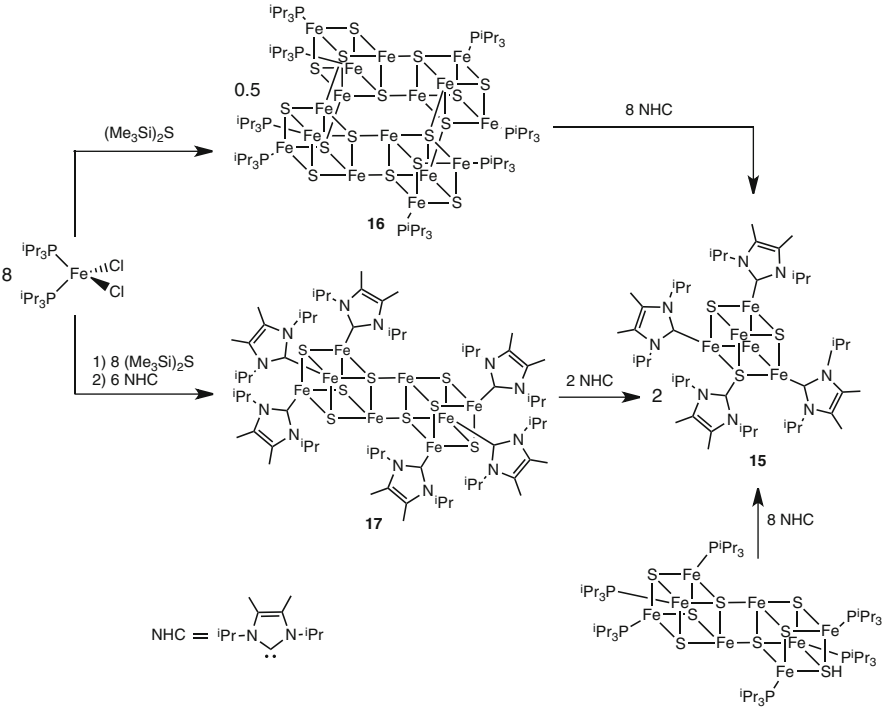

Fig. 13 Synthetic routes to NHC-based all-ferrous $[Fe_4S_4(NHC)_4]$

isomer shift of the synthetic compound is slightly lower than in the protein (Table 4), which may indicate more covalency at iron. Fitting variable-field Mössbauer spectra illuminated the spin coupling behavior: out of the four high-spin ferrous sites, three are aligned parallel to the cluster spin and the fourth antiparallel, giving a total spin of 4. This conclusion is consistent with computations predicting that a T_2 distortion is favorable. This T_2 distortion (along one Fe-centroid axis) also explains the 3:1 ratio of Mössbauer signals, and is fully consistent with all of the data. The observation of a similar distortion in the synthetic cluster and the protein-bound cluster implies that the 3:1 distortion is *not* imposed on the cluster by the protein/solvent environment [23, 61]. However, the extent of the distortion can be modulated by changes in terminal ligation or protein environment. Recently, these conclusions were strengthened by a DFT study that also shows a 3:1 pattern in both optimized geometry and calculated ^{57}Fe Mossbauer spectra and supports the idea that the exchange interaction are highly dependent on the core geometry [109].

In summary, systematic variations of the supporting ligands have recently enabled the isolation and detailed study of a synthetic all-ferrous [4Fe–4S] cluster for the first time. These studies have greatly enhanced our understanding of the protein-bound all-ferrous clusters because they show that the $S = 4$ ground state, the 3:1 ratio of iron environments, and the 510–520 nm electronic absorption band

are intrinsic features of the all-ferrous cubane core. The structural parameters for the synthetic compound are known in much greater precision than the protein-bound structure, which facilitates comparison to computations. Challenges for the future include ligand variation to enforce an *E*-symmetry distortion (2:2 ratio of iron environments), which could give an $S = 0$ ground state [108]. Isolation of such a cluster could help to understand the feasibility of the proposed "alternative" form of the all-ferrous nitrogenase Fe protein discussed in section 2.3. It will also be interesting to learn whether the NHC ligands can be removed to give reactivity at the highly reduced iron core. Finally, one hopes that the ability to make a large amount of synthetic all-ferrous cubane clusters will allow chemists to test the idea that such clusters can do two-electron transfer as proposed in nitrogenase.

5 Synthetic All-Ferrous Iron–Sulfur Clusters of Nuclearity Eight and Higher

5.1 Eight-Iron Clusters

Eight-iron clusters relevant to all-ferrous iron–sulfur chemistry have three different core structures (Fig. 14). As shown on the left of Fig. 14, [8Fe–6S] cores contain eight irons in a cube, capped on each face by a sulfur, and each iron is coordinated by a terminal ligand to complete its tetrahedral coordination. In the center of Fig. 14, [8Fe–7S] cores have two [4Fe–4S] cubanes that share a μ_6-sulfide. In contrast, the $[8Fe–8S]^0$ clusters consist of two [4Fe–4S] cubanes linked via two Fe–S bonds, as illustrated on the right of Fig. 14.

5.1.1 $[8Fe–6S]^{4+}$

The $[8Fe–6S]^{4+}$ core was identified in the compound $(PhCH_2NEt_3)_4[Fe_8S_6I_8]$ (**9**), which was the first all-ferrous iron–sulfur cluster to be isolated [110]. It was

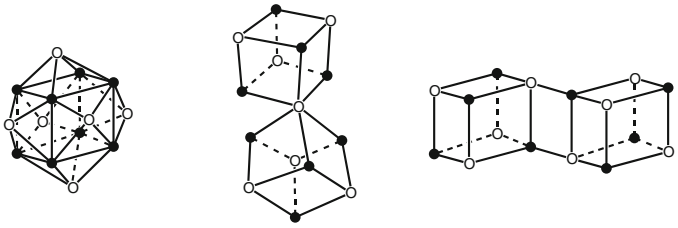

Fig. 14 Shapes of [8Fe–6S], [8Fe–7S], and [8Fe–8S] cores. The *black circles* represent iron atoms, and the *white circles* represent sulfur atoms. All iron atoms are four-coordinate with a pseudotetrahedral geometry, and their coordination spheres are completed by terminal ligands (not shown)

synthesized from a $[4Fe–4S]^{2+}$ precursor (Eq. 3), and the phosphine is present only in an basket-type intermediate $[Fe_6S_6I_2(PR_3)_4]$, but not in the final product. An excess of Fe^{2+} is required for this conversion, or else only amorphous iron sulfides are obtained. Alternatively, the $[Fe_6S_6I_2]^0$ intermediate can be avoided using bidentate phosphine ligated $[Fe_2I_2(dppe)_2]$, which does not form a basket intermediate. Cluster **9** is stable in air for a short time, but only X-ray characterization was given, and the electronic structure and coupling have not been reported.

$$[Fe_4S_4I_4]^{2-} \xrightarrow[THF/CH_3CN]{[FeI_2(PR_3)_2] \text{ or } [Fe_2I_2(dppe)_2]} [Fe_8S_6I_8]^{4-},\ PR_3 = PMePh_2. \quad (3)$$

Building from the observation that $[Fe_6S_6I_2(PR_3)_4]$ can react with $[FeI_2(PR_3)_2]$ to form a $[Fe_8S_6I_8]^{4-}$ core, a similar reaction was carried out using Ru^{2+} instead of Fe^{3+} (Eq. 4) [111]. This reaction also results in the formation of a $[8Fe–6S]^{4+}$ core, and in this case the core is attached to two octahedral Ru fragments via opposing sulfur atoms, in the compound $[(MeCN)_4(Ph_2MePS)Ru–Fe_8S_6I_8–Ru(Ph_2MePS)(MeCN)_4]$. The structure of this cluster was determined by X-ray diffraction, which evidenced a topologically identical $[Fe_8S_6I_8]^{4-}$ core with an elongation of the [8Fe–6S] core along the Ru–Ru axis. Similar reactions with Ni^{2+} have also been explored, and they incorporate various numbers of Ni atoms into the cubane core [112, 113].

$$\begin{array}{c} 2\,[Fe_6S_6I_2(PMePh_2)] \\ + \\ 4\,[RuI_2(MeCN)_4] \end{array} \longrightarrow \begin{array}{l} 4\,FeS + 2\,[RuI_2(PMe)] + 8\,MeCN + \\ [(MeCN)_4(Ph_2MePS)Ru\text{-}Fe_8S_6I_8\text{-} \\ Ru(Ph_2MePS)(MeCN)_4]. \end{array} \quad (4)$$

5.1.2 $[8Fe–7S]^{2+}$

These clusters are of interest because of their analogy to the P cluster of nitrogenase (Sect. 2.3.2). The development of these clusters has benefitted from the use of organic solvents and very bulky thiolates that protect the cluster. The first example, cluster **18**, was isolated from the reaction of $Fe[N(SiMe_3)_2]_2$, TipSH (Tip = 2,4,6-$^i Pr_3C_6H_2$), thiourea $SC(NMe_2)_2$, and elemental sulfur (S_8) in toluene [114]. Cluster **18** accurately reproduces the [8Fe–7S] core geometry of the reduced P^N cluster, even though the Mössbauer spectrum of **18** shows that it has a $6Fe^{2+}2Fe^{3+}$ oxidation state corresponding to P^{OX} [114]. In an effort to reduce the synthetic cluster to the all-ferrous level, **18** and some of its terminal ligand substituted analogues **19**–**21** were reduced electrochemically. Cyclic voltammetry showed two quasi-reversible one-electron reductions, which formally lead to the all-ferrous oxidation state (Fig. 15, Table 6) [115]. However, the all-ferrous product has not been isolated. Although mixed-metal clusters are formally outside the scope of this review, it

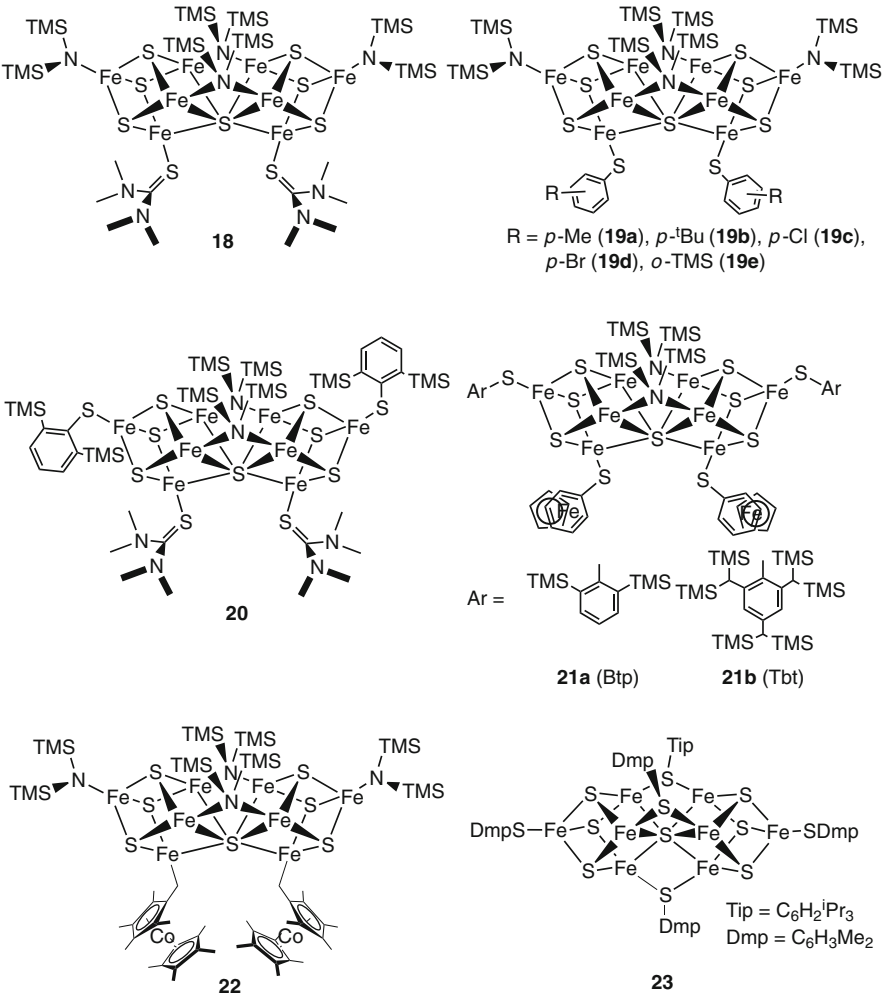

Fig. 15 Structures of synthetic [8Fe–7S] clusters

should be mentioned that Mo_2Fe_6 clusters of the same shape are known that have all of their iron atoms in the ferrous level [116–118].

Bulk preparation of all ferrous [8Fe–7S] clusters has been attempted using chemical reduction of **18** by decamethylcobaltocene (which has a potential of −1.7 V) [119]. However, the product did not correspond to simple reduction: instead, there is activation of a C–H bond of Cp^*_2Co, affording cluster **22** (Fig. 15). One possible mechanism for this transformation is that a highly reduced cluster intermediate deprotonates $Cp^*_2Co^+$; if so, then the reduced cluster intermediate (of unknown oxidation level) must be a formidable base. Since the oxidation

Table 6 Redox potentials of [8Fe–7S] clusters [115][a]

	$E_{1/2}{}^{0/-}$	$E_{1/2}{}^{1-/2-}$
18	−1.28	−1.68
19a	−1.73	−2.05
19b	−1.88	−2.18
19c	−1.76	−2.10
19d	−1.89	−2.24
19e	−1.80	−2.14
20	−1.17	−1.50
21a	−1.25	−1.56
21b	−1.32	−1.67

[a]Potentials converted from Ag^+ reference (+0.01 V)

state of cobalt in the decamethylcobaltocenyl group in the product is unknown, the oxidation state of the iron atoms in the clusters remains unclear.

The related cluster **23** with all-sulfur ligation is in the $Fe_3{}^{3+}Fe_5{}^{2+}$ oxidation level [120]. It has three quasireversible reductions evident by CV, with the third one (presumably leading to the all-ferrous form) at −1.4 V. This transiently generated species has not been examined further, but considering the apparent reversibility of the redox processes in the CV, it is a promising lead for continued study.

5.1.3 [8Fe–8S]^0

Synthesis

These clusters are conceptually derived from two [4Fe–4S] clusters through bonds between the iron and sulfur along a common edge of the cube, and thus are termed "edge-bridged." The neutral all-ferrous clusters $[Fe_8S_8(PR_3)_6]$ were first isolated during attempts to generate all-ferrous $[4Fe–4S]^0$ clusters with phosphine as terminal ligands [103, 105, 121]; as noted above, phosphines bind relatively weakly to [4Fe–4S] clusters. Since the edge-bridged clusters have poor solubility, the reaction may also be driven to the eight-iron cluster by precipitation of the product (LeChâtelier's principle). Similar $[8Fe–8S]^0$ clusters were generated with terminal NHC ligands [107]. On the other hand, cyanide-terminated clusters $[Fe_4S_4(CN)_4]^{4-}$ did not aggregate into edge-bridged dimers, perhaps due to the stronger binding of cyanide or the negative charge on the cluster [106].

Another route to prepare [8Fe–8S] clusters is by direct self-assembly from $FeCl_2(PR_3)_2$, a sulfur source and terminal ligands. This method (which was mentioned above in the context of Fig. 13) has been demonstrated to lead to $[Fe_8S_8(PCy_3)_6]$ (Eq. 5) [105], $[Fe_8S_8(P^iPr_3)_6]$ (Eq. 6) [122] and $[Fe_8S_8(NHC)_6]$ (**17** in Fig. 13) [107].

$$[FeCl_2(PEt_3)_2] \xrightarrow[PCy_3]{NaSPh,\ PhCH_2SSSCH_2Ph} [Fe_8S_8(PCy_3)_6] \tag{5}$$

Table 7 Comparison of ^{57}Fe Mössbauer parameters for $[8Fe–8S]^0$ clusters

	T (K)	δ (mm/s)	ΔE_Q (mm/s)	%
$[Fe_8S_8(PCy_3)_6]$ [105]	77	0.49	2.20	27
		0.60	1.14	47
		0.62	0.73	21
$[Fe_8S_8(P^iPr_3)_6]$ [103]	4.2	0.64	0.94	75
		0.53	2.49	25
$[Fe_8S_8(NHC)_6]$ [107]	4.2	0.55	2.93	25
		0.64	1.54	50
		0.65	0.82	25

$$[FeCl_2(PiPr_3)_2] \xrightarrow{(Me_3Si)_2S} [Fe_8S_8(PiPr_3)_6] \tag{6}$$

A third synthetic method proceeds through the intermediacy of the all-ferrous heptanuclear compound $[Fe_7S_6(PEt_3)_5Cl_2]$ by the addition of NHC (Eq. 7) [107]. However, one pitfall of this method is that the seven-iron cluster is not very stable and decomposes over several hours at room temperature. Finally, since the *N*-heterocyclic carbenes are stronger donors than phosphines, $[Fe_8S_8(NHC)_6]$ can also be generated by terminal ligand substitution from $[Fe_8S_8(P^iPr_3)_6]$ or $[Fe_{16}S_{16}(P^iPr_3)_8]$ (Eq. 8; see also Fig. 13) [107].

$$[Fe_7S_6(PEt_3)_5Cl_2] + 5\,NHC \longrightarrow [Fe_8S_8(NHC)_6] \tag{7}$$

$$[Fe_8S_8(PiPr_3)_6] + 6\,NHC \longrightarrow [Fe_8S_8(NHC)_6] + 6\,PiPr_3 \tag{8}$$

Properties

X-ray diffraction has been used to determine the structures of a number of [8Fe–8S] edge-bridged dicubanes [103, 105, 107]. All three [8Fe–8S] clusters, $[Fe_8S_8(PCy_3)_6]$, $[Fe_8S_8(P^iPr_3)_6]$ and $[Fe_8S_8(NHC)_6]$ have idealized C_{2h} symmetry, with similar dimensions. The bridging Fe_2S_2 rhomb is rigorously planar, with the intracubane Fe–S bonds consistently longer than the intercubane bonds. The dicubane structure is retained in benzene solution, as shown by ^{1}H NMR spectroscopy.

In keeping with the symmetry of the core, the Mössbauer spectra of $[8Fe–8S]^0$ clusters share a pattern of one quadrupole doublet (25% in intensity) with larger quadrupole splitting and one or two doublets (75% in intensity) with smaller quadrupole splitting (Table 7). The average isomer shifts of phosphine-ligated clusters ($\delta_{av} = 0.60$ mm/s) and NHC-ligated clusters ($\delta_{av} = 0.62$ mm/s) are similar and consistent with the all-ferrous oxidation level. The similarities in geometric and electronic structure of $[4Fe–4S]^0$ and $[8Fe–8S]^0$ clusters indicate that the spin ordering for the edge-bridged dicubanes is the same as that within the $[4Fe–4S]^0$ fragments (Fig. 3) [123]. The diamagnetic ground states of $[8Fe–8S]^0$ clusters are proposed to come from antiferromagnetic coupling of two $[4Fe–4S]^0$ fragments (Fig. 16).

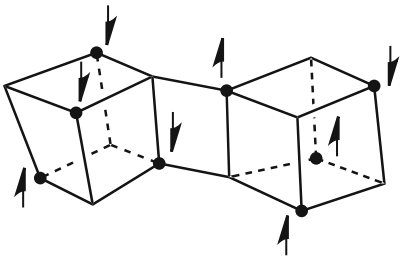

Fig. 16 Proposed spin ordering model for $[8Fe–8S]^0$ edge-bridged dicubanes

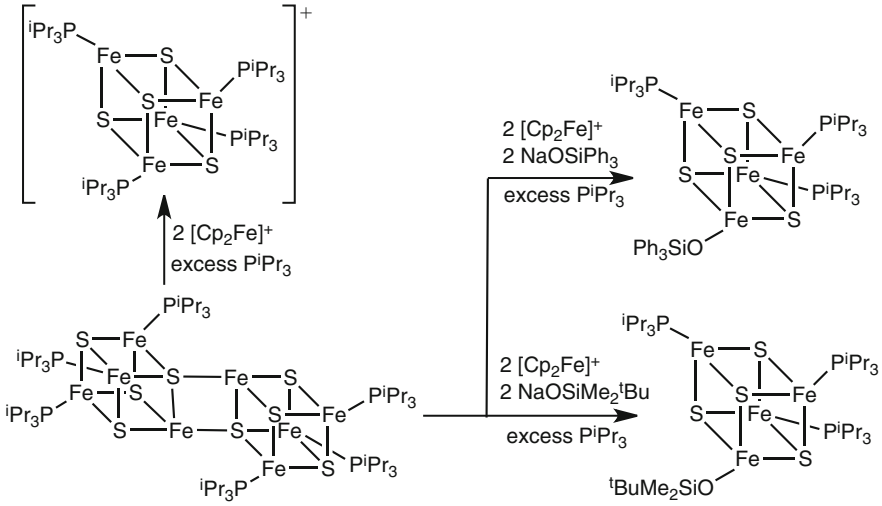

Fig. 17 Oxidation of $[Fe_8S_8(P^iPr_3)_6]$ with formation of $[4Fe–4S]^+$ clusters

Reactivity

The reactivity of $[Fe_8S_8(PCy_3)_6]$ has not been studied extensively, because it is insoluble in all common solvents. However, it reacts with chloroform or SCl_2 to give a mixture containing the all-ferrous cluster, $[Fe_8S_6(PCy_3)_4Cl_4]$ [105]. The $[8Fe–6S]^{4+}$ core of this molecule has the same structural motif described above in Sect. 5.1.1.

The analogous $[Fe_8S_8(P^iPr_3)_6]$ has been studied more thoroughly, as it is soluble in solvents such as benzene, toluene and THF [103, 122]. Treatment of this dicubane cluster with the oxidant $[Cp_2Fe]^+$ results in cleavage of edge-bridged Fe–S bonds and yields monocubane species with $[4Fe–4S]^+$ cores. When oxidation occurs in the presence of a bulky siloxide, it is possible to isolate neutral clusters with a single siloxide ligand (Fig. 17) [122].

Further study on $[8Fe–8S]^0$ clusters, particularly the new stabilized NHC-terminated clusters, is needed in order to understand the reaction chemistry of

this all-ferrous core. Since edge-bridged dicubane [2Mo–6Fe–8S] clusters have been demonstrated to be precursors to clusters with the topology of the P^N cluster of nitrogenase [118, 124], it will be interesting to see if similar core conversion can be realized in $[8Fe–8S]^0$ clusters to form new all-iron analogues of the P cluster.

5.2 *Sixteen-Iron Clusters*

5.2.1 Synthesis

The first $[16Fe–16S]^0$ clusters were discovered as a byproduct in efforts to isolate neutral $[Fe_4S_4(PR_3)_4]$ clusters; the same edge-bridging phenomena that give the $[8Fe–8S]^0$ clusters can also bridge additional edges to form $[16Fe–16S]^0$ species [103, 105]. The number of fused cubes seems to be dependent on the crystallization conditions, which control the opportunity to lose phosphine and aggregate [103, 105]. So far, $[16Fe–16S]^0$ cores are limited to phosphine-based clusters, and tetracubanes have not yet been reported with other terminal ligands, such as cyanide and NHC.

5.2.2 Properties

The structures of $[16Fe–16S]^0$ clusters have been determined by X-ray diffraction analysis. In these compounds, the four cubanes each bridge edges in a cyclic fashion so that all four cubanes are equivalent with overall D_4 symmetry (see compound **16** in Fig. 15). The pattern of distances and angles in each cubane and in the bridging rhomb resembles those seen in the dicubane $[8Fe–8S]^0$ cores discussed in Sect. 5.1.3. The solubility of $[Fe_{16}S_{16}(P^iPr_3)_8]$ and $[Fe_{16}S_{16}(P^tBu_3)_8]$ is appreciable in THF, benzene and toluene, while $[Fe_{16}S_{16}(PCy_3)_8]$ is only slightly soluble in all common solvents. Retention of the core structure is evident from the number of peaks in the ^1H NMR spectra in benzene [103, 105].

The $[16Fe–16S]^0$ clusters have been studied by CV and Mössbauer (Table 8) [103]. In THF, $[Fe_{16}S_{16}(P^tBu_3)_8]$ is oxidized in three steps at $E_{1/2} = -0.33$ V, +0.15 V, and +0.46 V, defining a one-electron-transfer series $[16Fe–16S]^{0/1+/2+/3+}$. Since the monocubane cluster with the same terminal ligand $[Fe_4S_4(P^tBu_3)_4]$ exhibits a $[4Fe–4S]^{+/0}$ redox potential of $E_{1/2} = -0.51$ V, it is apparent that the fusion of the four individual cubanes makes the reduction to the all-ferrous state slightly easier, presumably because the edge-bridging cube is less electron-donating than a phosphine. Since a number of closely spaced one-electron oxidations are observed, it suggests that there is electronic interaction among the clusters, where the oxidation of one influences the potential of the others.

The zero field ^{57}Fe Mössbauer spectra of $[Fe_{16}S_{16}(P^tBu_3)_8]$ and $[Fe_{16}S_{16}(P^tPr_3)_8]$ verify the all-ferrous oxidation level with average isomer shifts of δ 0.61–0.63 mm/s. In analogy to $[8Fe–8S]^0$ clusters, the spectra of $[16Fe–16S]^0$ clusters share the

Table 8 Comparison of Mössbauer parameters for $[Fe_{16}S_{16}(PR_3)_3]^0$ clusters

R	δ (mm/s)	ΔE_Q (mm/s)	%
^{t}Bu	0.64	1.09	75
	0.58	2.68	25
^{i}Pr	0.64	1.10	75
	0.55	2.63	25

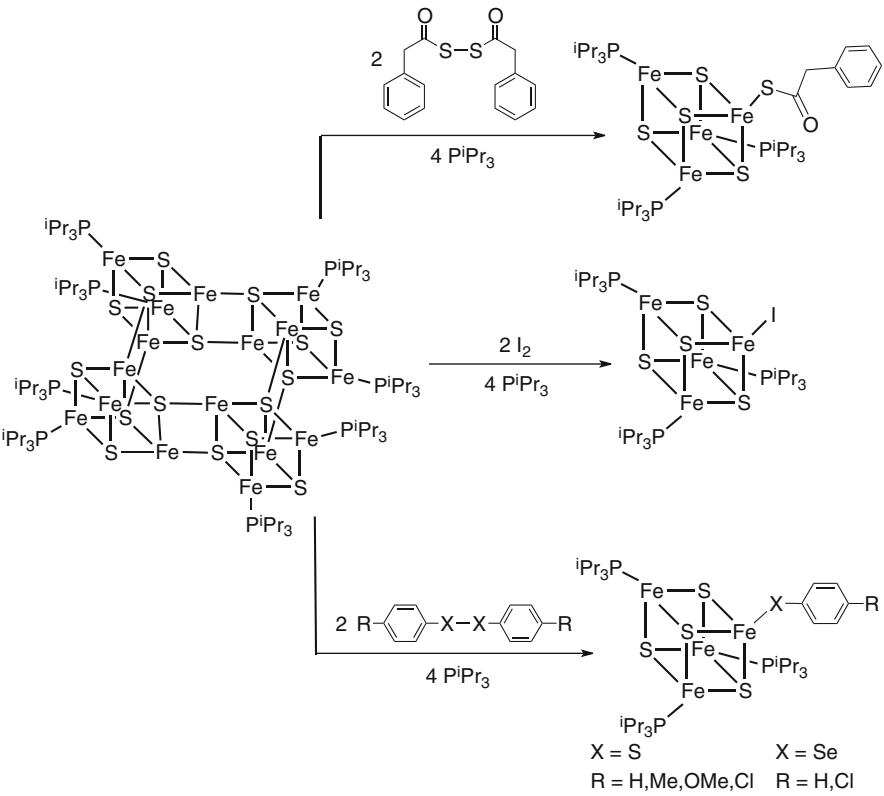

Fig. 18 Reduction of substrates by [16Fe–16S] clusters

pattern of two quadrupole doublets in an intensity ratio of 3:1, indicating that fusion does not significantly influence the spin coupling within each [4Fe–4S] cubane.

5.2.3 Reactivity

The reductive cleavage of ligand substrates by $[16Fe–16S]^0$ clusters has been reported [122]. Upon addition of the oxidants I_2, RSSR, or RSeSeR in the presence of phosphine, tetracubane $[Fe_{16}S_{16}(P^iPr_3)_8]$ dissociates into cubane fragments, each of which captures one phosphine ligand and one monoanion generated from

reductive cleavage of the oxidant (Fig. 18). Since $[Fe_{16}S_{16}(P^iPr_3)_8]$ is in equilibrium with $[Fe_8S_8(P^iPr_3)_6]$ in the presence of phosphine, it seems likely that the reaction is stepwise, with dissociation to $[Fe_8S_8(P^iPr_3)_6]$ preceding an oxidation reaction like that shown in Fig. 17.

6 Conclusion

The study of highly reduced iron–sulfur clusters is both long standing and undergoing current development. Research studies on these iron–sulfur clusters represent an interesting confluence of insights from metalloprotein isolation, spectroscopy, and synthetic work, and show the valuable interplay between these areas of bioinorganic research. Several themes have emerged. First, the coupling of protonation and reduction is evident in a number of the highly reduced biological clusters, and the influence of protons (whether as hydrogen bonds or as discrete proton transfers) plays a critical role in modulating their behavior. This fits into an increasing realization in bioinorganic chemistry that the "second coordination sphere" tunes redox potentials over a wide range [125, 126]. It is possible that the biological all-ferrous clusters described here (particularly the Fe protein of nitrogenase) use these tuning influences to enable multielectron transfer, which is of general interest in the context of solar energy research [127].

The synthesis of iron–sulfur clusters in highly reduced states has been a challenge for the synthetic chemistry community because of the sensitivity of the complexes and their tendency to decompose through a range of pathways. Key advances described above are the observation and isolation of all-ferrous clusters, particularly the *N*-heterocyclic carbene based $[4Fe–4S]^0$ clusters that could be directly compared to spectroscopy on biological all-ferrous clusters. This recent work has confirmed the oxidation state of the spectroscopically observed biological clusters, and given more detail into the geometric and electronic structure. It is clear that many more advances remain for future investigations.

References

1. Beinert H, Holm RH, Münck E (1997) Science 277:653
2. Beinert H (2000) J Biol Inorg Chem 5:2
3. Johnson DC, Dean DR, Smith AD, Johnson MK (2005) Annu Rev Biochem 74:247
4. Fontecave M (2006) Nat Chem Biol 2:171
5. Que L Jr, Holm RH, Mortenson LE (1975) J Am Chem Soc 97:463
6. Johnson MK, Duderstadt RE, Duin EC (1999) Adv Inorg Chem 47:1
7. Seino H, Hidai M (2011) Chem Sci 2:847
8. Crack JC, Green J, Thomson AJ, Le Brun NE (2012) Curr Opin Chem Biol 16:35
9. White MF, Dillingham MS (2012) Curr Opin Struct Biol 22:94
10. Brandt U (2006) Annu Rev Biochem 75:69

11. Beinert H, Kennedy MC, Stout CD (1996) Chem Rev 96:2335
12. Canfield DE (2005) Annu Rev Earth Planet Sci 33:1
13. Hagen KS, Reynolds JG, Holm RH (1981) J Am Chem Soc 103:4054
14. Blöchl E, Keller M, Wächtershäuser G, Stetter KO (1992) Proc Natl Acad Sci USA 89:8117
15. Huber C, Wächtershäuser G (1997) Science 276:245
16. Heinen W, Lauwers AM (1996) Orig Life Evol Biosph 22:131
17. Dörr M, Käßbohrer J, Grunert R, Kreisel G, Brand WA, Werner RA, Geilmann H, Apfel C, Robl C, Weigand W (2003) Angew Chem Int Ed 42:1540
18. Bill E (2012) Hyperfine Interact 205:139
19. Ogino H, Inomata S, Tobita H (1998) Chem Rev 98:2093
20. Lee SC, Holm RH (2004) Chem Rev 104:1135
21. Lee SC, Holm RH (2003) Proc Natl Acad Sci USA 100:3595
22. Rao PV, Holm RH (2004) Chem Rev 104:527
23. Torres RA, Lovell T, Noodleman L, Case DA (2003) J Am Chem Soc 125:1923
24. Dey A, Francis EJ, Adams MWW, Babini E, Takahashi Y, Fukuyama K, Hodgson KO, Hedman B, Solomon EI (2007) Science 318:1464
25. Im SC, Lam KY, Lim MC, Ooi BL, Sykes AG (1995) J Am Chem Soc 117:3635
26. Im SC, Kohzuma T, McFarlane W, Gaillard J, Sykes AG (1997) Inorg Chem 36:1388
27. Im SC, Worrall JAR, Liu G, Aliverti A, Zanetti G, Luchinat C, Bertini I, Sykes AG (2000) Inorg Chem 39:1755
28. Yoo SJ, Meyer J, Münck E (1999) J Am Chem Soc 121:10450
29. Verhagen M, Link TA, Hagen WR (1995) FEBS Lett 361:75
30. Leggate EJ, Bill E, Essigke T, Ullmann GM, Hirst J (2004) Proc Natl Acad Sci USA 101:10913
31. Duff JLC, Breton JLJ, Butt JN, Armstrong FA, Thomson AJ (1996) J Am Chem Soc 118:8593
32. Moreno C, Macedo AL, Moura I, Moura JJG, LeGall J (1994) J Inorg Biochem 53:219
33. Hirst J, Jameson GNL, Allen JWA, Armstrong FA (1998) J Am Chem Soc 120:11994
34. Mayer SM, Lawson DM, Gormal CA, Roe SM, Smith BE (1999) J Mol Biol 292:871
35. Peters JW, Stowell MHB, Soltis SM, Finnegan MG, Johnson MK, Rees DC (1997) Biochemistry 36:1181
36. Zimmermann R, Orme-Johnson WH, Münck E, Shah VK, Brill WJ, Henzl MT, Rawlings J (1978) Biochim Biophys Acta 537:185
37. Pierik AJ, Wassink H, Haaker H, Hagen WR (1993) Eur J Biochem 212:51
38. McLean PA, Papaefthymiou V, Ormejohnson WH, Münck E (1987) J Biol Chem 262:12900
39. Lanzilotta WN, Christiansen J, Dean DR, Seefeldt LC (1998) Biochemistry 37:11376
40. Danyal K, Mayweather D, Dean DR, Seefeldt LC, Hoffman BM (2010) J Am Chem Soc 132:6894
41. Lowe DJ, Fisher K, Thorneley RNF (1993) Biochem J 292:93
42. Chan JM, Christiansen J, Dean DR, Seefeldt LC (1999) Biochemistry 38:5779
43. Danyal K, Dean DR, Hoffman BM, Seefeldt LC (2011) Biochemistry 50:9255
44. Huyett JE, Chan JM, Christiansen J, Dean DR, Seefeldt LC (1999) J Inorg Biochem 74:173
45. Fisher K, Lowe DJ, Tavares P, Pereira AS, Huynh BH, Edmondson D, Newton WE (2007) J Inorg Biochem 101:1649
46. Tezcan FA, Kaiser JT, Mustafi D, Walton MY, Howard JB, Rees DC (2005) Science 309:1377
47. Thorneley RNF, Lowe DJ (1996) J Biol Inorg Chem 1:576
48. Watt GD, Reddy KRN (1994) J Inorg Biochem 53:281
49. Vincent KA, Tilley GJ, Quammie NC, Streeter I, Burgess BK, Cheesman MR, Armstrong FA (2003) Chem Commun 2590
50. Yoo SJ, Angove HC, Burgess BK, Hendrich MP, Münck E (1999) J Am Chem Soc 121:2534
51. Angove HC, Yoo SJ, Burgess BK, Münck E (1997) J Am Chem Soc 119:8730

52. Musgrave KB, Angove HC, Burgess BK, Hedman B, Hodgson KO (1998) J Am Chem Soc 120:5325
53. Angove HC, Yoo SJ, Münck E, Burgess BK (1998) J Biol Chem 273:26330
54. Strop P, Takahara PM, Chiu HJ, Angove HC, Burgess BK, Rees DC (2001) Biochemistry 40:651
55. Guo ML, Sulc F, Ribbe MW, Farmer PJ, Burgess BK (2002) J Am Chem Soc 124:12100
56. Lowery TJ, Wilson PE, Zhang B, Bunker J, Harrison RG, Nyborg AC, Thiriot D, Watt GD (2006) Proc Natl Acad Sci USA 103:17131
57. McKenna CE, Gutheil WG, Wei S (1991) Biochim Biophys Acta 1075:109
58. Collins JM, Uppal R, Incarvito CD, Valentine AM (2005) Inorg Chem 44:3431
59. Nyborg AC, Johnson JL, Gunn A, Watt GD (2000) J Biol Chem 275:39307
60. Erickson JA, Nyborg AC, Johnson JL, Truscott SM, Gunn A, Nordmeyer FR, Watt GD (1999) Biochemistry 38:14279
61. Hans M, Buckel W, Bill E (2008) J Biol Inorg Chem 13:563
62. Mayerle JJ, Frankel RB, Holm RH, Ibers JA, Phillips WD, Weiher JF (1973) Proc Natl Acad Sci USA 70:2429
63. Mascharak PK, Papaefthymiou GC, Frankel RB, Holm RH (1981) J Am Chem Soc 103:6110
64. Mayerle JJ, Denmark SE, Depamphilis BV, Ibers JA, Holm RH (1975) J Am Chem Soc 97:1032
65. Wong GB, Kurtz DM, Holm RH, Mortenson LE, Upchurch RG (1979) J Am Chem Soc 101:3078
66. Ballmann J, Dechert S, Bill E, Ryde U, Meyer F (2008) Inorg Chem 47:1586
67. Ballmann J, Sun XR, Dechert S, Schneider B, Meyer F (2009) Dalton 4908
68. Ballmann J, Albers A, Demeshko S, Dechert S, Bill E, Bothe E, Ryde U, Meyer F (2008) Angew Chem Int Ed 47:9537
69. Beardwood P, Gibson JF (1992) J Chem Soc Dalton 2457
70. Beardwood P, Gibson JF (1985) J Chem Soc Chem Commun 1345
71. Beardwood P, Gibson JF (1985) J Chem Soc Chem Commun 102
72. Beardwood P, Gibson JF (1988) Polyhedron 7:1911
73. Beardwood P, Gibson JF (1986) J Chem Soc Chem Commun 490
74. Ballmann J, Sun X, Dechert S, Bill E, Meyer F (2007) J Inorg Biochem 101:305
75. Albers A, Demeshko S, Dechert S, Bill E, Bothe E, Meyer F (2011) Angew Chem Int Ed 50:9191
76. Saouma CT, Kaminsky W, Mayer JM (2012) J Am Chem Soc 134:7293
77. Ballmann J, Dechert S, Demeshko S, Meyer F (2009) Eur J Inorg Chem 3219
78. DePamphilis BV, Averill BA, Herskovitz T, Que L, Holm RH (1974) J Am Chem Soc 96:4159
79. Wong GB, Bobrik MA, Holm RH (1978) Inorg Chem 17:578
80. Corazza F, Floriani C, Zehnder M (1987) Dalton 709
81. Dorfman JR, Girerd JJ, Simhon ED, Stack TDP, Holm RH (1984) Inorg Chem 23:4407
82. Mukherjee RN, Stack TDP, Holm RH (1988) J Am Chem Soc 110:1850
83. Berno P, Floriani C, Chiesivilla A, Guastini C (1989) Dalton 551
84. Vela J, Stoian S, Flaschenriem CJ, Münck E, Holland PL (2004) J Am Chem Soc 126:4522
85. Rodriguez MM, Stubbert BD, Scarborough CC, Brennessel WW, Bill E, Holland PL (2012) Angew Chem Int Ed 51: 8247
86. Henkel G, Tremel W, Krebs B (1981) Angew Chem Int Ed 20:1033
87. Hagen KS, Christou G, Holm RH (1983) Inorg Chem 22:309
88. Cambray J, Lane RW, Wedd AG, Johnson RW, Holm RH (1977) Inorg Chem 16:2565
89. Zhou CY, Raebiger JW, Segal BM, Holm RH (2000) Inorg Chim Acta 300:892
90. Balch AL (1969) J Am Chem Soc 91:6962
91. Tezuka M, Yajima T, Tsuchiya A, Matsumoto Y, Uchida Y, Hidai M (1982) J Am Chem Soc 104:6834

92. Nakazawa M, Mizobe Y, Matsumoto Y, Uchida Y, Tezuka M, Hidai M (1986) Bull Chem Soc Jpn 59:809
93. Tomohiro T, Uoto K, Okuno H (1990) Chem Commun 194
94. Tanaka M, Tanaka K, Tanaka T (1982) Chem Lett 767
95. Tanaka K, Tanaka M, Tanaka T (1981) Chem Lett 895
96. DuBois MR (1989) Chem Rev 89:1
97. Schwartz A, Van Tamelen EE (1977) J Am Chem Soc 99:3189
98. Van Tamelen EE, Gladysz JA, Miller JS (1973) J Am Chem Soc 95:1347
99. Schrauzer GN, Kiefer GW, Tano K, Doemeny PA (1974) J Am Chem Soc 96:641
100. Cleland WE, Holtman DA, Sabat M, Ibers JA, DeFotis GC, Averill BA (1983) J Am Chem Soc 105:6021
101. Snyder BS, Holm RH (1988) Inorg Chem 27:2339
102. Reynolds MS, Holm RH (1988) Inorg Chem 27:4494
103. Zhou HC, Holm RH (2003) Inorg Chem 42:11
104. Tyson MA, Demadis KD, Coucouvanis D (1995) Inorg Chem 34:4519
105. Goh C, Segal BM, Huang JS, Long JR, Holm RH (1996) J Am Chem Soc 118:11844
106. Scott TA, Berlinguette CP, Holm RH, Zhou HC (2005) Proc Natl Acad Sci USA 102:9741
107. Deng L, Holm RH (2008) J Am Chem Soc 130:9878
108. Chakrabarti M, Deng L, Holm RH, Münck E, Bominaar EL (2009) Inorg Chem 48:2735
109. Chakrabarti M, Münck E, Bominaar EL (2011) Inorg Chem 50:4322
110. Pohl S, Opitz U (1993) Angew Chem Int Ed 32:863
111. Pohl S, Barklage W, Saak W, Opitz U (1993) Chem Commun 1251
112. Saak W, Pohl S (1991) Angew Chem Int Ed 30:881
113. Junghans C, Saak W, Pohl S (1994) Chem Commun 2327
114. Ohki Y, Sunada Y, Honda M, Katada M, Tatsumi K (2003) J Am Chem Soc 125:4052
115. Ohki Y, Imada M, Murata A, Sunada Y, Ohta S, Honda M, Sasamori T, Tokitoh N, Katada M, Tatsumi K (2009) J Am Chem Soc 131:13168
116. Zhang YG, Holm RH (2003) J Am Chem Soc 125:3910
117. Zhang Y, Holm RH (2004) Inorg Chem 43:674
118. Berlinguette CP, Miyaji T, Zhang YG, Holm RH (2006) Inorg Chem 45:1997
119. Ohki Y, Murata A, Imada M, Tatsumi K (2009) Inorg Chem 48:4271
120. Ohki Y, Ikagawa Y, Tatsumi K (2007) J Am Chem Soc 129:10457
121. Cai LS, Segal BM, Long JR, Scott MJ, Holm RH (1995) J Am Chem Soc 117:8863
122. Deng LA, Majumdar A, Lo WN, Holm RH (2010) Inorg Chem 49:11118
123. Chakrabarti M, Deng L, Holm RH, Münck E, Bominaar EL (2010) Inorg Chem 49:1647
124. Berlinguette CP, Holm RH (2006) J Am Chem Soc 128:11993
125. Grove LE, Xie J, Yikilmaz E, Karapetyan A, Miller A-F, Brunold TC (2008) Inorg Chem 47:3993
126. Marshall NM, Garner DK, Wilson TD, Gao Y-G, Robinson H, Nilges MJ, Lu Y (2009) Nature 462:113
127. Karlsson S, Boixel J, Pellegrin Y, Blart E, Becker H-C, Odobel F, Hammarström L (2010) J Am Chem Soc 132:17977

Struct Bond (2014) 160: 39–56
DOI: 10.1007/430_2014_144

Published online: 26 March 2014

Dioxygen Activation by Biomimetic Iron Complexes of α-Keto Acids and α-Hydroxy Acids

Tapan Kanti Paine and Lawrence Que Jr.

Abstract A subset of the large family of nonheme iron oxygenases carries out the oxidative decarboxylation of α-ketocarboxylate and α-hydroxycarboxylate substrates in the presence of O_2. Iron complexes of α-ketocarboxylates and α-hydroxycarboxylates supported by tridentate and tetradentate ligands have been synthesized to act as functional models for these enzymes, and several have been structurally characterized. From studies of these model complexes and their reactivity toward various probe substrates, insights into the reaction mechanisms have been obtained, where iron(III)-superoxo and iron(IV)-oxo species have been implicated as key oxidants.

Keywords α-Hydroxy acids · α-Keto acids · Biomimetic complexes · Dioxygen · Iron

Contents

T.K. Paine
Department of Inorganic Chemistry, Indian Association for the Cultivation of Science, 2A&2B Raja S. C. Mullick Road, Jadavpur, Kolkata 700032, India
e-mail: ictkp@iacs.res.in

L. Que Jr. (✉)
Department of Chemistry and Center for Metals in Biocatalysis, University of Minnesota, 207 Pleasant Street SE, Minneapolis, MN 55455, USA
e-mail: larryque@umn.edu

1 Biochemical Background

The α-ketoglutarate (α-KG)-dependent oxidases and oxygenases [1] represent the largest subset of the superfamily of nonheme iron enzymes that possess a recurring 2-His-1-carboxylate facial triad structural motif that binds the active-site iron center [2]. These enzymes catalyze an amazing diversity of reactions related to the post-translational modification of protein side chains, the repair of alkylated DNA/RNA, biosynthesis of antibiotics and plant products, metabolism related to lipids, and biodegradation of a variety of compounds. The α-KG-dependent enzymes require α-ketoglutarate as a co-substrate in order to initiate the activation of dioxygen and generate an oxidant that carries out the initial cleavage of a substrate C–H bond that in turn becomes functionalized, resulting in the formation of a C–X bond where X=OH, Cl, Br, or SR. Related enzymes catalyze dehydrogenation, formation of heterocyclic rings, as well as heterocyclic ring expansion. Although they do not utilize α-KG as a co-substrate, some iron oxidases such as isopenicillin N synthase and 1-amino-cyclopropane 1-carboxylate oxidase resemble the Fe(II)/α-KG-dependent enzymes in structure and mechanism [3].

Much has been learned over the last 20 years from X-ray crystallography regarding the structures of these enzymes as well as aspects of their catalytic mechanisms. TauD, the prototypical enzyme of this class, catalyzes the hydroxylation of taurine (2-aminoethanesulfonate) at the C1 position, subsequently releasing sulfite. This enzyme has been crystallized in three forms: the as-isolated enzyme, the enzyme-α-KG complex, and the enzyme-α-KG-taurine complex [4]. In the as-isolated form, the iron center is coordinated to the 2-His-1-carboxylate facial triad and three water molecules (A in Fig. 1). Two of the latter are displaced upon bidentate binding of α-KG to the iron center (B in Fig. 1), while the third is displaced upon binding of taurine in the active site (C in Fig. 1). The substrate taurine itself does not coordinate to the iron center, so the iron center becomes 5-coordinate upon substrate binding, thereby providing an available site for O_2 to bind.

What happens in the enzyme active site after O_2 binding has not been established by X-ray crystallography. However, a plausible mechanism can be assembled (Fig. 1) that has found support from rapid kinetic and spectroscopic studies [5] and DFT calculations [6] as well as biomimetic complexes (see following sections). O_2 binding forms an adduct D that can be described as an iron(III)-superoxo complex. Superoxide, which is well established to be a strong nucleophile, is proposed to attack the electrophilic keto function of the bound α-KG to form alkylperoxo complex E. Complex E in turn breaks down by undergoing O–O and C–C bond cleavage to generate CO_2, succinate, and oxoiron(IV) intermediate F, which serves as the oxidant needed to break the substrate C–H bond and introduce an oxygen atom into the substrate to form the hydroxytaurine product. Product release then regenerates the iron(II) active site in A to start another catalytic cycle.

An important development in understanding the enzyme mechanism for α-KG-dependent enzymes has been the rapid freeze-quench trapping of an

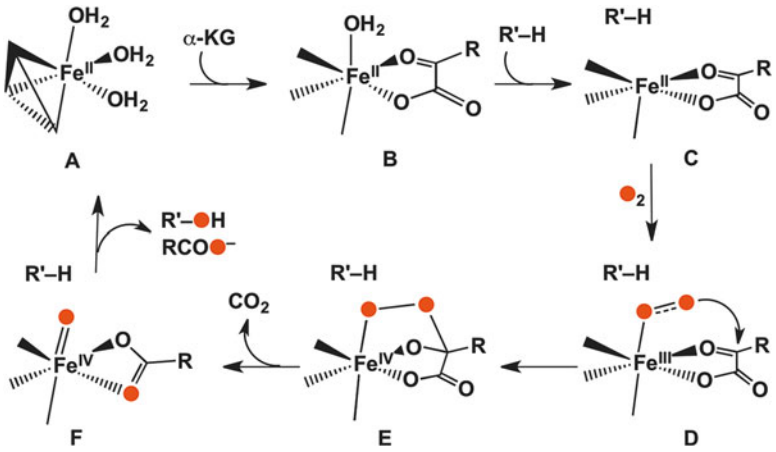

Fig. 1 Generally accepted mechanism for the α-KG-dependent enzymes

intermediate called **J** in the catalytic cycle of TauD by Bollinger and Krebs [7]. Related intermediates have subsequently been trapped for other α-KG-dependent enzymes such as prolyl hydroxylase [8] and halogenases CytC3 [9] and SyrB2 [10]. These intermediates exhibit Mössbauer spectra indicative of high-spin iron(IV) species [11] and EXAFS spectra that reveal a short (~1.62 Å) Fe=O bond [12, 13], properties that associate them with species F in Fig. 1. It is clear that this intermediate is the species responsible for C–H bond cleavage, as deuteration of the target C–H bond on the substrate results in a significant retardation in the rate of decay of the oxoiron (IV) intermediate (KIE ~50 in the case of TauD) [14].

Closely related to the α-KG-dependent enzymes are enzymes that catalyze the oxidation of α-hydroxycarboxylate substrates. One such example is CloR, an enzyme which converts a mandelate (2-hydroxy-2-phenylacetate) moiety to benzoate in the biosynthesis of the coumarin antibiotic chlorobiocin [15]. The mechanism for this oxidative transformation must differ from that of the α-KG-dependent enzymes because the mandelate substrate itself undergoes a $4e^-$-oxidation that results in the cleavage of the C1–C2 bond and the conversion of the C2–OH function to a carboxylate, concomitant with the release of CO_2. An iron(III)-superoxo species is proposed to initiate substrate oxidation by abstracting an H-atom from the substrate [16].

Studies of synthetic complexes that model structural and functional aspects of the metal active site can make important contributions to our understanding of metalloenzyme mechanisms. Thus, there have been efforts in parallel to those aimed at elucidating the structure and function of nonheme iron enzymes to develop models for those enzymes that use α-ketocarboxylic and α-hydroxycarboxylic acids as substrates. In general, iron complexes with polydentate supporting ligands are used to mimic the iron active site, leaving several coordination sites available for the coordination of substrate and O_2. These efforts over the past two decades are reviewed herein.

2 Biomimetic α-Ketocarboxylate Complexes of Tetradentate N4 Ligands

There are a number of synthetic complexes that have been characterized over the past 20 years that model the α-keto acid-dependent enzymes [3]. Typically the α-ketoglutarate is modeled with different α-keto acids like benzoylformic acid (HBF), pyruvic acid (HPRV), and phenylpyruvic acid (H_2PP), the BF ligand being the most used analog for α-KG in the synthetic complexes. The protein residues that bind the iron in the active site are modeled by tridentate or tetradentate supporting ligands with N-donors (Fig. 2).

Chiou and Que reported the first crystallographically characterized synthetic iron(II)-α-keto acid complexes using TPA (tris(pyridyl-2-methyl)amine) or 6-Me_3-TPA (tris(6-methyl-pyridyl-2-methyl)amine) as the tetradentate supporting ligand and BF as the α-keto acid [17, 18]. In the case of [(6-Me_3-TPA)Fe^{II}(BF)]$^+$, the BF monoanion acts as a bidentate ligand, while for [(TPA)Fe^{II}(BF)(MeOH)]$^+$, the BF coordinates as a monodentate ligand (Fig. 3). Bidentate binding of the α-keto acid ligand gives rise to a visible chromophore associated with a metal-to-ligand charge-transfer (MLCT) transition from a filled d-orbital of Fe^{2+} to the low-lying π* orbital of the keto group [19]. This transition gives [(6-Me_3-TPA)Fe^{II}(BF)]$^+$ a purple-blue color. A similar feature can be observed for α-KG-bound enzymes [20–23]. Given the nature of the chromophore, it is thus not surprising that the position of the charge-transfer band depends on the nature of the α-keto acid and on the Lewis basicity of the polydentate supporting ligand. For example, in a series of *para*-substituted BF complexes, the MLCT band is most redshifted for the complex with the most electron-withdrawing *para* substituent. On the other hand, the corresponding pyruvate complex [(6-Me_3-TPA)Fe^{II}(PRV)]$^+$ is orange in color, the MLCT band being blueshifted relative to that of [(6-Me_3-TPA)Fe^{II}(BF)]$^+$ and half as intense due to the loss of conjugation of the α-keto functionality with the aromatic ring [24]. In the case of [(TPA)Fe^{II}(BF)]$^+$, the appearance of the visible chromophore is solvent dependent. In coordinating solvents like MeOH and MeCN, BF binds as a monodentate ligand, so the complex is yellow in color. However, BF binding becomes bidentate in noncoordinating solvents like CH_2Cl_2, and the complex turns green in color [18].

The model α-keto acid complexes react with dioxygen [18, 24]. The six-coordinate iron(II)-BF complexes of N4 ligands slowly react with dioxygen to undergo oxidative decarboxylation and form the corresponding benzoate complexes in quantitative yield (Fig. 4) [18]. [(6-Me_3-TPA)Fe^{II}(BF)]$^+$ converts to [(6-Me_3-TPA)Fe^{II}(benzoate)]$^+$ over a period of 1 week, whereas [(TPA)Fe^{II}(BF)]$^+$ forms [(TPA)$_2$$Fe^{III}$$_2$(μ–O)(benzoate)$_2$]$^{2+}$ after 2 days. On the other hand, [(6-Me_3-TPA)Fe^{II}(PRV)]$^+$ does not react with oxygen under the same experimental conditions. The slowness of the reaction may be attributed to the lack of a vacant site for O_2 binding, requiring a ligand to dissociate first to initiate the reaction. Kinetic studies on a series of (6-Me_3-TPA)Fe^{II} complexes with *para*-substituted benzoylformates reveal that the rate of the oxidative decarboxylation increases as

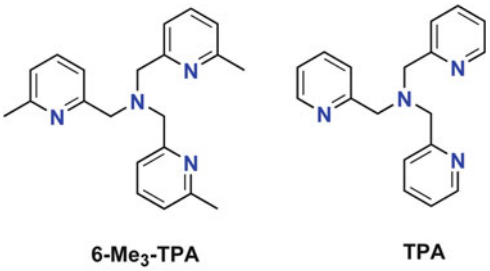

Fig. 2 Tetradentate tripodal ligands used in biomimetic chemistry

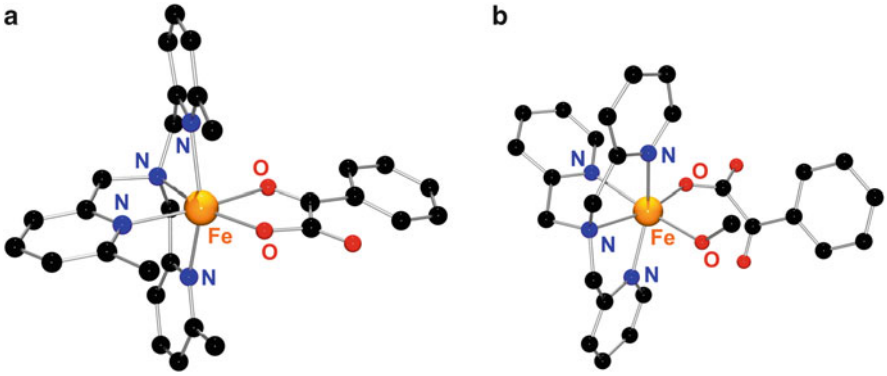

Fig. 3 Crystal structures of iron(II)-α-keto acid complexes of tetradentate tripodal ligands showing respective bidentate and monodentate binding of BF: (**a**) $[(6\text{-}Me_3\text{-}TPA)Fe^{II}(BF)]^+$ and (**b**) $[(TPA)Fe^{II}(BF)(MeOH)]^+$

the substituent of BF becomes more electron withdrawing, affording a positive Hammett ρ value of +1.07. This trend suggests that oxidative transformation involves a nucleophilic attack at the keto carbon of BF by a nucleophilic iron-oxygen species to initiate the decarboxylation reaction.

No direct evidence of any intermediate species could be found. However, some interception experiments provide useful insight into the nature of intermediate species involved in the oxidative decarboxylation reaction [18]. The model iron (II)-BF complexes react with dioxygen in the presence of 2,4-di-*tert*-butylphenol to afford 4,4′,6,6′-tetra-tert-butyl-2,2′-biphenol in almost stoichiometric yield. These observations demonstrate that the reaction of the iron(II)-BF complexes with O_2 generates an oxidant capable of hydrogen-atom abstraction from phenols. Additionally, the model complexes react with triphenylphosphine to form triphenylphosphine oxide, so the oxidant is also capable of oxygen-atom transfer. Indeed, ^{18}O-labeling experiments show that one oxygen atom from O_2 is incorporated into triphenylphosphine oxide and the other oxygen atom into the benzoate (Fig. 4), thereby mimicking the dioxygenase nature of the enzyme reactions.

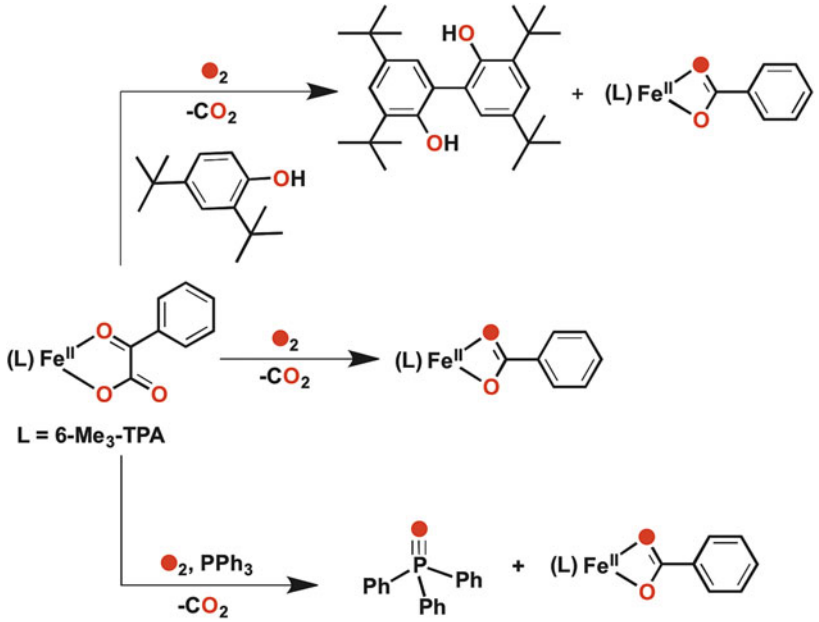

Fig. 4 Reactivity of [(6-Me$_3$-TPA)Fe^{II}(BF)]$^+$ with O_2 and substrates

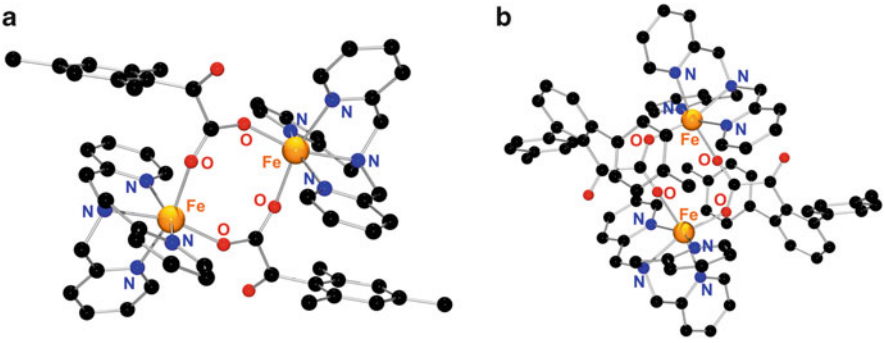

Fig. 5 Crystal structures of iron(II) complexes of bulky benzoylformates. (**a**) [(TPA)Fe(2,4,6-Me$_3$BF)]$_2^{2+}$ and (**b**) [(TPA)Fe(2,6-(p-tolyl)$_2$BF)]$_2^{2+}$

More recently, two iron(II) complexes of sterically bulky benzoylformates with the general formula [(TPA)Fe((O$_2$CC(O)Ar)]$_2$ (where Ar=2,4,6-trimethylphenyl or 2,6-di(p-tolyl)phenyl) have been synthesized and structurally characterized [25]. X-ray structures of the dinuclear complexes show two iron(II) centers bridged by two carboxylate groups from two bulky α-ketocarboxylates (Fig. 5). However, the dinuclear complexes dissociate in varying degrees to the corresponding monomers in solution as revealed from UV–vis and ^{1}H NMR spectroscopic studies.

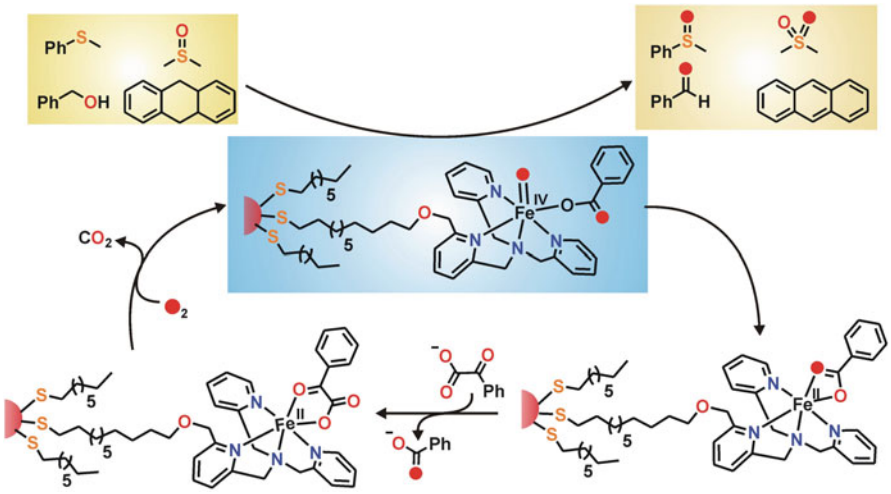

Fig. 6 Catalytic substrate oxidations by a biomimetic iron(II)-BF complex immobilized on a gold nanoparticle surface using O_2 as the oxidant and NaBF as the sacrificial reductant

While the complexes become oxidized in the presence of dioxygen, no oxidative decarboxylation of benzoylformate is observed. It is proposed that the steric bulk of the aryl groups prevents the attack of O_2 on the keto function needed to initiate the oxidative decarboxylation reaction.

The iron(II)-α-keto acid complexes discussed above at best carry out stoichiometric decarboxylation of the α-keto acid in their reactions with dioxygen. Very recently, Paine and co-workers [26] reported a biomimetic iron(II)-BF complex supported by a thiol-appended TPA-derived N4 ligand immobilized on gold nanoparticles that undergoes oxidative decarboxylation reaction exhibiting catalytic turnovers (Fig. 6). Gold nanoparticles provide a large surface area upon which to immobilize the iron complex, which inhibits the formation of catalytically inactive oxo-bridged diiron(III) by-products. The immobilized complex has been reported to catalyze oxo-atom transfer to thioanisole with a maximum TON of 6 in the presence of 20 equivalents of NaBF. This complex represents the first catalytically active functional model of α-keto acid-dependent oxygenases.

Phenylpyruvic acid (H_2PP) is related to the α-keto acid substrate of 4-hydroxyphenylpyruvate dioxygenase (HPPD), but its coordination chemistry is less well explored. Unlike other keto acids, H_2PP has two ionizable protons due to its tendency to enolize upon coordination with a metal ion. The extent of enolization of the HPP monoanion depends upon the nature of the supporting ligand and the Lewis acidity of the metal center. Iron complexes of phenylpyruvate with polydentate nitrogen donor ligands have been reported [24, 27]. While the $(Tp^{Ph2})Fe^{II}$ center binds phenylpyruvate in the conventional α-ketocarboxylate

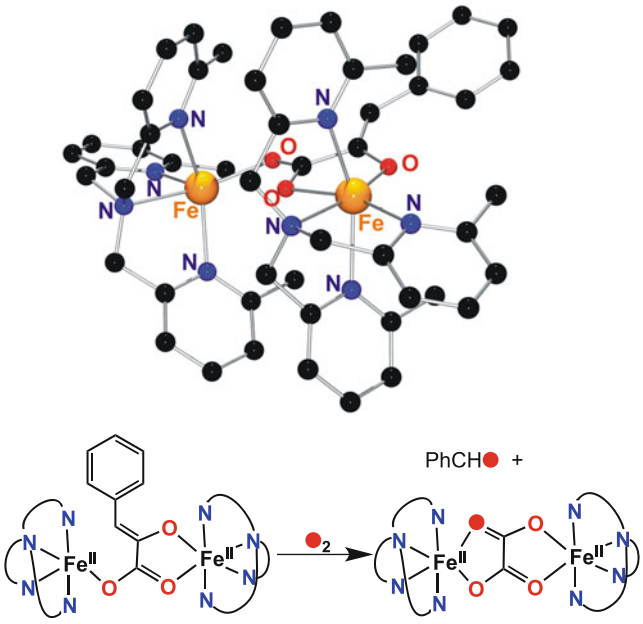

Fig. 7 The structure of $[(6\text{-}Me_3\text{-}TPA)_2Fe_2(PP)_2]^{2+}$ complex and its reaction with dioxygen

mode, the more Lewis acidic metal center in $[(6\text{-}Me_3\text{-}TPA)_2Fe_2(PP)]^{2+}$ promotes enolization of the coordinated phenylpyruvate and results in the formation of an unusual PP-bridged diiron complex. In its X-ray structure, one of the iron centers has a distorted octahedral coordination geometry, while the other iron center is five-coordinate. The PP dianion acts as a bidentate ligand on the 6-coordinate iron center, while the other carboxylate oxygen binds to the five-coordinate iron center (Fig. 7).

The diiron(II)-PP complex reacts with dioxygen to undergo oxidative cleavage of the C2–C3 bond of phenylpyruvate, instead of the C1–C2 bond [24] as observed for HPPD. In this reaction, an oxalate-bridged diiron(II) complex, $[(6\text{-}Me_3\text{-}TPA)_2\text{-}Fe_2(\mu\text{-oxalato})_2]^{2+}$, is formed along with benzaldehyde as the other product. ^{18}O labeling experiments show the incorporation of one oxygen atom into the oxalato moiety and the other oxygen atom into benzaldehyde. Subsequent to this report, it has been found that this aliphatic C2–C3 bond cleavage reactivity can also be observed when O_2 and phenylpyruvate are reacted in the active site of the β-diketone dioxygenase Dke1, producing the same products as the model reaction [28]. Functional models of Dke1 and related aliphatic C–C bond cleaving dioxygenases have been reviewed recently by Allpress and Berreau [29].

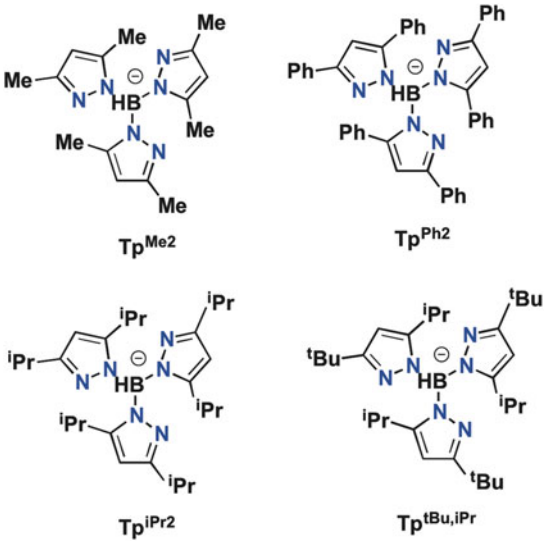

Fig. 8 Tris(pyrazolyl) borate ligands used in biomimetic chemistry

3 α-Ketocarboxylate Complexes of Tridentate N3 Ligands

Hydridotris(pyrazolyl)borate ligands have been useful for the preparation of structural and functional models of nonheme iron oxygenases (Fig. 8), as the monoanionic tris(pyrazolyl)borates provide a facial N3 donor environment at the metal center and mimic the "2-His-1-carboxylate facial triad motif" observed in a large number of nonheme iron oxygenases [30]. In addition, the pyrazole rings can easily be functionalized with different alkyl substituents in order to tune the steric and electronic properties of the facial N3 ligand. Thus, a number of Fe($Tp^{R,R'}$) (α-ketocarboxylate) complexes have been prepared and shown to have a range of reactivity properties.

[(Tp^{Me2})Fe^{II}(BF)] represents the first example of a synthetic iron(II)-α-ketocarboxylate complex with a facial N3 supporting ligand, which was prepared by Valentine and co-workers [31]. Although not structurally characterized, this complex exhibits characteristic iron(II)-to-keto charge-transfer bands in the visible region that indicate bidentate coordination of the BF ligand. Unlike the tetradentate TPA and 6-Me_3-TPA complexes discussed in the previous section, [(Tp^{Me2})Fe^{II}(BF)] reacts with oxygen within 2 min, undergoing three color changes (from blue purple to green to yellow to orange) and resulting in the oxidative decarboxylation of the BF ligand to form benzoate. This reaction generates an oxidant that is capable of epoxidizing cyclohexene and *cis*-stilbene. The latter occurs with retention of configuration, strongly implicating a metal-based oxidant, analogous to species F in Fig. 1. Interestingly, *trans*-stilbene is not epoxidized by the model complex, suggesting that the oxidant generated is formed within a pocket capable of discriminating between the *cis* and *trans* isomers of the olefin substrate.

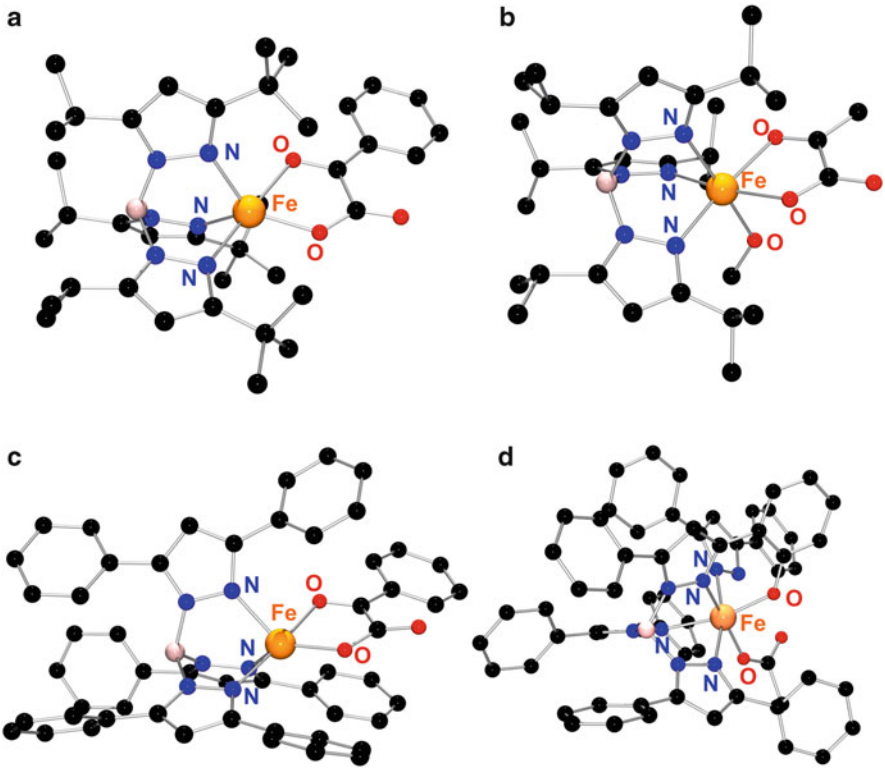

Fig. 9 Crystal structures of iron(II)-α-keto acid complexes of facial $Tp^{R,R'}$ ligands: (**a**) [$Tp^{3tBu,5iPr}$)Fe^{II}(BF)], (**b**) [(Tp^{iPr2})Fe^{II}(PRV)], (**c**) [(Tp^{Ph2})Fe^{II}(BF)], and (**d**) [(Tp^{Ph2*})Fe^{III}(O_2CMe)]

Subsequently Hikichi et al. prepared an iron(II)-BF complex with $Tp^{3tBu,5iPr}$, which is at the other extreme of steric bulk for Tp ligands [32]. Two different crystalline forms of this complex were isolated and structurally characterized, a tetrahedral iron(II) complex with a monodentate BF and a trigonal bipyramidal iron (II) complex with a chelated BF (Fig. 9a), the two binding modes possibly arising from the effect of the sterically bulky *tert*-butyl substituents on BF binding. In fact, the five-coordinate complex exhibits thermochromism in solution, being almost colorless at room temperature and becoming deep bluish purple with a decrease in temperature. This complex does not react at all with dioxygen, presumably because of the steric hindrance of the bulky $Tp^{3tBu,5iPr}$ ligand in the vicinity of the iron center.

Following up on the early efforts presented above, Que, Fujisawa, and co-workers focused on iron(II)-α-ketocarboxylate complexes with Tp^{iPr2} or Tp^{Ph2} as the supporting ligand and gained important mechanistic insights in their reactivity with O_2 [21, 27, 33, 34]. Five additional crystal structures of [(Tp^{R2})Fe^{II}(α-ketocarboxylate)] complexes were obtained; as shown by the two examples

of complexes in Fig. 9b, c, the iron(II) centers are five-coordinate and the α-ketocarboxylates coordinate in a bidentate fashion. One exception is the [(Tp^{iPr2})Fe^{II}(BF)] complex, which crystallizes from CH_2Cl_2/pentane as a dimeric species with the carbonyl oxygen of the coordinated carboxylate binding to the vacant site of the iron on the adjacent unit.

These complexes react with dioxygen over the course of an hour, reflecting rates that are two orders of magnitude faster than the iron(II)-α-keto acid complexes with tetradentate ligands. This comparison emphasizes the importance of having an available coordination site at the iron center for dioxygen binding. However, among the Tp^{R2} complexes, the reaction times decrease in the order Tp^{Ph2} (1 h) [33] > Tp^{iPr2} (15 min) [34] >Tp^{Me2} (2 min) [31], suggesting that the steric bulk of the pyrazole substituents can play an important role in controlling O_2 reactivity.

Reaction of [(Tp^{iPr2})Fe^{II}(PRV)] with O_2 at room temperature results in immediately observable spectral changes consisting of the replacement of the MLCT band at 500 nm that is characteristic of the bidentate iron(II)-α-ketocarboxylate unit with an intense feature at 370 nm associated with the oxidation product [34]. ESI-MS analysis of the latter reveals an ion at *m*/*z* 536 that has a mass and an isotope distribution pattern matching that of {[Fe(Tp^{iPr2}) + O–H}$^+$, suggesting the conversion of a C–H bond to a C–O$^-$ moiety that would indicate hydroxylation of one of the alkyl substituents on the Tp ligand, very likely the methine C–H bond on one of the isopropyl groups (Fig. 10, bottom right). Indeed, analogous attack of the isopropyl 3°–C–H bond has been demonstrated previously in the reactions of O_2 with [Mn$^{II}_2$(Tp^{iPr2})$_2$(μ-OH)$_2$] [35] or [Co^{I}(Tp^{iPr,Me})] [36], and a crystal structure has been reported for the alkoxomanganese product.

The mechanism proposed for the α-KG-dependent iron enzymes depicted in Scheme 1 shows two key intermediates derived from dioxygen: the iron(III)-superoxo species D and the iron(IV)-oxo species F. Indirect evidence for both of these key intermediates has been obtained from reactivity studies of the synthetic complexes. The observation that an intramolecular hydroxylation of one of the ligand isopropyl groups is likely to occur in the reaction of [(Tp^{iPr2})Fe^{II}(PRV)] with O_2 [34] raises the possibility that an Fe^{IV}=O oxidant may be formed to carry out the initial H-atom abstraction from an isopropyl 3°–C–H bond followed by rapid oxygen rebound to form the C–O bond of the alkoxoiron product. The putative Fe^{IV}=O oxidant can be intercepted intermolecularly by addition of an excess of thioanisole to form the corresponding sulfoxide in excellent yield in place of the ligand hydroxylated product.

Evidence for the participation of an iron(III)-superoxo intermediate has been obtained at −40°C [34]. Without added exogenous substrate, [(Tp^{iPr2})Fe^{II}(PRV)] reacts with O_2 at −40°C to form a peroxo-bridged diiron(III) complex with spectroscopic characteristics (λ_{max} 682 nm, ε = 1,700 M^{-1} cm^{-1}; $\gamma_{O\text{-}O}$ 889 cm^{-1} and $\gamma_{Fe\text{-}O}$ 424 cm^{-1}) quite similar to those previously found by Kitajima for the reversible O_2 adduct of [(Tp^{iPr2})Fe^{II}(O_2CPh)] [37]. The most likely mechanism for the formation of the dinuclear O_2 adduct involves initial generation of a mononuclear iron-O_2 adduct like the iron(III)-superoxo species D proposed in Fig. 1, which can in principle be intercepted by addition of exogenous substrates. This notion has been

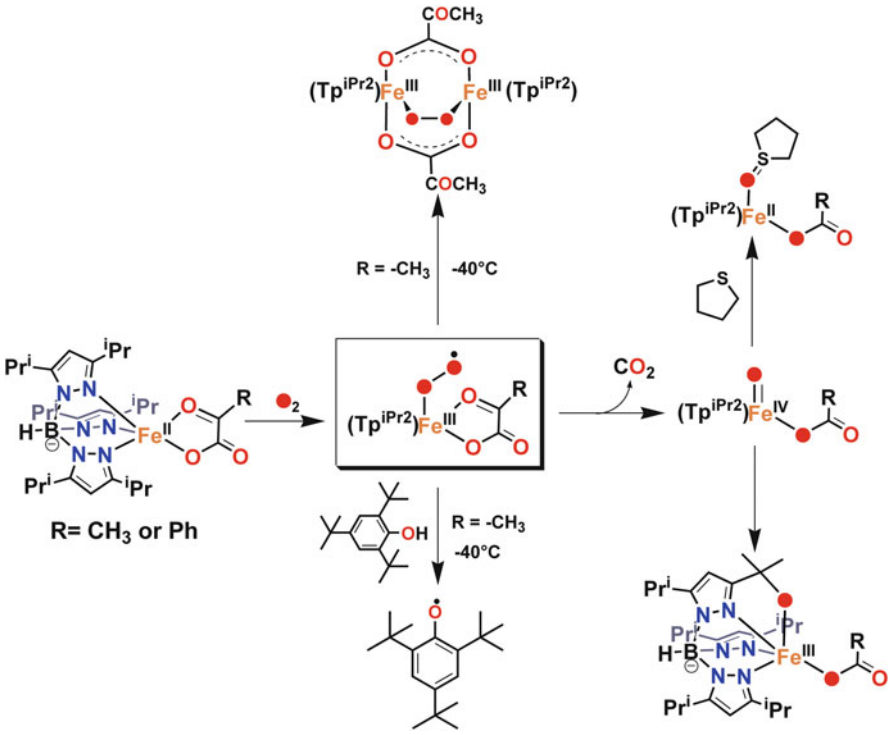

Fig. 10 Reactions of [$(Tp^{iPr2})Fe^{II}$(α-ketocarboxylate)] complexes with O_2 under various reaction conditions implicating a key iron(III)-superoxide intermediate

tested by the addition of tetrahydrothiophene or 2,4,6-tri-*tert*-butylphenol. Oxygenation of a solution of [$(Tp^{iPr2})Fe^{II}$(PRV)] in the presence of tetrahydrothiophene does not affect the outcome of the oxygenation, which is not surprising as tetrahydrothiophene is an oxo-atom acceptor, but superoxide is not an oxo-atom donor. However, the presence of 2,4,6-tri-*tert*-butylphenol prevents formation of the Kitajima O_2-adduct and instead yields 2,4,6-tri-*tert*-butylphenoxyl radical in 80% yield (Fig. 10). As phenoxyl radical is not formed when 2,4,6-tri-*tert*-butylphenol is added after formation of the Kitajima O_2-adduct, these observations exclude the O_2-adduct as the oxidizing intermediate and implicate a reactive species that is a precursor of the O_2-adduct. The most likely candidate would be the initially formed monoiron(III)-superoxo species, which should be capable of carrying out H-atom abstraction from the O–H bond of a phenol (Fig. 10).

Parallel experiments with the Tp^{Ph2} complexes provide further insight. These complexes also react with O_2 but afford instead a stable green product. This chromophore has been demonstrated to arise from a phenolate-to-iron(III) charge-transfer band by resonance Raman spectroscopy, suggesting that a ligand phenyl group has been hydroxylated (Fig. 11) [27, 33]. Consistent with this conclusion, ESI-MS analysis of the green product shows a dominant ion at $m/z = 740.2$, which has a mass and isotope distribution pattern characteristic of the $\{[Fe(Tp^{Ph2}) + O - H\}^+$ ion.

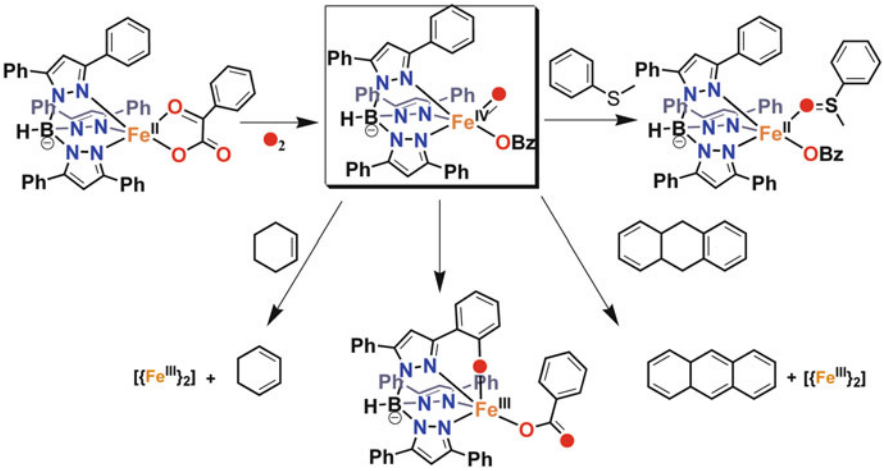

Fig. 11 Reactions of [(Tp^{Ph2})Fe^{II}(BF)] with dioxygen in the presence of different reagents that can intercept the putative oxoiron(IV) oxidant

Furthermore, $^{18}O_2$-labeling experiments demonstrate the incorporation of one oxygen atom into the Tp^{Ph2} ligand backbone and the other oxygen atom into the benzoate, establishing the dioxygenase nature of the reaction. Lastly, the X-ray structure of this green complex shows a hydroxylated Tp^{Ph2} (Tp^{Ph2*}) that acts as a tetradentate ligand to the iron center (Fig. 9d).

With the green chromophore providing a convenient spectroscopic probe, kinetic data could be obtained by monitoring the change of absorbance at 650 nm [33]. The observed rate shows a first-order dependence on the concentrations of both the iron(II) complex and O_2, suggesting that the binding of O_2 to the iron center must be a component of the rate-determining step. In addition, the rate of reaction is also dependent on the nature of the *para* substituent on the BF moiety. A Hammett ρ value of +1.3 is obtained from this linear correlation, indicative of a nucleophilic attack of the BF moiety. A likely candidate for this nucleophile is the superoxide that would form upon O_2 binding to the iron center. Taken together, the data strongly suggest that the rate-determining step occurs in the early half of the reaction sequence, perhaps leading to the formation of the oxidant that carries out the intramolecular ligand hydroxylation.

DFT calculations [38, 39] suggest that this oxidant is a high-spin iron(IV)=O intermediate, which corresponds to intermediate **J** in the TauD catalytic cycle (species F in Fig. 1) and is responsible for the observed intramolecular ligand hydroxylation. (A review of synthetic work aimed at modeling such biological oxoiron(IV) species has recently been published [40].) As observed for [(Tp^{iPr2})Fe^{II}(BF)], the ligand hydroxylation can be prevented by the addition of a slight excess of thioanisole [38]. Instead, oxo-atom transfer to thioanisole occurs and the corresponding oxide is obtained. More interestingly, cyclohexene and 9,10-dihydroanthracene can also act as intercepting agents to afford dehydrogenated

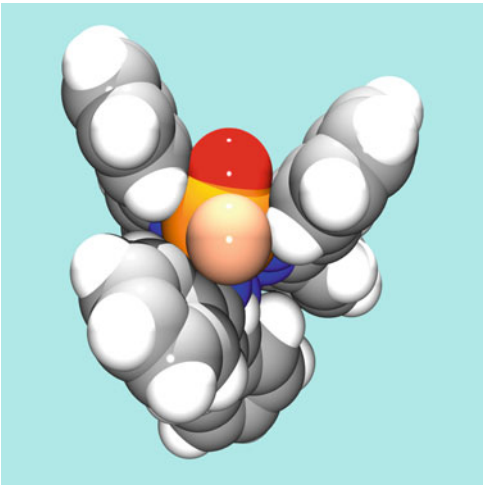

Fig. 12 DFT-calculated structure for the putative $[(Tp^{Ph2})Fe^{IV}(O)(O_2CPh)]$ oxidant derived from the reaction of $[(Tp^{Ph2})Fe^{II}(BF)]$ with O_2. The red atom represents the oxo, while the peach-colored atom is the coordinated oxygen atom of the benzoate ligand. The benzoyl moiety has been removed to provide a clearer view of the Fe=O pocket. Reprinted from [38]

products, showing that the putative oxoiron(IV) intermediate can also abstract the hydrogen atoms from substrates. 9,10-Dihydroanthracene is converted to anthracene, while cyclohexene is oxidized only to 1,3-cyclohexadiene, with no allylic oxidation by-products observed. Despite the fact that cyclohexene has an allylic C–H bond that is at least 5 kcal/mol stronger than that of dihydroanthracene, only a tenfold excess of cyclohexene is required to achieve maximal interception compared to a hundredfold excess for 9,10-dihydroanthracene; these results suggest a preference of the putative oxoiron(IV) intermediate to react with the sterically less bulky substrate despite its having a stronger C–H bond. Indeed, the DFT calculations show that the Fe=O moiety sits in a pocket surrounded by the ligand phenyl groups that may act to control substrate access to the oxidant (Fig. 12). Importantly, the reaction time remains the same (1 h) for all the interception reactions, emphasizing the fact that the rate-determining step for this reaction is not the decay of the oxoiron(IV) oxidant but rather its formation.

4 α-Hydroxycarboxylate Complexes

The discovery that some nonheme iron enzymes like CloR catalyze the oxidative decarboxylation of α-hydroxycarboxylates and related compounds has led to the synthesis of corresponding model complexes. Complexes of mandelate and lactate were obtained with 6-Me_3-TPA as the supporting tetradentate ligand [41]. The crystal structure of $[6\text{-}Me_3\text{-}TPA)Fe^{II}(mandelate)]^+$ shows the mandelate coordinated to the iron center via a carboxylate oxygen and the neutral hydroxyl group (Fig. 13). Upon exposure to O_2 this complex reacts over a period of 6 h to form $[6\text{-}Me_3\text{-}TPA)Fe^{II}(benzoate)]^+$ in quantitative yield, mimicking the corresponding

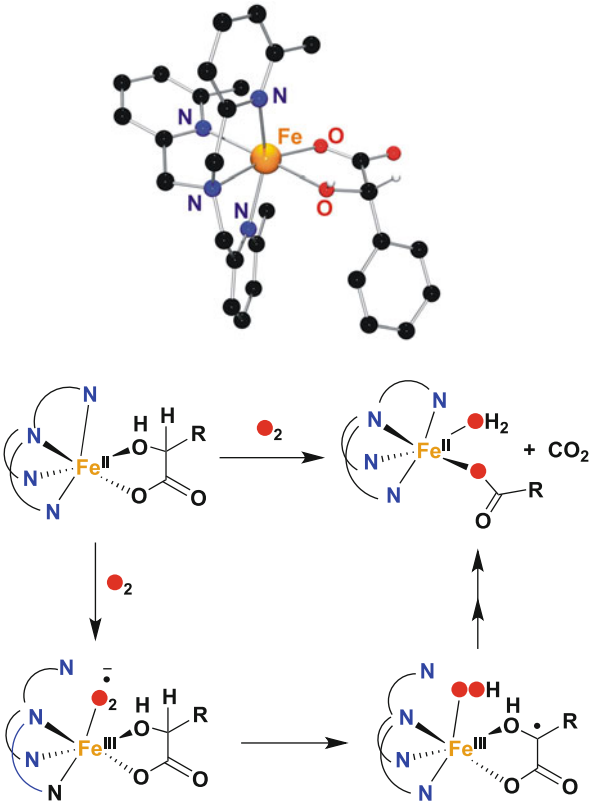

Fig. 13 Molecular structure of [(6-Me_3-TPA)Fe^{II}(mandelate)]$^+$ (*top*) and the proposed mechanism for its reaction with O_2 (*bottom*)

reaction catalyzed by CloR. ^{18}O labeling experiments clearly demonstrate the incorporation of one oxygen atom into the product benzoate, the other oxygen atom presumably being converted to water.

The reaction mechanism for the oxidative decarboxylation of α-hydroxycarboxylates parallels to some extent that for α-KG-dependent enzymes; however they must differ in some aspects due to the differences in the nature of the two substrates and the fact that the oxidative decarboxylation of α-hydroxycarboxylates entails a 4-e^- oxidation (versus a 2-e^- process for α-ketoglutarate). It is proposed that the two complexes share a common first step that entails formation of an O_2 adduct but clearly diverge at the next step. The nascent superoxide of the BF complex acts as a nucleophile to attack the electrophilic keto group, but the corresponding species for the mandelate complex must act as an electrophile to abstract a hydrogen atom from the α–C–H bond. Thus this step generates an Fe^{III}–OOH/substrate radical species that results in the oxidative decarboxylation of the substrate.

Interestingly, [6-Me_3-TPA)Fe^{II}(mandelate)]$^+$ is found to react with O_2 more than an order of magnitude faster than [6-Me_3-TPA)Fe^{II}(BF)]$^+$. It is conjectured that the coordination of the more Lewis basic OH moiety should afford a more electron-rich iron(II) center that would enhance formation of the initial O_2 adduct. The cleavage

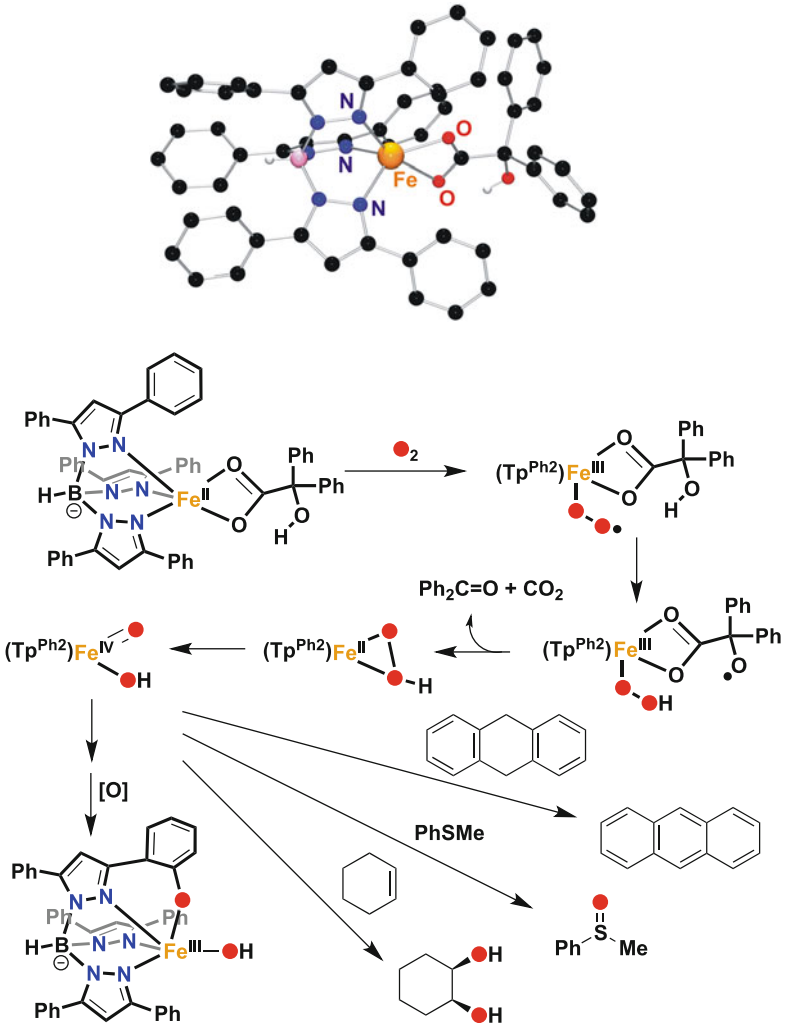

Fig. 14 Molecular structure of [(Tp^{Ph2})Fe^{II}(benzilate)] complex (*top*) and the proposed mechanism for its reaction with dioxygen and substrates (*bottom*)

of the α–C–H bond by the nascent superoxide is also a component of the rate-determining step, as replacement of mandelate with mandelate-d_1 or lactate doubles the reaction time. Furthermore, the addition of TEMPOH as the radical scavenger inhibits the oxidative decarboxylation.

As an extension of the [6-Me$_3$-TPA)Fe^{II}(mandelate)]$^+$ study, Paria, Que, and Paine replaced the tetradentate ligand with Tp^{Ph2} and the mandelate with benzilate (2,2-diphenyl-2-hydroxyacetate) to obtain complex [(Tp^{Ph2})Fe^{II}(benzilate)] [42]. The crystal structure of this complex shows the binding of the benzilate monoanion to the iron via a bidentate carboxylate with the hydroxyl group uncoordinated (Fig. 14 top).

Despite the absence of an α–C–H bond on the benzilate, this complex nevertheless reacts with O_2 leading to its oxidative cleavage and formation of CO_2 and benzophenone, a 2-e^- oxidation product (Fig. 14 bottom). There are thus two oxidizing equivalents remaining from the activation of O_2, which can be used to hydroxylate a phenyl ring on the Tp^{Ph2} ligand, as observed for [$(Tp^{Ph2})Fe^{II}$(BF)]. Like that formed from the reaction of O_2 with [$(Tp^{Ph2})Fe^{II}$(BF)], the presumed oxoiron(IV) oxidant formed from [$(Tp^{Ph2})Fe^{II}$(benzilate)] is also capable of oxidizing added substrates like thioanisole and 9,10-dihydroanthracene. However, its reaction with cyclohexene does not afford 1,3-cyclohexadiene, as observed for [$(Tp^{Ph2})Fe^{II}$(BF)] [38], nor cyclohexene oxide, as observed for [$(Tp^{Me2})Fe^{II}$(BF)] [31], but instead yields *cis*-cyclohexane-1,2-diol with both oxygen atoms derived from O_2. The observation that both oxygen atoms from O_2 can be transferred to a substrate in this reaction can be rationalized by the fact that the oxidative decarboxylation of benzilate results in the formation of CO_2 and benzophenone, neither being good ligands to the iron(II) center. The O_2 thus 2-e^- reduced and protonated becomes a hydroperoxo moiety, which binds side-on to the iron(II) center and then undergoes O–O bond cleavage to form a $LFe^{IV}(O)(OH)$ oxidant (in place of the $LFe^{IV}(O)(O_2CR)$ intermediate proposed to be formed in the corresponding [$(Tp^{Ph2})Fe^{II}$(BF)] reaction). This is the first instance for which an iron(IV)-oxo-hydroxo oxidant has been documented.

5 Summary

Iron complexes of α-ketocarboxylates and α-hydroxycarboxylates supported by tridentate and tetradentate ligands have been synthesized to act as functional models for nonheme iron oxygenases that catalyze the oxidative decarboxylation of α-ketocarboxylate and α-hydroxycarboxylate substrates in the presence of O_2. From studies of these model complexes and their reactivity toward various probe substrates, iron(III)-superoxo and iron(IV)-oxo species have been implicated as key oxidants. These results demonstrate the utility of biomimetic complexes for providing insights into the mechanisms of nonheme iron oxygenases.

Acknowledgments The authors are supported respectively by the DST, Govt. of India (Project: SR/S1/IC-51/2010), and the US National Science Foundation (Grant CHE-1058248). We thank Dr. Caleb Allpress for a careful reading of the final manuscript.

References

1. Hausinger RP (2004) Crit Rev Biochem Mol Biol 39:21–68
2. Koehntop KD, Emerson JP, Que L Jr (2005) J Biol Inorg Chem 10:87–93
3. Costas M, Mehn MP, Jensen MP, Que L Jr (2004) Chem Rev 104:939–986
4. Elkins JM, Ryle MJ, Clifton IJ, Hotopp JCD, Lloyd JS, Burzlaff NI, Baldwin JE, Hausinger RP, Roach PL (2002) Biochemistry 41:5185–5192
5. Price JC, Barr EW, Hoffart LM, Krebs C, Bollinger JM Jr (2005) Biochemistry 44:8138–8147

6. Sinnecker S, Svensen N, Barr EW, Ye S, Bollinger JM Jr, Neese F, Krebs C (2007) J Am Chem Soc 129:6168–6179
7. Price JC, Barr EW, Tirupati B, Bollinger JM Jr, Krebs C (2003) Biochemistry 42:7497–7508
8. Hoffart LM, Barr EW, Guyer RB, Bollinger JM Jr, Krebs C (2006) Proc Natl Acad Sci USA 103:14738–14743
9. Galonić DP, Barr EW, Walsh CT, Bollinger JM Jr, Krebs C (2007) Nat Chem Biol 3:113–116
10. Matthews ML, Krest CM, Barr EW, Vaillancourt FH, Walsh CT, Green MT, Krebs C, Bollinger JM Jr (2009) Biochemistry 48:4331–4343
11. Krebs C, Fujimori DG, Walsh CT, Bollinger JM Jr (2007) Acc Chem Res 40:484–492
12. Riggs-Gelasco PJ, Price JC, Guyer RB, Brehm JH, Barr EW, Bollinger JM Jr, Krebs C (2004) J Am Chem Soc 126:8108–8109
13. Galonić Fujimori DB, Barr EW, Matthews ML, Koch GM, Yonce JR, Walsh CT, Bollinger JM Jr, Krebs C, Riggs-Gelasco PJ (2007) J Am Chem Soc 129:13408–13409
14. Price JC, Barr EW, Glass TE, Krebs C, Bollinger JM Jr (2003) J Am Chem Soc 125: 13008–13009
15. Pojer F, Kahlich R, Kammerer B, Li S-M, Heide L (2003) J Biol Chem 278:30661–30668
16. van der Donk W, Krebs C, Bollinger JM Jr (2010) Curr Opin Struct Biol 20:673–683
17. Chiou Y-M, Que L Jr (1992) J Am Chem Soc 114:7567–7568
18. Chiou Y-M, Que L Jr (1995) J Am Chem Soc 117:3999–4013
19. Ho RYN, Mehn MP, Hegg EL, Liu A, Ryle MJ, Hausinger RP, Que L Jr (2001) J Am Chem Soc 123:5022–5029
20. Pavel EG, Kitajima N, Solomon EI (1998) J Am Chem Soc 120:3949–3962
21. Hegg EL, Ho RYN, Que L Jr (1999) J Am Chem Soc 121:1972–1973
22. Hegg EL, Whiting AK, Saari RE, McCracken J, Hausinger RP, Que L Jr (1999) Biochemistry 38:16714–16726
23. Ryle MJ, Padmakumar R, Hausinger RP (1999) Biochemistry 38:15278–15286
24. Paine TK, England J, Que L Jr (2007) Chem Eur J 13:6073–6081
25. Friese SJ, Kucera BE, Young VG Jr, Que L Jr, Tolman WB (2008) Inorg Chem 47:1324–1331
26. Sheet D, Halder P, Paine TK (2013) Angew Chem Int Ed 52:13314–13318
27. Paine TK, Zheng H, Que L Jr (2005) Inorg Chem 44:474–476
28. Di Giuro CML, Buongiorno D, Leitner E, Straganz GD (2011) J Inorg Biochem 105: 1204–1211
29. Allpress CJ, Berreau LM (2013) Coord Chem Rev 257:3005–3029
30. Burzlaff N (2009) Angew Chem Int Ed 48:5580–5582
31. Ha EH, Ho RYN, Kisiel JF, Valentine JS (1995) Inorg Chem 34:2265–2266
32. Hikichi S, Ogihara T, Fujisawa K, Kitajima N, Akita M, Moro-oka Y (1997) Inorg Chem 36:4539–4547
33. Mehn MP, Fujisawa K, Hegg EL, Que L Jr (2003) J Am Chem Soc 125:7828–7842
34. Mukherjee A, Cranswick MA, Chakrabarti M, Paine TK, Fujisawa K, Münck E, Que L Jr (2010) Inorg Chem 49:3618–3628
35. Kitajima N, Osawa M, Tanaka M, Moro-oka Y (1991) J Am Chem Soc 113:8952–8953
36. Reinaud OM, Theopold KH (1994) J Am Chem Soc 116:6979–6980
37. Kitajima N, Tamura N, Amagai H, Fukui H, Moro-oka Y, Mizutani Y, Kitagawa T, Mathur R, Heerwegh K, Reed CA, Randall CR, Que L Jr, Tatsumi K (1994) J Am Chem Soc 116: 9071–9085
38. Mukherjee A, Martinho M, Bominaar EL, Münck E, Que L Jr (2009) Angew Chem Int Ed 48:1780–1783
39. Usharani D, Janardanan D, Shaik S (2011) J Am Chem Soc 133:176–179
40. McDonald AR, Que L Jr (2013) Coord Chem Rev 257:414–428
41. Paine TK, Paria S, Que L Jr (2010) Chem Commun 46:1830–1832
42. Paria S, Que L Jr, Paine TK (2011) Angew Chem Int Ed 50:11129–11132

Struct Bond (2014) 160: 57–88
DOI: 10.1007/430_2012_87

Published online: 8 June 2013

Properties of $\{FeNO\}^8$ and $\{CoNO\}^9$ Metal Nitrosyls in Relation to Nitroxyl Coordination Chemistry

Brian C. Sanders, Melody A. Rhine, and Todd C. Harrop

Abstract While nitric oxide (NO) is an important signaling molecule and contributes to important physiological processes in humans, the one-electron reduced analogue of NO, namely nitroxyl (NO^- or HNO), is quickly establishing its own unique biological role. For example, HNO has been demonstrated to increase myocardial contractility by interacting with thiols in receptor molecules of heart muscle cells. These types of properties have made this particular nitrogen oxide molecule an attractive target for certain therapeutics. Since most of the underlying chemical biology of nitroxyl is mediated by heme proteins and Fe-nitroxyl intermediates have been proposed as key intermediates in denitrifying enzymes, several iron–porphyrin–NO coordination complexes of the Enemark–Feltham $\{FeNO\}^8$ notation have been pursued. Herein we describe the collective efforts on the synthetic, structural, spectroscopic, electrochemical, and theoretical work that have been performed on biologically relevant iron- and cobalt–NO complexes that afford the rare $\{FeNO\}^8$ and $\{CoNO\}^9$ notations. This compilation has provided a somewhat unifying picture into the electronic structure of this important {MNO} unit as well as the benchmark properties that will enable the bioinorganic community to characterize and determine the fate of these species in biology, especially at the active sites of metalloenzymes involved in the global nitrogen cycle.

Keywords Cobalt · Iron · Nitric oxide · Nitrosyl · Nitroxyl

Contents

B.C. Sanders, M.A. Rhine, and T.C. Harrop (✉)
Department of Chemistry and Center for Metalloenzyme Studies, The University of Georgia, 1001 Cedar Street, Athens 30602, GA, USA
e-mail: tharrop@uga.edu

1 Introduction

The biological importance of the gaseous diatom nitric oxide (NO) has been firmly established for over 30 years dating back to the early 1980s when NO was first determined to be the endothelium-derived relaxing factor (EDRF) [1, 2], a Nobel prize worthy finding in 1998 in the category of Physiology or Medicine [3–5]. In addition to NO, other related reactive nitrogen species (RNS) such as peroxynitrite ($ONOO^-$), nitrite (NO_2^-), and nitrogen dioxide (NO_2) have also become the subject of increased interest. However, among all the nitrogen oxides, the one-electron reduced (and protonated depending on pH) congener of NO, namely nitroxyl (NO^-/HNO), remains less understood due to its high reactivity with itself; a condensation reaction to afford N_2O and H_2O ($K = 8 \times 10^6\ M^{-1}\ s^{-1}$) [6–8]. It is relatively well known that nitroxyl engages in intriguing chemical and biochemical reactions that are distinct from NO [9, 10]. These include its preference for Fe(III) heme centers to form Fe(II)–NO species, a reductive nitrosylation reaction resulting in reduction of Fe(III) to Fe(II) and formation of the very stable {FeNO}^{7} heme fragment with concomitant release of a proton [11–14]. HNO is also thiophilic and preferentially targets thiol-containing biomolecules such as glutathione (GSH) to form *N*-hydroxysulfenamides (disulfides also form depending on the reaction conditions), which can disrupt intracellular redox processes [15–17]. Additionally, nitroxyl has proven therapeutic benefits and is the alcohol deterrent in the active mode of the anti-alcoholism drug cyanamide ($H_2N–C{\equiv}N$) [18]. This molecule with the aid of catalase/H_2O_2 breaks down to form HNO, which reacts with a cysteine thiol residue in the active site of aldehyde dehydrogenase effectively shutting down alcohol metabolism [19]. HNO also appears to be effective as a therapeutic against heart failure and has been demonstrated to enhance the force of contraction of the heart and increase contractility (positive inotropic effect) [20, 21]. Although the endogenous formation of nitroxyl has yet to be absolutely established, there is sufficient evidence for its formation from nitric oxide synthase (NOS) enzymes, *S*-nitrosothiols, and as transient species in the microbial denitrifying enzymes, nitrite reductase (NiR) and NO reductase (NOR) [6, 9]. In addition, the endogenous generation of HNO has been proposed to occur from a variety of nitrogen-containing substrates via oxidative mechanisms mediated by heme proteins [22]. As demonstrated by the examples listed above, metals especially heme iron appear as likely sites for production of and targets for HNO/NO^-. Furthermore, understanding the fundamental chemistry and biology of HNO-metal interactions (potential binding modes shown in Fig. 1) could have numerous benefits to human health.

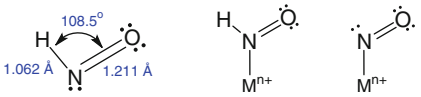

Fig. 1 Lewis structure and metric parameters of free HNO [23, 24] (*left*). Proposed mode of coordination of HNO to a generic metal center (M^{n+}) (*center*). Proposed mode of coordination of NO^- to a generic metal center (M^{n+}) (*right*). Parameters for metal-nitroxyl complexes are described in the text

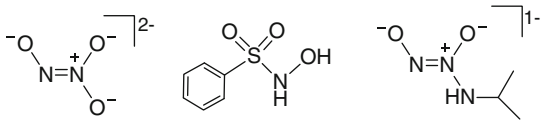

Angeli's Salt (dianion of $Na_2N_2O_3$) Piloty's Acid IPA/NO

Fig. 2 Common employed nitroxyl donor compounds: Angeli's salt (*left*); Piloty's acid (*center*); isopropylamine NONOate (IPA/NO, *right*)

The fundamental chemistry of nitroxyl, however, is less defined than NO due to its short half-life and the necessity to use HNO-generating molecules. The high reactivity of HNO requires the use of donor molecules such as Angeli's salt ($Na_2N_2O_3$) (Fig. 2), a molecule known since the beginning of the twentieth century [25, 26] and it has been extensively employed to understand HNO chemical and biochemical properties (Figs. 1 and 3). Other HNO-donors include sulfohydroxamic acids such as $PhSO_2NH$–OH (Piloty's acid), and amine diazeniumdiolates (NONOates) as depicted in Fig. 2. Each donor has different mechanisms of HNO release/pH profiles/by-products and the reader is referred to other sources for further information [7, 24]. Once formed, HNO is diamagnetic (singlet ground state) with a bent H–N–O angle of ~109° [23] and a ν_{NO} stretch and bend at 1,565 and 1,500 cm^{-1} [29, 30], respectively (other parameters are given in Fig. 1). Indeed, much of the ill-defined nature of HNO is due to its acid–base equilibrium, thermochemical properties, and spin-state variability. Free HNO is more stable by 20 kcal/mol in the singlet state with an estimated pK_a of 11.6 [27]. Clearly, the diamagnetic and protonated ^{1}HNO is the predominant species in physiological solution. In contrast, the NO^- anion is a ground state triplet and is stabilized by ~16–21 kcal/mol versus its singlet state; however, $^3NO^-$ is 16 kcal/mol less stable than ^{1}HNO (Fig. 3). This discontinuity in the spin-state of nitroxyl and its anion complicates their interconversion in solution. This also begs the question as to which state would be favored upon coordination to a metal center. It is evident that free HNO is unlikely to be formed from NO itself due to the unfavorable thermodynamic parameters associated with its reduction: $E^o = -0.81$ V (vs. NHE; ~−1 V vs. SCE) for the NO ↔ $^3NO^-$ couple [27]. Thus, if HNO were to form endogenously, a metal center seems to be a likely candidate. This further proffers the question of the M–HNO spin-state, electrochemical potentials, pK_a, as well as M–(H)NO and (H)N–O bond strengths.

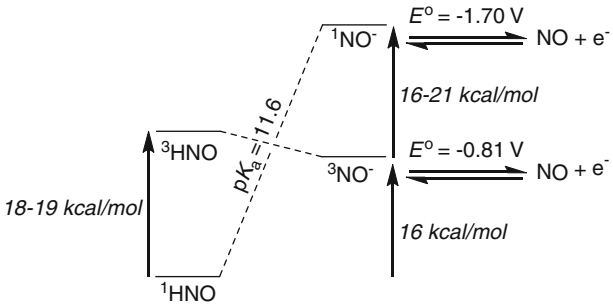

Fig. 3 Thermochemical scheme of the acid–base and redox properties of free nitroxyl. Figure 3 is a modified version from [7] and compiles values from [8, 24, 27, 28]

Low molecular weight metal-HNO/NO^- coordination complexes do exist and their properties have been reviewed elsewhere [24, 31]. The majority of these complexes involve second- or third-row transition metals such as ruthenium, iridium, or osmium that often employ phosphine and C≡O supporting ligands making their properties not as relevant from the overall perspective of biological nitroxyl genesis and target sites. While these complexes can be quite useful from a mechanistic perspective, the synthesis and properties of nitroxyl complexes of first-row transition metals such as iron and cobalt are more beneficial due to their prevalence in biology. Therefore, the specific aim of this review is to describe what is known about the coordination chemistry of iron- and cobalt-coordinated nitroxyl complexes. These unique types of systems have been designated as $\{FeNO\}^8$ and $\{CoNO\}^9$, according to the notation developed by Enemark and Feltham (EF notation) that describes the total number of metal *d* and NO π* electrons in the entire MNO unit [32]. Thus, the content of this review will focus solely on $\{FeNO\}^8$ and $\{CoNO\}^9$ coordination complexes. The purpose of this review is several-fold: (1) to describe appropriate and practical synthetic pathways toward $\{FeNO\}^8$ and $\{CoNO\}^9$ complexes; (2) to define their corresponding structural, electronic, spectroscopic, and reactivity properties from combined theoretical and experimental data; (3) to provide a unifying picture of these intrinsic properties in order to aid in the identity of such entities traversed in biology (such as in biochemical nitrogen metabolism); and finally (4) to suggest molecular design strategies for the bioinorganic community toward the stabilization of such units for the successful synthesis and application of HNO-donor molecules in future therapeutics.

2 $\{FeNO\}^8$ Heme Coordination Complexes

The interaction of small gaseous molecules, such as NO, CO, and O_2, with the prototypical heme proteins hemoglobin (Hb) and myoglobin (Mb) has long been of fundamental interest given their imperative role in aerobic physiology [33]. Even in 2011, new insights into reactions mediated by Hb have implicated these finely tuned

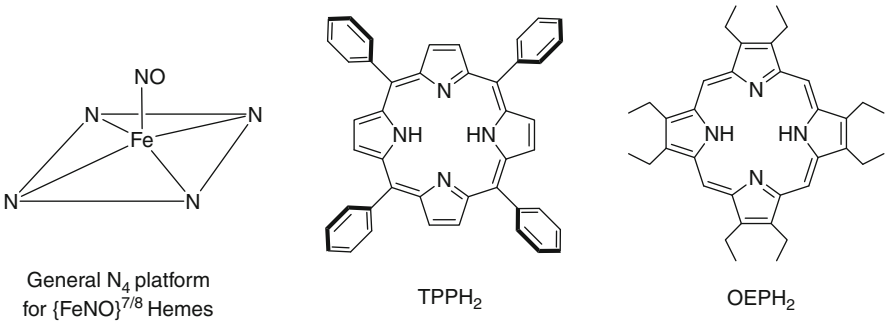

Fig. 4 The N_4 platform (*left*) represents the general coordination of the FeNO unit in porphyrin-based ligand systems that are also described in Figs. 5–7. The porphyrin ligands (*center, right*, H represents dissociable ligand protons) support the $\{FeNO\}^n$ complexes in [Fe(TPP)(NO)] (**1**), $[Fe(TPP)(NO)]^-$ (**2**), and $[Fe(OEP)(NO)]^-$ (**3**) (abbreviations defined in the text)

reaction centers as being involved in more than just oxygen transport, such as the hypoxic generation of NO and nitrite anhydrase activity [34–36]. Collectively, discrete Fe-porphyrin (Fe-por) complexes have provided valuable insights into the role of heme iron in a variety of small molecule activation pathways [37]. Motivated by the numerous examples of heme–NO interactions, synthetic chemists have focused their efforts on constructing heme models utilizing a variety of porphyrin derivatives. Analogous to the variations in the heme cofactor of proteins, synthetic porphyrins also provide suitable ancillary ligand platforms that can be systematically varied with regard to peripheral C–H bond saturation (sp^3 vs. sp^2 hybrids) and functional group modification. Indeed, nature has employed such variations on the peripheral carbon backbone of hemes to impart subtle differences in electronic properties. Understanding the fundamental properties and the reaction chemistry of heme proteins has in part been made possible through the synthesis and characterization of specific low molecular weight or small molecule Fe-por complexes [38].

2.1 *Synthesis and Experimental Properties of Heme $\{FeNO\}^8$ Complexes*

Due to their roles in mammalian physiology, Hb and Mb have been studied for more than 140 years [34, 39]. In light of the similar structural and electronic properties of the heme ligand in these proteins, Fe-por complexes have long been used as models. The first reported work (1973) of a nitrosyl Fe-por (Fe-por–NO) involved the binding of NO to Fe(II) porphyrins in order to extrapolate kinetic and thermodynamic parameters of the Fe–O_2 interaction using NO as an analogue due to its rich spectroscopic markers [40]. Shortly thereafter spectroscopic [41] and structural [42] characterization of the first Fe-por–NO complex was reported in 1974 with the tetraphenylporphyrin (TPP) ligand, which has been used widely as a platform in numerous metal constructs (Fig. 4). The report of the very stable [Fe(TPP)(NO)] (**1**)

complex (Fig. 4), an $\{FeNO\}^7$ species as defined by the EF notation [32], involved its synthesis, and structural/spectroscopic characterization [41]. These early investigations suggested the nitrosyl to be a neutral NO• ligand coordinated to a low-spin (LS) Fe(II) center ($S_{tot} = 1/2$) when six-coordinate (6C), which has been further verified recently (2005–2006) by detailed density functional theory (DFT) computational work from Lehnert and coworkers [43, 44]. However, 5C $\{FeNO\}^7$ complexes such as **1** display a strong mixing between Fe d_z^2 and NO π* orbitals in their frontier MOs and suggest more LS Fe(I)–NO^+ character in these systems [45]. Establishment of the electronic structure of this $\{FeNO\}^7$ system is crucial since it is the principal entry point for nearly all of the $\{FeNO\}^8$-por systems that are described in the discussion below. This assignment and its corresponding spectroscopic benchmarks therefore set the stage in addressing the fate of the electron in the $\{FeNO\}^7$-to-$\{FeNO\}^8$ reduction (i.e., localized on Fe or NO).

The first account of an $\{FeNO\}^8$-por complex was communicated in early 1982 by Kadish and Olson, which described the electrochemical properties of $[Fe(TPP)(NO)]^-$ (**2**) and $[Fe(OEP)(NO)]^-$ (**3**) (where OEP = dianion of octaethylporphyrin) (Fig. 4) [46]. Both complexes displayed reversible diffusion-controlled cyclic voltammograms (CVs), which afforded $E_{1/2}$ values of −0.93 and −1.10 V (vs. SCE, CH_2Cl_2) for the $\{FeNO\}^7 \leftrightarrow \{FeNO\}^8$ redox couple of **1** and **2**, respectively (Table 1). Similar electrochemical experiments were performed in neat pyridine with little change to $E_{1/2}$, inferring minor (if any) influence of a second axial *N*-donor or on solvent polarity. Additional redox waves were found in the CV that were assigned to other processes demonstrating the rich redox chemistry associated with the Fe-por unit. Unfortunately, attempts to isolate the $\{FeNO\}^8$ complexes **2** and **3** after exhaustive electrolysis at −1.20 V only resulted in the corresponding $\{FeNO\}^7$ derivatives. At the time, the unstable nature of the $\{FeNO\}^8$ species was proposed to be due to disproportionation or decomposition in the electrochemical cell even at the highly reducing potentials used. However, it appears that the non-isolability of **2** and **3** could be due to the reaction $\{FeNO\}^8 + H^+ \rightarrow \{FeNO\}^7 + ½H_2(g)$ via a transient Fe–HNO that results from the presence of trace water as a proton source in the solvent (vide infra). Although not suggested at the time, this initial report was indicative of the difficult nature in isolating this elusive species and only limited spectroscopic and theoretical analyses have been the norm in terms of characterization (vide infra).

The electrochemical observation of the $\{FeNO\}^7 \leftrightarrow \{FeNO\}^8$ redox couple in the TPP and OEP systems inspired further modes of characterization, including the spectroelectrochemistry of the complexes in numerous organic solvents with various donor properties [58]. It was hypothesized that these measurements would shed light on the role solvents play in stabilizing and ultimately in isolating the $\{FeNO\}^8$ complex. Similar to the initial CVs for **2** and **3** in CH_2Cl_2, CVs in various polarity/donorability solvents revealed two reversible, diffusion-controlled, redox events that were assigned to the $\{FeNO\}^{6/7/8}$ redox couples. The $E_{1/2}$ values for the $\{FeNO\}^{7/8}$ couple for **2** and **3** were in the −0.75 to −0.95 V range (vs. SCE) depending on the solvent. In general, the $\{FeNO\}^8$-por complex was stabilized (shifted to more positive potentials) in higher dielectric solvents such as DMF.

Table 1 Electrochemical and spectroscopic data of {FeNO}$^{7/8}$ heme systems

Molecule	$E_{1/2}$ (V)[a]	ν_{NO} (cm^{-1})	$\Delta\nu_{NO}$ (cm^{-1})[b]	ν_{FeN} (cm^{-1})[c]	Ref
{FeNO}^{7}					
[Fe(TPP)(NO)] (**1**)	−0.93[d]	1,681[e]	–	525[e]	[46, 47]
MbNO (**12**)	−0.87[f]	1,612[f]	–	552[f]	[48, 49]
{FeNO}^{8}					
[Fe(TPP)(NO)]$^-$ (**2**)	–	1,496[e]	−185	549[e]	[46, 47]
[Fe(OEP)(NO)]$^-$ (**3**)	−1.08[g]	1,441[h]	−229	–	[50, 51]
[Fe(OEC)(NO)]$^-$ (**4**)	−1.08[g]	–	–	–	[50]
[Fe(OEiBC)(NO)]$^-$ (**5**)	−1.11[g]	–	–	–	[50]
[Fe(OEPone)(NO)]$^-$ (**6**)	−0.71[e]	1,442[h]	−220	–	[51, 52]
[Fe(2,4-OEPdione)(NO)]$^-$ (**7**)	−0.65[e]	1,442[h]	−223	–	[51, 52]
[Fe(TFPPBr$_8$)(NO)]$^-$ (**9**)	−0.19[d]	1,547[i]	−165	–	[53]
[Fe(TPPS)(NO)]$^{5-}$ (**11**)	−0.63[f]	–	–	–	[54]
[Fe(TMPyP)(NO)]$^{3+}$	−0.57[f]	–	–	–	[55]
MbHNO (**13**)	–	1,385[f]	−227	649[f]	[49, 56]

[a]Data represents the $E_{1/2}$ value for the {FeNO}$^{7/8}$ redox couple normalized to the saturated calomel reference electrode (SCE) based on the information found in [57]
[b]Denotes the change in stretching frequency upon reduction from {FeNO}^{7}-to-{FeNO}^{8}
[c]Possible coupling of ν_{FeN} with the Fe–N–O bend can also occur
[d]CH_2Cl_2
[e]THF
[f]H_2O
[g]^{n}BuCN
[h]THF-d_8
[i]Solid-film on NaCl

This stabilization is presumably due to efficient solvation of the anionic species although solvent coordination at the vacant axial position of these 5C complexes is possible but has not been suggested.

The electrochemical properties of {FeNO}^{8}-por complexes do not appear to change significantly with modifications to the porphyrin unit. For example, the $E_{1/2}$ for the {FeNO}^{7} ↔ {FeNO}^{8} redox couple is ~ −1 V (vs. SCE) for many derivatized porphyrins (Table 1). Such values include: −1.08 (OEP) (**3**), −1.08 (OEC = dianion of octaethylchlorin) (**4**), −1.11 V (OEiBC = dianion of octaethylisobacteriochlorin) (**5**) (vs. SCE, ^{n}BuCN) (Fig. 5, Table 1) [50]. It has been suggested that the invariance of $E_{1/2}$ supports an FeNO-centered reduction that is nearly independent of the macrocycle and may actually be more localized on NO-based MOs rather than Fe AOs [58]. Though seemingly accurate, this proposal should be modified to incorporate the non-innocent nature of the NO ligand, i.e., the similarity in $E_{1/2}$ suggests primarily {FeNO} unit reduction as opposed to exclusive Fe- or NO-based reduction. As suggested in this work and now verified by the numerous studies on both heme and non-heme Fe–NO complexes (vide infra), these results support a unique bonding behavior of the Fe–NO subunit and conclude no distinct advantage of one porphyrin macrocycle over the other in terms of NO binding and electrochemical reduction potentials [50].

At this point (early 1990s) the existence of {FeNO}^{8} nitrosyls was proposed based on primarily electrochemical evidence [46, 47, 50, 54, 55, 58]; however,

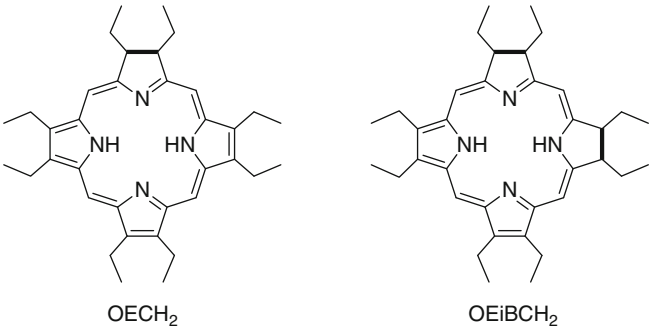

Fig. 5 Porphyrin ligand platforms (H represents dissociable ligand protons) with varying degrees of peripheral C–H saturation that support the $\{FeNO\}^n$ complexes, $[Fe(OEC)(NO)]^-$ (**4**) and [Fe (OEiBC)(NO)]$^-$ (**5**) (abbreviations defined in the text). The general coordination of the FeNO subunit is as described in Fig. 4

other standard measurements were clearly needed. Indeed, vibrational spectroscopy (infrared: IR or resonance Raman: rR) would be the most useful due to the nature of the frontier MOs in these systems, i.e., π* NO. IR and/or rR analysis could confirm reduction and provide vibrational expectation values by establishing the relative and absolute changes in the N–O and Fe–N stretching frequencies (ν_{NO} and ν_{FeN}, respectively). Thus, Ryan and coworkers expanded the work on **2** and **3** utilizing spectroelectrochemical techniques coupled with vibrational analysis. The use of UV–vis and rR measurements provided the first vibrational spectroscopic benchmarks for the $\{FeNO\}^8$ heme platform [47].

Complex **2** was generated by electrochemical reduction of $\{FeNO\}^7$ **1** in THF and its rR spectrum (Soret excitation) was recorded. Comparison of the rR of **1** and **2** revealed complete disappearance of the ν_{NO} band of [Fe(TPP)(NO)] (**1**) at 1,681 cm^{-1} with the appearance of a very weak but reproducible ν_{NO} at 1,496 cm^{-1} ($\Delta\nu_{NO} = 185$ cm^{-1} from $\{FeNO\}^7$), which was confirmed by ^{15}NO labeling ($\nu_{15NO} = 1{,}475$ cm^{-1}; $\Delta\nu_{NO} = 21$ cm^{-1}). The low-energy region of the rR spectrum also contained a second isotope-sensitive peak, assigned as the Fe–N(O) (ν_{FeN}) stretch. Interestingly, the ν_{FeN} band blue-shifted by 24 cm^{-1} upon reduction to 549 cm^{-1} in the $\{FeNO\}^8$ complex **2** (525 cm^{-1} in **1**) (Table 1). The 185 cm^{-1} red-shift in ν_{NO} points toward a dramatic decrease in the N–O bond order, which is consistent with additional occupation of an NO π*-like MO in the $\{FeNO\}^8$ complex. However, there is a significant blue-shift in ν_{FeN} implying an increase in the order of this bond. Based on a low-level computed MO diagram [41, 59] of Fe-por–NO complexes, the singly occupied MO (SOMO) of the $\{FeNO\}^7$ precursor contains both N–O π* and Fe(d_z^2)–N(O) σ-based orbital contributions. Thus, according to this MO analysis, reduction to **2** should theoretically decrease ν_{NO} and increase ν_{FeN}. Indeed, the weakening of the N–O bond and strengthening of the Fe–N bond is what is observed experimentally; however, other effects such as coupling to the Fe–N–O bend may be a more suitable explanation (vide infra).

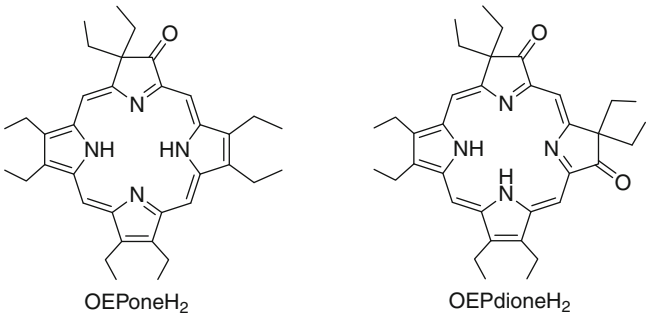

Fig. 6 Porphinone ligand platforms (H represents dissociable ligand protons) that support the {FeNO}^{n} complexes, [Fe(OEPone)(NO)]$^-$ (**6**) and [Fe(OEPdione)(NO)]$^-$ (**7**) (abbreviations defined in the text). The general coordination of the FeNO subunit is as described in Fig. 4

Collectively, **2** was proposed to be 5C and contain a LS Fe(II) coordinated to NO$^-$ (the spin-state of the nitroxyl anion, i.e., singlet or triplet was not assigned).

The vibrational analysis of {FeNO}^{8}-por systems was further expanded by Ryan's group in 2010 to include more significant modifications on the porphyrin ligand than described previously. These included the [Fe(por)(NO)]$^-$ complexes where por = OEP (**3**), OEPone (dianion of octaethylporphinone) (**6**), and OEPdione (dianion of octaethylporphinedione) (**7**) [51] (Fig. 6). The por ligands in **6** and **7** were used since they mimic the peripheral features in heme d_1 that contain C=O groups commonly referred to as porphinones. Furthermore, heme d_1 is present at the active site of one of the key microbial enzymes involved in denitrification, NiR, which goes through a proposed {FeNO}^{8} transition state in the catalytic reduction of nitrite-to-nitric oxide at the heme center [60–62]. The electro/spectroelectrochemistry of the FeNO porphinones was first reported in 1997 [52] and the corresponding $E_{1/2}$ values were similar to previous Fe-por–NO systems: −0.71 (**6**) and −0.65 V (**7**) (vs. SCE, THF) (Table 1). The overall shift of ~0.4 V toward more positive potentials from the OEP derivative **3** was attributed to the greater electron-withdrawing nature of the corresponding macrocyclic ligands in the following order: OEP < OEPone < OEPdione. Interestingly, although $E_{1/2}$ changed, the vibrational frequencies are seemingly unaffected by the respective oxidized macrocycles with ν_{NO} at ~1,665 cm^{-1} for {FeNO}^{7} and ~1,442 cm^{-1} ($\Delta\nu_{NO}$ ~ 220 cm^{-1}) for {FeNO}^{8} (**3**, **6**, **7**) in all three OEP derivatives (Table 1). It appears that the C=O groups on the porphyrin have little influence on the degree of bonding/anti-bonding character in the FeNO unit, which was further supported by DFT calculations (vide infra).

As of 2010, knowledge of synthetic {FeNO}^{8} heme complexes were at the same level as in the 1990s, i.e., non-isolable and synthesized in situ with electrochemical and vibrational information in terms of overall characterization. Stabilization of {FeNO}^{8} had only been modest with electron-withdrawing peripheral groups providing, at best, a ~ 0.40 V cathodic shift in $E_{1/2}$ [51]. In hopes of stabilizing *and* isolating the elusive {FeNO}^{8} species, Doctorovich utilized a fully halogenated TPP-derivative (Fig. 7) in expectation of a more stable {FeNO}^{8} system due to the

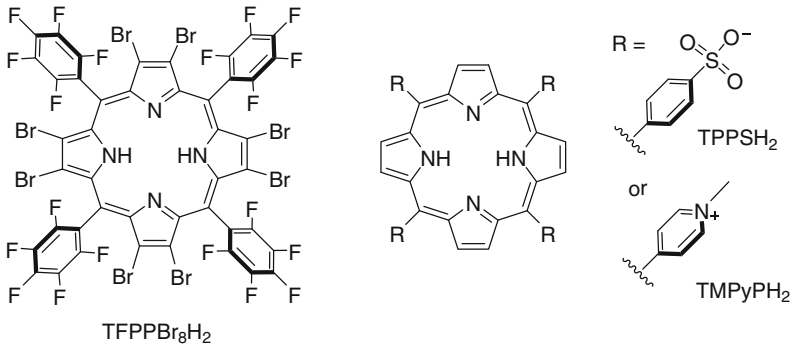

Fig. 7 Porphyrin ligand platforms (H represents dissociable ligand protons) that support the $\{FeNO\}^n$ complexes [Fe(TFPPPBr$_8$)(NO)] (**8**), [Fe(TFPPPBr$_8$)(NO)]$^-$ (**9**), [Fe(TPPS)(NO)]$^{4-}$ (**10**), [Fe(TPPS)(NO)]$^{5-}$ (**11**), and [Fe(TMPyP)(NO)]$^{3+}$ (abbreviations defined in the text). The general coordination of the FeNO subunit is as described in Fig. 4

electron-withdrawing nature of the halogen substitution [53, 63]. This work was an extension of earlier work done with halogenated Fe porphyrins [64]. The $\{FeNO\}^7$ complex, namely [Fe(TFPPPBr$_8$)(NO)] (**8**) (where TFPPBr$_8$ = 2,3,7,8,12,13,17,18-octabromo-5,10,15,20-[tetrakis-(pentafluorphenyl)]porphyrin), was obtained through reductive nitrosylation of [Fe^{III}(TFPPPBr$_8$)Cl] in a 2:1 CH_2Cl_2/MeOH solvent mixture with NO(g). Chemical reduction of **8** with cobaltocene ([Co(Cp)$_2$]; $E_{1/2} \sim -1.00$ V vs. SCE [57]) in CH_2Cl_2 afforded the $\{FeNO\}^8$ complex [Co(Cp)$_2$][Fe(TFPPPBr$_8$)(NO)] (**9**) as a solid in 90% yield (Fig. 7). This report in 2010 marked the first account of an isolable and thermally stable heme $\{FeNO\}^8$ complex. As expected, the CV of **8** in CH_2Cl_2 revealed two positively-shifted (with respect to TPP analogue **1**) reversible reduction waves with the $\{FeNO\}^{7/8}$ couple at $E_{1/2} = -0.19$ V (vs. SCE, CH_2Cl_2). Notably, this value is the most positive of all the $\{FeNO\}^8$ complexes reported to date. The effectiveness of the redox modulation is most distinct when compared to the $\{FeNO\}^{7/8}$ $E_{1/2}$ of the non-halogenated TPP in **1** (−0.93 V vs. SCE in CH_2Cl_2), that is cathodically shifted by nearly 1 V ($\Delta E_{1/2} = 0.74$ V) in **8**.

The additional stabilization of the $\{FeNO\}^8$ complex **9** allowed for more detailed spectral characterization than in previous reports. The ^{1}H NMR spectrum of **9** showed only one signal corresponding to the $[Co(Cp)_2]^+$ protons of the countercation. Furthermore, ^{15}N NMR measurements of **9**-^{15}NO displayed a single peak at +790 ppm (vs. CH_3NO_2 in CD_2Cl_2), a value at the upper limit of previously characterized and severely bent $\{CoNO\}^8$ nitrosyls having M–N–O angles of ~130° [65, 66]. It is well established that the ^{15}N NMR signal is quite sensitive to the redox state and angle of the MNO unit, supporting the assignment of a severely bent Fe–N–O angle and $S = 0$ ground state for **9**. Solution-state FTIR data for **9** proved difficult to interpret since the ν_{NO} of **9** was masked by intense vibrational bands between 1,450 and 1,550 cm^{-1} from the por ligand. However, solid-state FTIR (solid-film NaCl) revealed a weak shoulder at ~1,550 cm^{-1}, which was assigned to the ν_{NO} of **9**. Notably, even in the solid-state, the 1,550 cm^{-1} band slowly decreased

within minutes of data collection, with reappearance (although not quantitative) of the 1,715 cm^{-1} ν_{NO} band of the $\{FeNO\}^7$ species **8**. In support of the presence of an intact Fe–NO bond in **9**, chemical oxidation with ferrocenium quantitatively regenerated the $\{FeNO\}^7$ complex **8**. Additional reactivity of the complex with biologically relevant targets was not discussed; however, protonation of **9** with strong acids such as trifluoroacetic acid (TFA) afforded the $\{FeNO\}^7$ along with $H_2(g)$ evolution via a proposed $\{FeHNO\}^8$ intermediate, similar to the probable side-reaction in the electrochemical synthesis of **2** and **3** [47]. Only strong acids such as TFA facilitated this reaction indicating the coordinated NO^- to be a relatively weak base. Although this unique $\{FeNO\}^8$-por complex was isolable and relatively stable under anaerobic conditions, the apparent absence of crystallographic data highlights the instability of this species in solution. DFT calculations have served an integral part of rationalizing the bonding description of the unique $\{FeNO\}^8$ EF notation, which is highlighted in a forthcoming section.

Meyer and coworkers investigated the electrocatalytic reduction of NO_2^- to NH_3 in neutral to acidic solutions, using a water-soluble Fe(III)-por complex, $[Fe(TPPS)(H_2O)]^{3-}$ (TPPS = hexaanion of *meso*-tetrakis(*p*-sulfonatophenyl)porphyrin) as an NiR model (Fig. 7, Table 1) [54]. Chemical reduction of the $\{FeNO\}^6$ complex $[Fe(TPPS)(NO)]^{3-}$ was achieved with a large excess of $NaNO_2$ and NO(g), resulting in the clean generation of $[Fe(TPPS)(NO)]^{4-}$ (**10**), the $\{FeNO\}^7$ species. Differential pulse polarography revealed a well-defined, pH-dependent peak at −0.63 V (pH > 2.6 vs. SCE, H_2O) indicating that rapid reduction occurs at this potential and is consistent with formation of the putative $\{FeNO\}^8$ species, $[Fe(TPPS)(NO)]^{5-}$ (**11**). The first reduction associated with the FeNO unit, $\{FeNO\}^6$-to-$\{FeNO\}^7$, is independent of pH, whereas the second reduction has a complex pH dependence, similar to that seen in polypyridine Ru- and Os-NO complexes [67]. The second reduction is pH-independent at pH > 2.6; however, in the range 2.6 > pH > 1.4, the electrochemical reaction assumes pH dependence. The authors note that there is no pH dependence seen in this range for the solvato species, $[Fe(TPPS)(H_2O)]^{3-}$, which supports protonation at NO and not the sulfonate groups of TPPS. The mechanism of nitrite reduction to ammonia mediated by NiR has been postulated to go through a series of proton-coupled electron transfer reactions at the coordinated nitrogen oxide substrate [60–62]. Support for this mechanism was also provided by a series of Ru–NO and Os–NO polypyridine complexes that are not structurally related to NiR [67, 68]. Furthermore, analogous chemistry with Os nitrosyls inferred the assignment of this species to be the coordinated HNO complex, $[Fe(TPPS)(HNO)]^{4-}$ [69]. Mechanistically speaking, the Os and Ru systems do offer insight into the mechanism for reduction of nitrite via an $\{FeNO\}^8$ species; however, a major difference is the apparent lability of the axial NO ligand in **11** with subsequent loss of HNO. This chemistry is in contrast to the continuously coordinated NO in the Os or Ru systems. This deligation process appears to be the reason why the reduction of **10** to **11** is not reported as reversible. Further reductions, past the $\{FeNO\}^8$ $[Fe(TPPS)(NO)]^{5-}$ (**11**) species, are consistent with the production of ammonia (NH_3), nitrous oxide (N_2O), and hydroxylamine (H_2NOH) depending on the $[NO_2^-]$/[Fe(III)] ratio, as well as the electrons added per NO_2^- and the

electrolysis time [54]. Complimentary results were obtained with an additional water-soluble cationic porphyrin, $[Fe(TMPyP)(H_2O)]^{5+}$ (where TMPyP = dication of *meso*-tetrakis(*N*-methyl-4-pyridyl)porphine) (Fig. 7, Table 1), under similar conditions described above [55].

While synthetic efforts on Fe-por–NO complexes have provided many of the spectroscopic benchmarks for $\{FeNO\}^8$, the challenge still remains to isolate discrete molecules and understand their underlying reactivity. Much work has been done involving protein-heme adducts of the $\{FeNO\}^7$ notation, in particular MbNO (**12**), though the surprising stability ($t_{1/2}$ > weeks) of the $\{FeHNO\}^8$ adduct of Mb, namely MbHNO (**13**), has allowed for the first experimental parameters of this unique EF notation in a metalloprotein. Reported in 2000 by Farmer and coworkers [70], **13** can be synthesized by a variety of different routes. For example, **13** can be prepared by the traditional biochemical procedure in which metMb (Fe(III)Mb), nitrite (NO_2^-), and dithionite ($S_2O_4^{2-}$) are mixed with the formation of **13** monitored by UV–vis although caution should be noted as the spectrum of **13** is similar to the $\{FeNO\}^7$ MbNO (**12**) [71]. Furthermore, **13** can be produced efficiently through trapping of free HNO from a donor molecule such as Angeli's salt with deoxyMb [70, 72–74]. Another report demonstrated that the $\{FeNO\}^6$ MbNO species could be reduced by two electrons with hydride sources such as $NaBH_4$ to also generate **13** [75]. Regardless of the route employed, all afford **13** as the predominant isolable material.

Due to its inherent stability, $\{FeHNO\}^8$ **13** has been characterized by numerous techniques including ^1H NMR [76], rR, and even structural methods such as X-ray absorption spectroscopy (XAS) [56]. The protonated state of the NO ligand in **13** was confirmed from ^1H NMR where the HNO proton displays a broad but relatively well-defined resonance at 14.8 ppm (20% D_2O/80% pH 10 carbonate buffer) [74]. Other advanced NMR techniques including $^1H/^{15}N$-coupled experiments lend further validity to this peak assignment. The rR spectrum of **13** (λ_{ex} = 413 nm; pH 10 carbonate buffer) showed the expected shift of the ν_{NO} band at 1,612 cm^{-1} from MbNO [77] to 1,385 cm^{-1} for **13** ($\Delta\nu_{NO}$ = 227 cm^{-1}). This was further confirmed by ^{15}N isotopes as ν_{NO} of **13-**^{15}NO shifted to 1,355 cm^{-1} ($\Delta\nu_{NO}$ = 30 cm^{-1}). Another isotope-sensitive band also appeared at 649 cm^{-1} (**13-**^{15}NO = 636 cm^{-1}; $\Delta\nu_{NO}$ = 13 cm^{-1}) that has been traditionally assigned as the ν_{FeN} band [56]. Interestingly, this band is blue-shifted by ~100 cm^{-1} compared to $\{FeNO\}^7$ MbNO (**12**) at 552 cm^{-1} [77], which is much larger than the blue-shift found in the $\{FeNO\}^8$ TPP complex **2** [47]. As stated previously, the blue-shift does not necessarily imply a stronger force constant for the Fe–N bond in MbHNO **13** compared to that in MbNO **12**. Possible explanations to this significant change could be (1) coupling of the Fe–N stretch with the Fe–N–O bend and (2) the reduced Fe–N–O angle in **13** compared to **12**, which lowers the effective reduced mass in the harmonic oscillator equation due to the proton-N bond. Either scenario could result in an increase in the low-energy frequency, an effect that is completely independent of a change in the bond order [48].

The heme site in **13** also provided the first insight into the structure of a biological $\{FeNO\}^8$ species (Table 2) [56]. This work was compared to earlier research

Table 2 Geometric parameters of 5C and 6C heme {FeNO}$^{7/8}$ systems

Molecule	Geometric parameters[a]				Ref
	Fe–N (Å)	N–O (Å)	∠Fe–N–O (°)	Fe–N_{trans} (Å)	
{FeNO}^{7}					
[Fe(TPP)(NO)][b] (**1**)	1.739	1.163	144.4	–	[78]
[Fe(TPP)(NO)(MI)]	1.750	1.182	138	2.173	[79]
[Fe(P)(NO)] -calc.	1.705	1.179	146	–	[43]
[Fe(P)(NO)(MI)] (**14**) -calc.	1.734	1.186	140	2.179	[43]
$[Fe(P)(NO)(CH_3S)]^-$ -calc.	1.788	1.198	138	2.416	[80]
MbNO[c,d] (**12**)	1.76	1.12	150	2.05	[81]
[Fe(TFPPBr$_8$)(NO)] (**8**)-calc.	1.711	1.182	144.4	–	[53]
{FeNO}^{8}					
MbHNO (**13**)	1.82	1.24	131	2.09	[56]
$[Fe(P)(NO)(MI)]^-$ (**15**) -calc.	1.795	1.211	124	2.439	[80]
[Fe(P)(HNO)(MI)] -calc.	1.789	1.236	132	2.082	[45]
$[Fe(P)(NO)(CH_3S)]^{2-}$ (**16**)-calc.	1.776	1.215	131	2.587	[80]
$[Fe(P)(HNO)(CH_3S)]^-$ -calc.	1.824	1.252	133	2.354	[80]
$[Fe(P)(NO)(ImH)]^-$ (**17**)-calc.	1.814	1.215	120.3	2.419	[82]
[Fe(P)(HNO)(ImH)] -calc.	1.811	1.217	132	2.098	[82]
$[Fe(P)(NO)(NH_3)]^-$ -calc.	1.790	1.21	126	2.271	[60]
[Fe(P)(HNO)(NH_3)] -calc.	1.782	1.23	131	2.090	[60]
$[Fe(TFPPBr_8)(NO)]^-$ (**9**)-calc.	1.790	1.201	122.7	–	[53]
$[Fe(P)(NO)]^-$ -calc.	1.778	1.211	123.1	–	[53]

[a]Data consists of experimental and DFT calculated parameters (denoted by calc.)
[b]Crystal structure obtained at 33 K in order to reduce disorder in FeNO unit
[c]Data obtained from EXAFS [56, 81]
[d]Additional crystallographic data from sperm whale Mb has been obtained: Fe–N(O) 1.89 Å; N–O 1.15 Å; Fe–N–O 112°; Fe–N_{trans} 2.18 Å [83] and from horse heart Mb in which two distinct structures are observed dependent on the preparation method: Fe–N(O) 1.87 Å (2.13 Å); N–O 1.20 Å (1.17 Å); Fe–N–O 144° (120°); Fe–N_{trans} 2.08 Å (2.15 Å) [84, 85]

pertaining to MbNO (**12**) in which EXAFS was used in determination of the primary coordination sphere structure [81]. Therefore upon reduction of **12** to **13**, both the N–O and Fe–N(O) bond lengths increase from 1.12 Å to 1.24 Å and 1.76 Å to 1.82 Å, respectively. The Fe–N(O) bond in **13** is quite long, but subsequent theoretical calculations provide support for the elongated bond [82]. The Fe–N–O bond angle of 131° is notably decreased in **13** from 150° in **12** [56]. To date (2012), these parameters are *the only experimental structural parameters of an {FeNO}^{8}-por system* (small molecule or macromolecule) and are quite complementary with what has been determined theoretically at the heme site in Mb and the aforementioned synthetic analogues (vide infra). Formal oxidation state assignments for Fe and NO in **13** have not been made; however, XANES data suggest considerable reduction at Fe implying an Fe(I) oxidation state, which is further corroborated by the long Fe–NO bond of MbHNO. As suggested below, a formal resonance structure that highlights the extent of metal-ligand covalency in the FeNO unit of heme {FeNO}^{8} systems seems viable.

2.2 Theoretical Descriptions of Heme {FeNO}^{8} Complexes

DFT calculations have provided a critical perspective into the rich bonding of M–N–O complexes [45]. This is particularly the case for {FeNO}^{8}-por complexes since an X-ray crystal structure of this species has yet to be reported. Furthermore, only minimal experimental parameters for these systems have been obtained [56]. The ability to probe the electronic structure of heme active sites in silico certainly proves valuable in this particular area of metal-nitrosyl chemistry. Undoubtedly the work of many researchers involving theoretical studies pertaining to {FeNO}^{7} porphyrins has been paramount to the understanding of the reduced {FeNO}^{8} congeners, which are the focus of this review. More detailed analysis on the {FeNO}^{7} EF notation is the subject of other articles [43, 86] and will only be discussed here in reference to {FeNO}^{8} systems.

In an effort to generate structural and electronic information on possible nitroxyl intermediates involved in biological NO_x processing, theoretical accounts of the heme {FeNO}^{7} [Fe(P)(MI)(NO)] (**14**) and {FeNO}^{8} complexes [Fe(P)(MI)(NO)]$^-$ (**15**) (where P = porphine^{2-} and MI = 1-methylimidazole) have been performed. The computations by Lehnert [80] were performed with BP86/TZVP to elucidate the mechanism and potential intermediates involved in NO reduction in the fungal NOR (P450nor) enzymes with the model [Fe(P)(CH_3S)(NO)]$^{2-}$ (**16**) where comparisons with **15** were made. Both 6C models generate similar structural properties and MO assignments; therefore, we will limit the majority of our discussion to **15** since {FeNO}^{8} heme complexes involving thiolate ligation have yet to be synthesized. Additional DFT studies on a similar 6C [Fe(P)(ImH)(NO)]$^-$ (**17**) (where ImH = Imidazole) have also been performed with the B3LYP and BLYP functionals, which yielded similar results to **15**. For simplicity we will focus the majority of our theoretical descriptions with the BP86 results of **15**.

The optimized structure of the {FeNO}^{7} complex [Fe(P)(MI)(NO)] (**14**) was described as a LS Fe(II)–NO• species (S_{tot} = 1/2) with distinct radical character on the N of NO [44]. Evaluation of the electronic ground state revealed 88% Fe(II)–NO• character with a 12% contribution from a ligand-field excited state. The single electron is found in a mixed SOMO consisting primarily of Fe d_z^2/d_{xz} and NO π^*_h (horizontal to the plane formed by Fe–N–O). In fact, the Fe and NO of **14** equally define this orbital accounting for 42% and 43% contributions, respectively. This large degree of Fe and NO character is demonstrative of large covalent character in the Fe–NO bond of **14**. Reduction of **14** to [Fe(P)(MI)(NO)]$^-$ (**15**) resulted in few changes to the nature of the frontier MOs from **14** viz., the incoming electron spin-pairs and resides with the lone electron in the former Fe–N σ-bonding SOMO of {FeNO}^{7} resulting in a singlet (S_{tot} = 0) ground state. While the triplet state of **15**, **16**, and **17** was shown to be nearly isoenergetic to their respective singlet state, no experimental evidence of this electronic species exists. Thus, in terms of orbital character, the HOMO in **15** consists of nearly equal Fe and NO contributions, which supports reduction occurring across the FeNO entity as a whole. Separate DFT studies (BP86/TZVP) on the derivatized porphyrins

$[Fe(OMPone)(NO)]^-$ and $[Fe(OMPdione)(NO)]^-$ (where OMP = the dianion of octamethylporphinone/dione) also draw similar conclusions [51]. Therefore, considering only the existence of the singlet ground state for these $\{FeNO\}^8$ heme complexes, the oxidation state designation can be described as intermediate between LS Fe(II)–NO^- ↔ LS Fe(I)–NO•.

As expected, the reduction to $[Fe(P)(MI)(NO)]^-$ (**15**) and [Fe(P)(ImH)(NO)] (**17**) has a pronounced effect on the structural and spectroscopic parameters of the DFT-generated $\{FeNO\}^8$ complexes (Table 2) [80, 82]. For example, upon reduction of **14** to **15**, the Fe–N(O) and N–O bonds increased in length (Fe–N(O): 1.734 Å to 1.795 Å; N–O: 1.186 Å to 1.211 Å) and showed lower calculated force constants (3.26–2.50,12.22–10.29, and 0.61–0.21 mdyn/Å for the Fe–N(O), N–O, and $Fe–N_{trans}$, respectively) [80]. This decrease in bond order correlated with a calculated ν_{NO} of 1,511 cm^{-1} (BP86) for **15** and 1,578 cm^{-1} (B3LYP) for **17**. Additionally, the Fe–N–O angle decreased from 140° to ~120° for both **15** and **17**, and the axial imidazole $Fe–N_{trans}$ distance increased from 2.179 to 2.439 Å in **15** [80, 82]. This dramatic bond elongation is not a manifestation of improper functional choice as analogous results were obtained for **17** using B3LYP and BLYP [82]. Accordingly, the *trans*-influence of NO^- is large. However, this particular result does not correlate with the experimental $Fe–N_{trans}$ of histidine from MbHNO **13**, which was observed to be ~2 Å (EXAFS) [56]. This difference appears to be a question of the *trans* labilizing ability of NO^- versus HNO, which one would expect to be larger for the anionic ligand. Indeed, analysis of the HNO version of **17** (BLYP) [82] revealed a calculated $Fe–N_{trans}$ = 2.144 Å and ν_{NO} = 1,416 cm^{-1} comparable to the same experimental parameters found for MbHNO **13** ($Fe–N_{trans}$ = 2.09 Å; ν_{NO} = 1,385 cm^{-1}) [56]. Collectively, the calculated bond distances, angles, and vibrational properties of **17** (when discriminating HNO and NO coordination) are remarkably similar to those obtained experimentally from the EXAFS of MbHNO, thus lending some validity to the accuracy and overall predictive power of these methods.

Analogous structural and electronic parameters were obtained for the halogenated 5C FeNO complexes **8** and **9** [53]. The computed geometry for the 5C $\{FeNO\}^7$ complex $[Fe(TFPPBr_8)(NO)]$ (**8**) (LANDL2DZ/PBE exchange-correlation) compared favorably to experiment aside from the determined atypical N–O bond length of 1.42 Å likely due to the dramatic ruffling of this highly substituted porphyrin, whereas theory provides a more reasonable N–O bond length of 1.182 Å. Moreover, the Fe–N(O) bond of 1.711 Å and Fe–N–O angle of 144.4° for $[Fe(TFPPBr_8)(NO)]$ serves as a point of reference prior to reduction [53]. Subsequent addition of an electron to form the $\{FeNO\}^8$ complex $[Fe(TFPPBr_8)(NO)]^-$ (**9**) revealed an N–O and Fe–N(O) bond increase to 1.201 and 1.790 Å, respectively. The decreased Fe–N–O angle (122.7°) is indicative of FeNO unit reduction and double occupation of an Fe-d_z^2 σ/NO π* orbital analogous to the simple 6C porphyrin complex **15**. The HOMO of **9** consisted of more Fe (44%) than NO (27%) character with some ligand contributions symptomatic of a decrease in covalency of the Fe–NO bond. This contrasts with the near equivalent contributions of Fe and NO to the HOMO of **15** likely attributed to the strong electron-withdrawing character of the por ligand in **9**. In further support of the nature of

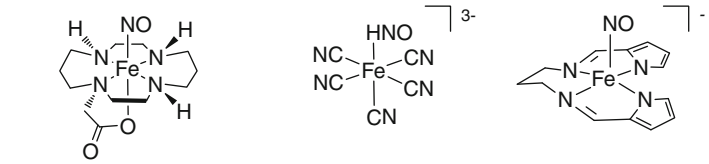

trans-[Fe(NO)(cyclam-ac)] **19** $[Fe(CN)_5(HNO)]^{3-}$ **22** $[Fe(LN_4)(NO)]^{-}$ **24**

Fig. 8 Non-heme iron $\{FeNO\}^8$ complexes

reduction, a natural population analysis (NPA) was performed and the atomic charges were computed for the $\{FeNO\}^7$ species **1** and **8** and the $\{FeNO\}^8$ species **2** and **9**. This analysis showed strong similarity in both cases revealing a net reduced charge on Fe and NO when comparing the $\{FeNO\}^7$ and $\{FeNO\}^8$ species. Importantly, the computed charges for **1** and (**2**) are as follows: Fe, 0.69 (0.56); NO, −0.02 (−0.21); for **8** and (**9**) are: Fe, 0.66 (0.55); NO, 0.01 (−0.13) [53].

3 $\{FeNO\}^8$ Non-heme Coordination Complexes

There are relatively fewer examples of non-heme compared to heme $\{FeNO\}^8$ systems and only one non-heme metalloenzyme has been found in this particular EF notation [87]. Although these species are not defined explicitly in biology, they do offer promise as potential HNO therapeutics and offer key insight into how one treats the $\{FeNO\}^n$ unit in such platforms. Formation of $\{FeNO\}^8$ complexes has been primarily limited to ligands with N_4 tetradentate or N_4O pentadentate constructs as well as a derivative of the nitroprusside (NP) anion. The synthesis, spectroscopy, and theoretical description are reported in the forthcoming sections along with a brief account of the reactivity of such reduced iron-nitrosyl units. Additional 5C trigonal bipyramidal phosphine-ligated $\{FeNO\}^8$ complexes have also been reported, but these species will not be discussed in this review [88–90].

3.1 Synthesis and Experimental Properties of Non-heme $\{FeNO\}^8$ Complexes

Inspired by earlier work involving electrochemical [91] and DFT [92] characterization of 6C mononuclear non-heme $\{FeNO\}^7$ iron-nitrosyls, Wieghardt and coworkers reported a detailed study of an $\{FeNO\}^{6/7/8}$ series supported by one common N_4O platform, namely *trans*-$[Fe(NO)(cyclam\text{-}ac)]^{2+/1+/0}$ (where cyclam-ac = monoanion of 1,4,8,11-tetraazacyclotetradecane-1-acetic acid) (Fig. 8) [93]. Previous studies involving the related 5C $\{FeNO\}^7$ complex, *trans*-[Fe(NO)(Cl)

(cyclam)]$^+$ (S_{tot} = 1/2), displayed a reversible $\{FeNO\}^{7/8}$ couple at −0.90 V (vs. SCE, MeCN, 298 K) [94]. It is likely that the cyclam-ac ligand would provide more stability to the corresponding NO complexes since it only contains one vacant coordination site thus limiting reaction chemistry to one axial position. The $\{FeNO\}^7$ species [Fe(NO)(cyclam-ac)]$^+$ (**18**) was synthesized via reductive nitrosylation of the Fe(III) complex [FeCl(cyclam-ac)]$^+$ with $LiBEt_3H$ and NO(g). Complex **18** was then reduced using [$Co(Cp)_2$] at ambient temperature in MeCN to furnish the $\{FeNO\}^8$ complex, *trans*-[Fe(NO)(cyclam-ac)] (**19**), which was not stable in solution and difficult to isolate. In spite of the inherent lack of stability of **19**, a multitude of spectroscopic studies were performed at low temperature and, combined with DFT, provided the initial insight of a non-heme $\{FeNO\}^8$ system. While the cyclam-ac ligand nicely supports the $\{FeNO\}^{6/7/8}$ series, our discussion below will focus on the implications derived from the $\{FeNO\}^{7/8}$ complexes.

A series of in situ measurements (primarily at low temperature) combined with DFT computations were performed to obtain the spectroscopic, electrochemical, and structural parameters of **19**. The CV displayed a reversible $\{FeNO\}^7 \leftrightarrow \{FeNO\}^8$ redox couple at $E_{1/2} = -0.99$ V (vs. SCE, MeCN, 293 K). Low-temperature spectroelectrochemical experiments were obtained using an OTTLE cell to monitor the in situ changes upon reduction of **18**-to-**19** with UV–vis (MeCN, 273 K) and FTIR (MeCN, 253 K) spectroscopies [93]. The UV–vis of the **18**-to-**19** conversion revealed several isosbestic points with the disappearance of peaks at 395 nm and 540 nm and the generation of new broad absorbance features at 440 nm and 590 nm. As expected, the strong ν_{NO} for **18** (1,607 cm^{-1}) significantly red-shifted to a less intense band centered at 1,271 cm^{-1} ($\Delta\nu_{NO}$ = 336 cm^{-1}) in the $\{FeNO\}^8$ complex **19**. This assignment was further confirmed utilizing $^{15}N^{18}O$ to afford ν_{NO} at 1,228 cm^{-1} ($\Delta\nu_{NO}$ = 43 cm^{-1}, a value in close agreement with that calculated for a classic harmonic oscillator = 1,214 cm^{-1}). Additional insight was obtained from evaluation of the ν_{CO} stretching frequencies of the ligand, which trended toward larger values. This change is consistent with a weakening of the $Fe–O_{carboxylate}$ bond *trans* to NO upon reduction of the nitrosyl ligand, which supports our previous discussion on the *trans*-influence of nitroxyl anion in heme systems (vide supra). For example, ν_{CO} bands in $\{FeNO\}^7$ **18** were observed at 1,657 and 1,355 cm^{-1}, whereas $\{FeNO\}^8$ **19** were at 1,619 and 1,380 cm^{-1} for the C=O and C–O, respectively (in situ IR measurements in MeCN). Another interesting feature in the IR spectrum of **19** is the disappearance of the ν_{NH} of cyclam-ac (3,223 cm^{-1} for **18**) that is supportive of an H···O–N hydrogen-bonding interaction between the cyclam-ac NH group with the coordinated NO^-. Further support for this assignment was provided by the appearance of a broadened ν_{ND} at 2,400 cm^{-1} when using deuterated cyclam-ac to form **19**. The broadening is rationalized based on the reduced Fe–N–O bond angle (122.4° from DFT, vide infra) along with the anionic nature of the formal NO^- ligand in **19**. It is also noted that this H-bond could factor into stabilization of the $\{FeNO\}^8$ [93] (Table 4).

To propose a possible oxidation state assignment of the Fe center in **18** and **19**, zero-field Mössbauer (MB) experiments at 80 K were also performed. The MB spectrum of solid **18** displayed an isomer shift value (δ) of 0.26 mm s^{-1} and a

Table 3 Electrochemical and spectroscopic data of $\{FeNO\}^{7/8}$ non-heme systems

Molecule	$E_{1/2}$ (V)[a]	ν_{NO} (cm^{-1})	$\Delta\nu_{NO}$ (cm^{-1})[b]	Ref
$\{FeNO\}^7$				
trans-$[Fe(NO)(cyclam\text{-}ac)]^+$ (**18**)	−0.99[c]	1,607[c]	–	[93]
$[Fe(CN)_5(NO)]^{3-}$ (**20**)	−1.00[d]	1,648[e]	–	[91, 95]
$[Fe(LN_4)(NO)]$ (**23**)	−0.98[c]	1,704[f]	–	[96]
$\{FeNO\}^8$				
trans-$[Fe(NO)(cyclam\text{-}ac)]$ (**19**)	–	1,271[c]	−336	[93]
$[Fe(CN)_5(HNO)]^{3-}$ (**22**)	–	1,384[d]	−264	[97]
$[Fe(LN_4)(NO)]^-$ (**24**)	–	1,604[f]	−100	[96]

[a]Data represents the $E_{1/2}$ value for the $\{FeNO\}^{7/8}$ redox couple; normalized to the saturated calomel reference electrode (SCE) based on information found in [57]
[b]Denotes the change in stretching frequency upon reduction from $\{FeNO\}^7$-to-$\{FeNO\}^8$
[c]MeCN
[d]H_2O
[e]D_2O
[f]KBr

quadrupole splitting (ΔE_Q) of +0.74 mm s^{-1} consistent with other $\{FeNO\}^7$ complexes [98]. In comparison, the MB spectrum of a frozen MeCN solution of **19** (prepared in situ from chemical reduction of **18**) displayed $\delta = 0.41$ mm s^{-1} and $\Delta E_Q = +1.69$ mm s^{-1}. Importantly, the signal due to **19** only accounted for 40% of the total spectrum with the remaining 60% from reformed **18** highlighting the relative instability of this non-heme $\{FeNO\}^8$ species. The small difference in the isomer shift value ($\Delta\delta = +0.15$ mm s^{-1}) upon reduction of **18**-to-**19** implies more of an NO-based reduction in **19**. Collectively, the spectroscopic and theoretical analyses (vide infra) point to an LS Fe(II) center coordinated to $^1NO^-$ ($S_{tot} = 0$) as the oxidation state assignments for the non-heme complex **19**.

Another 6C non-heme Fe-nitrosyl that has furnished the $\{FeNO\}^8$ notation is the hypotensive agent $[Fe(CN)_5(NO)]^{2-}$, commonly referred to as nitroprusside (NP). It is well established that the Fe center in NP stabilizes the nitrosyl ligand as an NO^+ cation bound to LS Fe(II). Upon introduction to biological fluids, NP can release NO and cause vasorelaxation; thusly, the utility of NP can be found in its therapeutic potential. However, the exact mechanism of in vivo reduction of NP, an $\{FeNO\}^6$ complex, to $\{FeNO\}^7$ $[Fe(CN)_5(NO)]^{3-}$ (**20**) has yet to be clarified. It has been shown that further reduction to the formal $\{FeNO\}^8$ state, $[Fe(CN)_5(NO)]^{4-}$ (**21**) or the protonated version $[Fe(CN)_5(HNO)]^{3-}$ (**22**), could be achieved at a Hg electrode held at ~−1.0 V (vs. SCE, H_2O) [91]. Computational [92] and more recent (2009) spectroscopic [97] studies of **21** and **22** set out to fully characterize the Fe-bound nitroxyl species in aqueous solution. These studies provided the first insight into the bonding/stability and subsequent fate of this non-heme nitroxyl species under biologically relevant conditions.

Initial spectroscopic proof for the formation of **21** came from in situ UV–vis monitoring of the sequential reduction of NP with dithionite [91, 97]. The intense band of the $\{FeNO\}^7$ NP complex **20** at 348 nm disappeared with the appearance of a new band at 445 nm, which was assigned as a metal-to-ligand charge transfer

(MLCT) band in the $[Fe(CN)_5(NO)]^{4-}$ complex **21** (pH 10, 25 °C) and was supported by earlier theoretical studies [92, 97]. Additional equivalents of dithionite caused these bands to decay, presumably due to further reduction and loss of the NO ligand. The stability of **21** has an apparent pH dependence and solution pHs $\geq$ 10 lead to immediate decomposition. The oxidation back to the $\{FeNO\}^7$ complex **20** is the bulk product in basic media where **21** has a half-life of ~50 min. The solution stability of the $\{FeNO\}^8$ complex is better at slightly acidic to neutral pHs of 6–7 presumably due to protonation of the NO^- in **21**, thus forming the HNO complex **22**. In this pH range, complex **22** is the primary species and is stable even in the presence of potential oxidants such as ferricyanide ($[Fe(CN)_6]^{3-}$), $[Fe(H_2O)_6]^{3+}$, or methyl viologen. In contrast to the stability at near neutral pH, sequential addition of the same oxidants at basic pH to **21** resulted in stoichiometric regeneration of the $\{FeNO\}^7$ and $\{FeNO\}^6$ species. It was suggested that the difference in the pH-dependent decomposition pathways support complex **21** as a strong reducing agent at basic pH providing its electron to an oxidant and regenerating the $\{FeNO\}^7$ species, $[Fe(CN)_5(NO)]^{3-}$ (**20**), whereas **22**, the conjugate acid of **21**, decomposes to $[Fe(CN)_6]^{4-}$ and N_2O at pH 6–7 through loss of HNO via the known dehydrative dimerization to N_2O and H_2O [97].

Additional solution-state FTIR spectroscopic studies of the $\{FeNO\}^8$ species **22** formed in phosphate buffer at pH 6 revealed a ν_{NO} band at 1,384 cm^{-1}, which shifted to 1,352 cm^{-1} ($\Delta\nu_{NO} = 32$ cm^{-1}) using ^{15}NO-labeled NP. This value is significantly lower than the ν_{NO} of NP (1,938 cm^{-1}) and the $\{FeNO\}^7$ analogue of NP **20** (1,648 cm^{-1}; $\Delta\nu_{NO}$ from $\{FeNO\}^8$ **22** = 264 cm^{-1}). These values are consistent with primary reduction occurring at the nitrosyl ligand and are assigned to the Fe–HNO derivative **22** based on the pH used and the increased stability of the protonated species. The dramatic red-shift in ν_{NO} upon reduction supports principal electron occupation in NO π* MOs. Further vibrational analysis from rR studies ($\lambda_{ex} = 457.9$ nm) corroborated the IR assignments as seen in the two ν_{NO} bands at 1,380 cm^{-1} (ν_{15NO} = 1,350 cm^{-1}) and 1,304 cm^{-1} (ν_{15NO} = 1,286 cm^{-1}) corresponding to symmetric and asymmetric stretches of the HNO of **22**, respectively (pH 6 buffer). An additional isotope-sensitive band occurred at 662 cm^{-1} (^{15}NO = 649 cm^{-1}), which has been assigned as a mixed ν_{FeN}/δ_{FeNO} mode. Interestingly, the ν_{FeN} stretch shifted to lower energy, in contrast to the heme models discussed previously (vide supra). Typically for heme systems, ν_{FeN} shifts to higher energies in $\{FeNO\}^7 \rightarrow \{FeNO\}^8$ reductions due to a combination of π-backbonding and electron occupation in an MO that has Fe–N(O) σ-bonding character although other reasons for the heme blue-shifts have been postulated (see above). Therefore, it seems that protonation has an effect on the nature and strength of this backbonding interaction and additional electron density is now involved in the H–N(O) bond and is thus less available for constructive NO π*-Fe d_z^2 overlap [97].

Additional support of the HNO-ligand in **22** comes from ^1H NMR, which revealed a downfield singlet at $\delta = 20.02$ ppm (pH 6 phosphate buffer, 25% D_2O) that is split into a doublet ($J_{NH} = 71.14$ Hz) in the ^{15}NO labeled isotopomer. This measurement strongly supports the assignment of the HNO-bound adduct and

a diamagnetic ($S_{tot} = 0$) ground state for **22**. Importantly, the solution stability of **22** allowed for the determination of the pK_a for an Fe-bound HNO by an ^{1}H NMR pH titration. This result provided the first experimentally determined pK_a for an Fe-bound HNO molecule and is critical to the mechanistic proposals for the proton-dependent enzymatic cycles involving reduction of Fe-coordinated NO, e.g., NOR, NOS, and NiR. Based on the titration experiment, a pK_a value of 7.7 was determined [97] and, as expected, is lower than that of free ^{1}HNO (pK_a = 11.6) [27].

In an effort to bridge heme and non-heme nitrosyl chemistry, Harrop and coworkers synthesized the $\{FeNO\}^7$ and $\{FeNO\}^8$ complexes $[Fe(LN_4)(NO)]$ (**23**) and $[Co(Cp^*)_2][Fe(LN_4)(NO)]$ (**24**), respectively (where LN_4 represents the dianionic-di-imine-di-pyrrolide planar tetradentate ligand of a hybrid heme ligand, see Fig. 8) [96]. The $\{FeNO\}^7$ complex **23** is very stable and does not react with excess O_2 or NO and is not photolabile. Spectroscopic studies of **23** are typical of 5C sq-py $\{FeNO\}^7$ species (ν_{NO} = 1,704 cm^{-1} (KBr); $S_{tot} = {}^1/_2$). X-ray analysis revealed that the Fe center is in a distorted sq-py geometry derived from the four basal N-donors of $[LN_4]^{2-}$ that are coordinated in an asymmetric fashion. Complex **23** is unique from most 5C $\{FeNO\}^7$ systems as noted in the quasi-linear nature of its Fe–N–O angle of ~160°, whereas the N–O and Fe–N distances of 1.171 and 1.700 Å, respectively, are more typical for $\{FeNO\}^7$ species [99]. The unexpected linearity in the Fe–N–O bond has been ascribed to considerable d_z^2-p_z mixing in the HOMO of **23**, which minimizes repulsion between the Fe d_z^2 and the σ lone-pair of NO [99]. Lastly, analogous to the porphyrin models, the CV of **23** displayed a reversible redox wave at $E_{1/2} = -0.98$ V (vs. SCE, MeCN), which has been assigned to the $\{FeNO\}^{7/8}$ redox couple. This demonstrated that on the CV time-scale, the LN_4 imine/pyrrolide platform can support a reduced nitrogen oxide ligand and the $\{FeNO\}^8$ unit [96].

As suggested from the electrochemistry of **23**, the corresponding $\{FeNO\}^8$ complex was isolable. The $\{FeNO\}^8$ complex **24** was thus obtained by reduction of **23** with $[Co(Cp^*)_2]$ ($E_{1/2} \sim -1.50$ V vs. SCE [57]) in toluene at RT under N_2 to produce the violet solid $[Co(Cp^*)_2][Fe(LN_4)(NO)]$ (**24**) in quantitative yield. In contrast to other $\{FeNO\}^8$ complexes that have been synthesized and studied in situ, complex **24** was isolated as an air-sensitive solid at RT. Additionally, **24** could be chemically oxidized with $FcPF_6$ in MeCN to quantitatively regenerate **23**. Thus, the NO ligand remains bound throughout the $\{FeNO\}^7 \leftrightarrow \{FeNO\}^8$ redox process. Complex **24** exhibited modest stability in solvents such as MeCN ($t_{1/2}$ = 4.25 h), which allowed for extensive spectroscopic characterization of this $\{FeNO\}^8$ complex utilizing UV–vis, FTIR, FTMS, ^{15}N NMR, and MB [96]. The electronic absorption spectrum of **24** displayed bands at 560 nm (ε = 1,800 M^{-1} cm^{-1}) and 781 nm (ε = 450 M^{-1} cm^{-1}), differing from **23** with λ_{max} at 661 nm (ε = 640 M^{-1} cm^{-1}) and 720 nm (ε = 510 M^{-1} cm^{-1}) both reported in MeCN. The low-energy band appears to be *d*–*d* in nature while the 560 nm band is of CT character. The FTIR spectrum of **23** displays a very strong ν_{NO} at 1,704 cm^{-1}, which shifted to 1,673 cm^{-1} ($\Delta\nu_{NO}$ = 31 cm^{-1}) in the ^{15}NO isotopomer (KBr). Upon reduction, the intense ν_{NO} of **23** disappeared with the appearance of a new isotope-sensitive ν_{NO} stretch at 1,604 cm^{-1} (1,570 cm^{-1} for ^{15}NO; $\Delta\nu_{NO}$ = 34 cm^{-1} in KBr). This would

be more in-line with an overall $S_{tot} = 0$ LS Fe(II)–NO^- ↔ LS Fe(I)–NO• resonance structure in contrast to the LS Fe(II)–NO^- assignment for Wieghardt's complex **19** [93]. Furthermore, ^1H and ^{15}N NMR in CD_3CN confirmed the diamagnetism of **24** implying an overall $S = 0$ ground state. The ^{15}N NMR displayed one signal at 743 ppm [96] consistent with a severely bent Fe–N–O angle similar to the reported ^{15}N NMR data for $\{FeNO\}^8$ complex **9** ($\delta = 790$ ppm in CD_2Cl_2) [53].

The zero-field MB of $\{FeNO\}^8$ **24** revealed a mixture with the predominant species (75%) being the $\{FeNO\}^8$ exhibiting $\delta = 0.51$ mm s^{-1} and $\Delta E_Q = +1.41$ mm s^{-1} [93, 96]. These values are similar to **19** ($\delta = 0.41$ mm s^{-1}, $\Delta E_Q = +1.69$ mm s^{-1}; generated at 253 K in MeCN), which has been formally assigned as containing a LS Fe(II) center. The most logical comparison of **24** is with its oxidized congener $\{FeNO\}^7$ **23**, which displayed $\delta = 0.11$ mm s^{-1} and $\Delta E_Q = 1.41$ mm s^{-1}. Interestingly, the δ value for **23** is similar to 5C $\{FeNO\}^6$ complexes [98] that display more NO^+ character for the coordinated nitrosyl. Accordingly, the best way to interpret the resulting MB parameters is as a change in the overall π-accepting ability of the NO ligand. The MB δ value appears to *increase* with a *decrease in the π-accepting* ability in a series of related Fe–L–NO complexes [93] and this seems to be the trend when comparing **23** and **24**. Thus, the stark difference in δ upon reduction of **23** to **24** indicates a change in the overall π-accepting ability of the ligand, as is seen in the reduction of complex **18** to **19**. This analysis is suggestive of NO^-/NO• character of the bound nitrosyl in **24**. As a whole, complex **24** is the first example of a relatively stable and isolable non-heme $\{FeNO\}^8$ complex.

Complex **24** was also shown to engage in reaction chemistry typical of HNO-forming molecules such as Angeli's salt and Piloty's acid (see Fig. 2). For example, **24** demonstrated its HNO-donor characteristics in its reaction with Fe(III)-myoglobin (metMb) under physiological conditions (phosphate-buffered saline, pH 7.2). Reaction of **24** with equine skeletal metMb efficiently formed MbNO via a reductive nitrosylation mechanism, where NO^-/HNO serves as both the reductant and NO source. This reaction was shown to be quantitative by UV–vis spectroscopy where the corresponding heme Soret (422 nm) and Q-bands (540, 575 nm) of MbNO appear almost instantaneously (~2 min) upon addition of the $\{FeNO\}^8$ complex. This reaction is comparable to the reaction of other Mb species such as sperm whale metMb with Angeli's salt, which takes 15.5 min for the production of MbNO to go to completion [73]. Additional reactivity with thiols such as GSH was also tested since thiols are known biological targets for HNO [15–17]. Indeed, reductive nitrosylation of metMb was completely inhibited when GSH was present. In contrast to the known reaction of thiols with HNO to form disulfides and *N*-hydroxysulfenamides, it appeared that the main product of **24** with GSH was the formation of the dinitrosyl compound $[Fe_2(\mu\text{-}GS)_2(NO)_4]^-$ (or reduced Roussin's red ester = rRRE by UV–vis and ESI-MS). While the exact nature of the NO ligand in complex **24** cannot be completely verified, preliminary reactivity of this $\{FeNO\}^8$ complex is somewhat consistent with classic HNO-donor molecules. In fact, complexes such as **24** offer new avenues for HNO therapeutics that have yet to be explored with other $\{FeNO\}^8$ systems.

Table 4 Geometric parameters of 5C and 6C non-heme $\{FeNO\}^{7/8}$ systems

Molecule	Geometric parameters[a]				Ref
	Fe–N (Å)	N–O (Å)	∠Fe–N–O (deg)	Fe–N_{trans} (Å)	
$\{FeNO\}^7$					
trans-$[Fe(NO)(cyclam\text{-}ac)]^+$ (**18**)	1.722	1.167	148.7	2.012	[93]
$[Fe(CN)_5(NO)]^{3-}$ (**20**)-calc.	1.737	1.199	146.6	–	[92]
$[Fe(LN_4)(NO)]$ (**23**)-calc.	1.690	1.183	149.9	–	[96]
$\{FeNO\}^8$					
trans-[Fe(NO)(cyclam-ac)] (**19**)-calc.	1.752	1.261	122.4	2.127	[93]
$[Fe(CN)_5(HNO)]^{3-}$ (**22**)-calc.	1.783	1.249	137.5	–	[92]
$[Fe(LN_4)(NO)]^-$ (**24**)-calc.	1.681	1.219	142.0	–	[96]

[a]Data consists of experimental and DFT calculated parameters (denoted by calc.)

3.2 *Theoretical Descriptions of Non-heme $\{FeNO\}^8$ Complexes*

Prior to the informative characterization of the nitroxyl species $[Fe(CN)_5(HNO)]^{3-}$ (**22**), Olabe [92] reported theoretical efforts to elucidate the electronic structures of the FeNO unit in NP analogues of various EF notations [100, 101]. The computed and synthesized (vide supra) results revealed a sizeable stability imparted on the Fe–HNO complex **22** relative to the nitroxyl anion Fe–NO^- complex **21**. The HNO complex was found to be more stable as a ground state singlet ($S_{tot} = 0$). Furthermore, protonation at N of NO^- was favored over other sites, e.g. NO–H or H–CN, by ~24 kcal/mol [92]. The considerable energy differences suggested significant charge density residing primarily on the N of NO thus facilitating protonation. This analysis is further supported by the computed structural parameters of the $\{FeNO\}^7$ **20** and $\{FeNO\}^8$ **22** NP species. The major structural changes upon reduction/protonation include a decrease in the Fe–N–O angle from 146.6° to 137.5° ($\Delta_{FeNO} = 9.1°$) with a subsequent increase in Fe–N (1.737 Å to 1.783 Å), as well as an increase in N–O (1.199 Å to 1.249 Å) (Table 4) [92]. These results infer occupation of an orbital primarily centered on NO upon formation of **22**. The calculated ν_{NO} vibrational modes of 1,394 and 1,338 cm^{-1} are in good agreement with the experimental rR bands, $\nu_{NO} = 1{,}380, 1{,}304\ cm^{-1}$ for the symmetric and asymmetric stretch, respectively [92, 97]. The large decrease in the N–O bond strength of **22** associated with the reduced N–O stretching frequency and increased bond length supports mainly NO π* MO occupation by the reducing electron. Collectively, the experimental and theoretical results firmly support a LS Fe(II) coordinated to ^{1}HNO (formally an NO^- ligand) oxidation state.

Similar computational results were obtained for the non-heme $\{FeNO\}^8$ complex **19** containing the cyclam-ac ligand (BP86/TZVP) [93]. A qualitative bonding description of **19** is, much like **22**, suggestive of an LS Fe(II) coordinated to $^1NO^-$ ($S_{tot} = 0$), but further insight into the bonding profile of this non-heme complex advocates the notion of a more localized NO unit reduction. Given the multiple oxidation state assignments possible for $\{FeNO\}^8$ and other EF notations, the relative energies of all possible $\{FeNO\}^8$ derivatives, i.e. singlet vs. triplet, protonated vs. non-protonated, N vs. O protonation among others were considered.

Of these possibilities, the singlet, non-protonated $\{FeNO\}^8$ version of **19** was the electronic ground state. The structural parameters of the $\{FeNO\}^7$ species **18** serves as a comparison to the theoretically established $\{FeNO\}^8$ **19**. Therefore, upon reduction (see Table 4) to form **19**, the Fe–N bond was shown to elongate from 1.723 (exptl: 1.722) Å to 1.752 Å in **19**. Correspondingly, the N–O bond increases a considerable extent from 1.204 Å (exptl: 1.167 Å – DFT often overestimates bond lengths in open shell systems) to 1.261 Å in the $\{FeNO\}^8$ complex. As a result of the increased *trans*-effect of NO^-, the Fe–$O_{carboxylate}$ bond in **19** increases by 0.12 Å. A dramatic change in the Fe–N–O angle was seen from 140.6° (exptl: 148.7°) to 122.4° and, taken with the considerable elongation of the N–O bond by ~0.06 Å, is supportive of more NO-π* occupation in the former SOMO of **18**. Further insight into the nature of the Fe–NO bonding in **19** is gained from NPA on atomic charges in the molecule. Based on NPA, the charge on the Fe center decreased slightly in going from **18** (+1.005) to **19** (+0.882) supporting more electron density about Fe in **19**. A more significant change though is seen in the charge on the NO ligand, which is more negative in **19** (−0.672) versus **18** (−0.230). The NPA results clearly point to an NO-centered reduction in the **18**-to-**19** conversion and are in agreement with the experimental results (ν_{NO}, MB). Taken together, the experimental and DFT results support the LS Fe(II)–NO^- ($S = 0$) assignment for complex **19**.

The non-heme $\{FeNO\}^8$ complex **24** offers some insight into the bonding parameters of the Fe–NO unit exhibited in a pseudo-heme coordination sphere [96]. As usual, DFT analysis (OLYP/STO-TZP) of **24** (singlet is the electronic ground state) starts from the stable $\{FeNO\}^7$ precursor **23**. The Fe–N bond of **23** was calculated to be 1.690 Å (exptl: 1.700) Å, which was shown to shorten slightly upon reduction to 1.681 Å. As expected, the N–O bond increases from 1.183 Å (exptl: 1.171 Å) in **23** to 1.219 Å in $\{FeNO\}^8$ **24**. The near linear Fe–N–O angle observed in **23** (158°) differs more significantly from theory (150°), but this discrepancy has been substantiated due to an effectively barrierless Fe–N–O bending potential. Furthermore, the calculated angle for **24** decreased slightly (142°) after reduction. The transition from **23** to **24** reveals a decrease in the Mulliken charges at the Fe (0.894–0.795) and NO (−0.165 to −0.385) as well as a number of atoms of the LN_4 ligand suggesting the reduction is neither Fe- nor NO-centered. These computed changes upon reduction are similar to those observed in heme $\{FeNO\}^8$ systems in that the reduction is delocalized over the entire Fe–N–O unit. This behavior is in contrast to what is typically observed in non-heme systems (see **18**-to-**19** and **20**-to-**22**) [93, 97], where the reduction occurs primarily on the coordinated nitrosyl lending support to the heme-like character of LN_4 in **24** [96]. As with heme systems, a limited bonding description can be proposed as intermediate between LS Fe(II)–$^1NO^-$ and LS Fe(I)–NO•.

4 $\{CoNO\}^9$ Coordination Complexes

Analogous to the $\{FeNO\}^8$ notation for iron, $\{CoNO\}^9$ is rare for cobalt nitrosyls with $\{CoNO\}^8$ being the most common EF designation [98, 102, 103] and a number of 5C sq-py $\{CoNO\}^8$ complexes have been synthesized and extensively

Table 5 Spectroscopic and structural data of $\{CoNO\}^{8/9}$ systems

Molecule	$E_{1/2}$ (V)[a]	ν_{NO} (cm^{-1})	S_{tot}	Co–N, N–O (Å)	∠CoNO (°)	Ref
$\{CoNO\}^8$						
[Co(TPP)(NO)] (**25**)	−1.18[b]	1,689[c]	0	1.833, 1.01	135.2	[104, 105]
[Co(N_2S_2)(NO)] (**26**)	−1.32[d]	1,604[b]	0	1.787, 1.187	123.8	[106]
[Co(N_2S_2)(NO)][W(CO)$_4$] (**27**)	−0.83[d]	1,638[b]	0	1.80, 1.21	123.1	[106]
[Co(LN_4)(NO)] (**28**)	−1.00[e]	1,645[c]	0	1.7890, 1.1551	125.97	[96]
$\{CoNO\}^9$						
[Co(CO)$_3$(NO)] (**29**)	–	1,818[f]	–	1.665, 1.165	180.0	[107]
[Co(np_3)(NO)](BPh_4) (**30**)	–	1,680[g]	1/2	1.83, 1.14	165	[88, 108]
[Co($Tp^{t\text{-}Bu,Me}$)(NO)] (**31**)	–	1,736[c]	–	1.671, 1.071	180.000	[109]
[Co(Tp*)(NO)] (**32**)	–	1,732[c]	1/2	1.627, 1.164	176.8	[110]

[a]Data represents the $E_{1/2}$ value for the $\{CoNO\}^{8-9}$ redox couple normalized to the saturated calomel reference electrode (SCE) based on the information found in [57]
[b]CH_2Cl_2
[c]KBr
[d]DMF
[e]MeCN
[f]Ar matrix
[g]Nujol mull

characterized [98]. Indeed, the 5C $\{CoNO\}^8$ complex [Co(TPP)(NO)] (**25**) was the first metalloporphyrin nitrosyl complex that was structurally characterized by Scheidt's group in 1973 [104]. Similar to **25**, many other $\{CoNO\}^8$-por derivatives have been characterized and display the following average structural and vibrational parameters: Co–N(O) = 1.84 Å, N–O = 1.12 Å, Co–N–O = 125°; ν_{NO} = 1,675–1,696 cm^{-1} (KBr or Nujol) [98, 102]. The predominant oxidation state assignment in these systems evokes a LS Co(III) d^6 ion with a coordinated $^1NO^-$ resulting in a diamagnetic ($S_{tot} = 0$) complex. While a reduced nitrogen oxide ligand is postulated in these constructs, very little has been reported with respect to the reactivity of the putative $^1NO^-$ although it should be noted that the less stable singlet state of the nitroxyl anion is stabilized on Co(III) and relatively nonreactive. Perhaps this nonreactivity should be expected as a result of the kinetically-inert Co(III) center. Additionally, the structural properties, especially the severely bent Co–N–O angle, appear to support this assignment although the Co(II)–NO• resonance structure has also been proposed [96]. Similar to $\{FeNO\}^7$ systems, some $\{CoNO\}^8$ complexes also display diffusion-controlled electrochemical waves arising from what has been assigned as the $\{CoNO\}^{8/9}$ redox couple. These couples have been observed in several $\{CoNO\}^8$ systems. For example, **25** (−1.18 V) [105], [Co(N_2S_2)(NO)] (**26**) (−1.32 V) [106], [Co(N_2S_2)(NO)][W(CO)$_4$] (**27**) (−0.83 V) [106], and [Co(LN_4)(NO)] (**28**) (−1.00 V) [96] (all vs. SCE, see Table 5 and Fig. 9). However, there is yet to be a report on the isolation and characterization of a discrete $\{CoNO\}^9$ complex among these 5C systems. The known 4C distorted tetrahedral $\{CoNO\}^9$ systems will thus serve as a point of reference; however, reports of these types of $\{CoNO\}^9$ complexes are scarce and very much preliminary as of 2012.

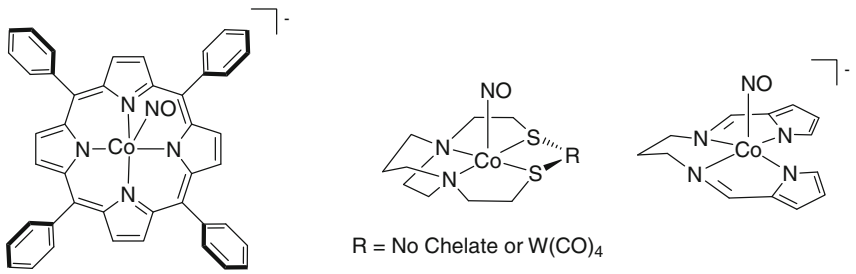

Fig. 9 5C sq-py {CoNO}^{8} complexes: [Co(TPP)(NO)] (**25**), [Co(N_2S_2R)(NO)] (**26**, R = no chelate; **27**, R = W(CO)$_4$), [Co(LN_4)(NO)] (**28**) that exhibit reversible {CoNO}^{8} ↔ {CoNO}^{9} redox couples. The {CoNO}^{9} state for each system has yet to be isolated

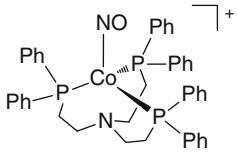

Fig. 10 Structure of the {CoNO}^{9} complex, [Co(np_3)(NO)]$^+$ (**30**) [88]

Although the {CoNO}^{9} notation is rare, it dates back nearly 100 years to the early 1930s in the synthesis of the tetrahedral organometallic complex [Co(CO)$_3$(NO)] (**29**) [111, 112]. Numerous subsequent publications on the synthesis and properties of **29** also appeared over the next 50 years. This organometallic cobalt nitrosyl will not be discussed in detail; however, its corresponding structural and spectroscopic properties (Table 5) will serve as the benchmark of comparison for the 4C tetrahedral {CoNO}^{9} complexes that will be described. As of 2012, the synthesis and structural characterization of only three {CoNO}^{9} complexes have been reported [88, 109, 110].

Sacconi and coworkers reported the synthesis and structure of the first non-organometallic {CoNO}^{9} species, namely [Co(np_3)(NO)](BPh$_4$) (**30**), where np_3 = tris(2-diphenylphosphinoethyl)amine (Fig. 10) [88, 108]. Complex **30** was obtained as a green crystalline material via NO(g) purge to an CH_2Cl_2 solution of the Co(I)-hydrido complex, [Co(np_3)H], containing NaBPh$_4$ in the reaction medium [88]. The 4C Co center in **30** was determined to be in a distorted tetrahedral geometry arising from the three tertiary phosphines and the nitrosyl to afford an NP_3 coordination sphere. The notable structural data indicated a Co–N–O bond angle of 165° with Co–N(O) and N–O bond distances of 1.83 Å and 1.14 Å, respectively. These values were somewhat atypical of cobalt nitrosyls; however, the low quality crystal data presumably explains the noted deviation. A ν_{NO} IR peak for **30** was observed at 1,680 cm^{-1} (Nujol), which is significantly lower than that observed in [Co(CO)$_3$(NO)] (**29**) ν_{NO} = 1,818 cm^{-1} (Ar matrix, 7 K) [88, 107]. The σ-donating aryl phosphines seemingly account for significant back-donation from Co into the NO of **30** whereas the three CO ligands of **29** effectively compete for this electron

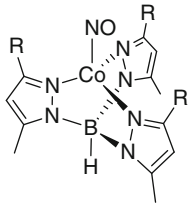

Fig. 11 Structure of $\{CoNO\}^9$ complexes, with the hydrotris(3-R-5-methylpyrazolyl)borato ligand where R = *t*-Butyl in **31** [109] and CH_3 in **32** [110]

density to result in the higher ν_{NO}. Solid-state magnetic susceptibility measurements indicated a μ_{eff} of 1.98 μ_B at 293 K, which is close to the spin-only value for one unpaired electron, thus indicating an $S_{tot} = 1/2$ ground state for **30**. Solutions of **30** in 1,2-dichloroethane display shoulders at λ_{max} of 575 nm ($\varepsilon = 400\ M^{-1}\ cm^{-1}$) and 1,399 nm ($\varepsilon = 51\ M^{-1}\ cm^{-1}$) in the electronic absorption spectrum which are attributed to a Co-to-ligand MLCT transition and a ligand-field $^2E \leftarrow {}^2A_1$ transition, respectively. Although further analysis of **30** was lacking, this report offered the first insight into the structural and spectroscopic properties expected of non-organometallic 4C tetrahedral $\{CoNO\}^9$ complexes.

Analogous to the NP_3 supporting ligand of **30**, two other $\{CoNO\}^9$ complexes have been reported that utilize the N_3 chelate of tris-pyrazolyl borate derivatized ligands (Fig. 11) [109, 110]. Theopold and coworkers synthesized the green crystalline $\{CoNO\}^9$ complex, [Co(Tp$^{t\text{-Bu,Me}}$)(NO)] (**31**) (where Tp$^{t\text{-Bu,Me}}$ = hydrotris(3-tert-butyl-5-methylpyrazolyl)borato), in 60% yield by purging NO(g) through a pentane solution of [Co(Tp$^{t\text{-Bu,Me}}$)(N_2)] [109]. Quite in contrast to **30**, the corresponding Co–N(O) and N–O distances are much shorter in **31**, 1.671 Å and 1.071 Å, respectively. Additionally, the Co–N–O angle was perfectly linear and reported to be 180.000°. The idealized bond angle and short N–O bond length are not consistent with the $\{CoNO\}^9$ notation and is likely the result of positional disorder of the O-atom in the NO ligand, which has been observed in a variety of metal nitrosyls [42, 104]. A strong ν_{NO} IR peak was observed at 1,736 cm^{-1} (KBr), which is blue-shifted by 56 cm^{-1} from the ν_{NO} of **30**. The π-donor nature of the phosphine ligands in **31** appears to have a dramatic influence on ν_{NO} in these otherwise isostructural $\{CoNO\}^9$ complexes. Several ligand-field bands were also observed in the UV–vis spectrum of **31** at λ_{max} (ε, $M^{-1}\ cm^{-1}$) of 449 (117), 554 (31), and 656 (76) nm in THF. While spectroscopic studies were available at this point, a more thorough investigation of the electronic structure and possible oxidation state assignments were lacking. However, an in-depth theoretical in conjunction with experimental paper was reported in 2011 for a near identical CoTp $\{CoNO\}^9$ species.

Wieghardt described a more detailed account of a similar 4C $\{CoNO\}^9$ complex utilizing a methylated version of the Tp ligand, namely $[Co(Tp^*)(NO)]^-$ (**32**) (Fig. 11) (where Tp* = hydrotris(3,5-dimethylpyrazolyl)borato) [110]. Complex **32** was synthesized via a ligand exchange reaction in THF with the cobalt dinitrosyl complex, $[(TMEDA)Co(NO)_2][BPh_4]$ (TMEDA = *N*,*N*,*N*′*N*′-tetramethylethylenediamine), and KTp* to yield the dark green product in 45% yield. Like **30** and **31**, complex **32**

exhibited a pseudotetrahedral coordination geometry about Co with Co–N(O) and N–O distances of 1.627 Å and 1.164 Å (average values of two independent molecules in the lattice), respectively. The Co–N–O bond angle was reported to be 176.8° (average values of two independent molecules in the lattice). Unlike **31** severe disorder of the NO oxygen was not observed in **32**, thus providing a more reliable handle on the metric parameters expected for a tetrahedral 4C $\{CoNO\}^9$ complex. Vibrational measurements on **32** revealed a single ν_{NO} peak at 1,732 cm^{-1} (KBr), which is consistent with the IR data for **31** considering the extreme structural similarities between these compounds. Four predominant features were also observed in the UV–vis at λ_{max}, nm (ε, M^{-1} cm^{-1}) of 438 (234), 493 (183), 658 (141), and 1,620 (14). The distribution of the 1,620 nm peak precluded a determination of the vibronic origin of the signal; however, the higher energy peaks were assigned as *d–d* transitions. The spin-state assignments were supported by EPR, which was lacking in **31**. The EPR spectrum of **32** displayed an anisotropic signal with resonances at $g_x = 1.814$, $g_y = 1.910$, $g_z = 3.505$ with an especially large hyperfine coupling of the g_z component to the $I = 7/2$ nucleus of Co ($A_x = 28.2 \times 10^{-4}$ cm^{-1}, $A_y = 29.0 \times 10^{-4}$ cm^{-1}, $A_z = 213.0 \times 10^{-4}$ cm^{-1}) indicative of primarily metal-centered spin density. This spectrum is suggestive of a ground state doublet ($S_{tot} = 1/2$) for **32**, and the assignment of a HS Co(II) center ($S_{Co} = 3/2$) antiferromagnetically coupled to $^3NO^-$ ($S_{NO} = 1$) for the CoNO unit in **32**. DFT (B3LYP/CP(PPP)) and CASSCF calculations further confirm this description and predict a non-bonding d_{xy} orbital (98% Co-based) as the SOMO suggesting that the $\{CoNO\}^9$-to-$\{CoNO\}^8$ transformation should be relatively facile in these 4C complexes. Complex **32** has been shown to coordinate an additional NO ligand to form a $Co(NO)_2$ dinitrosyl, which appears to activate olefins [110]. Thus, the $\{CoNO\}^9$ state in 4C tetrahedral Co complexes is accessible and sufficiently stable as evidenced by the isolation of the aforementioned systems. Furthermore, the $\{CoNO\}^9$ frontier MOs demonstrate non-bonding character making redox transformations and their associated reaction chemistry (such as nitroxyl donation) a considerable possibility for the future applications of such constructs.

5 Conclusions

The synthesis and properties of $\{FeNO\}^8$ and $\{CoNO\}^9$ coordination units have now become more clear over the past decade with the construction of small molecule complexes along with the isolation of MbHNO. From a synthetic vantage point, the most logical and prevalent method for making such complexes has been from chemical or electrochemical reduction procedures. However, MbHNO is synthesized directly from HNO-donor molecules. This activity has provided the bioinorganic community with some structural, electrochemical, and spectroscopic benchmarks to aid in the identification of such species, which are summarized in Fig. 12. Some notable features are the subtle differences between the heme and non-heme complexes. And, amongst the hemes, a significant modification is observed

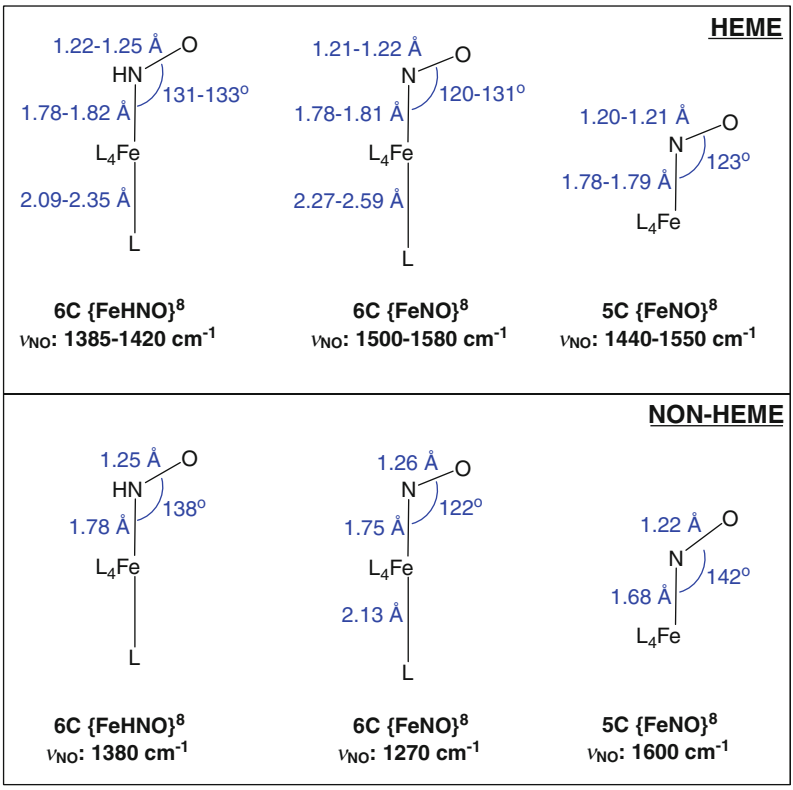

Fig. 12 General structural and vibrational properties of compiled heme (*top*) and non-heme (*bottom*) $\{FeNO\}^8$ coordination complexes and MbHNO (see Tables 1–4 and the text)

between coordinated HNO versus NO^- especially if there is a ligand trans to it. In sum, the Fe–N–O angle in HNO complexes is larger than the corresponding NO^- complexes due to the increased repulsion between the lone pair on NO^- and the bonding pair in the Fe–NO bond. In turn, this results in a slight overall increase in the N–O bond lengths (see Table 2 and Fig. 12). Additionally, non-heme $\{FeNO\}^8$ complexes have the longest N–O bond, which is consistent with a LS Fe(II)–$^1NO^-$ depiction and is supported by the low ν_{NO} values in their IR spectra. In contrast, heme $\{FeNO\}^8$ assignments evoke more of a resonance picture with no definitive oxidation state, i.e., LS Fe(II)–$^1NO^-$ ↔ LS Fe(I)–NO•. In general, coordination of nitroxyl to Fe centers results in LS diamagnetic complexes that appear to coordinate nitroxyl as either ^{1}HNO or $^1NO^-$. The singlet state for free nitroxyl anion, however, is inaccessible (the ground electronic state is triplet by ~20 kcal/mol, see Fig. 3) and the metal must promote this presumably unstable state. This result, along with the measured pK_a of 7.7 for HNO coordinated to a non-heme Fe(II) center, has important implications in the reduction of NO and its derivatives that are part of the catalytic cycles of NiR and NOR. Complexes formulated as $\{CoNO\}^9$ are

extremely rare and less than a handful of these systems have been synthesized. The reported 4C tetrahedral systems have been thoroughly characterized and suggest a HS Co(II)–$^3NO^-$ oxidation state. Although several 5C $\{CoNO\}^9$ complexes structurally analogous to heme $\{FeNO\}^8$ systems have been electrochemically formulated, none have been isolated. Thus, the synthesis and properties of these types of $\{CoNO\}^9$ complexes are still an uncharted territory waiting to be explored.

These reports and the analysis of these unique EF notations lead to some design rationale for the binding and stability of HNO or NO^- to first-row transition metals. Firstly, the ligand environment should be electronically flexible to support multiple metal spin-states. This prerequisite is not too surprising as the reversible binding of O_2 to hemes is completely dependent on the HS-to-LS spin-state transition when O_2 coordinates and releases from heme Fe. In fact, all known $\{FeNO\}^8$ complexes, including MbHNO, are diamagnetic LS coordination complexes. Secondly, the ligand platform should not be electron-rich but should be capable of enhancing the π-donation of the metal to the nitroxyl. Pyrrole donors have fit this requirement quite nicely in heme and non-heme constructs. These donor platforms also provide the coordinated nitroxyl a metal center that is not extremely electron-rich (no $d\pi$–$p\pi$ anti-bonding repulsions) with just enough π-basicity to participate in the stabilizing backbonds associated with heteronuclear diatom–metal interactions. Lastly, the secondary and tertiary coordination sphere bonding profiles must also be considered. Ligand hydrogen-bonding functional groups have long been utilized in stabilizing O_2-binding (e.g., picket-fence porphyrins) and high valent metal-oxos. These functionalities should be provided to interact with the coordinated nitroxyl. Indeed, the extreme stability of MbHNO has been attributed to an extended H-bonding network from the active site residues that H-bond to the nitroxyl and surround the Fe–HNO coordination unit. Collectively, these design criteria along with the consensus of the structure and bonding of these unique EF notations for Fe and Co have clarified our understanding of (1) biological NO_x reduction/processing and (2) the construction of suitable coordination complexes that provide new avenues for improved HNO-donor therapeutics.

References

1. Ignarro LJ (2000) Nitric oxide biology and pathobiology. Academic, San Diego
2. Moncada S, Higgs EA (2006) Br J Pharmacol 147:S193
3. Ignarro LJ (1999) Angew Chem Int Ed 38:1882
4. Furchgott RF (1999) Angew Chem Int Ed 38:1870
5. Murad F (1999) Angew Chem Int Ed 38:1856
6. Fukuto JM, Dutton AS, Houk KN (2005) Chembiochem 6:612
7. Miranda KM (2005) Coord Chem Rev 249:433
8. Shafirovich V, Lymar SV (2002) Proc Natl Acad Sci USA 99:7340
9. Irvine JC, Ritchie RH, Favaloro JL, Andrews KL, Widdop RE, Kemp-Harper BK (2008) Trends Pharmacol Sci 29:601
10. Flores-Santana W, Switzer C, Ridnour LA, Basudhar D, Mancardi D, Donzelli S, Thomas DD, Miranda KM, Fukuto JM, Wink DA (2009) Arch Pharm Res 32:1139

11. Miranda KM, Katori T, Torres de Holding CL, Thomas L, Ridnour LA, McLendon WJ, Cologna SM, Dutton AS, Champion HC, Mancardi D, Tocchetti CG, Saavedra JE, Keefer LK, Houk KN, Fukuto JM, Kass DA, Paolocci N, Wink DA (2005) J Med Chem 48:8220
12. Fukuto JM, Switzer CH, Miranda KM, Wink DA (2005) Annu Rev Pharmacol Toxicol 45:335
13. Miranda KM, Nims RW, Thomas DD, Espey MG, Citrin D, Bartberger MD, Paolocci N, Fukuto JM, Feelisch M, Wink DA (2003) J Inorg Biochem 93:52
14. Flores-Santana W, Salmon DJ, Donzelli S, Switzer CH, Basudhar D, Ridnour L, Cheng R, Glynn SA, Paolocci N, Fukuto JM, Miranda KM, Wink DA (2011) Antioxid Redox Signal 14:1659
15. Turk J, Corbett JA, Ramanadham S, Bohrer A, McDaniel ML (1993) Biochem Biophys Res Commun 197:1458
16. Wong PS-Y, Hyun J, Fukuto JM, Shirota FN, DeMaster EG, Shoeman DW, Nagasawa HT (1998) Biochemistry 37:5362
17. Doyle MP, Mahapatro SN, Broene RD, Guy JK (1988) J Am Chem Soc 110:593
18. Paolocci N, Jackson MI, Lopez BE, Miranda K, Tocchetti CG, Wink DA, Hobbs AJ, Fukuto JM (2007) Pharmacol Ther 113:442
19. Nagasawa HT, DeMaster EG, Redfern B, Shirota FN, Goon DJW (1990) J Med Chem 33:3120
20. Paolocci N, Katori T, Champion HC, St. John ME, Miranda KM, Fukuto JM, Wink DA, Kass DA (2003) Proc Natl Acad Sci USA 100:5537
21. Paolocci N, Saavedra WF, Miranda KM, Martignani C, Isoda T, Hare JM, Espey MG, Fukuto JM, Feelisch M, Wink DA, Kass DA (2001) Proc Natl Acad Sci USA 98:10463
22. Reisz JA, Bechtold E, King SB (2010) Dalton Trans 39:5203
23. Dalby FW (1958) Can J Phys 36:1336
24. Farmer PJ, Sulc F (2005) J Inorg Biochem 99:166
25. Angeli A, Angelico A, Scurti F (1902) Chem Zentralbl 73:691
26. Angeli A (1903) Gazz Chim Ital 33:245
27. Bartberger MD, Liu W, Ford E, Miranda KM, Switzer C, Fukuto JM, Farmer PJ, Wink DA, Houk KN (2002) Proc Natl Acad Sci USA 99:10958
28. Benderskii VA, Krivenko AG, Ponomarev EA (1990) Elektrokhimiya 26:318
29. Clough PN, Thrush BA, Ramsay DA, Stamper JG (1973) Chem Phys Lett 23:155
30. Johns J, McKellar A (1977) J Chem Phys 66:1217
31. Sulc F, Farmer PJ (2008) Bioinorganic chemistry of HNO ligand. In: Ghosh A (ed) The smallest biomolecules: diatomics and their interactions with heme proteins. Elsevier, Amsterdam, p 429
32. Enemark JH, Feltham RD (1974) Coord Chem Rev 13:339
33. Angelo M, Hausladen A, Singel DJ, Stamler JS (2008) Methods Enzymol 436:131
34. Gladwin MT, Grubina R, Doyle MP (2009) Acc Chem Res 42:157
35. Berto TC, Lehnert N (2011) Inorg Chem 50:7361
36. Hopmann KH, Cardey B, Gladwin MT, Kim-Shapiro DB, Ghosh A (2011) Chem Eur J 17:6348
37. Tolman WB (ed) (2006) Activation of small molecules: organometallic and bioinorganic perspectives. Wiley-VCH, Weinheim
38. Guilard R, Kadish KM (1988) Chem Rev 88:1121
39. Reeder BJ (2010) Antioxid Redox Signal 13:1087
40. Stynes DV, Cleary Stynes H, James BR, Ibers JA (1973) J Am Chem Soc 95:4087
41. Wayland BB, Olson LW (1974) J Am Chem Soc 96:6037
42. Scheidt WR, Frisse ME (1975) J Am Chem Soc 97:17
43. Praneeth VKK, Näther C, Peters G, Lehnert N (2006) Inorg Chem 45:2795
44. Praneeth VKK, Neese F, Lehnert N (2005) Inorg Chem 44:2570
45. Goodrich LE, Paulat F, Praneeth VKK, Lehnert N (2010) Inorg Chem 49:6293
46. Olson LW, Schaeper D, Lançon D, Kadish KM (1982) J Am Chem Soc 104:2042

47. Choi I-K, Liu Y, Feng D, Paeng K-J, Ryan MD (1991) Inorg Chem 30:1832
48. Vogel KM, Kozlowski PM, Zgierski MZ, Spiro TG (1999) J Am Chem Soc 121:9915
49. Bayachou M, Lin R, Cho W, Farmer PJ (1998) J Am Chem Soc 120:9888
50. Fujita E, Fajer J (1983) J Am Chem Soc 105:6743
51. Wei Z, Ryan MD (2010) Inorg Chem 49:6948
52. Liu Y, DeSilva C, Ryan MD (1997) Inorg Chim Acta 258:247
53. Pellegrino J, Bari SE, Bikiel DE, Doctorovich F (2010) J Am Chem Soc 132:989
54. Barley MH, Takeuchi KJ, Meyer TJ (1986) J Am Chem Soc 108:5876
55. Barley MH, Rhodes MR, Meyer TJ (1987) Inorg Chem 26:1746
56. Immoos CE, Sulc F, Farmer PJ, Czarnecki K, Bocian DF, Levina A, Aitken JB, Armstrong RS, Lay PA (2005) J Am Chem Soc 127:814
57. Connelly NG, Geiger WE (1996) Chem Rev 96:877
58. Lançon D, Kadish KM (1983) J Am Chem Soc 105:5610
59. Waleh A, Ho N, Chantranupong L, Loew GH (1989) J Am Chem Soc 111:2767
60. Einsle O, Messerschmidt A, Huber R, Kroneck PMH, Neese F (2002) J Am Chem Soc 124:11737
61. Williams PA, Fülöp V, Garman EF, Saunders NFW, Ferguson SJ, Hajdu J (1997) Nature 389:406
62. Einsle O, Messerschmidt A, Stach P, Bourenkov GP, Bartunik HD, Huber R, Kroneck PMH (1999) Nature 400:476
63. Pellegrino J, Hübner R, Doctorovich F, Kaim W (2011) Chem Eur J 17:7868
64. Grinstaff MW, Hill MG, Birnbaum ER, Schaefer WP, Labinger JA, Gray HB (1995) Inorg Chem 34:4896
65. Bultitude J, Larkworthy LF, Mason J, Povey DC, Sandell B (1984) Inorg Chem 23:3629
66. Mason J, Larkworthy LF, Moore EA (2002) Chem Rev 102:913
67. Murphy WR Jr, Takeuchi K, Barley MH, Meyer TJ (1986) Inorg Chem 25:1041
68. Murphy WR Jr, Takeuchi KJ, Meyer TJ (1982) J Am Chem Soc 104:5817
69. Wilson RD, Ibers JA (1979) Inorg Chem 18:336
70. Lin R, Farmer PJ (2000) J Am Chem Soc 122:2393
71. Arnold EV, Bohle DS (1996) Methods Enzymol 269:41
72. Bazylinski DA, Goretski J, Hollocher TC (1985) J Am Chem Soc 107:7986
73. Bazylinski DA, Hollocher TC (1985) J Am Chem Soc 107:7982
74. Sulc F, Immoos CE, Pervitsky D, Farmer PJ (2004) J Am Chem Soc 126:1096
75. Daiber A, Nauser T, Takaya N, Kudo T, Weber P, Hultschig C, Shoun H, Ullrich V (2002) J Inorg Biochem 88:343
76. Sulc F, Fleischer E, Farmer PJ, Ma D, La Mar GN (2003) J Biol Inorg Chem 8:348
77. Yu N-T, Kerr EA (1988) In: Spiro TG (ed) Biological applications of Raman spectroscopy, vol 3. Wiley, New York
78. Silvernail NJ, Olmstead MM, Noll BC, Scheidt WR (2009) Inorg Chem 48:971
79. Wyllie GRA, Schulz CE, Scheidt WR (2003) Inorg Chem 42:5722
80. Lehnert N, Praneeth VKK, Paulat F (2006) J Comput Chem 27:1338
81. Rich AM, Armstrong RS, Ellis PJ, Lay PA (1998) J Am Chem Soc 120:10827
82. Linder DP, Rodgers KR (2005) Inorg Chem 44:8259
83. Brucker EA, Olson JS, Ikeda-Saito M, Phillips GN Jr (1998) Proteins Struct Funct Genet 30:352
84. Copeland DM, West AH, Richter-Addo GB (2003) Proteins Struct Funct Genet 53:182
85. Copeland DM, Soares AS, West AH, Richter-Addo GB (2006) J Inorg Biochem 100:1413
86. Scheidt WR, Barabanschikov A, Pavlik JW, Silvernail NJ, Sage JT (2010) Inorg Chem 49:6240
87. Ye S, Price JC, Barr EW, Green MT, Bollinger JM Jr, Krebs C, Neese F (2010) J Am Chem Soc 132:4739
88. Di Vaira M, Ghilardi CA, Sacconi L (1976) Inorg Chem 15:1555
89. Di Vaira M, Tarli A, Stoppioni P, Sacconi L (1975) Cryst Struct Commun 4:653

90. Stephens FS (1972) J Chem Soc Dalton Trans 2257
91. Mašek J, Mášlová E (1974) Collect Czech Chem Commun 39:2141
92. González-Lebrero MC, Scherlis DA, Estiú GL, Olabe JA, Estrin DA (2001) Inorg Chem 40:4127
93. Serres RG, Grapperhaus CA, Bothe E, Bill E, Weyhermüller T, Neese F, Wieghardt K (2004) J Am Chem Soc 126:5138
94. Hauser C, Glaser T, Bill E, Weyhermüller T, Wieghardt K (2000) J Am Chem Soc 122:4352
95. Schwane JD, Ashby MT (2002) J Am Chem Soc 124:6822
96. Patra AK, Dube KS, Sanders BC, Papaefthymiou GC, Conradie J, Ghosh A, Harrop TC (2012) Chem Sci 3:364
97. Montenegro AC, Amorebieta VT, Slep LD, Martín DF, Roncaroli F, Murgida DH, Bari SE, Olabe JA (2009) Angew Chem Int Ed 48:4213
98. McCleverty JA (2004) Chem Rev 104:403
99. Conradie J, Ghosh A (2011) Inorg Chem 50:4223
100. Boulet P, Buchs M, Chermette H, Daul C, Gilardoni F, Rogemond F, Schläpfer CW, Weber J (2001) J Chem Phys A 105:8991
101. Boulet P, Buchs M, Chermette H, Daul C, Furet E, Gilardoni F, Rogemond F, Schläpfer CW, Weber J (2001) J Chem Phys A 105:8999
102. Wyllie GRA, Scheidt WR (2002) Chem Rev 102:1067
103. Richter-Addo GB, Legzdins P (1992) Metal nitrosyls. Oxford University Press, New York
104. Scheidt WR, Hoard JL (1973) J Am Chem Soc 95:8281
105. Kadish KM, Mu XH, Lin XQ (1988) Inorg Chem 27:1489
106. Hess JL, Conder HL, Green KN, Darensbourg MY (2008) Inorg Chem 47:2056
107. Wang X, Andrews L (2001) J Phys Chem A 105:4403
108. Feltham RD, Enemark JH (1981) Structures of metal nitrosyls, vol 12. Topics in inorganic and organometallic stereochemistry. Wiley, New York
109. Thyagarajan S, Incarvito CD, Rheingold AL, Theopold KH (2003) Inorg Chim Acta 345:333
110. Tomson NC, Crimmin MR, Petrenko T, Rosebrugh LE, Sproules S, Boyd WC, Bergman RG, DeBeer S, Toste FD, Wieghardt K (2011) J Am Chem Soc 133:18785
111. Blanchard AA, Rafter JR, Adams WB Jr (1934) J Am Chem Soc 56:16
112. Coleman GW, Blanchard AA (1936) J Am Chem Soc 58:2160

Struct Bond (2014) 160: 89–114
DOI: 10.1007/430_2012_85

Published online: 24 March 2013

The Active Site of Nitrile Hydratase: An Assembly of Unusual Coordination Features by Nature

Pradip K. Mascharak

Abstract The enzyme nitrile hydratase (NHase) catalyzes hydration of organic nitriles to the corresponding amides. It contains either a non-heme Fe(III) or a non-corrinoid Co(III) center at the active site. The coordination structure around the M(III) (M = Fe, Co) center at the active-site comprises several unusual features that raised a high level of curiosity among bioinorganic chemists. Such features include (a) direct coordination of two deprotonated carboxamido-N donors and (b) two out of three coordinated Cys-S centers post-translationally oxygenated to cysteine-sulfenato and cysteine sulfinito moieties. In addition, the inactive (dark) form of Fe-NHase contains a bound NO at the sixth site that is replaced by water upon illumination. A metal-bound hydroxide appears to be responsible for the hydration of the nitrile substrates. Systematic synthetic analogue approach and theoretical studies have been employed to unravel the roles of these unusual coordination features of the active site of NHase. Research results from several laboratories have established a good structure–function correlation in NHase. The correlation provides clear understanding of nature's choice for such atypical coordination features in NHase and underscores the potential of molecular design in bioinorganic chemistry.

Keywords Cobalt proteins · Cysteine-sulfinic acid · Hydration · Nitriles · Non-heme iron

Contents

P.K. Mascharak (✉)
Department of Chemistry and Biochemistry, University of California, Santa Cruz, CA 95060, USA
e-mail: Pradip@ucsc.edu

1 Introduction

The enzyme *Nitrile hydratase* (NHase) catalyzes the bioassimilation of organic nitriles which are key metabolites of the plant world. The types of nitriles are quite diverse and they play a variety of crucial roles in plants [1–3]. For example, indole-3-acetonitrile (Fig. 1) and its derivatives are plant hormones that promote germination and plant growth. Plants also contain cyanoglycosides (Fig. 1) such as dhurrin, prunasin, linamarin, and cyanolipids (Fig. 1) in their roots, leaves, and seeds. These nitriles are readily hydrolyzed to release HCN and provide protection against casual herbivores. Ricinine (Fig. 1), present in castor seeds and castor oil, is a potent toxin while mandelonitrile (present in bitter almonds) is highly allergenic. Although many plants and crops such as wheat and barley are known to be cyanogenic, the harmful effects of the cyanoglycosides are diminished significantly during their processing. High amounts of nitriles also enter the biosphere due to production and usage of man-made nitriles (Fig. 2) such as acetonitrile (a common solvent) and acrylonitrile (extensively used in fiber, plastics, and paper pulp industry). In recent years, use of nitrile-based herbicides such as bromoxynil and dichlobenil (Fig. 2) has also increased the level of nitriles in the eco system. The latter pesticides are already in the EPA list of harmful chemicals that require special environmental regulations.

Microbes present in the soil, wastewater, and runoffs that utilize nitriles as their C and N source play a significant role in their bioassimilation. The two enzymes that are involved in such processes are *nitrilase* and *NHase*. These two nitrile hydrolases employ distinctly different active sites to hydrolyze nitriles in two somewhat different pathways. Nitrilase enzymes catalyze the hydrolysis of nitriles to carboxylic acids and ammonia without the formation of free amide intermediates (Fig. 3). This class of enzymes is involved in natural product biosynthesis in plants, animals, fungi, and certain prokaryotes. They have also found use in preparative organic chemistry in regioselective hydrolysis of amides under mild conditions [4, 5]. The general structure of the nitrilase enzyme consists of a polypeptide chain of ~260 amino acid residues with a common αββα structural fold and a -cys-glu-lys- active site motif [6, 7]. The unique cysteine in the catalytic triad reacts with the nitrile to form a thioimidate intermediate that is rapidly hydrolyzed to NH_4^+ ion and the corresponding carboxylate (Fig. 4).

Unlike nitrilases, NHases catalyzes hydration of nitriles to the corresponding amides (Fig. 3) at a metal-containing active site [8]. The amide products are subsequently converted into acid and ammonia by amidases which are almost invariably co-expressed with the NHases. Interest in both classes of nitrile hydrolase

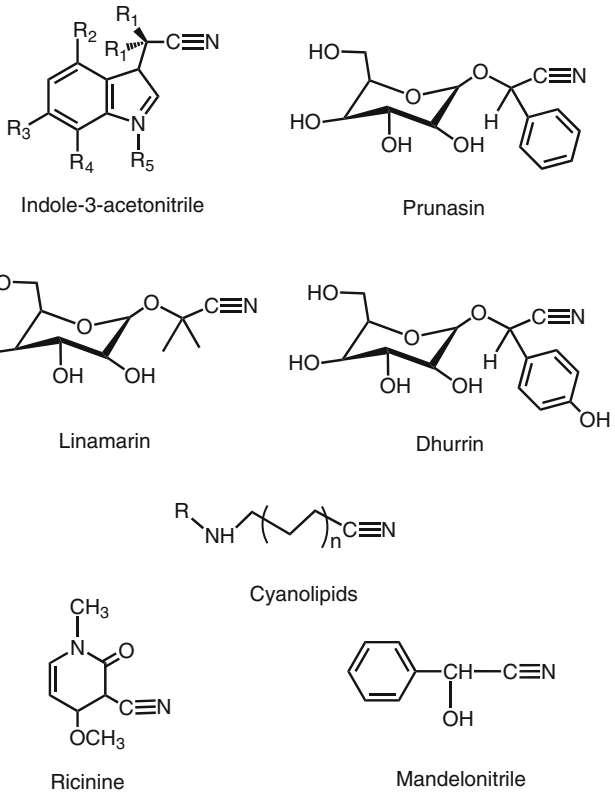

Fig. 1 Plant-derived nitriles released in biosphere

Fig. 2 Man-made nitriles present in the biosphere

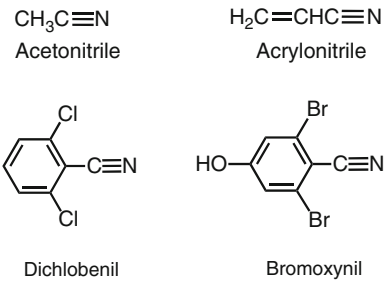

has surged in recent years due to their potential use as catalysts for the "green" production of valuable amides and acids from the corresponding nitriles [9–11]. Indeed, the large-scale (30,000 tons per year) production of acrylamide from acrylonitrile by NHase in genetically engineered *Rhodococcus rhodohrous* J1 immobilized cells is the first example of an industrial bioconversion process for the manufacture

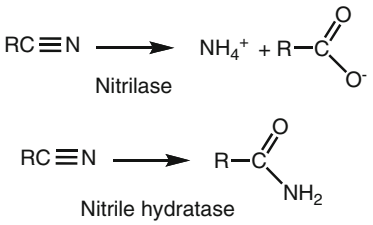

Fig. 3 Transformation of nitriles by nitrilase and nitrile hydratase

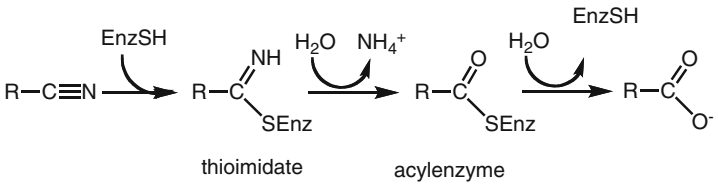

Fig. 4 Hydrolysis of nitriles by the Cys residue of nitrilase

of a commodity chemical. Production of nicotinamide with NHase by Lonza Corporation is an example of the use of NHase in health products. The potential of the green use of NHases in various chemical processes and in bioremediation of nitriles in industrial and agricultural wastewater has also been recognized in recent years [8, 12].

The unusual physical and biochemical properties of the metal-containing active sites of NHases have drawn the attention of many researchers in several subdisciplines over the past few decades. Studies on these active sites have established new paradigms of structure–function correlations in bioinorganic chemistry. Close scrutiny of the coordination architecture of the non-heme iron and non-corrinoid cobalt sites of NHases isolated from various microorganisms has revealed quite a few structural features observed for the first time in metalloenzymes [13]. The roles of these atypical features have been determined successfully via modeling approach by a number of research groups [14–16]. A critical account of the uncommon structural aspects of the active sites and their roles in the overall functions of the NHases (as revealed by the modeling and theoretical studies) are presented in the following sections.

2 General Structural Aspects

NHases are a class of metalloenzymes that promote rapid hydration of a variety of aliphatic and aromatic nitriles to their corresponding amides. Present in many microorganisms, NHases contain either a non-heme low-spin Fe(III) or a non-corrinoid low-spin Co(III) catalytic center. For example, the NHase in the *Rhodococcus* sp. N-771 is a Fe-NHase while a Co-NHase is isolated from

R. rhodochrous J1. The structures of a number of NHases have been determined by different groups and the enzymes have been well investigated at the protein and gene levels. NHases are composed of two types of subunits of mass around 23 kDa, α and β, which do not show homology in amino acid sequence. The enzyme exists as αβ dimers or $\alpha_2\beta_2$ tetramers and binds one metal atom per αβ unit. The catalytic metal site is coordinated exclusively by amino acid side chain donors of the α subunit which consists of a long extended N-terminal arm containing two α-helices, and a C-terminal domain with a αββα four-layered structure. The β subunit consists of a long N-terminal loop that wraps around the α subunit, a helical domain that packs with the N-terminal domain of the α subunit, and a C-terminal domain consisting of a β-roll and one short helix [17–20]. This intimate association of the two subunits is essential for the catalytic activity. Among the several major subunit–subunit interactions, two arginines from the β subunit (viz. βArg 56 and βArg 141 in the Fe-NHase from *Rhodococcus* sp. N-771) interact strongly with the coordination sphere of the metal center that resides in a novel fold at the interface. The metal is bound to a stretch of Cys-rich residues of the α subunit (viz. –Val109-Cys-Ser-Leu-Cys-Ser-Cys115– in the Fe-NHase from *Rhodococcus* sp. N-771). In all known NHases, the cysteine cluster regions of the α subunit and the two arginine residues of the β subunit are fully conserved.

3 Unusual Coordination Structure of the Metal Sites in NHases

In the resting state of most non-heme iron enzymes, the iron center exists in the +2 oxidation state, reacts with dioxygen, and participates in redox processes leading to oxygenase activity [21, 22]. Quite contrary to this paradigm, the iron center of Fe-NHase does *not* exhibit any redox activity; instead it acts as a Lewis acid in catalyzing the hydration of the nitriles to amides. This surprising behavior of the iron center raised curiosity in the bioinorganic community from the very beginning. The first insight in this direction came from the initial crystal structure of the Fe-NHase from *Rhodococcus* sp. R-312 by Nelson and coworkers [17]. Although spectroscopic data on Fe-NHase indicated that the low-spin Fe(III) center of this enzyme is ligated to Cys-S donors [23–25], the crystal structure demonstrated that in addition to three Cys-S donors (αCys110, αCys113 and αCys115), the iron center is coordinated to two deprotonated carboxamido-N donors derived from αSer114 and αCys115 of the metal-binding locus. At the time of this discovery, such binding of carboxamido-N to Fe(III) center was quite unexpected; the only other example was the nitrogenase P-cluster in which one Fe–N(amido) bond was noted [26]. The concept of ligation by the carboxamide group of the peptide chain in metalloenzymes had been controversial because of the high pK_a value of this moiety. However, soon after this report, Endo and coworkers reported binding of carboxamido-Ns from αSer113 and αCys114 to the Fe(III) site of NHase from *Rhodococcus* sp. N-771 [18]. A few years later, similar binding of two carboxamido-Ns from αSer112 and αCys113 to the Co(III) center in Co-NHase from *Pseudonocardia thermophila* JCM 3095 was

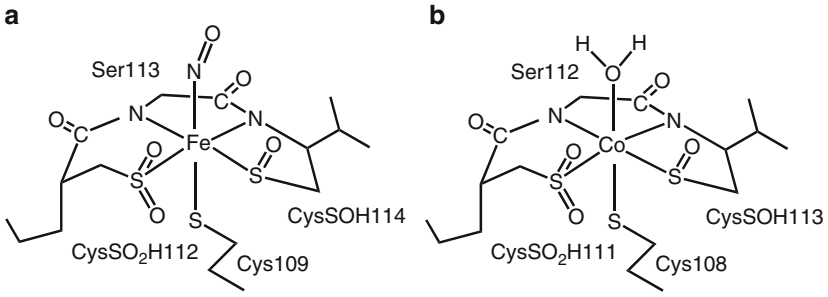

Fig. 5 The unique coordination structure of (**a**) the Fe site in *Rhodococcus* sp. N-771 NHase and (**b**) the Co site in *Pseudonocardia thermophila* JCM 3095 NHase

reported [19]. The unique ligation mode of the peptide backbone to the metal centers thus emerged as the first unusual coordination feature of the active sites of NHases. Also, the question of whether or not the lack of redox activity of the metal centers of NHases is a consequence of this coordination feature prompted intense research activity in the bioinorganic community.

The second unusual feature of the coordination architecture of the NHase active sites was evident in the high-resolution (1.7 Å) structure of the Fe-NHase reported by Endo and coworkers [18]. The crystal structure revealed that the two Cys-S donor centers (αCys112 and αCys114) at the equatorial plane of the octahedral Fe(III) center have been post-translationally modified to Cys-sulfinic (–Cys-SO_2H) and Cys-sulfenic (–CysSOH) acid moieties, respectively (Fig. 5a). The extra electron densities around Sγ of Cys112 and Cys114 were not apparent in the low-resolution (2.65 Å) structure previously reported by Nelson and coworkers. It was also noted that αCys112-SO_2H and αCys114-SOH form hydrogen bonds with βArg56 and βArg141 which are conserved in all known NHases. Although these oxygenated Cys-S centers initially raised the possibility of accidental oxidation of the Cys-S centers in the protein, careful experiments by Endo and coworkers have established the fact that the post-translation modification is essential for the catalytic activity of NHase [27]. The *Rhodococcus* sp. N-771 NHase reconstituted under argon from recombinant unmodified subunits exhibited activity only after aerobic incubation and ESI-LC/MS analysis clearly demonstrated that formation of the oxygenated Cys-S residues correlates well with the activity acquired during such incubation. Interestingly, the high-resolution (1.3 Å) structure of the Fe-NHase from *Rhodococcus erythropolis* AJ270 reveals that in this Fe-NHase, both αCys112 and αCys114 are modified to Cys-sulfinic (–Cys-SO_2H) acid [20]. Finally, in the 1.8 Å structure of the Co-NHase from *P. thermophila* JCM 3095 (Fig. 5b), the aCys111 and aCys113 (both coordinated to Co(III) in the equatorial plane) are also found as Cys-sulfinic (–Cys-SO_2H) and Cys-sulfenic (–Cys-SOH) acid, respectively [19]. Fe-SCys ligation is quite common in iron proteins such as ferredoxins [28] and cytochrome P450 family [29]; in most cases, such bonds do not require further oxygenation for catalytic activity. The required post-translational oxygenation of the equatorial Cys residues at the active sites of NHases is therefore the second unusual coordination feature that makes the active site unique.

Results of initial research work on Fe-NHases revealed another unusual activity of the non-heme iron sites [30, 31]. The Fe-NHases require light for catalytic activity. During aerobic incubation in the dark, the NHase activity decreases considerably and could be recovered upon illumination with light. Spectroscopic studies confirmed that in the "dark" inactive form, a molecule of nitric oxide (NO) is bound at the sixth site of iron that is replaced by a water molecule (or hydroxide, depending on pH) upon illumination [32–35]. A nitric oxide synthase involved in this photo-regulation of Fe-NHases via binding of NO has been identified [36]. Based on the crystal structure of the dark form of the *Rhodococcus* sp. N-771 NHase, Endo and coworkers proposed that the NO ligand bound at the iron site is stabilized by a "claw-setting of oxygen atoms" arising from the oxygenated Cys-S moieties at the equatorial plane [19]. Structural changes upon illumination cause breakage of the Fe–N(O) bond and give rise to the "active" form in which the sixth site is occupied by a water (or hydroxide) molecule [31, 35]. Such photo-regulation is unique in metalloenzymes and raised curiosity ever since its discovery. Binding of NO to Fe(III) center and its loss upon illumination is therefore counted as the third unusual feature of the iron site in Fe-NHase. Incidentally, the Co-NHases do not exhibit any photo-regulation via NO binding and the crystal structure (Fig. 5b) shows the presence of a bound water at the sixth site of Co(III) in the structure of *P. thermophila* JCM 3095 NHase [19].

Taken together, a close look at the Fe-site of the *Rhodococcus* sp. N-771 NHase (Fig. 5a) clearly attests to the fact that the active site architecture of NHase includes several unusual features that require clarifications in terms of their roles in the overall catalytic activity of this class of enzymes. In case of Fe-NHase, the hydrolytic activity instead of oxygen activation and the intriguing photo-regulation via binding of NO are both uncommon in non-heme iron enzymes. Another unusual finding is the occurrence of a kinetically inert low-spin Co(III) in place of a low-spin Fe(III) at the active site (Fig. 5b). Substitution of this kind raises the possibility that the active site metal ion might not be involved in rapid binding of substrates and loss of products during the catalytic turnovers; rather the metal center participates in activating water molecules and promotes hydration of nitriles nested at the active site pocket (vide infra). In this regard, the mechanism of hydration of nitriles by NHase calls for attention. Although binding of nitriles to metal centers of coordination complexes renders them susceptible toward hydration under mild basic conditions [37–40], direct binding of nitriles to the metal center (Fig. 6a) in NHase has been a point of contention. For example, the crystal structure of Fe-NHase from *R. erythropolis* AJ270 indicates that a water molecule occupies the sixth ligand position when the nitrile molecule is present [20]. There is, however, consensus that the hydration reaction occurs near the metal center [13, 20]. In this mechanism, binding of substrate occurs in the proximity of metal-bound water (or hydroxide) which then either attacks the nitrile carbon (Fig. 6b) or activates a water molecule which in turn can act as a nucleophile (Fig. 6c). Results of modeling and theoretical studies, included in the following section, have now provided more insights into this issue.

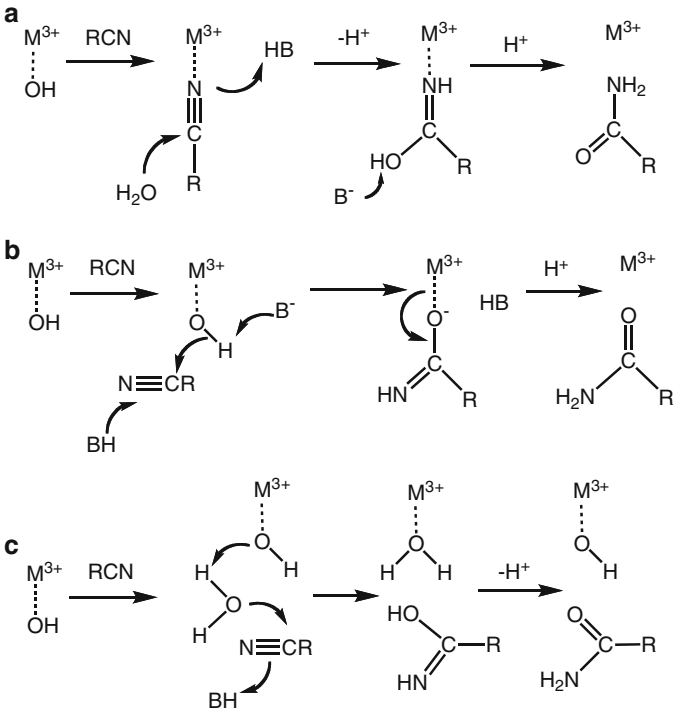

Fig. 6 Proposed mechanisms of nitrile hydration by NHase with the metal ion acting as Lewis acid. Mechanisms (**a**) and (**b**) involve ligand exchange. The slow rates for ligand exchange for low-spin M(III) ion (Co(III) in particular) are in favor of mechanism (**c**) which assumes outer-sphere activation of a bulk water molecule by the metal-bound hydroxide

4 Insights Provided by the Modeling Work

Performed almost side by side with the exploration of the enzyme and its biochemistry, synthetic modeling work has been very valuable in elucidating the roles of the unusual coordination features of the active sites of NHases. As mentioned above, coordination of deprotonated carboxamido-N donors to Fe(III) center was especially controversial due to anticipated precipitation of $Fe(OH)_3$ (and other hydroxo- and oxo-bridged species) under the high pH conditions required for deprotonation of the –C(O)–NH– unit. However, synthetic modeling work by Mascharak and coworkers clearly established that such ligation occurs readily in aprotic media [41] and once formed, the resulting species resist decomposition in aqueous media [42]. In order to test the effects of simultaneous coordination of carboxamido-N and thiolato-S donors to Fe(III) centers, this group synthesized low-spin Fe(III) complexes derived from a set of designed ligands (Fig. 7) and demonstrated that active site model of the type **1** (Fig. 8) can be easily isolated in DMF. Careful electrochemical studies on $(Et_4N)[Fe(PyPepS)_2]$ (**1**) and structurally similar species **2** (a complex with imino-N

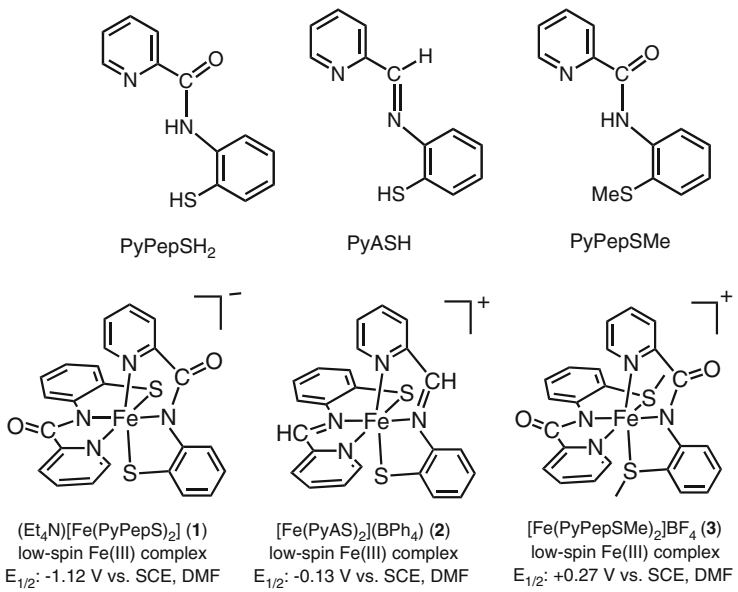

Fig. 7 Modeling work (Mascharak and coworkers) that elucidates the roles of carboxamido-N and thiolato-S donors at the active site of Fe-NHase

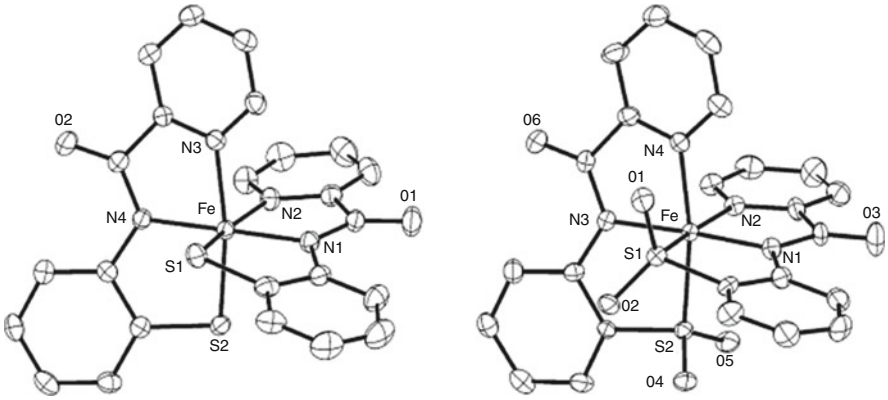

Fig. 8 Structures of $Fe(PyPepS)_2]^-$ (anion of **1**) and $[Fe(PyPepSO_2)_2]^-$ (anion of **4**)

and thiolato-S coordination) and **3** (a complex with carboxamido-N and thioether-S coordination) demonstrated for the first time that the combination of carboxamido-N and thiolato-S centers provides exceptional stability of the iron center in +3 oxidation state [43]. This in turn provides an understanding of why the Fe(III) center in Fe-NHase acts as a Lewis acid and does not exhibit any redox activity. In addition, **1** resists decomposition in aqueous solution quite in contrast with conventional wisdom. Also in DMF, reaction of H_2O_2 with **1** proceeds smoothly and affords the corresponding S-bound bis-sulfinato species $Na[Fe(PyPepSO_2)_2]$ (**4**) as the

exclusive product (Fig. 8) [44]. Complexes **2** and **3**, on the other hand, suffer rapid decomposition in oxidation attempts. Very similar behavior was observed with the corresponding low-spin Co(III) complex in methanol [44]. Even exposure to dioxygen results in the bis-sulfinato species $[Co(PyPepSO_2)_2]^-$ in this case.

A close scrutiny of the spectroscopic and redox parameters of the model complexes **1**–**4** is required at this point. The strong ligand field of the $PyPepSH_2$ (Hs re the dissociable amide protons) is reflected in the low-spin configuration of the Fe(III) center of **1** which exhibits an EPR spectrum ($g = 2.22, 2.14, 1.98$) [23] resembling that of the Fe-NHase ($g = 2.28, 2.14, 1.97$) [43]. Strong σ-donation of electron density by the carboxamido-N donors to Fe(III), as evidenced by the shift of the CO stretching frequency (ν_{CO}) to 1,612 cm^{-1} from 1,688 cm^{-1} in free ligand, raises its reduction potential to a great extent ($E_{1/2} = -1.12$ V vs. SCE in DMF). This exceptional stability of the Fe(III) center of the model complex **1** is a direct consequence of the coordination of two deprotonated carboxamido-N donors to the metal ion since simple exchange of the carboxamido-N to imine-N (good π-acceptor) lowers the $E_{1/2}$ value of $[Fe(PyAS)_2]BPh_4$ (**2**, Fig. 7) to −0.13 V versus SCE (in DMF). Another interesting aspect of the synthesis of **1** is the fact that addition of the deprotonated thiolate ligand $PyPepS^{2-}$ to the Fe(III) starting salt in DMF does not result in the anticipated reduction of Fe(III) to Fe(II). This is, however, not true with $PyAS^-$ (a ligand devoid of carboxamido-N center) which causes immediate reduction of the Fe(III) starting salt. The Fe(III) complex $[Fe(PyAS)_2]BPh_4$ (**2**) can only be synthesized via careful oxidation of the corresponding Fe(II) complex with $[(Cp)_2Fe]^+$ in DMF. The choice of the two functionalities namely, carboxamido-N and thiolato-S, is thus optimal for the assembly of the highly stable Fe(III) center of the Fe-NHase model **1**. Clean oxidation of the thiolato-S centers of **1** by H_2O_2 to the sulfinato moieties also indicates that the same choice is responsible for the rapid oxygenation observed during the post-translational modification of Fe-NHase. Important is to note that the model complex **4** (and its Co(III) analogue) includes two unusual coordination features of the active sites of NHase (Fig. 5). Not surprisingly, the green color of the model complex $Na[Fe(PyPepSO_2)_2]$ (**4**) (broad band with $\lambda_{max} \sim 690$ nm in water), arising from S-to-Fe charge-transfer matches well with that of the Fe-NHase ($\lambda_{max} = 710$ nm in water). This modeling work by Mascharak and coworkers therefore provides unambiguous explanation for nature's choice of carboxamido-N and thiolato-S coordination to a non-heme Fe(III) (or Co(III)) center in making it a Lewis acid center for nitrile hydration. The results also suggest that such thiolato-S centers are prone to oxygenation as shown in case of Fe-NHase [27].

In the second phase of their modeling attempts, Mascharak and coworkers synthesized the designed pentadentate ligand $PyPSH_4$ with two carboxamide, one pyridine, and two thiolate donor groups in the same ligand frame (Fig. 9). The goal was to keep one site on the metal center free for substrate binding and further reactivity. The structure of the mononuclear Fe(III) complex of this ligand namely, $(Et_4N)[Fe(PyPS)]$ (**5**) exhibits a pseudo trigonal bipyramidal geometry with two deprotonated carboxamido-N, two thiolato-S and one pyridine N as donors (Fig. 9) [45]. This model complex **5** binds a variety of Lewis bases (CN^-,

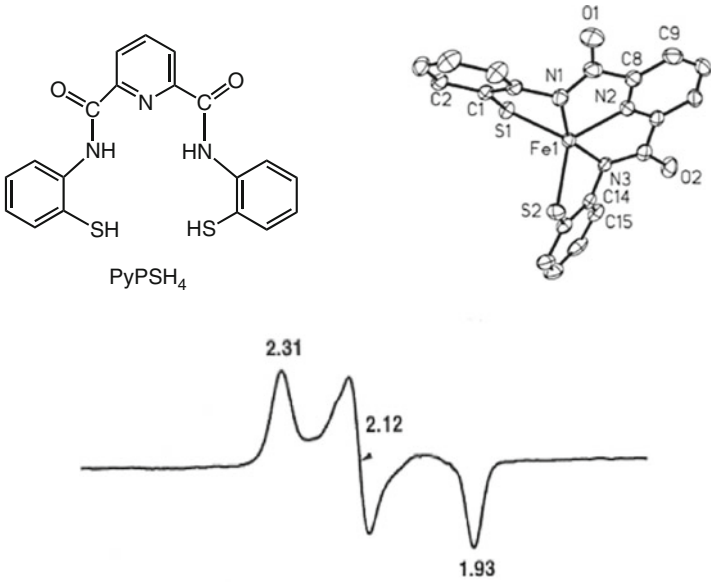

Fig. 9 (*Top panel*) Structure of the pentadentate ligand $PyPSH_4$ and of $[Fe(PyPS)]^-$, the anion of $(Et_4N)[Fe(PyPS)]$ (**5**). (*Bottom panel*) X-band EPR spectrum of $[Fe(PyPS)(OH)]^{2-}$ in acetone: water (60:40) glass at 4 K

N-MeIm, PhS^-) at the sixth site at low temperature to afford green solutions with a broad band around 700 nm and the low-spin Fe(III) centers of the six-coordinate adducts all exhibit EPR spectra very similar to the EPR spectrum of the enzyme. Interestingly, exposure to dioxygen leads to the formation of the bis-sulfinato species $(Et_4N)[Fe(PyP(SO_2)_2]$ (**6**) which isomerizes to the corresponding O-bound sulfinato species if the sixth site is not occupied [45]. The $E_{1/2}$ value of **5** (−0.65 V vs. SCE in DMF) indicates high stability of the Fe(III) center. Since the $E_{1/2}$ value drops to −0.36 V versus SCE in DMF in case of **6**, it appears that oxygenation of the thiolato-S centers in this type of coordination pulls away electron density from the negatively charged sulfur which in turn makes the iron center more prone to reduction. The Fe(III) center of **5** binds (a) water reversibly and the pK_a of the bound water bound is 6.3 ± 0.4 and (b) the green hydroxide adduct $[Fe(PyPS)(OH)]^{2-}$ exhibits an EPR spectrum (g = 2.22, 2.12, 1.99) which resembles that of Fe-NHase closely (Fig. 9). The most surprising discovery was the fact that **5** *does not* bind any nitrile even at low temperature (vide infra).

Although the OH-adduct of **5** namely, $[Fe(PyPS)(OH)]^{2-}$, provided opportunity to study hydration of nitriles with a metal-bound hydroxide (mechanism b or c of Fig. 6), the limited stability of this species in aqueous media did not allow such measurements. To circumvent this problem, Mascharak and coworkers first synthesized $(Et_4N)_2[Co(PyPS)(CN)]$ (**7**) (Fig. 10, Top panel) from the initially formed dimeric Co(III) species $(Et_4N)_2[Co_2(PyPS)_2]$ (via bridge-splitting with CN^- in MeCN) [46]. When dissolved in water, this cyano-adduct rapidly lost

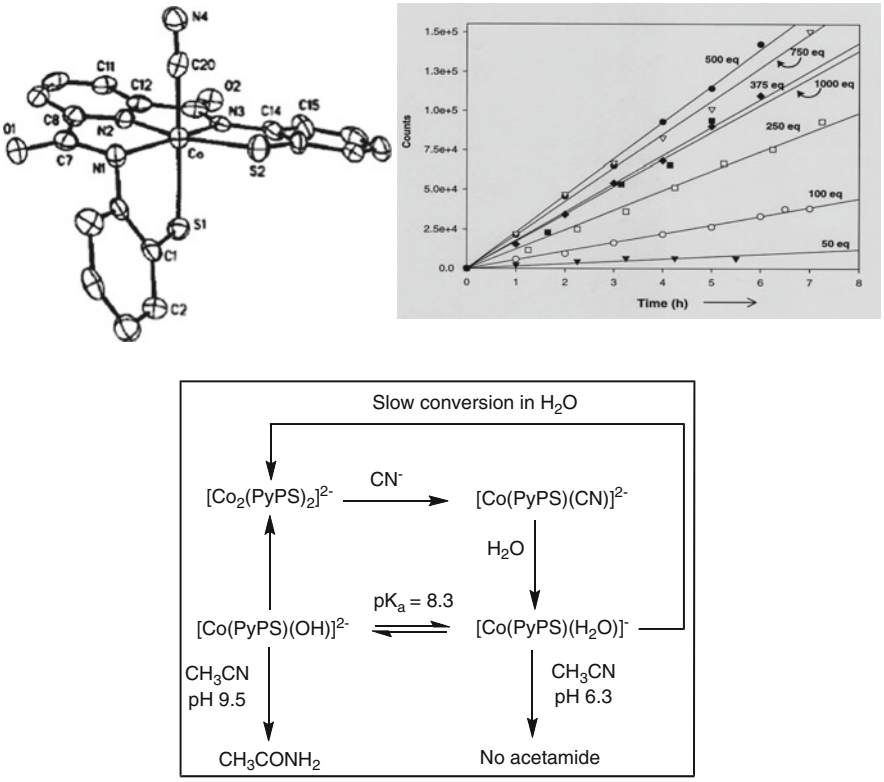

Fig. 10 (*Top panel*) Structure of $[Co(PyPS)(CN)]^{2-}$ (anion of **7**) and hydration profile (60°C, pH 9.5) of MeCN with $[Co(PyPS)(OH)]^{2-}$ (**9**) with increasing amounts of MeCN. (*Bottom panel*) Reaction scheme showing interconversion of species involved in the chemistry of $[Co(PyPS)(H_2O)]^{-}$, a *functional model* of the Co-site in Co-NHase

CN^{-} and formed the desired $[Co(PyPS)(H_2O)]^{-}$ (**8**) species. The unexpected lability of the CN^{-} ligand is noteworthy. The pK_a of the bound water in $[Co(PyPS)(H_2O)]^{-}$ (8.3 ± 0.2) lies within the biological range. This active site mimic of Co-NHase does promote hydration of MeCN to acetamide in Tris buffer in the pH range 9–12 but not below pH 7 (Fig. 10) [46]. The latter fact strongly suggests that a metal-bound hydroxide is involved in the mechanism of hydration. Since typical $[Co(L)(H_2O)]^{+}$ complexes (L = analogous ligand with all nitrogen donors) [47] do not initiate any hydration of nitriles, this result also indicates that thiolato sulfurs around Co(III) are crucial for such activity. A close look at the hydration profile of $[Co(PyPS)(OH)]^{2-}$ (**9**, Fig. 10, Top panel) reveals another interesting feature. As the relative concentration of water in the fixed 3 mL H_2O: MeCN reaction mixtures (as used in this experiment) decreased with increasing percentage of MeCN, the rate of acetamide formation first increased steadily up to 500 equiv. of MeCN. However, as the amount of MeCN reached higher values (750 and 1,000 equiv.), the rate of acetamide formation started falling off. This fact

clearly indicates that water turned out to be the limiting reagent in the reaction mixture under these conditions. Collectively, these observations suggest that the Co-bound hydroxide activates a bulk water molecule which in turn initiates nucleophilic attack on MeCN to produce acetamide (mechanism c in Fig. 6). More studies are, however, required to firmly establish this mechanism of hydration by the model complexes as well as the enzymes.

Quite parallel to the work mentioned above, Kovacs and coworkers attempted to model the active sites of NHases with the help of a set of designed ligands that include imine-N and thiolato-S donors in their framework (Fig. 11). The Fe(III) complexes $[Fe(AMIT)_2]Cl$ and $[Fe(ADIT)_2]Cl$ are low-spin much like $(Et_4N)[Fe(PyPepS)_2]$ (**1**) and exhibit EPR and absorption spectra that resemble those of Fe-NHase [48, 49]. In addition, coordination of the alkyl thiolato-S donors raises the reduction potential of the Fe(III) and provides significant stability to the Fe(III) centers. This group also synthesized five-coordinated Fe(III) and Co(III) complexes with N_3S_2 donor set namely, $[Fe(S_2{}^{Me2}N_3(Pr,Pr)]PF_6$ (**11**, Fig. 11) [50] and $[Co(S_2{}^{Me2}N_3(Pr,Pr)]PF_6$ (**12**) [51] that served as good structural models for the metal sites in NHases. Interestingly, the Co(III) center in **12** exists in $S = 1$ state while **11** exhibits mixed-spin behavior (low-spin at low temperature). Despite the absence of carboxamido-N donors (a key feature of the coordination sphere of the metal sites in NHases), the X-ray spectra of these two models matched well with those of the enzymes and established the thiolato-S ligation at the active sites. The Fe(III) center of **11** binds azide reversibly in MeOH and the EPR spectrum of the six-coordinated species resembles that of the azide-bound Fe-NHase. Also, the azide-adduct displays an intense band at 708 nm (in MeOH) that resembles the absorption band of Fe-NHase (710 nm in water at pH 7.3). Exposure to air converts the trigonal bipyramidal **12** into a more square pyramidal complex $[Co(S^{Me2}(S^{O2})N_3(Pr,Pr))]PF_6$ (a low-spin species) in which one of the thiolato-S center is oxygenated to sulfinic moiety [51]. Addition of H_2O_2 to this species eventually converts it into the corresponding sulfenato–sulfinato species $[Co((\eta^2\text{-}SO)(S^{O2})N_3(Pr,Pr))]PF_6$ (**13**, Fig. 11) in which the sulfenato moiety binds the Co(III) via both S and O centers [51]. Clearly, the thiolato-S centers in these model complexes exhibit oxygenation activity that mimics post-translational modifications of NHases. Kovacs and coworkers also reported that the azide- and thiocyanate-adduct of **12** (an $S = 1$ species) exhibit loss of the bound sixth ligand at rates faster than predicted for low-spin Co(III) center [52]. On the basis of this finding, this group predicted direct binding of nitriles at the metal sites of NHases (mechanism a of Fig. 6) and latter demonstrated direct binding of nitriles to the Fe(III) center of $[Fe(S_2{}^{Me2}N_3(Et,Pr)]PF_6$, a structural variation of **11** [53], at low temperatures through spectroscopic techniques [54]. However, in absence of any nitrile hydration, this finding provides little help in elucidation of the mechanism of nitrile hydration by the model complexes.

Binding of NO to the Fe(III) center of Fe-NHases and its role in photoactivation of the enzyme have also been explored with all these model complexes. Kovacs and coworkers studied the binding of NO to $[Fe(S_2{}^{Me2}N_3(Pr,Pr)]^+$ in detail [55, 56]. The diamagnetic NO-adduct $[Fe(S_2{}^{Me2}N_3(Pr,Pr)(NO)]PF_6$ exhibits ν_{NO} at

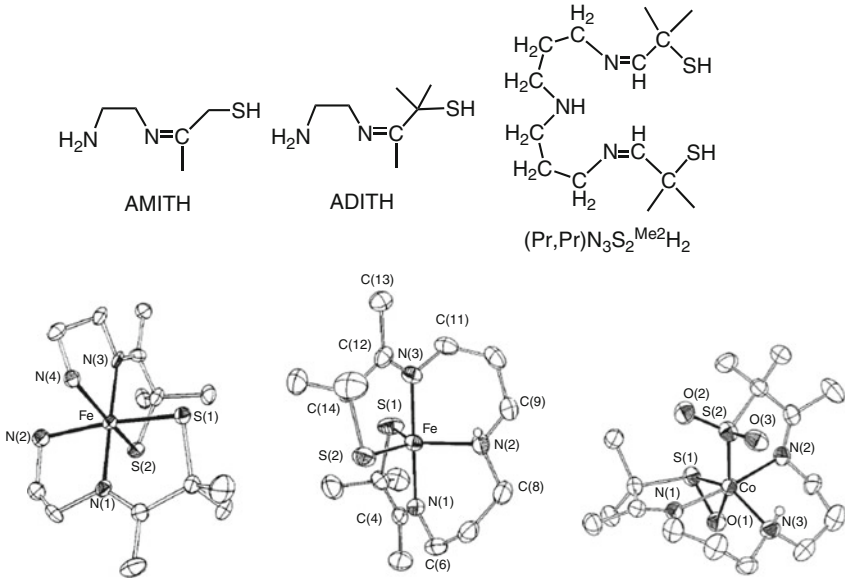

Fig. 11 (*Top panel*) Structure of ligands designed by Kovacs and coworkers. (*Bottom panel*) Structures of $[Fe(ADIT)_2]^+$, $[Fe(S_2{}^{Me2}N_3(Pr,Pr)]^+$, cation of **11**, and $[Co((\eta^2\text{-}SO)(S^{O2})N_3(Pr,Pr))]^+$, cation of **13**

1822 cm^{-1} close to that of Fe-NHase(dark) (1853 cm^{-1}). Also, the Fe–N(O) distance (1.676(3) Å) and Fe–N–O angle (172.2(3)°) are similar to those noted for the NO-bound (dark form) of the enzyme (1.65 Å and 158.6°, respectively). These similarities are quite surprising since both carboxamido-N and sulfe(i)nato-S donors are absent in the coordination sphere of Fe(III) in $[Fe(S_2{}^{Me2}N_3(Pr,Pr)(NO)]^+$. Recently, Mascharak and coworkers have provided more useful clues toward this issue. With the use of the designed ligand $Cl_2PhPepSH_4$, this group isolated the five-coordinated model complex $(Et_4N)[(Cl_2PhPepS)Fe(DMAP)]$ (**14**) in which the iron center is coordinated to two carboxamido-N and two thiolato-S (in *cis*-cofiguration) in the equatorial plane while the pyridine-N (of DMAP) occupies an axial site (Fig. 12) [57]. The Fe(III) complex **14** binds NO reversibly to afford the NO adduct $(Et_4N)[(Cl_2PhPepS)Fe(DMAP)(NO)]$ (**15**) with Fe-N(O) bond length of 1.612(10) Å and Fe–N–O bond angle of 173.2(8)°. In addition, **15** exhibits its ν_{NO} at 1849 cm^{-1}. Important is to note that despite all these similarities, **15** does not exhibit any NO photolability much like the behavior of $[Fe(S_2{}^{Me2}N_3(Pr,Pr)(NO)]PF_6$ under illumination. Oxygenation of **15** with oxazidirine in chloroform affords the corresponding disulfinic species $(Et_4N)[(Cl_2PhPep\{SO_2\}_2)Fe(DMAP)(NO)]$ (**16**) which displays its ν_{NO} at 1849 cm^{-1} and an absorption band at 440 nm (λ_{max} for the dark form of NHase ~ 400 nm). This nitrosyl, however, loses NO readily upon exposure to visible light with a quantum yield value of $\phi_{450} = 0.55$ which is close to that of Fe-NHase ($\phi_{355} = 0.48$) [33]. These results clearly demonstrate that oxygenation of the thiolato-S centers promotes NO photolability in **16**, a model complex that resembles

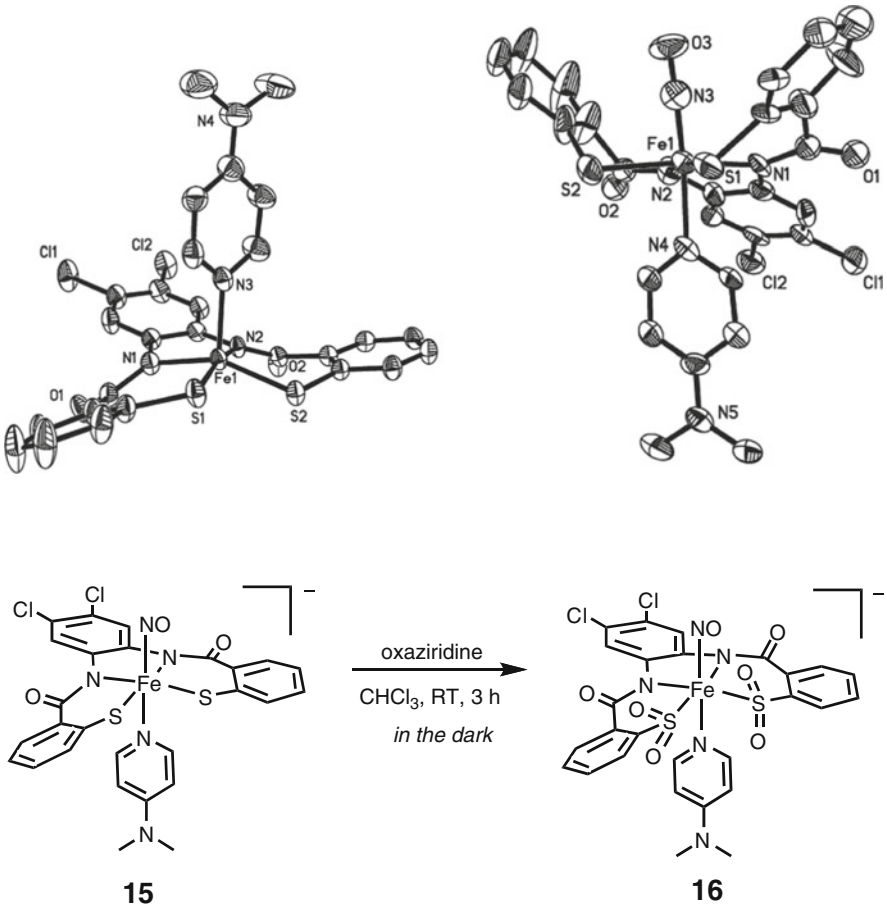

Fig. 12 (*Top panel*) Structures of $[(Cl_2PhPepS)Fe(DMAP)]^-$ (anion of **14**) and $[(Cl_2PhPepS)Fe(DMAP)(NO)]^-$ (anion of **15**). (*Bottom panel*) Formation of the bis-sulfinato species $)[(Cl_2PhPep\{SO_2\}_2)Fe(DMAP)(NO)]^-$ (anion of **16**)

the active site of the "dark form" of Fe-NHase. Mascharak and coworkers have probed into this NO photolability further via density functional theory (DFT) and time-dependent DFT (TDDFT) calculations [58]. The results indicate that in case of **15**, strong S–Fe–NO bonding interactions prevent the release of NO upon illumination. As shown on the left side of top panel of Fig. 13, the strong negative charge of the thiolato-S traverses the Fe center and continues into the Fe–N(O) bond. S-oxygenation weakens Fe–S bonding through transfer of electron density from S to the O atoms (shown on the right side of top panel of Fig. 13) and that strong transitions near 470 nm transfer an electron from a carboxamido-N/sulfinato-SO_2 MO to $d\pi(Fe)$-$\pi^*(NO)$/$d_{z2}(Fe)$-$\sigma^*(NO)$ antibonding orbitals in **16** (Fig. 13, bottom panel). Such transition weakens the Fe–NO bond and causes NO photorelease. Together,

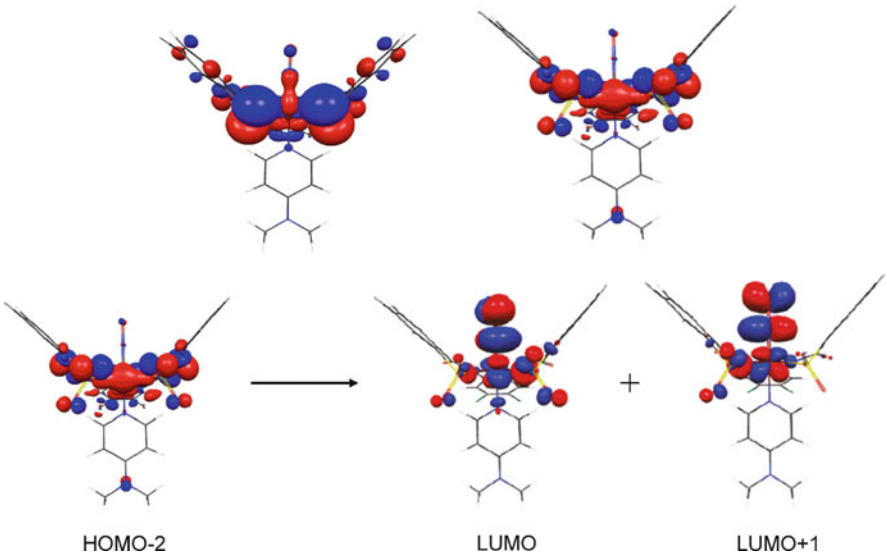

Fig. 13 (*Top panel*) HOMO-2 of **15** showing strong S–Fe–NO interaction (*left*) and the same HOMO-2 in **16** showing transfer of electron density from S to O (*right*). (*Bottom panel*) The 470 nm transition that causes NO photorelease in **16**

the results strongly suggest that oxygenated Cys-S centers play an important role in the process of NO regulation of Fe-NHases and coordination of carboxamido-N donors *is required* for such NO photolabilty.

In recent years, several groups have identified a variety of roles of post-translational oxidative modification of Cys-S centers in proteins in regulation of various biological processes [59, 60]. For example, oxygenation of an active site Cys residue regulates the enzyme tyrosine phosphatase involved in cell growth. Results of the theoretical work by Mascharak and coworkers as described above now suggest that oxygenation of Cys-S residues could be related to NO photoregulation of Fe-NHases. The same group has proposed additional role of the oxygenated Cys-S centers in NHases. Since the pK_a of the water bound at the sixth site of [Co(PyPS)$(H_2O)]^-$ (8.3 ± 0.2) is lowered upon oxygenation of one of the thiolato-S donors in [Co(PyPS)$(SO_2)(H_2O)]^-$ (7.20 ± 0.06) (Fig. 14), it was suggested that S-oxygenation increases the acidity of the bound to the metal site in NHases [61]. Such alteration presumably makes the enzyme functional at physiological pH via a metal-bound hydroxide (Fig. 6). However, because the axial thiolate is oxygenated in [Co(PyPS)$(SO_2)(H_2O)]^-$ (Fig. 14), it is not certain whether oxygenation of the equatorial Cys-S donors in NHase will cause similar shift of the pK_a of the water bound at the metal site in the enzyme. Solomon and coworkers have shown that the sulfur K-edge X-ray absorption spectra of Fe-NHase as well as model complexes $[Fe(ADIT)_2]^+$ and $[Co((\eta^2\text{-}SO)(S^{O2})N_3(Pr,Pr))]^+$ (cation of **13**) undergo changes upon S-oxygenation and protonation in case of the sulfenate [62]. Since oxygenated sulfur ligands are weaker donors that can increase the Lewis acidity of the Fe(III)

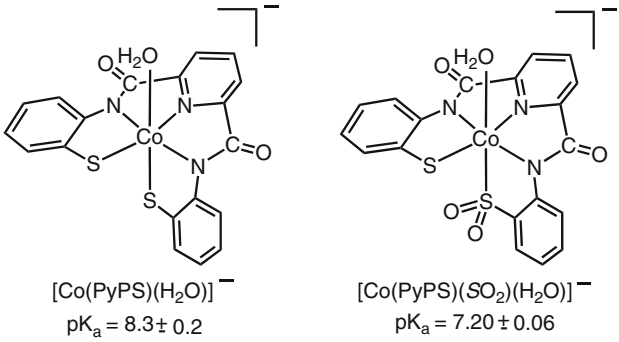

Fig. 14 The pK_a values for $[Co(PyPS)(H_2O)]^-$ and $[Co(PyPS)SO_2)(H_2O)]^-$

center, the authors suggest that cysteine oxygenation could modulate the ligand binding affinity to the vacant catalytically relevant exchangeable coordination site.

Artaud and coworkers have reported the Co(III) complex $(Et_4N)[Co(N_2S_2)]$ (**17**, Fig. 15) as a model for Co-NHase [63, 64]. This four-coordinated $S = 1$ species binds NO, CN^-, and isonitrile (CNR) at the axial sites but exhibits no affinity for H_2O, OH^-, or imidazole. Coordination of carboxamido-N and alkyl thiolato-S (both strong σ-donors) decreases the Lewis acidity of the Co(III) center in this model and allows binding of only π-accepting ligands such as NO and CN^-. The thiolato-S centers of the isonitrile-adduct $[Co(N_2S_2)(CN^tBu)_2]^-$ can be oxygenated to the corresponding $S = 0$ bis-sulfinato species (S-bound) $[Co(N_2(SO_2)_2)(CN^tBu)_2]^-$ (**18**, Fig. 15) with dioxirane. This model complex contains two oxygenated thiolato-S moieties in the equatorial plane of the Co(III) center much like the enzyme active site. Also, transfer of electron density from the thiolato-S donors following oxidation results in strong binding of two isonitrile donors (σ-donors) in the axial positions in **18**. Chottard and coworkers have also reported similar square-planar and octahedral Co(III) model complexes $Na[Co(L\text{-}N_2S_2)]$ (**19**) and $Na[Co(L\text{-}N_2S_2)(^tBuNC)_2]$ (**20**) derived from a designed ligand $L\text{-}N_2S_2$ containing alkyl thiolato-S and carboxamido-N donors (Fig. 15) [65, 66]. Oxidation of **20** with H_2O_2/urea mixture affords the bis-sulfenato (S-bound) species $Na[Co(N_2SOSO)(^tBuNC)_2]$ (**21**) while oxidation of **19** with H_2O_2 in presence of excess ^{t}BuNC affords the corresponding S-bound bis-sulfinato species $Na[Co(N_2SO_2SO_2)(^tBuNC)_2]$ (**22**) (Fig. 15). Interestingly, at 4°C in HOAc/NaOAc buffer (1M, pH 4.8), **21** (but not **22**) catalyzes hydration of MeCN to afford acetamide (40 turnovers). Since the catalyst is coordinatively saturated, Chottard and coworkers have proposed that the nucleophilic character of sulfenato (but not sulfinato) moieties promotes general acid catalysis in this case. Clearly, this hypothesis is another interesting role of oxygenated thiolato-S moiety proposed in NHase chemistry. In the absence of further studies, it is, however, not certain whether such a mechanism is indeed responsible for the fast nitrile hydrolysis observed with the enzyme.

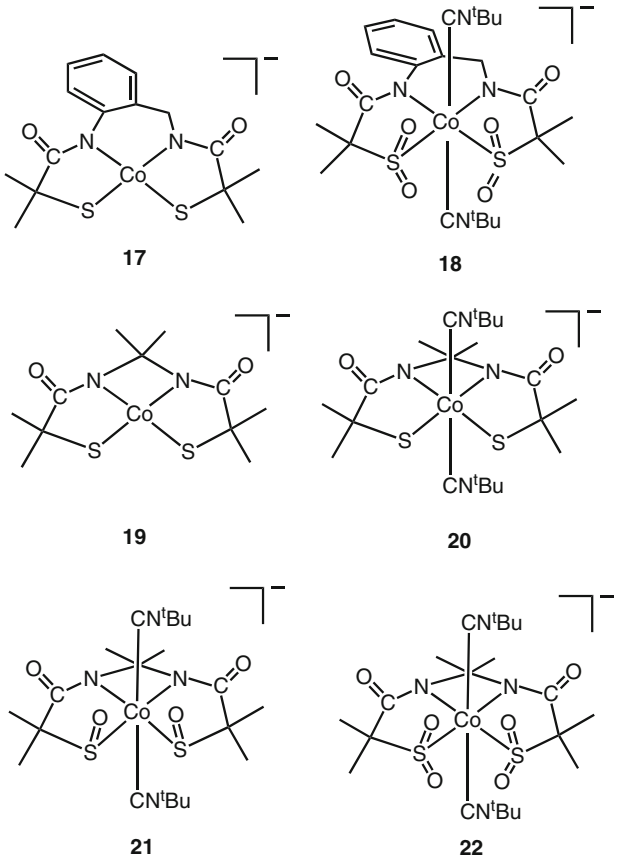

Fig. 15 Structures of $[Co(N_2S_2)]^-$ (anion of **17**), $[Co(N_2S_2)(CN^tBu)_2]^-$ (anion of **18**), $[Co(L\text{-}N_2S_2)]^-$ (anion of **19**), $[Co(L\text{-}N_2S_2)(^tBuNC)_2]^-$ (anion of **20**), $[Co(N_2SOSO)(^tBuNC)_2]^-$ (anion of **21**) and $[Co(N_2SO_2SO_2)(^tBuNC)_2]^-$ (anion of **22**)

5 Theoretical Studies: More Insights

Results of theoretical studies by various groups have provided support to several conclusions discussed above. Richards and coworkers have employed projection unrestricted Hartree–Fock (PUHF) calculations to determine the spin preferences of a series of iron(III) model [67]. When used in combination with INDO/S semiemperical model, the calculations supported the hypothesis that coordination of the carboxamido-N donors stabilizes the low-spin Fe(III) ground state as noted with the active site of Fe-NHases. Based on the results of additional DFT studies, this group assigned the low-energy electronic transition (reason for the typical green color of the enzyme) observed for the active form of Fe-NHase to a d–d transition that is coupled with charge-transfer transitions involving the metal ion and its sulfur ligands [68]. DFT studies on model complexes by Solomon and

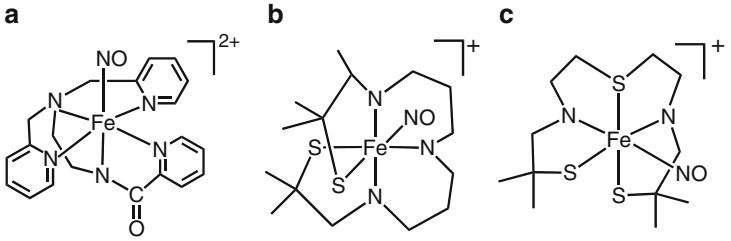

Fig. 16 Structures of (**a**) $[Fe(PaPy_3)(NO)]^{2+}$, (**b**) $[Fe(S_2{}^{Me2}N_3(Pr,Pr)(NO)]^{+}$, and (**c**) [(bmmp-TASN)Fe(NO)]$^{+}$: three NO-adducts used for theoretical studies by Richards and coworkers [72]

coworkers also supported this assignment [69]. Richards and coworkers have also looked into the ground state bonding in three diamagnetic iron nitrosyls namely, $[Fe(PaPy_3)(NO)](ClO_4)_2$ [70, 71], $[Fe(S_2{}^{Me2}N_3(Pr,Pr)(NO)]PF_6$ (NO adduct of **11**) [56] and [(bmmp-TASN)Fe(NO)]BPh_4 [72] (Fig. 16) and investigated the nature of electronic transition(s) that is responsible for NO photolability. Out of the three NO-bound models of Fe-NHase, only $[Fe(PaPy_3)(NO)](ClO_4)_2$ loses NO upon exposure to low-power visible light and the process is reversible. The second model complex $[Fe(S_2{}^{Me2}N_3(Pr,Pr)(NO)]PF_6$ loses NO via decomposition upon exposure to light while [(bmmp-TASN)Fe(NO)]BPh_4 does not show any NO photolability. Results of DFT and INDO/S calculations indicate that (a) the presence of carboxamido-N donor is necessary for the observed photodissociation of Fe–NO bond in $[Fe(PaPy_3)(NO)](ClO_4)_2$ and (b) promotion of an electron from a (dπ)Fe-carboxamido-pyridine MO to an dπ(Fe)-π*(NO) MO of $[Fe(PaPy_3)(NO)](ClO_4)_2$ causes weakening of the Fe–NO bond [73]. Additional DFT studies by this group on theoretical Fe-NHase models also revealed that the near-UV peak at 370 nm of the "dark form" of Fe-NHase results from promotion of an electron to the Fe–NO antibonding orbital from a molecular orbital associated with the sulfinate ligand [74]. This latter result is in accord with the conclusion of Mascharak and coworkers who concluded that post-translation oxygenation of the Cys-S ligands is required for the NO photoregulation of the enzyme [58].

Nowak and coworkers have investigated structural changes at the active site of Fe-NHase upon NO photorelease with the help of DFT calculations [75]. The results indicate substantial structural changes upon loss of NO. The major change includes a shift of the position of the iron center with respect to the four equatorial donors. The cysteine-sulfinic residue (Cys-12) appears to be very strongly polarized in this model. Since photoactivation of Fe-NHase requires replacement of the bound NO by a water molecule, both the trajectory of leaving NO molecule and rearrangement of water molecules near the active site are important structural issues. Nowak and coworkers have therefore studied the dynamics of light-active and dark-inactive forms of NHase using molecular dynamics (MD) modeling [76]. The results reveal fast movement of NO at the active site pocket with little stabilization by the so-called "claw-like setting" of the oxygen atoms as proposed by Endo and coworkers [18]. These oxygen atoms are more involved in H-bonding.

The trajectory of NO, however, depends on the protonation state of the active site model. Analysis of the NO-protein atom collisions indicates that the βTyr-76 is a probable steric determinant of NHase catalytic activity. Interestingly, this residue (a part of the highly conserved αSer112-βTyr68-βTrp72 catalytic triad [77]) has been identified as one that orients the nitrile substrate and also stabilizes the imidate intermediate [78]. NO also collides with several water molecules.

Endo and coworkers have looked closely into the distribution of the water molecules in the crystal structure of *Rhodococcus* sp. N-771 NHase [79]. In addition to several (~50) water molecules that glue the subunits together, 20 additional water molecules are involved in extensive H-bonding network that stabilizes the active site structure. The network also narrows down of the entrance channel to the metal site. This latter fact is presumably responsible for the substrate specificity of the enzyme, recognizing small aliphatic substrates rather than aromatic ones. Studies on water dynamics in NHase by Nowak and coworkers [76] have refined this static picture further. The results suggest that water molecules can easily get to the active site from the bulk solvent. Out of 20–25 water molecules in the NHase channel and active site, some 6–7 molecules move in and out during 1 ns of MD. The highly hydrophilic (protonated) channel of NHase allows the active site of NHase such ready access to water. In addition, collision counts between NO and water molecules identify at least two active site water molecules one of which is located at the central part of the oxygen claw settings and suggest that as NO leaves the active site, these water molecules move toward the active side with no mechanical obstacles.

To date, quantum-chemical studies have provided limited information on the mechanism of nitrile hydration by NHase. A recent DFT study demonstrated that simple coordination of nitrile to the low-spin iron center does not sufficiently activate it toward a nucleophilic attack by water [80]. Instead, this study suggests that the Cys114-SO^- could be involved in activation of water via proton abstraction and the iron site is involved in electrostatic stabilization of the imidate intermediate. This hypothesis is supported by the work of Chottard and coworkers [65] and also by the observation that Cys114-SO^- is essential for NHase activity [27]. Quite in contrast, results of MD and docking studies by Nowak and coworkers [76, 81] support the mechanism (b) of Fig. 6 in which a metal-bound hydroxide activates the nitrile and a second water molecule performs a nucleophilic attack on the nitrile carbon. Direct nucleophilic attack of water on a nitrile bound to the metal site of NHase thus remains as an issue yet to be supported by theoretical studies although such a mechanism has not been ruled out [68].

6 Conclusions

Results from research over the past three decades have started to merge toward a coherent understanding of the roles of the unusual coordination features of the active sites of the NHase family as revealed by crystal structure determination.

A variety of biochemical, physicochemical, kinetic, and modeling approach by several groups have contributed to elucidation of the function of this novel class of enzymes. These exercises underscore the power of the design principles in modeling that one employs in bioinorganic chemistry to study complex macromolecular systems. Since their initial discovery, some atypical structural features of NHases have now been identified in several other enzymes. For example, binding of carboxamido-N to nickel ion has been observed in Ni-containing enzymes such as Ni-SOD (superoxide dismutase) [82] and CO-dehydrogenase (at the Ni_d center) [83]. Also, post-translationally oxygenated cysteines have been noted at the active sites of enzymes such as peroxiredoxins [84] and tyrosine phosphatase [85]. However, in NHase, coordination of carboxamido-N and oxygenated Cys-S donors to metal ions (M = Fe, Co) serves very *different purposes*. In addition, NO photoregulation is a unique feature of Fe-NHase and so far has not been found in any other metalloenzyme. Also, among non-heme iron enzymes, Fe-NHase is an exception as being a hydrolytic enzyme (no redox activity). And finally, Co-NHase belongs to an exclusive class of cobalt enzyme with a kinetically inert low-spin Co (III) center; most cobalt proteins contain Co(II) ions at their active sites [86]. All these distinctions have their origin at the unusual active site architecture of NHase that nature has assembled for a distinct purpose namely, hydration of robust nitrile substrates.

References

1. Lechtenberg M (2011) Cyanogenesis in higher plants and animals. eLS (Plant Science). doi:10.1002/9780470015902.a0001921.pub2
2. Conn EE (1980) Cyanogenic compounds. Annu Rev Plant Physiol 31:433–451
3. Moller BL, Selgler DS (1999) Biosynthesis of cyanogenic glycosides, cyanolipids, and related compounds. In: Singh B (ed) Plant amino acids: biochemistry and biotechnology. Marcel Dekker, New York
4. Mylerová V, Martinková L (2003) Synthetic applications of nitrile-converting enzymes. Curr Org Chem 7:1–17
5. Singh R, Sharma R, Tewari N, Rawat G, Rawat DS (2006) Nitrilase and its application as a "green" catalyst. Chem Biodivers 3:1279–1287
6. Raczynska JE, Vorgias CE, Antranikian G, Rypniewski W (2010) Crystallographic analysis of a thermoactive nitrilase. J Struct Biol 173:294–302
7. Pace HC, Brenner C (2001) The nitrilase superfamily: classification, structure and function. Genome Biol 2:1–9
8. Kobayashi M, Shimizu S (1998) Metalloenzyme nitrile hydratase: structure, regulation, and application to biotechnology. Nat Biotechnol 16:733–736
9. Prasad S, Bhalla TC (2010) Nitrile hydratses (NHases): at the interface of academia and industry. Biotechnol Adv 28:725–741
10. Kobayashi M, Shimizu S (2000) Nitrile hydrolases. Curr Opin Chem Biol 4:95–102
11. Yamada H, Kobayashi M (1996) Nitrile hydratase and its application to industrial production of acrylamide. Biosci Biotechnol Biochem 60:1391–1400
12. Banerjee A, Sharma R, Banerjee UC (2002) The nitrile-degrading enzymes: current status and future prospects. Appl Microbiol Biotechnol 60:33–44

13. Harrop TC, Mascharak PK (2004) Fe(III) and Co(III) centers with carboxamido nitrogen and modified sulfur coordination: lessons learned from nitrile hydratase. Acc Chem Res 37:253–260
14. Kovacs JA (2004) Synthetic analogues of cysteinate-ligated non-heme iron and non-corrinoid cobalt enzymes. Chem Rev 104:825–848
15. Mascharak PK (2002) Structural and functional models of nitrile hydratase. Coord Chem Rev 225:201–214
16. Artaud I, Chatel S, Chauvin AS, Bonnet D, Kopf MA, Leduc P (1999) Nitrile hydratase and related non-heme iron sulfur complexes. Coord Chem Rev 190–192:577–586
17. Huang W, Jia J, Cummings J, Nelson M, Schneider G, Lindqvist Y (1997) Crystal structure of nitrile hydratase reveals novel iron center in a novel fold. Structure 5:691–699
18. Nagashima S, Nakasako M, Dohmae N, Tsujimura M, Takio K, Odaka M, Yohda M, Kamiya N, Endo I (1998) Novel non-heme iron center of nitrile hydratase with a claw setting of oxygen atoms. Nat Struct Biol 5:347–351
19. Miyanaga A, Fushinobu S, Ito K, Wakagi T (2001) Crystal structure of cobalt-containing nitrile hydratase. Biochem Biophys Res Commun 288:1169–1174
20. Song L, Wang M, Shi J, Xue Z, Wang M, Qian S (2007) High-resolution X-ray molecular structure of the nitrile hydratase from *Rhodococcus erythropolis* AJ270 reveals post-translational oxidation of two cysteines into sulfinic acids and a novel biocatalytic nitrile hydration mechanism. Biochem Biophys Res Commun 362:319–324
21. Costas M, Mehn MP, Jensen MP, Que L Jr (2004) Dioxygen activation at mononuclear nonheme iron active sites: enzymes, models, and intermediates. Chem Rev 104:939–986
22. Solomon EI, Wong SD, Liu LV, Decker A, Chow MS (2009) Peroxo and oxo intermediates in mononuclear non-heme iron enzymes and related active sites. Curr Opin Chem Biol 13:99–113
23. Sugiura Y, Kuwahara J, Nagasawa T, Yamada H (1987) The first non-heme iron enzyme with a typical low-spin iron(III) active center. J Am Chem Soc 109:5848–5850
24. Nelson MJ, Jin H, Turner IM, Grove G, Scarrow RC, Brennan BA, Que L Jr (1991) A novel iron-sulfur center in nitrile hydratase from Brevibacterium sp. J Am Chem Soc 113:7072–7073
25. Scarrow RC, Brennan BA, Cummings JG, Jin H, Duong DJ, Kindt JT, Nelson MJ (1996) X-ray spectroscopy of nitrile hydratase at pH 7 and 9. Biochemistry 35:10078–10088
26. Peters JW, Stowell MHB, Soltis SM, Finnegan MG, Johnson MK, Rees DC (1997) Redox-dependent structural changes in the nitrogenase P-cluster. Biochemistry 36:1181–1187
27. Murakami T, Nojiri M, Nakayama H, Odaka M, Yohda M, Dohmae N, Takio K, Nagamune T, Endo I (2000) Post-translational modification is essential for catalytic activity of nitrile hydratase. Protein Sci 9:1024–1030
28. Johnson D, Dean DR, Smith AD, Johnson MK (2005) Structure, function and formation of biological iron–sulfur clusters. Annu Rev Biochem 74:247–281
29. Ortiz de Montellano PR (ed) (2005) Cytochrome P450: structure mechanism, and biochemistry, 3rd edn. Kluwar Academic/Plenum, New York
30. Bonnet D, Artaud I, Moali C, Petre D, Mansuy D (1997) Highly efficient control of iron-containing nitrile hydratases by stoichiometric amounts of nitric oxide and light. FEBS Lett 409:216–220
31. Endo I, Odaka M, Yohda M (1999) An enzyme controlled by light: the molecular mechanism of photoactivity in nitrile hydratase. Trends Biotechnol 17:244–248
32. Noguchi T, Hoshino M, Tsujimura M, Odaka M, Inoue Y, Endo I (1996) Resonance Raman evidence that photodissociation of nitric oxide from the non-heme iron center activates nitrile hydratase from *Rhodococcus* sp. N-771. Biochemistry 35:16777–16781
33. Odaka M, Fuji K, Hoshino M, Noguchi T, Tsujimura M, Nagashima S, Yohda M, Nagamune T, Inoue Y, Endo I (1997) Activity regulation of photoactive nitrile hydratase by nitric oxide. J Am Chem Soc 119:3785–3791
34. Popescu VC, Munck E, Fox BG, Sanakis Y, Cummings JG, Turner IM, Nelson MJ (2001) Mossbauer and EPR studies of the photoactivation of nitrile hydratase. Biochemistry 40:7984–7991

35. Jin H, Turner IM, Nelson MJ, Gurbiel RJ, Doan PE, Hoffman BM (1993) Coordination sphere of the ferric ion in nitrile hydratase. J Am Chem Soc 115:5290–5291
36. Sari MA, Moali C, Boucher JL, Jaouen M, Mansuy D (1998) Detection of a nitric oxide synthase possibly involved in the regulation of *Rhodococcus* sp. R312 nitrile hydratase. Biochem Biophys Res Commun 250:364–368
37. Nagao H, Hirano T, Tsuboya N, Shiota S, Mukaida M, Oi T, Yamasaki M (2002) Reactions of acetonitrile coordinated to a nitrosylruthenium complex with H_2O or CH_3OH under mild conditions: structural characterization of imido-type complexes. Inorg Chem 41:6267–6273
38. Curtis NJ, Sargeson AM (1984) Synthesis and base hydrolysis of pentaammine N, N-dimethylforamide and acetonitrile complexes of Rh(III) and Ir(III). J Am Chem Soc 106:625–630
39. Zanella A, Ford PC (1975) Base hydrolysis of coordinated organonitriles: reactions of ruthenium(III) and rhodium(III) complexes. Inorg Chem 14:42–47
40. Pinnell D, Wright GB, Jordan RB (1972) Hydrolysis of coordinated nitriles to carboxamide complexes of pentaamminecobalt(III). J Am Chem Soc 94:6104–6106
41. Marlin DS, Olmstead MM, Mascharak PK (1999) Carboxamido nitrogens are good donors for Fe(III): syntheses, structures, and properties of two low-spin nonmacrocyclic iron(III) complexes with tetracarboxamido-N coordination. Inorg Chem 38:3258–3260
42. Marlin DS, Mascharak PK (2000) Coordination of carboxamido nitrogen to tervalent iron: insight into a new chapter of iron chemistry. Chem Soc Rev 29:69–74
43. Noveron JC, Olmstead MM, Mascharak PK (1998) Effect of carboxamido N coordination to iron on the redox potential of low-spin non-heme iron centers with N, S coordination: relevance to the iron site of nitrile hydratase. Inorg Chem 37:1138–1139
44. Tyler LA, Noveron JC, Olmstead MM, Mascharak PK (1999) Oxidation of metal-bound thiolato sulfur centers in Fe(III) and Co(III) complexes with carboxamido nitrogens and thiolato sulfurs as donors; relevance to the active sites of nitrile hydratases. Inorg Chem 38:616–617
45. Noveron JC, Olmstead MM, Mascharak PK (2001) A synthetic analogue of the active site of Fe-containing nitrile hydrates with carboxamido N and thiolato S as donors: synthesis, structure and reactivities. J Am Chem Soc 123:3247–3259
46. Noveron JC, Olmstead MM, Mascharak PK (1999) Co(III) complexes with carboxamido N and thiolato S donor centers: models for the active site of Co-containing nitrile Hydratase. J Am Chem Soc 121:3553–3554
47. Chavez FA, Nguyen CV, Olmstead MM, Mascharak PK (1996) Synthesis, properties, and structure of a stable cobalt(III) alkyl peroxide complex and its role in the oxidation of cyclohexane. Inorg Chem 35:6282–6291
48. Shoner SC, Barnhart D, Kovacs JA (1995) A model for the low-spin, non-heme, thiolate-ligated iron site of nitrile hydratase. Inorg Chem 34:4517–4518
49. Jackson HL, Shoner SC, Rittenberg D, Cowen JA, Lovell S, Barnhart D, Kovacs JA (2001) Probing the influence of local coordination environment on the properties of the Fe-type nitrile hydratase model complexes. Inorg Chem 40:1646–1653
50. Ellison JJ, Nienstedt A, Shoner SC, Barnhart D, Cowen JA, Kovacs JA (1998) Reactivity of five-coordinate models for the thiolate-ligated Fe site of nitrile hydratase. J Am Chem Soc 120:5691–5700
51. Kung I, Schweitzer D, Shearer J, Taylor WD, Jackson HL, Lovell S, Kovacs JA (2000) How does oxidized thiolate ligands affect the electronic and reactivity properties of a nitrile hydratase model compound? J Am Chem Soc 122:8299–8300
52. Shearer J, Kung IY, Lovell S, Kaminsky W, Kovacs JA (2001) Why is there an "inert" metal center in the active site of nitrile hydratase? Reactivity and ligand dissociation from a five-coordinate Co(III) nitrile hydratase model. J Am Chem Soc 123:463–468
53. Schweitzer D, Shearer J, Rittenberg DK, Shoner SC, Ellison JJ, Loloee R, Lovell S, Barnhart D, Kovacs JA (2002) Enhancing reactivity via structural distortion. Inorg Chem 41:3128–3136

54. Shearer J, Jackson HL, Schweitzer D, Rittenberg DK, Leavy TM, Kaminsky W, Scarrow RC, Kovacs JA (2002) The first example of a nitrile hydratase model complex that reversibly binds nitriles. J Am Chem Soc 124:11417–11428
55. Scarrow RC, Strickler BS, Ellison JJ, Shoner SC, Kovacs JA, Cummings JG, Nelson MJ (1998) X-ray spectroscopy of nitric oxide binding to iron in inactive nitrile hydratase and a synthetic model compound. J Am Chem Soc 120:9237–9245
56. Schweitzer D, Ellison JJ, Shoner SC, Lovell S, Kovacs JA (1998) A synthetic model for the NO-inactivated form of nitrile hydratase. J Am Chem Soc 120:10996–10997
57. Rose MJ, Betterley NM, Mascharak PK (2009) Thiolato S-oxygenation controls nitric oxide (NO) photolability of a synthetic iron nitrile hydratase (Fe-NHase) model derived from mixed carboxamide/thiolate ligand. J Am Chem Soc 131:83410–88341
58. Rose MJ, Betterley NM, Oliver AG, Mascharak PK (2010) Binding of nitric oxide to a synthetic model of iron-containing nitrile hydratase (Fe-NHase) and its photorelease: relevance to photo-regulation of Fe-NHase by NO. Inorg Chem 49:1854–1864
59. Reddie KG, Carroll KS (2008) Expanding the functional diversity of proteins through cysteine modification. Curr Opin Chem Biol 12:746–754
60. Poole LB, Nelson KJ (2008) Discovering mechanisms of signaling-mediated cysteine oxidation. Curr Opin Chem Biol 12:18–24
61. Tyler LA, Noveron JC, Olmstead MM, Mascharak PK (2003) Modulation of the pK_a of metal-bound water via oxidation of thiolato sulfur in model complexes of Co(III) containing nitrile hydratase: insight into the possible effect of cysteine oxidation in Co-nitrile hydratase. Inorg Chem 42:5751–5761
62. Dey A, Chow M, Taniguchi K, Lugo-Mas P, Davin S, Maeda M, Kovacs JA, Odaka M, Hodgson KO, Hedman B, Solomon EI (2006) Sulfur K-edge XAS and DFT calculations on nitrile hydratase: geometric and electronic structure of the non-heme iron active site. J Am Chem Soc 128:533–541
63. Chatel S, Rat M, Dijols S, Leduc P, Tuchagues JP, Mansuy D, Artaud I (2000) Toward model complexes of Co-containing nitrile hydratases: synthesis, complete characterization and reactivity towards ligands such as CN^- and NO of the first square planar Co(III) complex with two different carboxamido nitrogens and two thiolato sulfur donors. J Inorg Biochem 80:239–246
64. Rat M, de Sousa RA, Vaissermann J, Leduc P, Mansuy D, Artaud I (2001) Clean oxidation of thiolates to sulfinates in a four-coordinate Co(III) complex with a mixed carboxamido N-thiolato S donor set: relevance to nitrile hydratase. J Inorg Biochem 84:207–213
65. Heinrich L, Li Y, Vaissermann J, Chottard J-C (2001) A bis(carboxamido-*N*)diisocyanidobis (sulfenato-*S*)cobalt(III) complex, model for the post-translational oxygenation of nitrile hydratase thiolato ligands. Eur J Inorg Chem 1407–1409
66. Heinrich L, Mary-Verla A, Li Y, Vaissermann J, Chottard J-C (2001) Cobalt(III) complexes with carboxamido-N and sulfenato-*S* or sulfinato-*S* ligands suggest that a coordinated sulfenato-*S* is essential for the catalytic activity of nitrile hydratases. Eur J Inorg Chem 2203–2206
67. Boone AJ, Cory MG, Scott MJ, Zerner MC, Richards NGJ (2001) Investigating the structural and electronic properties of nitrile hydratase model iron(III) complexes using projected unrestricted Hartree–Fock (PUHF) calculations. Inorg Chem 40:1837–1845
68. Greene SN, Richards NGJ (2006) Electronic structure, bonding, spectroscopy and energetics of Fe-dependent nitrile hydratase active-site models. Inorg Chem 45:17–36
69. Kennepohl P, Neese F, Schweitzer D, Jackson HL, Kovacs JA, Solomon EI (2006) Spectroscopy of non-heme iron thiolate complexes: insight into the electronic structure of the low-spin active site of nitrile hydratase. Inorg Chem 44:1826–1836
70. Patra AK, Afshar R, Olmstead MM, Mascharak PK (2002) The first non-heme iron(III) complex with a ligated carboxamido group that exhibits photolability of a bound NO ligand. Angew Chem Int Ed 41:2512–2515
71. Patra AK, Rowland JM, Marlin DS, Bill E, Olmstead MM, Mascharak PK (2003) Iron nitrosyls of pentadentate ligand containing a single carboxamide group: syntheses, structures, electronic properties, and photolability of NO. Inorg Chem 42:6812–6823

72. Grapperhaus CA, Patra AK, Mashuta MS (2002) First $\{Fe–NO\}^6$ complex with an $N_3S_3Fe–NO$ core as a model of NO-inactivated iron-containing nitrile hydratase: are thiolates and thioethers equivalent donors in low-spin iron complexes? Inorg Chem 41:1039–1041
73. Greene SN, Richards NGJ (2004) Theoretical investigations of the electronic structure and spectroscopy of mononuclear, non-heme $\{Fe–NO\}^6$ complexes. Inorg Chem 43:7030–7041
74. Greene SN, Chang CH, Richards NGJ (2002) The role of post-translational modification in the photoregulation of Fe-type nitrile hydratase. Chem Commun 2386–2387
75. Nowak W, Ohtsuka Y, Hasegawa J, Nakatsuji H (2002) Density functional study on geometry and electronic structure of nitrile hydratase active site model. Int J Quantum Chem 90:1174–1187
76. Kubiak K, Nowak W (2008) Molecular dynamics simulations of the photoactive protein nitrile hydratase. Biophys J 94:3824–3838
77. Mitra S, Holz RC (2007) Unraveling the catalytic mechanism of nitrile hydratases. J Biol Chem 282:7397–7404
78. Miyanaga A, Fushinobu S, Ito K, Shoun H, Wakagi T (2004) Mutational and structural analysis of cobalt-containing nitrile hydratase on substrate and metal binding. Eur J Biochem 271:429–438
79. Nakasako M, Odaka M, Yohda M, Dohmae N, Takio K, Kamiya N, Endo I (1999) Tertiary and quaternary structures of photoactive Fe-type nitrile hydratase from *Rhodococcus* sp. N-7771: roles of hydration water molecules in stabilizing the structures and the structural origin of the substrate specificity of the enzyme. Biochemistry 38:9887–9898
80. Hopmann KH, Guo J-D, Himo F (2007) Theoretical investigation of the first-shell mechanism of nitrile hydratase. Inorg Chem 46:4850–4856
81. Peplowski L, Kubiak K, Nowak W (2007) Insights into catalytic activity of industrial enzyme Co-nitrile hydratase: docking studies of nitriles and amides. J Mol Model 13:725–730
82. Wuerges J, Lee JW, Yim YI, Yim HS, Kang SO, Carugo KD (2004) Crystal structure of nickel-containing superoxide dismutase reveals another type of active site. Proc Natl Acad Sci USA 101:8569–8574
83. Dobbek H, Svetlitchnyl V, Gremer L, Huber R, Meyer O (2001) Crystal structure of a carbon monoxide dehydrogenase reveals a [Ni-4Fe-4S] cluster. Science 293:1281–1285
84. Vivancos AP, Castillo EA, Biteau B, Nicot C, Ayte J, Toledano MB, Hidalgo EA (2005) A cysteine-sulfinic acid in peroxiredoxin regulates H2O2-sensing by the antioxidant Pap 1 pathway. Proc Natl Acad Sci USA 102:8875–8880
85. Barford D, Flint AJ, Tonks NK (1994) Crystal structure of human protein tyrosine phosphatase 1B. Science 263:1397–1404
86. Kobayashi M, Shimizu S (1999) Cobalt proteins. Eur J Biochem 261:1–9

Struct Bond (2014) 160: 115–150
DOI: 10.1007/430_2012_86

Published online: 20 April 2013

Biomimetic Chemistry with Tris(triazolyl)borate Ligands: Unique Structures and Reactivity via Interactions with the Remote Nitrogens

Elizabeth T. Papish, Natalie A. Dixon, and Mukesh Kumar

Abstract A review of the structures and reactivity of tris(triazolyl)borate (Ttz) ligands and closely related triazole-based ligands is presented, with an emphasis on complexes of the transition metals. Ttz ligands can form mononuclear complexes or coordination polymers of various dimensionalities. The extra nitrogens in Ttz ligands (relative to trispyrazolylborate, Tp, ligands) can bind to additional metals or acidic hydrogens, and through the latter interactions water solubility is improved. Ttz ligands are also weaker donors than Tp ligands, and this often leads to an increased coordination number in metal complexes. An in-depth discussion of recently developed bulky Ttz ligands and their use in forming biomimetic structures and catalyzing reactions is included.

Keywords Bioinorganic chemistry · Coordination polymers · Copper · Hydrogen bonding · Molybdenum · Transition metals · Triazole · Tris(triazolyl)borate · Water soluble · Zinc

Contents

E.T. Papish (✉), N.A. Dixon, and M. Kumar
Department of Chemistry, Drexel University, Philadelphia, PA 19104, USA
e-mail: elizabeth.papish@drexel.edu

1 Introduction

1.1 Unique Facets of the Ttz Ligand Class

Tris(triazolyl)borate (Ttz) ligands are analogous to tris(pyrazolyl)borate (Tp) ligands in their ability to supply three nitrogen donors to facially cap a metal, but they are also significantly different. Ttz ligands can bind to one metal or several and create mononuclear and polynuclear complexes and coordination polymers with fundamentally different topologies than seen with Tp complexes. This is due to the extra nitrogens that can bind to an additional metal or acidic hydrogens, thus creating a ditopic ligand, with two unique binding sites. The extra nitrogens also create significant electronic differences, and if the substituents are the same, Ttz is usually a weaker donor. These electronic differences can lead to significant reactivity differences if the chemistry is sensitive to these changes. In some cases, Ttz complexes have allowed for the isolation of rare species that are not stable as the Tp analogs. Thus, Ttz ligands can play an important role in forming biomimetic structures and enabling studies of catalytic processes.

1.2 Nomenclature, Abbreviations, and Basic Principles

Throughout this review, we will employ the same nomenclature used by Swiatoslaw Trofimenko [1, 2], with the substituents in the three and five positions given as R and R′, respectively, in $Ttz^{R,R'}$. Abbreviations used herein include Ttz = tris(triazolyl)borate, Tp = tris(pyrazolyl)borate, Btz = bis(triazolyl)borate, Bp = bis(pyrazolyl)borate, Ttzm = tris(triazolyl)methane, and Btzm = bis(triazolyl)methane. Significantly, Ttz and Btz ligands are monoanionic, and the hydridic BH rarely interacts with the metal or donates H^-. In contrast, Ttzm and Btzm are neutral ligands that feature a methane linker. These charges dictate, in some cases, which metal oxidation states are most readily isolated.

All of the tridentate ligands described herein can be called scorpionates, a term coined by Trofimenko [1]. They can bind through two claws and one tail, and for the Ttz complexes described herein all binding groups are equivalent, so they are homoscorpionates. However, Ttz is further functionalized relative to Tp, since each of the three arms has two distinct binding sites. This resembles a cross between a scorpion and a cephalopod, in which there are still three binding sites as seen in scorpionates, but the remote nitrogens (in the fourth position on the triazole rings)

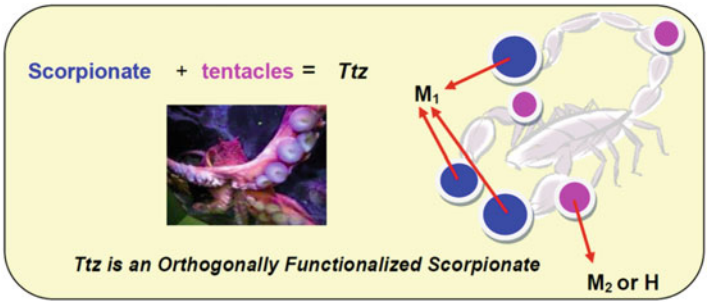

Fig. 1 Shows that Ttz ligands can bind to additional electropositive groups and can be considered "orthogonally functionalized scorpionates"

represent an additional binding site, much like the suction cups on the tentacles of octopuses (Fig. 1). We can think of Ttz ligands as being orthogonally functionalized scorpionates, whereby binding a metal ion or H^+ to the extra nitrogens (schematically shown in magenta in Fig. 1) results in new structures and altered electronic properties.

2 Literature Review Organized by Ligand Type

2.1 Borohydride Linkers for Tris Triazole-Based Ligands

2.1.1 $Ttz^{H,H}$ Complexes

The first scorpionate ligands made with 1,2,4-triazole rings were reported in 1967 by Trofimenko [3]. The unsubstituted $KTtz^{H,H}$ was prepared from triazole and KBH_4, and $KTtz^{H,H}$ was treated with Co(II) without further purification. This initial report described the $Co(Ttz^{H,H})_2$ complex as being water soluble, presumably due to the six extra nitrogens relative to $Co(Tp^{H,H})_2$. Subsequent papers reported other homoleptic Ttz complexes (also referred to as sandwich complexes herein), specifically a 1991 report presented $(Ttz^{H,H})_2M$ (M = Mn, Fe, Co, Ni, Cu, Zn, and Cd) complexes (Fig. 2b), that were monomeric or were coordination polymers in which the four position N binds to an additional metal atom (exopolydentate) (Fig. 2a) [4]. While the propensity of this ligand for formation of coordination polymers was first mentioned based on solubility observations [4], extensive structural characterization came later in the papers by Janiak, discussed below. The homoleptic complexes of transition metals with $Ttz^{H,H}$ will be described first, with an emphasis on what these studies teach us about the features of the Ttz ligand class, followed by the use of $Ttz^{H,H}$ for formation of supramolecular structures.

Evidence of the unique role of the remote nitrogen in tris(triazolyl)borate complexes comes from a combined X-ray crystallography and theoretical study

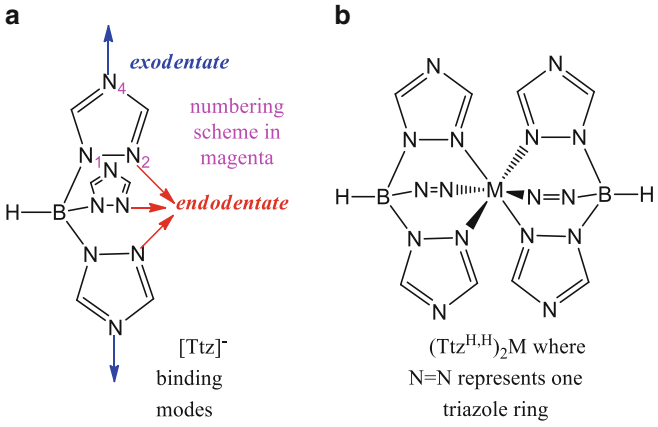

Fig. 2 (**a**) Ttz ligand showing endodentate and exodentate coordination and (**b**) homoleptic, bis ligand complexes of the Ttz ligand

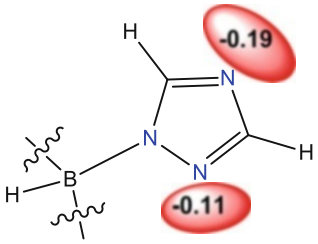

Fig. 3 Picture showing the location of electron density and charge on N-2 and N-4 of triazole within $Ttz^{H,H}$. Schematic drawing is similar in content to figure in [5]

by Janiak [5]. An AM-1 calculation shows that the four position N in $[Ttz^{H,H}]^-$ has more charge on it (−0.19) than the two position nitrogen (−0.11) (Fig. 3). This was later confirmed by ^{15}N NMR on potassium salts of the Ttz and Btz ligands [6]. Nonetheless, it is N-2 that usually coordinates to the metal (as it does here), presumably due to formation of an ideal chelate ring size of six atoms.

Janiak has also explored the use of tris(tetrazolyl)borate complexes (Fig. 4), which are actually less suitable for exodentate hydrogen bonding interactions due to anionic charge being more spread out (cf. Fig. 3), according to calculations [5]. Also, tris(tetrazolyl)borate ligands do not allow for any steric encumbrance at the three position, and they typically form coordination polymers with the transition metals explored thus far.

Thus Ttz ligands seem ideal for construction of chelates from nitrogen-containing heterocycles with a proclivity for both endodentate and exodentate interactions. The exodentate interactions are most commonly to another metal (to form multimetallic species or coordination polymers) or to protons, either as H^+ or an acidic, bound hydrogen. As the steric bulk at the three position increases, we see the nature of the exodentate interaction shift from interactions with metals towards interactions with the much smaller hydrogen atoms.

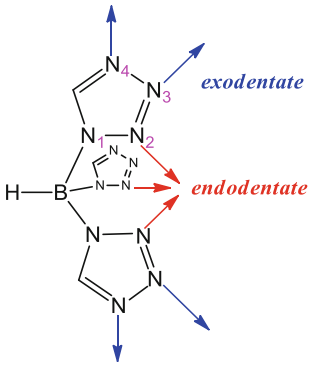

Fig. 4 The tris(tetrazolyl) borate ligand

The concept of using protonation of the triazole rings within $Co(Ttz^{H,H})_2$ to control the geometry at the metal was first put forward in 1972 [7]. An ^{1}H-NMR study showed how increasing the acid concentration (D_2SO_4/D_2O ratio) changed the chemical shift of the coordinated triazole rings in Ttz. This was interpreted as being indicative of a change in binding mode within $Co(Ttz^{H,H})_2$ due to triazole arms coming off the metal and being partially displaced by solvent coordination. It was also suggested that acid causes this change by binding D^+ to the exodentate nitrogens thereby modulating the donor properties of the triazole rings. This study was complicated by the fact that acid cleaves B–N bonds and the author notes partial decomposition of the Ttz ligands. However, the authors believe that they could distinguish free triazole from uncoordinated Ttz arms based on different chemical shifts.

In general, the molecular chelate complex, $M(Ttz^{H,H})_2$, is favored for M = Fe, Co, Ni, and Cu(II) [8]. With M = Mn, a 1D coordination polymer results, and while Zn can form the molecular chelate complex or the 3D coordination polymer, the 3D coordination polymer is thermodynamically favored. This trend is related to the Irving Williams series, which describes how ligand field stabilization energy (LFSE) increases from Mn through Cu, and is lowest for Mn and Zn(II) [9]. Thus the coordination of N-4, which has the most negative charge, should be thermodynamically favored [8]. So, coordination of N-4 is sometimes realized for Mn and Zn (II) since the lack of LFSE for d^5 and d^{10} metals means that achieving octahedral geometry is not paramount and other geometries are possible as the ligand binding to these metals is primarily ionic. The formation of thermodynamically disfavored mononuclear $(Ttz)_2M$ complexes with M = Mn, Zn (II) can be attributed to kinetic control of recrystallization. If the first N to coordinate to the metal is an endodentate N, then this will favor formation of the molecular chelate complex as the kinetic product (Fig. 5). Similarly, initial coordination of the exodentate N favors coordination polymer formation (see [8] for more details).

With copper, initial studies reported the molecular chelate complex $Cu(Ttz^{H,H})_2$, but later studies using $Co(Ttz^{H,H})_2$ as a starting material for transmetallation with $CuCl_2$ produced copper (II) containing Ttz coordination polymers [10]. Depending on the reaction time, either a 2D or a 3D coordination polymer was formed. The 3D coordination polymer structure is interesting from a biomimetic perspective

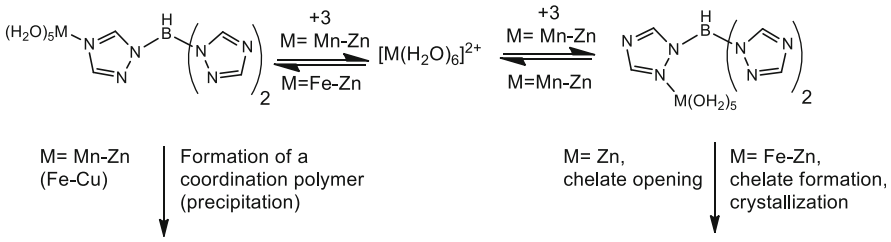

Fig. 5 An equilibrium between exodentate and endodentate coordination modes controls the recrystallization product obtained. Reproduced from [8]

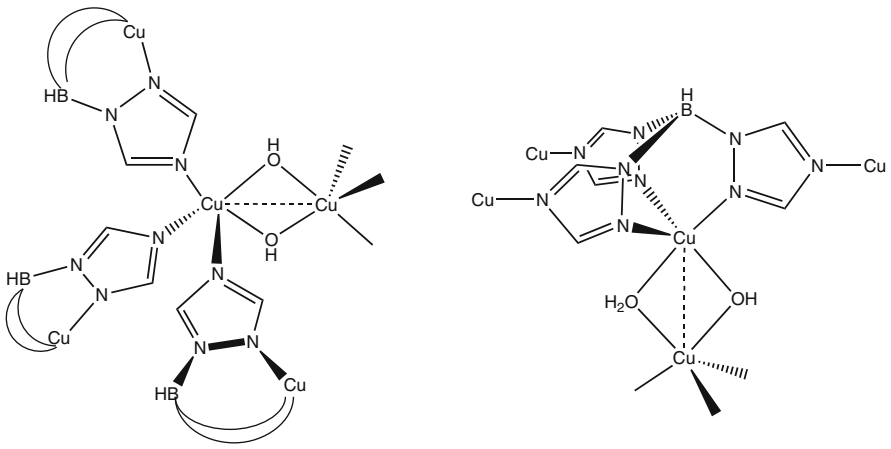

Fig. 6 This shows the coordination environments around the coppers in the 3D coordination polymer, $[[Cu_2(\mu_4\text{-Ttz})(\mu\text{-OH})_2]Cl{\bullet}6H_2O]_n$ (modified from [10])

(Fig. 6). There are two unique Cu environments. In one environment Cu ions are bridged by OH groups ($Cu(\mu\text{-OH})_2Cu$) and each Cu is coordinated by three exodentate Ns. In the second environment, the two Cu ions are bridged by OH and aqua ligands and each Cu is coordinated to three endodentate Ns. These structures are reminiscent of various binuclear enzymes and proteins that feature ligation of three histidines to each metal, including hemocyanin [11].

Furthermore, these studies show that hydrogen bonds in Ttz complexes can provide a design principle that allows (in some situations) control of the structure formed. Most of the molecular chelate complexes (e.g., $[M(Ttz^{H,H})_2]{\bullet}6H_2O$ where M = Fe, Co, Ni, Zn, and $Cu(Ttz^{H,H})_2{\bullet}4CH_3OH$) form hydrogen bonds to either methanol or water [12, 13]. In these octahedral complexes that form hydrates, N-4 is hydrogen bonded to water molecules that crystallize in 2D layers (Fig. 7) [5]. These solid state structures can be described as clathrates that show water in a semi-organized state, in between a few water molecules and bulk water [5]. This has allowed a detailed study of the phase transitions (from liquid to solid) and the structure of water in 2D layers that exist between layers of $Ni(Ttz^{H,H})_2$ [14]. The electron-withdrawing effect of the extra N enhances the acidity of C–H bonds of the triazole, such that weak [15] C–H···O hydrogen bonds can form [16].

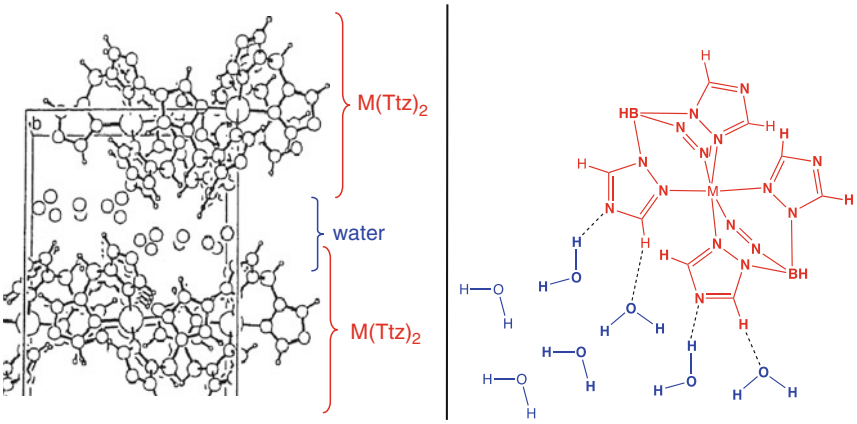

Fig. 7 The isomorphous structures $M(Ttz)_2$ where M = Fe, Co both show 2D water layers between metal complex layers. The *left hand section* is reproduced from [5] and modified. The *right hand section* is a schematic diagram showing hydrogen bonds

Further studies of $[M(Ttz^{H,H})_2]$ (M = Fe, Co) indicated that the Ttz complexes, relative to the Tp complexes, are slightly weaker σ donors, and much weaker π donors (in fact they are often π acceptors) [6]. This causes a slight shift in the UV–vis absorbance (528 vs. 533 nm for L_2Fe with L = Tp and Ttz, respectively), but a more dramatic change in the oxidation potential for the Fe(II/III) couple as measured by CV (from 185.5 to 920.5 mV). Thus the Ttz complexes are much more difficult to oxidize, due to an electron-withdrawing effect. There was a similar shift in oxidation potentials for L_2Co complexes when L is changed from Tp to Ttz. This can be used to trap metalloradicals or other species in oxidation states that are unstable for Tp complexes (see below, e.g., $Ttz^{Me,Me}$ was used to isolate and characterize Mo(V) species [17]).

Sandwich complexes of Ttz can be used as "metalloligands" since the exodentate Ns can coordinate to other metals. The arrangement of these nitrogens is in a trigonal antiprism, and lends itself to formation of 3D coordination polymers. Ko, Jun, et al. used $[Ttz^{H,H}{}_2Fe^{III}](ClO_4)_3 \bullet xH_2O$ as a water soluble starting material for the formation of $[Ttz^{H,H}{}_2Fe^{II}][Rh_2(OAc)_4]_3 \bullet x(\text{solvent})$ which has an unusual topological structure and is the first bimetallic coordination polymer made from the Ttz ligand class (Fig. 8) [18]. The source of reducing equivalents that resulted in formation of Fe(II) in this reaction is unclear, although the borate ligand is the proposed reducing agent. XAS and magnetic studies confirm that Fe(II) is formed. The Fe/Rh 3D coordination polymer is potentially very interesting for giving a measure of how Rh coordination changes the electron donor properties of the triazole rings; in this structure the $Fe–N_{endo}$ distances are 2.007(3) Å. Unfortunately, $Fe(Ttz^{H,H})_2$ (solvent free) has not been made, but $Fe(Ttz^{H,H})_2 \bullet 6H_2O$ shows $Fe–N_{endo}$ distances of ~1.99 Å [5], and thus water and Rh coordination to N_{exo} have similar influences on donor strength, at least as measured crystallographically. Similarly, $[Ttz^{H,H}{}_2Fe^{II}][Mn^{III}(salen)]ClO_4 \bullet 2CH_3CN \bullet CH_3OH$ forms a 1D

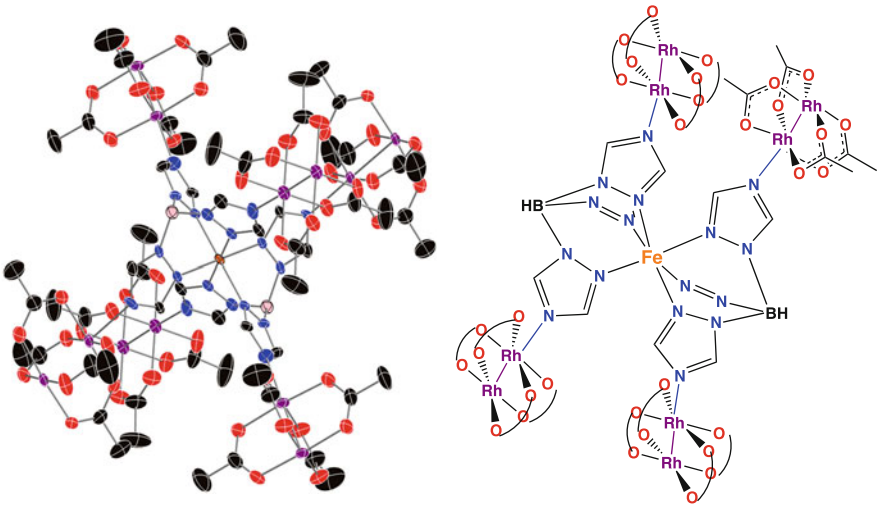

Fig. 8 *Left hand section* shows the structure of $[Ttz^{H,H}{}_2Fe^{II}][Rh_2(OAc)_4]_3 \bullet x$(solvent) with solvent molecules and hydrogens omitted for clarity. Color code: Fe *orange*, Rh *purple*, N *blue*, O *red*, B *pink*, C *black* [18]. *Right hand section* shows schematic diagram; all triazole rings have exodentate N to Rh interactions, but only four are shown for clarity

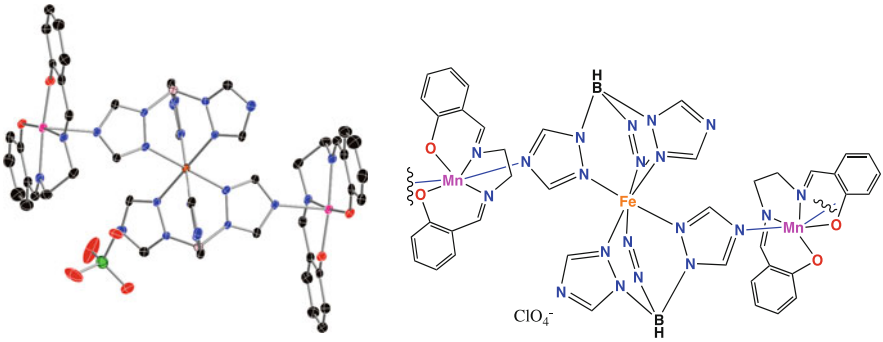

Fig. 9 *Left hand section* shows the monomeric unit that forms the 1D coordination polymer of $[Ttz^{H,H}{}_2Fe^{II}][Mn^{III}(salen)]ClO_4 \bullet 2CH_3CN \bullet CH_3OH$ with solvent molecules and hydrogens omitted for clarity**.** Color code: as in Fig. 8 plus Mn *magenta*, Cl *green*. *Right hand section* shows a schematic diagram; exodentate bonds are in blue and these show that the coordination polymer extends beyond this diagram via further Mn to $Ttz^{H,H}$ interactions

coordination polymer with exodentate N's bound to Mn (Mn–N_{exo} ~2.3 Å) [19]. In this structure, Fe–N distances range from ~1.97–2.02 Å, and surprisingly the Mn (exodentate) bound triazole rings do not consistently give the longest Fe–N_{endo} distances. This may have to do with packing arrangements and the placement of ClO_4^- ions (Fig. 9).

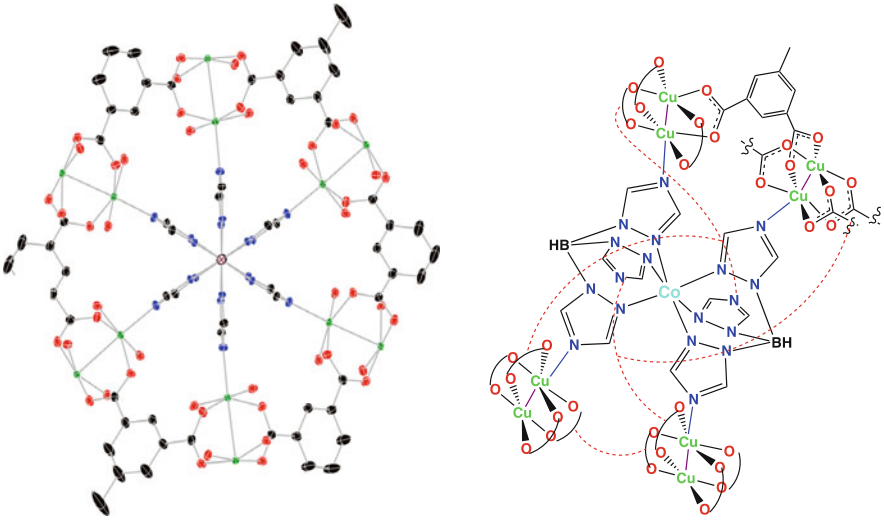

Fig. 10 *Left section* shows the MOF complex built of Co and Cu units. $Co(Ttz^{H,H})_2$ is in the center, viewed down the B-M-B axis. Paddlewheel $Cu_2(CO_2)_4$ are shown, and these connect to other $Co(Ttz^{H,H})_2$ units (not shown). B in *pink*, Co in *aqua blue*, Cu in *green*, O in *red*, N in *blue*, and C in *black*, hydrogens omitted for clarity [20]. *Right section* shows a simplified schematic drawing of the same structure, from a different angle. The *red dashed lines* show how the 5-methyl-isopthalate links triazole rings within one $Co(Ttz^{H,H})_2$ unit, and also links to other Co $(Ttz^{H,H})_2$ units that are not shown (〰)

This concept has been recently extended to the creation of a magnetic metal organic framework (MOF) complex, via the use of $[Co(Ttz^{H,H})_2]$ as a metalloligand that coordinates to Cu(II) [20]. Each $[Co(Ttz^{H,H})_2]$ coordinates to six Cu(II) ions, and these Cu(II) ions are in $Cu_2(CO_2)_4$ paddlewheel units (CO_2 is from 5-methyl-isopthalate) (Fig. 10). Solvent can be removed from this high surface area 3D nanoporous bimetallic framework, and solvent absorption and desorption change the magnetic properties from paramagnetic to exhibiting short-range magnetic order.

Formation of 1:1 complexes with Ttz and first row transition metals has required the use of soft Cu(I) and bulky co-ligands [21]. For example, $(Ttz^{H,H})Cu(R_3P)_n$ complexes ($n = 1, 2$) formed readily as mononuclear (Fig. 11a) or 1D coordination polymer structures. The coordination polymer formed featured an uncoordinated triazole ring, and two triazoles bridging through N-4 (Fig. 11b). A subsequent study used Tp, Ttz, and tris(pyrazolyl)methane sulfonate (Tpms) complexes of Cu(I) with a water soluble phosphine ($PPh_2(p\text{-}C_6H_4COOH)$) to measure superoxide scavenging activity [22]. Among the Cu(I) complexes, Tpms performed the best, $Tp^{Me,Me}$ was among the worst, but all (including Ttz) degraded superoxide fast enough to be considered useful for in vivo studies. Thus, these Cu(I) complexes should be further investigated mechanistically as superoxide dismutase (SOD) mimics that may be useful for preventing biological damage from reactive oxygen species.

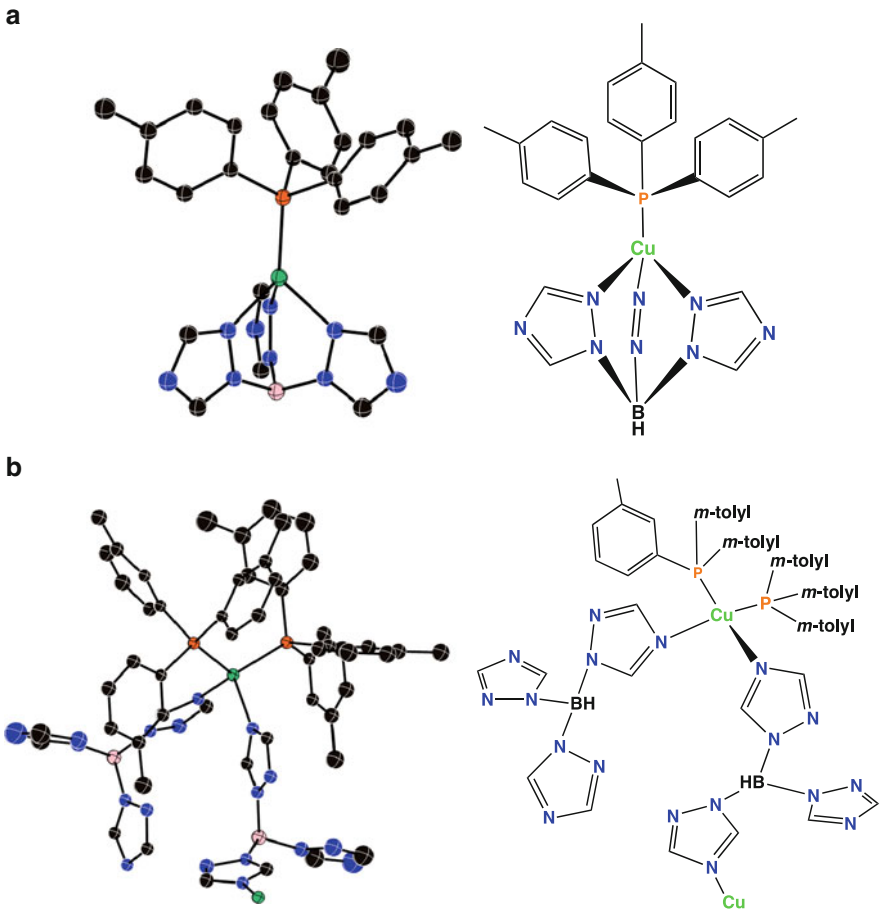

Fig. 11 (**a**) The mononuclear complex, $(Ttz^{H,H})Cu(p\text{-}tolyl_3P)$. (**b**) The coordination polymer formed from $(Ttz^{H,H})Cu(Ar_3P)_2$ where Ar = *m*-tolyl. For both (**a**) and (**b**): crystal structure is on *left*, and schematic drawing is on *right*, with Cu in *green*, P in *orange*, N in *blue*, B in *pink*, and C in *black*, hydrogens omitted for clarity

Unsubstituted Ttz (and Tp) ligands commonly form six- and seven-coordinate molybdenum complexes. Piano stool complexes $LMo(CO)_2(S,S)$ have been reported, where S,S is dithiocarbamate and L is $Ttz^{H,H}$ or $Tp^{H,H}$ (Fig. 12). The seven-coordinate complex is stabilized with L = Ttz due to its small size and relatively weak electron donor properties [23]. Surprisingly, the substitution of Tp with Ttz not only increases CO stretching frequencies in the IR (in accordance with Ttz being a weaker donor), but also significantly changes the geometry of the dithiocarbamate ligand (Fig. 12). A later study reported that $[LMo(CO)_3]^-$ (L = $Ttz^{H,H}$, $PhB(1,2,4\text{-triazolyl})_3$, and other Tp ligands) complexes react with electrophiles (E) to give $LMo(CO)_3E$ [24].

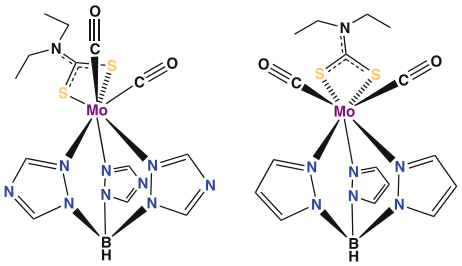

Fig. 12 $LMo(CO)_2(S,S)$ complexes, where S,S is dithiocarbamate and L is $Ttz^{H,H}$ (*left*) and $Tp^{H,H}$ (*right*)

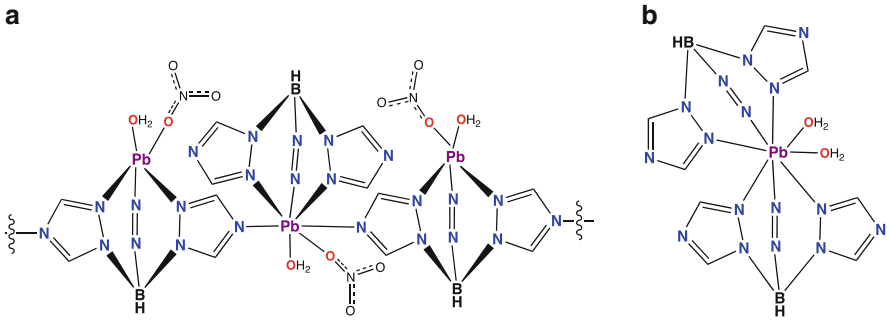

Fig. 13 (**a**) A truncated structure of the coordination polymer of $(Ttz)Pb(NO_3)(H_2O)$ that slowly adds water to form (**b**) $(Ttz)_2Pb•2H_2O$. In diagram (**a**), a vacant coordination site is occupied by a stereochemically active lone pair

Furthermore, studies with Ca, Sr, and Pb are relevant to biology, but these metals are usually not found playing a catalytic role in enzyme active sites. The various geometries that can be obtained by Pb are relevant to understanding lead toxicity, and how lead displaces zinc in catalytic and structural sites in biological enzymes and proteins. Particularly interesting is the observation that unlike six-coordinate Tp_2Ca and Tp_2Pb complexes, eight-coordinate complexes are observed with $Ttz_2M•2H_2O$ (M = Ca, Sr, Pb) [25]. This increase in coordination number between Tp and Ttz complexes is attributed to the more ionic nature of Ttz complexes, and it is also worth noting that waters of crystallization are hydrogen bonded to neighboring triazole rings through the exodentate nitrogens. This Pb complex of Ttz (Fig. 13b) has a stereochemically inactive lone pair, in contrast to Tp_2Pb which has a stereochemically active lone pair. During the recrystallization, an intermediate was observed that slowly (over several days) added water to form the structure in Fig. 13b as the final product. The intermediate had a seven-coordinate lead and a stereochemically active lone pair (Fig. 13a). In contrast, one study reports ($Ttz^{H,H}$) M'Cl complexes (M' = Hg, Pb, VO) which suggests much lower coordination numbers if these are monomeric, but structural data are not reported [4].

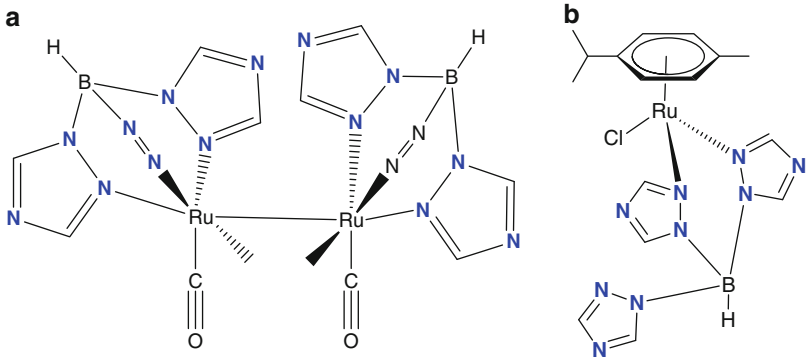

Fig. 14 (**a**) Structure of $[RuTtz^{H,H}(CO)_2]_2$. (**b**) Structure of (cymene)RuCl(κ^2-Ttz)

Studies of the $Ttz^{H,H}$ ligand with non-biological metals have included the use of Ru [26], Ag [27, 28] (in particular for the complexes unusual optical properties [29]), and Ir (in κ^2 complexes that are potentially useful for light-emitting devices [30]). While the details are beyond the scope of this work, the insight into the differences between Tp and Ttz ligands are relevant here. Structural and spectroscopic studies of $[RuTtz^{H,H}(CO)_2]_2$ (Fig. 14a), which contains a metal–metal bond, show that triazole is a very good π acceptor [26]. Our group has found that (arene) RuCl(κ^2-Ttz) (Fig. 14b) complexes are useful as transfer hydrogenation catalysts that function under base-free conditions and have good solubility in isopropanol [31]. Indeed, the solubility of Ttz complexes makes them suitable for application in water and alcohols, and in some cases Ttz (and Btz) compounds can even be the solvent! Ionic liquids formed as $[imidazolate]^+[Ttz]^-$ salts have been explored as solvents with high stability, low melting points, and good solubility properties [32].

These Ttz complexes are effective for mimicking active sites in enzymes when the metal has a natural preference for coordination numbers similar to those found in biological systems. But for many metals and oxidation states, coordination numbers are too high for catalytic chemistry. Therefore, greater steric bulk is needed to produce divalent first row transition metals with coordination numbers four or five, and for octahedral complexes of Mo that do not dimerize or aggregate.

2.1.2 $Ttz^{Me,Me}$ Complexes

In biology, the amino acids in the enzyme active sites serve to isolate and restrict movement of bound metal ions, such that reactive metal species cannot dimerize or aggregate. Thus, unsubstituted Tp and Ttz ligands are typically unsuitable for biomimetic chemistry, at least with hard metal ions that favor high coordination numbers. With first row divalent transition metals, unreactive octahedral L_2M complexes predominate. With Mo, octahedral complexes of Mo(VI) and Tp could be formed and are good structural models for many enzyme active sites, but upon reduction to Mo(V), as occurs in biology, decomposition reactions prevented the observation of biologically relevant processes such as oxo transfer and proton coupled electron transfer [33–35].

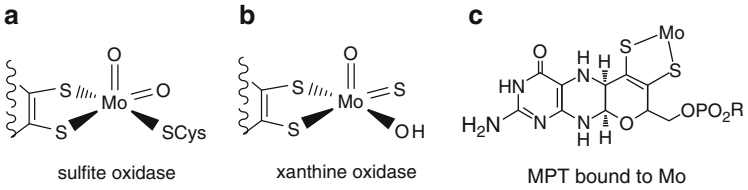

Fig. 15 Selected molybdenoenzyme active sites and the MPT cofactor

Methyl substituents at the 3 and 5 positions in $Ttz^{Me,Me}$ provide sufficient steric bulk to prevent undesirable side reactions from occurring in Mo complexes. Young et al. synthesized $K(Ttz^{Me,Me})$ in 79% yield from KBH_4 and the corresponding triazole, using a high temperature melt reaction as Trofimenko developed for the synthesis of Tp and its derivatives [36]. This ligand was used to synthesize $NEt_4[Ttz^{Me,Me}Mo(CO)_3]$, a six-coordinate Mo(0) complex which ν(CO) bands in the IR at 1,900 and 1,765 cm^{-1} in solution. The corresponding Tp complex, $NEt_4[Tp^{Me,Me}Mo(CO)_3]$, has bands at 1,891 and 1,751 cm^{-1}. Thus Ttz is a weaker electron donor than Tp and there is less Mo d to CO π^* backbonding in the Ttz complex. These changes are modest enough to be undetectable by crystallography, but the reactivity differences are quite significant and allow the isolation of reactive species, as discussed below. Like Tp and Ttz, $Ttz^{Me,Me}$ can also form seven-coordinate Mo complexes upon oxidation with I_2 resulting in $Ttz^{Me,Me}Mo^{II}(CO)_3I$.

The formation of *cis* dioxo- or *cis* thio,oxo- Mo(VI) complexes provides an entry point into biomimetic chemistry. Several enzymes, including xanthine oxidase and sulfite oxidase, use this motif for O atom transfer (Fig. 15). While the use of Tp or Ttz, both tridentate N donors, as a surrogate for the MPT dithiolene cofactor (Fig. 15c) is at first glance counterintuitive, the facial coordination of these N_3 ligands forces two oxo ligands *cis*, and also blocks dimerization of reactive intermediates when sufficient steric bulk is provided. The *cis* arrangement of oxo groups is essential for catalysis. In sulfite oxidase, the mechanism of sulfite oxidation to sulfite is believed to occur as follows (starting from top of Fig. 16): (1) $Mo^{VI}(=O)_2$ transfers an oxo to sulfite, (2) a reduced species, $Mo^{IV}(=O)OH_2$ is formed that loses one e^- and one H^+ (proton coupled electron transfer, PCET) to produce $Mo^{V}(=O)(OH)$, and (3) $Mo^{V}(=O)(OH)$ then does a second PCET to return to the starting $Mo^{VI}(=O)_2$ species (Fig. 16) [11]. Significantly, $(Tp^{Me,Me})Mo^{VI}O_2(SPh)$ is a model that allows observation of all processes in this cycle, and spectroscopic observation of all of the key intermediates [33].

However, for clean isolation and crystallographic characterization of Mo(V) species, $Ttz^{Me,Me}$ proved necessary. $LMo^{VI}O_2X$ (L = $Tp^{Me,Me}$, Tp^{iPr}, and $Ttz^{Me,Me}$; X = Cl, Br, NCS, OMe, OEt, OPh, S^{i}Pr, SPh, SCH_2Ph) complexes underwent electrochemical reduction to give Mo^V species that were observed by EPR [37]. In many cases the reduction was reversible, if solvents were thoroughly dried to prevent $Mo^{V}(=O)_2$ from being protonated. With L = $Ttz^{Me,Me}$, the electron-withdrawing properties of the ligand allow it to be reduced at less negative potentials, relative to the Tp Mo^{VI} complexes [38]. Remarkably, due to the reduced

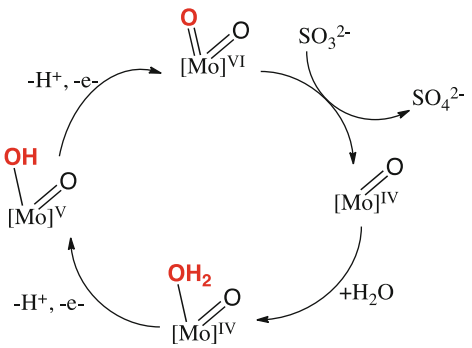

Fig. 16 Catalytic cycle for enzymatic sulfite oxidation. Here, [Mo] represents the Mo complex in sulfite oxidase with dithiolene and cysteinate ligands ($[Mo]^{VI}(=O)_2$, *top*, is as in Fig. 15a)

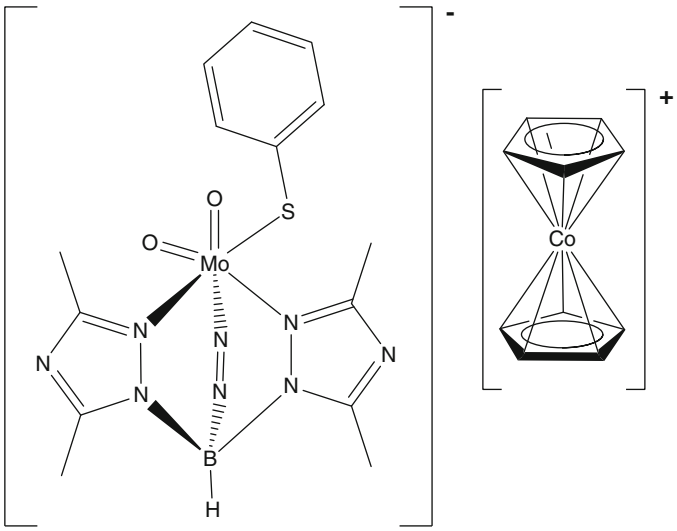

Fig. 17 The species $[Ttz^{Me,Me}Mo^{V}O_2SPh]^-$ $[Cp_2Co]^+$, in which the Mo complex is an anion radical.[17]N=N represents the third triazole ring

basicity of the oxo groups, $Mo^{V}(=O)_2$ was stable, even in the presence of wet solvents (it did react with air and electrophiles), and a crystal structure was obtained on the radical $[Cp_2Co]^+[Ttz^{Me,Me}Mo^{V}O_2SPh]^-$ (Fig. 17) [17]. This radical shows a lengthening of the Mo–O bonds that is consistent with repulsion between the d^1 electron and the Mo = O π bonds, and it shows a characteristic EPR spectrum. Such $Mo^{V}O_2$ species are not believed to occur in enzymes as $Mo^{V}O_2$ with biological ligands would be quite basic and EPR signals for such species have not been observed biologically. With the $Tp^{Me,Me}$ ligand, $(Tp^{Me,Me})Mo^{V}(=O)(OH)(SPh)$ was observed as a coprecipitate by EPR and is a good model for Mo^{V} in molybdenoenzymes (e.g., species on the left of Fig. 16) [38]. Furthermore, some of

these dioxo complexes readily exchange oxo for thio and create Mo(=O)(=S) species as analogs for xanthine oxidase [37].

Thus, prior to our work, the $Ttz^{Me,Me}$ ligand had only been used with Mo. We have recently used this ligand to make $(Ttz^{Me,Me})_2Co$ [39] and (η^6-arene)RuCl(κ^2-$Ttz^{Me,Me}$) complexes (structure similar to that in Fig. 14b) [31]. This ligand appears underutilized and can perhaps lead to interesting and rich chemistry with second and third row transition metals. It may also support reactivity studies with Cu(I), which seems soft enough to bind just one Ttz ligand, leaving an open site for catalytic chemistry. In our hands, the syntheses of 3,5-dimethyl-1,2,4-triazole and the ligand, $Ttz^{Me,Me}$, are both low yielding, and this could explain the paucity of studies with this ligand. Young et al. discuss the difficulty of reproducing literature yields of the triazole (they report 23% and the literature reports 63%) [36].

2.1.3 $Ttz^{CF3,CF3}$ Complexes

Fluorinated and halogenated Tp ligands ($Tp^{ArF,}$ Tp^{RF}, Tp^{X}) form complexes with Cu^I and Ag^I that activate small molecules (e.g., dioxygen) [40] and serve as potent electrophilic catalysts for C–H functionalization [41, 42]. Particularly noteworthy are the studies by Pérez and coworkers which demonstrate that ($Tp^{RF,ArF}$)Ag can activate methane in supercritical CO_2 [43]. The electron-withdrawing nature of halogens can be combined with weak donor Ttz ligands for even weaker donor ligands (Ttz^{RF}). Dias and coworkers have used fluorinated Tp and Ttz ligands to isolate rare species with late transition metals. In particular they have made progress at isolating complexes of the unreactive coinage metals (Ag, Au, Cu) in low-coordinate, sterically encumbered environments [44]. The new ligand $Ttz^{CF3,CF3}$ was synthesized in 2009 and has been used to form Na, Cu, and Ag complexes (Fig. 18) [45]. An unusual complex anion $[Na(Ttz^{CF3,CF3})_2]^-$ (Fig. 18a) was isolated as the salt of $[Na(THF)_6]^+$, and this anion features an octahedral sodium and is analogous to sodocene $[Cp_2Na]^-$.

Surprisingly, $(Ttz^{CF3,CF3})M^ICO$ (M = Cu, Ag) (Fig. 18b for Cu complex, Ag complex is similar) complexes show that the CO stretching frequencies are insensitive ($\Delta\nu$ = 0–1 cm^{-1}) to the change in ligand from $Tp^{CF3,CF3}$ [46]. A change of 10–20 cm^{-1} is expected just for swapping pyrazole for triazole from both the $[(Ttz^{Me,Me})Mo(CO)_3]^-$ experiments described above and from the $(Ttz^{tBu,Me})$CuCO experiments to be described below [47]. The gas phase acidities (calculated by DFT) of 3,5-$(CF_3)_2$-triazolium and 3,5-$(CF_3)_2$-pyrazolium suggest that the triazoles are weaker donors [45]. Thus, Dias et al. propose that the CO stretching frequencies are an insensitive measure of electron donor properties for metal complexes that are very electron poor (specifically when ν(CO) for the complex is near that of free CO). Consistent with this explanation, other experimental measures of donor ability including ^{1}H- and ^{13}C-NMR chemical shifts for $(Ttz^{CF3,CF3})M^I(\eta^2$-$CH_2CH_2)$ (M = Cu, Ag) (Fig. 18c for Ag complex, Cu complex is similar) show that the triazole rings are weaker electron donors, and this results in more Lewis acidic metal complexes than seen with fluorinated pyrazole ligands ($Tp^{CF3,CF3}$) [46]. These $Ttz^{CF3,CF3}$ ethylene

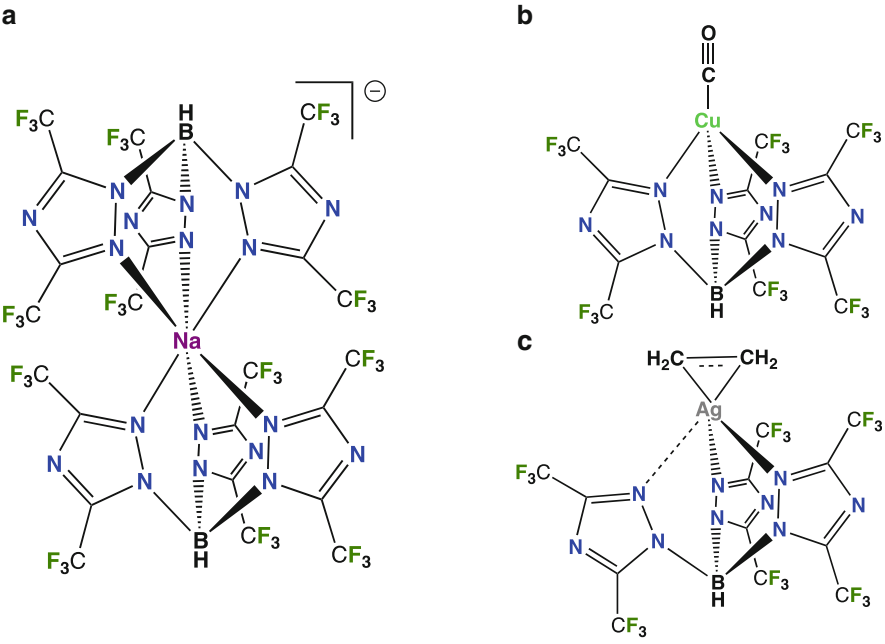

Fig. 18 (**a**) $[Na(Ttz^{CF3,CF3})_2]^-$, (**b**) $(Ttz^{CF3,CF3})Cu^{I}CO$, (**c**) $(Ttz^{CF3,CF3})Ag^{I}(\eta^2\text{-}CH_2CH_2)$

complexes also show a κ^2-distortion, wherein there are two short M–N bonds and one long M–N bond, and this distortion is largest with Cu.

In one example, $Ttz^{CF3,CF3}$ supports exodentate coordination through the four position nitrogen, and triazole thereby bridges two metal centers [46]. $[Ag(Ttz^{CF3,CF3})]_n$ is a coordination polymer, wherein each Ag is tetrahedral with three endodentate nitrogens from one ligand, and one exodentate N from a neighboring ligand (Fig. 19). The shortest Ag–N bond is actually an $Ag–N_{exo}$ interaction, in accord with the fact that this N usually has more negative charge on it (as Janiak showed above, Fig. 3). The longest interaction is the $Ag–N_{endo}$ bond, wherein N_{endo} comes from the bridging triazole, which may reflect how Ag coordination to the exodentate site removes electron density from that triazole ring. This suggests that it may be possible that these exodentate interactions can be used to control or catalyze chemical reactions, and that Ttz and fluorinated Ttz ligands can result in a very Lewis acidic metal appropriate for activation of strong bonds.

2.1.4 $Ttz^{Ph,Me}$ Complexes

An increase in steric bulk by placing phenyl rings at the three position, in $Ttz^{Ph,Me}$, increases the propensity for 1:1 complexes with first row transition metals, and decreases propensity for formation of coordination polymers. The hydrophobicity of the phenyl rings also leads to decreased water solubility, but the solubility properties of these complexes are still good in water/alcohol mixtures [48].

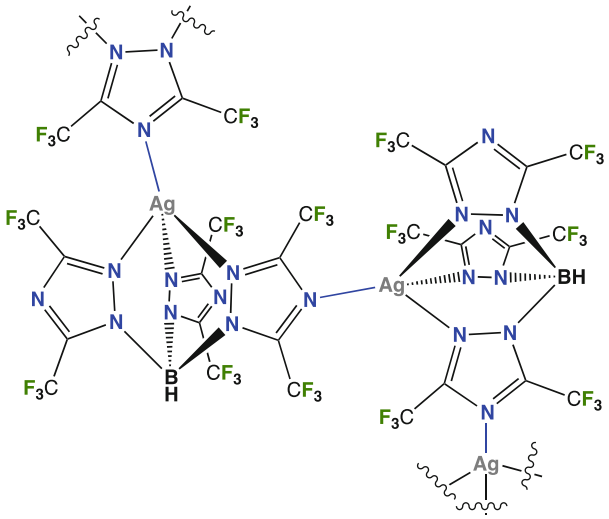

Fig. 19 A truncated section of the coordination polymer, $[Ag(Ttz^{CF3,CF3})]_n$. Exodentate N to silver bonds are shown in *blue*, and these form a 1D network

With zinc, tetrahedral complexes can be formed, including $(Ttz^{Ph,Me})ZnX$, where X = Cl [48], Br, Et (Fig. 20a, b) [39, 49]. Furthermore, the tetrahedral zinc alkyl complex, $(Ttz^{Ph,Me})ZnEt$ (Fig. 20b), is stable, but reacts with water to form a homoleptic complex, $(Ttz^{Ph,Me})_2Zn$ (Fig. 20c) [49]. $(Ttz^{Ph,Me})ZnEt$ also reacts with various (anhydrous) acids to form four- or five-coordinate complexes of the conjugate base (CB): $(Ttz^{Ph,Me})Zn(CB)$ [50]. Despite the fact that alkyl zinc complexes are known be very reactive towards acids and water (see references in this paper [49]), the protonolysis of these $Ttz^{Ph,Me}$ zinc alkyls was slow (often requiring days) and likely indicates some steric protection of the metal center by the ligand [50]. The chemistry of related zinc alkyl complexes with water is discussed below, in Sect. 3 wherein we describe our efforts to form biomimetic LZnOH complexes. However, when a suitable co-ligand is not present, e.g. from reaction of $Zn(ClO_4)_2 \cdot 6H_2O$ and $K(Ttz^{Ph,Me})$, the six-coordinate $(Ttz^{Ph,Me})_2Zn$ complex is formed (Fig. 20c) [39].

This propensity for forming octahedral complexes is further enhanced with the divalent first row metals, Mn through Cu [39]. Regardless of the metal to ligand ratio used or the presence of co-ligands, the stoichiometry of the major metal complex observed is always 1:2. The $(Ttz^{Ph,Me})_2$ M complexes (M = Mn, Fe, Co, Ni, Cu(II); Fig. 20c) were characterized by spectroscopic and crystallographic means, and these complexes show that while the phenyl rings are able to interdigitate the steric bulk causes distortions away from octahedral symmetry [39]. With both Ni and Cu(II), rearranged products are also observed, wherein the phenyl and methyl substituents are in swapped positions (5 and 3, respectively) in one triazole ring, this ligand is designated as $Ttz^{Ph,Me}*$. The side products formed are $(Ttz^{Ph,Me}*)_2Cu$ and $(Ttz^{Ph,Me}*)Ni(Ttz^{Ph,Me})$, and the formation of these products appears to be driven by achievement of shorter M–N distances and more perfectly octahedral bond angles (see Cu complexes Fig. 21) [39]. The shorter M–N bond distances allows Ni and Cu to maximize ligand

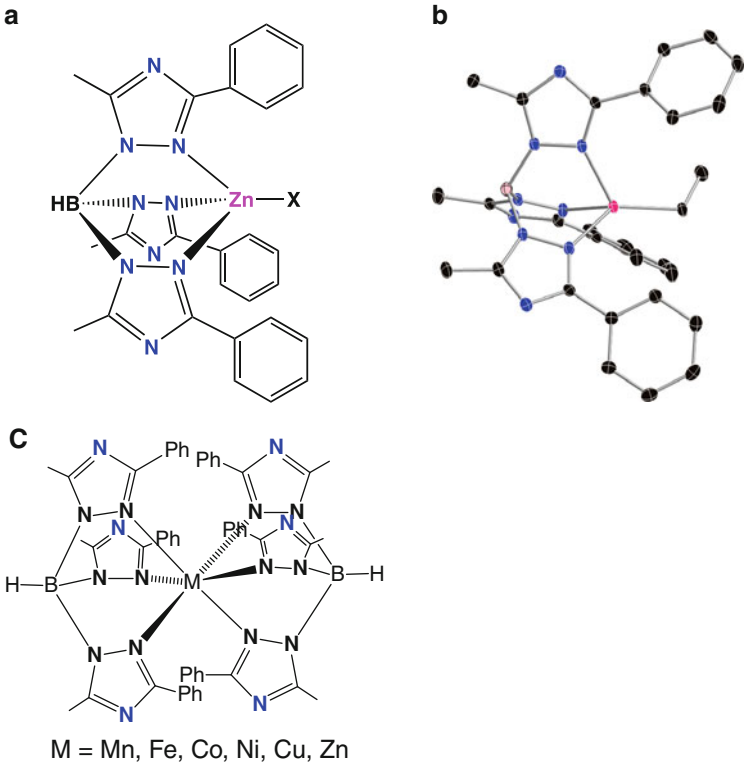

Fig. 20 (**a**) ($Ttz^{Ph,Me}$)ZnX. (**b**) ($Ttz^{Ph,Me}$)ZnEt crystal structure, with hydrogen atoms omitted for clarity, color code: B = *pink*, C = *black*, N = *blue*, Zn = *magenta*. (**c**) $(Ttz^{Ph,Me})_2$ M complexes

field stablilization energy, which is greatest for these metals due to their electronic configurations and is reflected in the Irving Williams series [9]. The presence of two isomers for the Ni and Cu sandwich complexes, which differ only in the sterics of one or two triazole rings, has allowed for a study of how subtle changes in geometry influence electronic properties, as manifested in the EPR and UV–vis spectra. EPR spectra for a series of Co complexes of Ttz, with varying steric bulk, suggest that Ttz engages in π bonding interactions with the metal; this is remarkable since Tp is primarily a sigma donor [39, 51]. The rearrangement of one triazole ring puts one methyl group at the three position and apparently gives a stronger field ligand with concomitant UV–vis spectroscopic changes [39].

As an aside, we have also observed $Ttz^{Ph,Me}$ rearrangement in (η^6-arene)RuCl (κ^2-$Ttz^{Ph,Me}$*) complexes [31], and here too the rearrangement is apparently driven by steric pressure.

During the isolation of the sandwich complexes of Ni described above, ($Ttz^{Ph,Me}$)NiCl(OH_2) (Fig. 22) was also isolated as a minor product and characterized crystallographically [39]. This five-coordinate complex is not coordinatively saturated and could provide a functional mimic for hydrolytic Ni enzymes, including ureases.

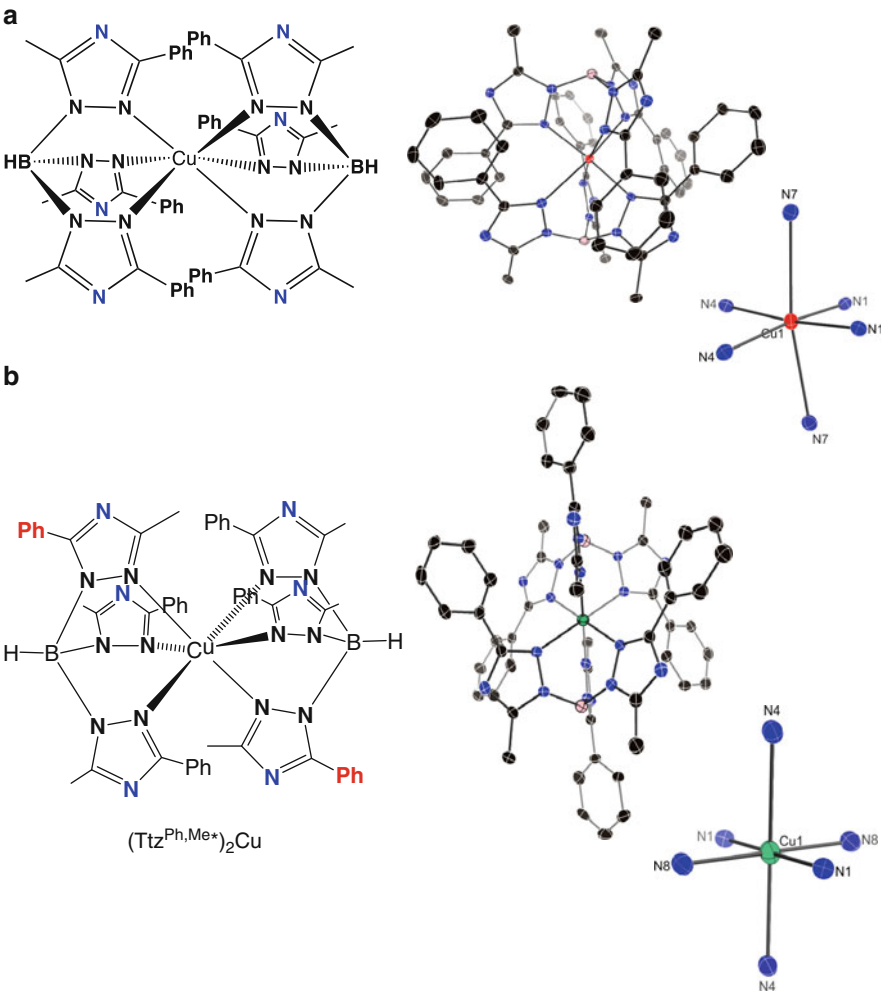

Fig. 21 $(Ttz^{Ph,Me})_2Cu$ (**a**), and its rearranged isomer, $(Ttz^{Ph,Me*})_2Cu$ (**b**) as schematic drawing and crystal structure (entire structure and coordination sphere). Cu shown in *red*, rearranged complex Cu in *green*, N in *blue*, B in *pink*, and C in *black*, and hydrogens were omitted for clarity

However, the low yield of this minor product has hindered further biomimetic studies. Thus a Ttz ligand of greater steric bulk is apparently needed.

In contrast to the above studies, $Tp^{Ph,H}$, $Tp^{Ph,Ph}$, $Tp^{Ph,Me}$ and related Tp ligands of similar steric bulk were sufficiently bulky, and strong enough electron donors, to allow formation of biomimetic complexes. The zinc complexes formed, $(Tp^{Ph,Me})$ ZnOH [52] (Fig. 23a) and $(Tp^{Ph,H})$ZnOH [53], are useful for hydrolytic chemistry, as models of carbonic anhydrase, and as models for matrix metalloproteinase inhibition. Similarly, low-coordinate iron complexes of $Tp^{Ph,Ph}$ (e.g., $(Tp^{Ph,Ph})$Fe

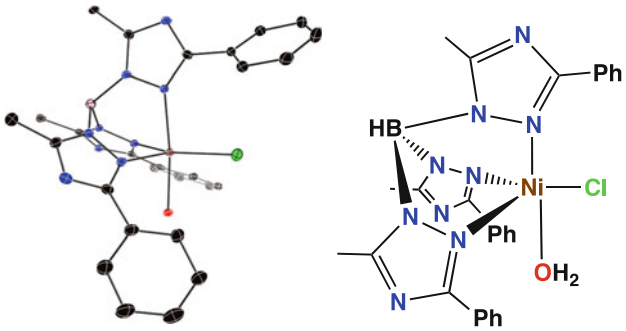

Fig. 22 ($Ttz^{Ph,Me}$)NiCl(OH_2), as both crystal structure and schematic drawing, color scheme: B in *pink*, C in *black*, Cl in *green*, N in *blue*, Ni in *brown*, O in *red*

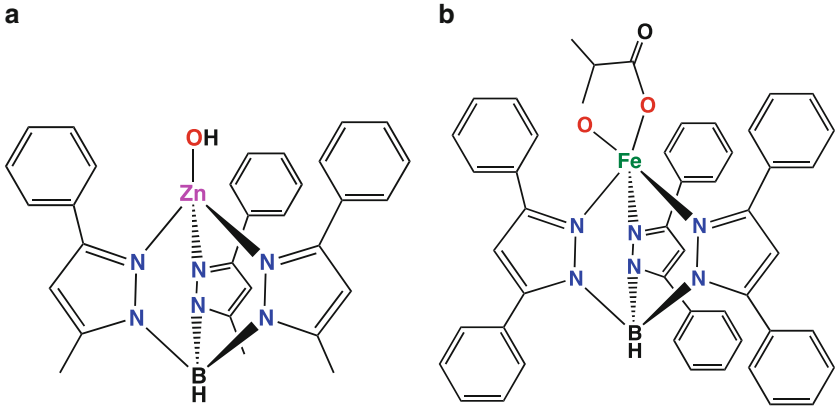

Fig. 23 (**a**) ($Tp^{Ph,Me}$)ZnOH and (**b**) ($Tp^{Ph,Ph}$)Fe(pyruvate)

(pyruvate)), (Fig. 23b) have allowed for productive studies in modeling dioxygen chemistry [54]. Thus it is surprising that $Ttz^{Ph,Me}$ has not been able to support biomimetic four-coordinate structures that are robust enough to prevent (or at least slow down) formation of homoleptic bis ligand complexes. A review of the literature, however, suggests that with all steric variants of Ttz and Tp, in general the Ttz complexes tend to have higher coordination numbers than Tp complexes of similar steric bulk. Janiak et al. have suggested that this is due to the bonding in Ttz complexes being more ionic and less covalent [25]. Furthermore, Ttz is a weaker donor than Tp, and for zinc the bonding is largely ionic with four-, five-, and six-coordinate complexes all roughly equal in energy. Thus with $Ttz^{Ph,Me}$ six-coordinate structures are favored, even with zinc.

In general, $Ttz^{Ph,Me}$ supports coordination to H and metals through the four position nitrogen, but this occurs less frequently than with other Ttz ligands. For comparison, $Ttz^{H,H}$ often forms coordination polymers and both $Ttz^{H,H}$ and $Ttz^{tBu,Me}$ (described below) frequently have water hydrogen bonded to the exodentate

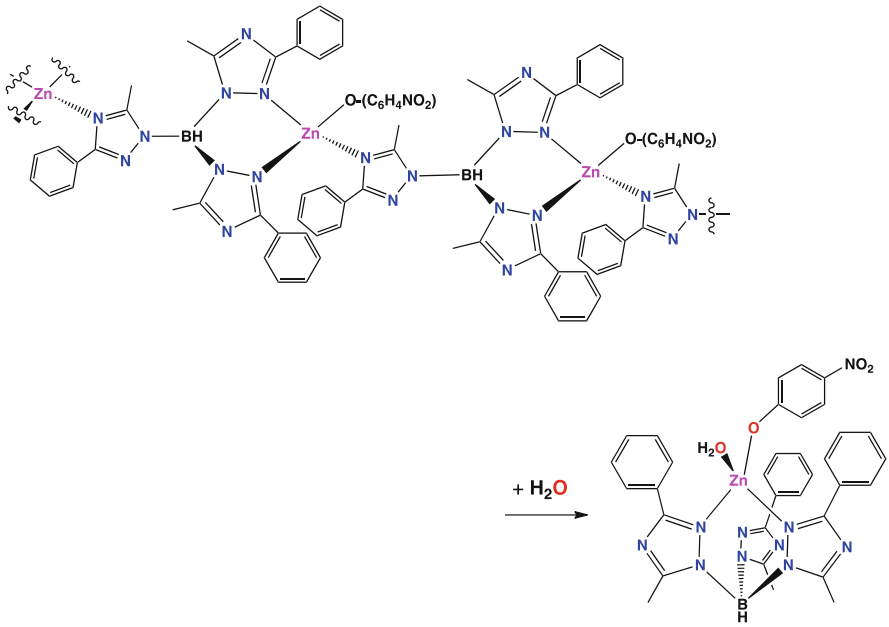

Fig. 24 Simplified view of the 1D coordination polymer, $[(Ttz^{Ph,Me})Zn(OC_6H_4\text{-}p\text{-}NO_2)]_n$, is shown on the *top*. The polymer is disrupted in the presence of moisture, and $(Ttz^{Ph,Me})Zn(OH_2)(OC_6H_4\text{-}p\text{-}NO_2)$ forms, shown on the *bottom*. This complex has H bonds between the Zn bound water and neighboring exodentate triazole Ns; it also has an unusual coordination mode around the zinc ion

nitrogens. Most of the sandwich complexes of $Ttz^{Ph,Me}$ described above do not show hydrogen bonding interactions, but $[NaTtz^{Ph,Me}]\bullet 6CH_3OH$ [48], $(Ttz^{Ph,Me})NiCl(OH_2)$ and $(Ttz^{Ph,Me})ZnCl\bullet(½CH_3OH)$ [48] and other mono ligand zinc complexes [50] do form hydrogen bonding interactions. A coordination polymer is observed in one case, for $[(Ttz^{Ph,Me})Zn(OC_6H_4\text{-}p\text{-}NO_2)]_n$, and this complex involves coordination of one exodentate nitrogen to one zinc and coordination of two endodentate nitrogens to another zinc, creating a one-dimensional polymer chain (Fig. 24). However, this extended structure does not form in the presence of water or excess *p*-nitrophenol, thus, coordination polymers do not dominate the chemistry of this ligand [50].

In conclusion, we believe that $Ttz^{Ph,Me}$ is a ligand that holds great promise with softer metals (e.g., Cu(I)), but with the divalent first row metals sandwich complexes predominate. With Zn(II), there is a rich, but limited chemistry of the $Ttz^{Ph,Me}$ provided that a suitable co-ligand is present and conditions limit the formation of sandwich complexes [50]. Thus there is a need for bulkier Ttz ligands.

2.1.5 $Ttz^{iPr,iPr}$ Complexes

The $Ttz^{iPr,iPr}$ ligand is expected to have greater steric bulk near the metal center than the $Ttz^{Ph,Me}$ ligand, but that bulk does not extend out as far into space and

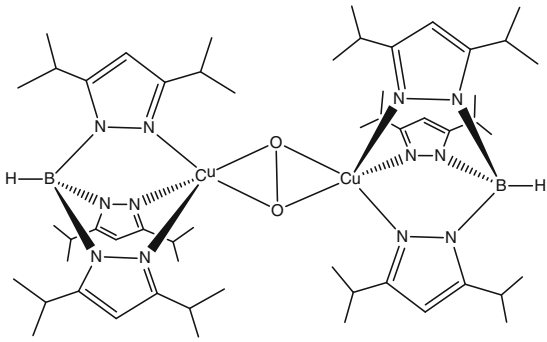

Fig. 25 $(Tp^{iPr,iPr})Cu(\mu\text{-}O_2)Cu(Tp^{iPr,iPr})$ as a model for hemocyanin, which has a similar coordination geometry to that shown but histidines are the N donors

does not lead to as large of a protective pocket. Due to rotation, isopropyl groups can sweep out a cone that is as large as with t-butyl groups, but if rotation is restricted, then tertiary CH will point near the metal center and the steric bulk can be less than that of t-butyl groups. Tp^{iPr2} has formed some of the best structural and functional models for the facial tri-histidine motif in enzymes, including formation of a $(Tp^{iPr,iPr})ZnOH$ complex as a carbonic anhydrase model [55] and $[(Tp^{iPr,iPr})Cu(\mu\text{-}\eta^2\text{:}\eta^2O_2)Cu(Tp^{iPr,iPr})]$ as a hemocyanin [56, 57] model (Fig. 25). Due to the great success of the $Tp^{iPr,iPr}$ ligand in biomimetic chemistry, we chose to synthesize $Ttz^{iPr,iPr}$ which should support four- and five-coordinate complexes but will not be vulnerable to rearrangement reactions (as $Ttz^{Ph,Me}$ was).

$Ttz^{iPr,iPr}$ has been made recently by us as the potassium salt and does support the formation of $(Ttz^{iPr,iPr})ZnCl$, $[(Ttz^{iPr,iPr})CuCl]_2$, and other complexes with first row transition metals. Further synthesis and reactivity studies are ongoing in our laboratory. Also discussed below (in Sect. 2.2) are our preliminary results with the closely related $Ttzm^{iPr,iPr}$ ligand. This ligand is similar to $Ttz^{iPr,iPr}$ in that it offers sterically encumbered triazole donors, but with a neutral methane linker.

2.1.6 $Ttz^{tBu,Me}$ Complexes

The steric bulk of the $Ttz^{tBu,Me}$ ligand is enough to support four- and five-coordinate complexes. In general, most of the structures have the same or slightly greater coordination number as compared with the corresponding $Tp^{tBu,Me}$ or Tp^{tBu} complexes. The slight increase in coordination number reflects that $Ttz^{tBu,Me}$ is a weaker electron donor. The steric bulk (relative to other Ttz ligands) serves to prevent the formation of coordination polymers. Similarly, metal coordination through the exodentate nitrogen has not yet been observed, but coordination to H^+ or H of a protic solvent through the exodentate nitrogen has frequently been observed. The solubility of $Ttz^{tBu,Me}$ complexes is good in polar solvents and in water and alcohols. The most significant of these features will be discussed further in greater detail.

The $Ttz^{tBu,Me}$ ligand is sterically the same as the corresponding Tp ligands, and any differences in structures can be attributed to electronics. Of the

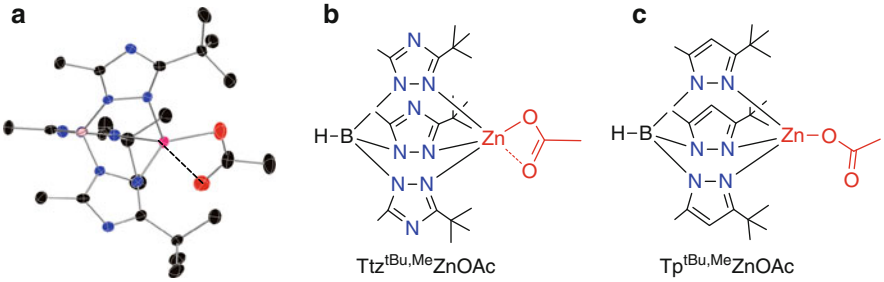

Fig. 26 Two views of ($Ttz^{tBu,Me}$)ZnOAc (**a** and **b**) and ($Tp^{tBu,Me}$)ZnOAc (**c**). Zn in *magenta*, O in *red*, N in *blue*, B in *pink*, C in *black* and hydrogens omitted for clarity

crystallographically characterized $Ttz^{tBu,Me}$ complexes, the vast majority (16 out of 19) are structurally very similar (in terms of bond lengths, angles, and coordination geometry) to Tp complexes of a similar steric profile (e.g., $Tp^{tBu,Me}$ or Tp^{tBu}). This includes our published works [47, 49, 50, 58, 59] and the unpublished structures of ($Ttz^{tBu,Me}$)MCl where M = Fe, Mn (Nieto I, Papish ET, unpublished). The only structures that show significant structural differences are ($Ttz^{tBu,Me}$)Zn(κ^2-OAc) (Fig. 26), and Cu(II) complexes of nitrite and nitrate [60]. The structural differences are more dramatic with the zinc acetate complexes, with which $Ttz^{tBu,Me}$ is approximately five-coordinate, although one Zn–O distance is long at 2.36 Å; in contrast both LZnOAc complexes (where L = $Tp^{tBu,Me}$ and Tp^{tBu}) are clearly four-coordinate (Fig. 26) [58]. It is our hypothesis that these structural differences reflect electronic differences, as a more electropositive zinc results with the $Ttz^{tBu,Me}$ ligand; further evidence for electronic differences is presented below. The differences between ($Ttz^{tBu,Me}$)Cu(κ^2-O_2NO) and ($Ttz^{tBu,Me}$)Cu(κ^2-O_2N) as compared with the Tp Cu^{II} nitrate and nitrite complexes of similar steric profile are more subtle, showing a change in geometry from square pyramidal to trigonal bipyramidal (or the reverse). Here these subtle structural changes hint at the dramatic electronic differences, and the EPR spectra and computational studies indicate that Ttz is both a stronger π acceptor and a stronger σ donor (to Cu^{II} at least) than Tp ligands [60].

Sometimes, this steric bulk has some unintended consequences. In one case we see rearrangement to produce ($Ttz^{tBu,Me}$*)ZnSPh and relieve steric pressure (Fig. 27a) [50]. Rearrangement occurs in this complex and not others with O donors because S prefers tighter bond angles. The steric protection of ($Ttz^{tBu,Me}$)Zn(alkyl) complexes is great enough to make protonolysis with acids in toluene quite slow, and hydrolysis does not occur due to kinetic stability. Our studies suggest that access to the zinc is blocked for these complexes, and protonolysis most likely requires a change from tridentate to bidentate coordination for the $Ttz^{tBu,Me}$ ligand [50]. The kinetic studies of protonolysis of LZnEt (L = $Tp^{tBu,Me}$, $Ttz^{tBu,Me}$) with *p*-nitrophenol in toluene suggests that a change in coordination mode is necessary and slow, we propose that the $Ttz^{Ph,Me}$ ligand goes κ^3 to κ^2 before the Zn–C bond is cleaved (Fig. 28) [50]. Of course in toluene, the acid is not appreciably dissociated

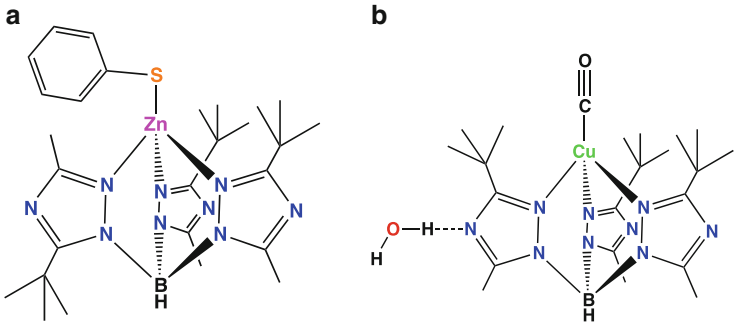

Fig. 27 (**a**) The ligand rearrangement occurs to form (Ttz^{tBu,Me}*)ZnSPh. (**b**) (Ttz^{tBu,Me})CuCO showing the hydrogen bond to water. Zn in *magenta*, Cu in *green*, O in *red*, S in *orange*, N in *blue*, B in *pink*, and C in *black*, most hydrogens omitted for clarity

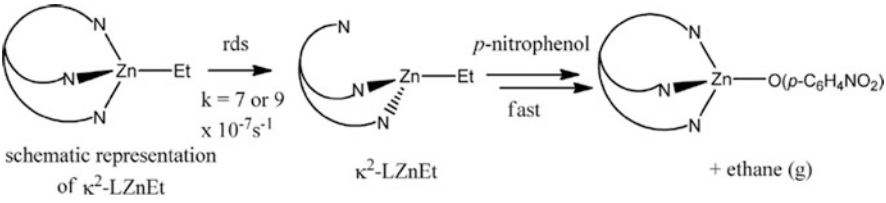

Fig. 28 Proposed mechanism of protonolysis of LZnEt (L = Ttz^{tBu,Me}, Tp^{tBu,Me}) with *p*-nitrophenol in toluene. The rate does not depend on the concentration of acid, but is first order in LZnEt [50]

so very little H^+ is available to bind to the exodentate site. Perhaps acid in a more ionizing solvent can catalyze these reactions by providing H^+ to bind to the exodentate N to promote a decrease in denticity. We have some preliminary evidence for H^+ reversibly altering the electronic features of (Ttz$^{R,R'}$)CuCO complexes (Dixon N A, Kraus J S, Papish E T, unpublished).

The study of copper (I) carbonyl complexes provides a means of measuring donor strength for various comparable ligands. For (Ttz^{tBu,Me})CuCO (Fig. 27b), the CO stretch occurs in a range that is sensitive to electronic changes, and the value of 2,080 cm^{-1} reflects the fact that Ttz^{tBu,Me} is a weaker donor than Tp^{tBu,Me} (cf. the CO stretch of (Tp^{tBu,Me})CuCO occurs at 2,059 cm^{-1}) [47]. We now believe that Ttz is actually a similar or stronger σ donor when compared with sterically similar Tp ligands [60], but the change in the CO stretch may reflect Ttz being a better π acceptor, with the net result being a Cu(I) that is less electron rich with Ttz ligands. Furthermore, this complex co-crystallizes with adventitious water and is remarkably water stable. The presence of water or oxygen does not result in detectable changes in the IR or UV–vis spectra, thus hydrogen bonding does not appreciably change the donor properties in this case (at least with *water* as hydrogen bond

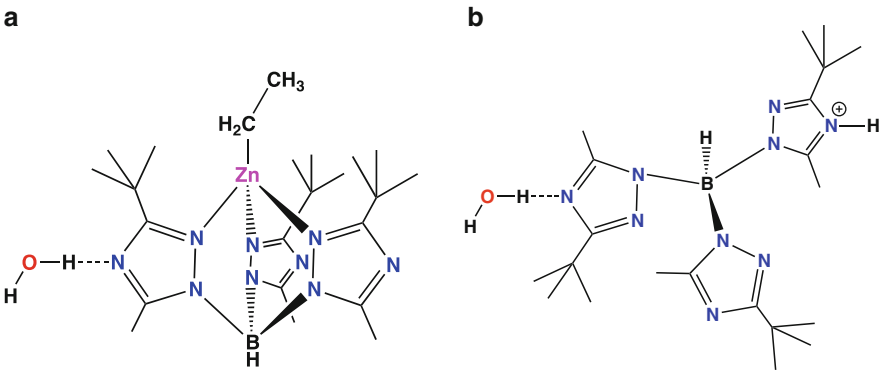

Fig. 29 Hydrogen bonding interactions in (**a**) ($Ttz^{tBu,Me}$)Zn(ethyl)•H_2O and (**b**) H($Ttz^{tBu,Me}$)•H_2O•CH_2Cl_2, with CH_2Cl_2 omitted for clarity. In the latter structure there are hydrogen bonds to each exodentate triazole N, although only one is shown

donor, the situation appears different with H^+) (Dixon N A, Kraus J S, Papish E T, unpublished), and a lack of reactivity suggests the CO is strongly bound to Cu [47].

The sources of the electron differences – the extra nitrogens in the azole rings – also provide a means of improving solubility in water and alcohols via a site for hydrogen bonding. The water solubility of the potassium salt of the ligand ($KTtz^{tBu,Me}$) is impressive at 99 mg/mL [58], but this solubility is diminished somewhat in transition metal complexes [59]. Most transition metal complexes of bulky Ttz ligands will dissolve in methanol/water mixtures, so for biomimetic studies of hydrophilic enzyme active sites and hydrolytic reactions, this represents an improvement over Tp metal complexes.

The improved water solubility is believed to derive from triazole rings functioning as hydrogen bond acceptors through the exodentate nitrogens. We have observed many crystal structures that have hydrogen bonding interactions, thus showing that steric bulk does not impede this interaction, at least when the N lone pair interacts with hydrogens rather than metal ions. In many cases, the hydrogen-bonded water is adventitious since Ttz ligands are hygroscopic. Noteworthy structures include ($Ttz^{tBu,Me}$)CuCO•H_2O and ($Ttz^{tBu,Me}$)Zn(alkyl)•H_2O (Figs. 27b, 29a); [47, 49] these illustrate that organometallic complexes can be water stable, provided there is a steric barrier to reactivity at the metal center. This ability to accept an H^+ at the N-4 position has allowed us to make $HTtz^{tBu,Me}$, and this is a synthetically useful starting material as described in Sect. 3. This allows entry into reactivity that is not possible with Tp ligands. The crystal structure shows how coordinating H^+ to N-4 leads to a network of hydrogen bonds (Fig. 29b) [50]. Our future studies aim to quantify how much these interactions (both protonation and accepting a hydrogen bond at N-4) alter the electronics of $Ttz^{tBu,Me}$ metal complexes (Dixon N A, Kraus J S, Papish E T, unpublished).

Ttz ligands have a rich chemistry. They tend to favor higher-coordinate structures than the Tp ligands due to being weaker donors. They can bind to an

additional metal (often forming coordination polymers) or to protic hydrogens, and thus offer improved water solubility. Steric bulk plays an important role in the chemistry of the Ttz ligands and can allow for the formation of structures resembling enzyme active sites. A discussion of the use of $Ttz^{tBu,Me}$ and $Ttz^{Ph,Me}$ in forming biomimetic structures follows in Sect. 3.

2.2 *Bis- and Tris(triazolyl)methane Ligands*

In 1969, Rees and Jones reported the first synthesis of a tris(triazolyl)methane ligand, namely tris-(3,5-dimethyl-1,2,4-triazol-1-yl)methane [61]. However, under the conditions employed using dichlorocarbene as the carbon source, the yield of this product ranged from 1.5 to 3.1% and the major product was the starting material, 3,5-dimethyl-1,2,4-triazole. A more rational synthesis of tris triazole ligands with methane linkers was achieved by using chloroform and base under phase transfer conditions [62, 63]. The tris(triazolyl)methane (Ttzm) ligand was made in this fashion and forms coordination polymers with various metals [4]. We recently made tris-(3,5-diisopropyl-1,2,4-triazol-1-yl)methane in this manner ($Ttzm^{iPr,iPr}$, Fig. 30), and preliminary experiments suggest that it is a good ligand for biomimetic chemistry with Zn and Cu (Dixon NA, Zeller M, Papish ET, unpublished). Similarly, bis-(3-t-butyl-5-methyl-1,2,4-triazol-1-yl)methane ($Btzm^{tBu,Me}$, Fig. 30) was made in our lab, but the lengthy, low yield procedure may limit the synthetic utility of this ligand (Klebon BD, Papish ET, unpublished). In general, ligands linked by C (rather than B) are usually more difficult to synthesize, but by using symmetric triazoles the purification steps (and loss of yield due to formation of regioisomers) are minimized. The advantage of C linked ligands is both in terms of stability long term and under highly acidic conditions, and the difference in charge. The stability advantage is more important when considering pyrazole-based Tp ligands (vs. tris(pyrazolyl)methane), as triazoles produce Ttz ligands that are acid stable [50] but will eventually decompose after lengthy heating in acid, in contrast Tp ligand are much more acid sensitive.

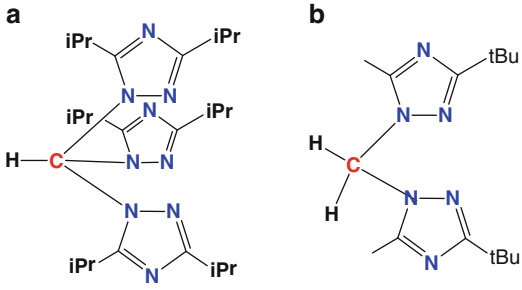

Fig. 30 The new ligands (**a**) $Ttzm^{iPr,iPr}$ and (**b**) $Btzm^{tBu,Me}$

2.3 Related Ligands: Bis(triazolyl)borates

A detailed discussion of the chemistry of Btz ligands is beyond the scope of this review, but a brief overview of the rather limited studies with this ligand is provided here. $(Btz^{H,H})_2M^{II}(OH_2)_2$ complexes are coordination polymers with Mn and Cu, but a molecular chelate is formed with Ni, the small number of complexes characterized makes it difficult to establish a trend [8, 64]. Similarly Ru(II) forms coordination polymers with $Btz^{H,H}$ [65]. It seems that Cu(I) does allow the formation of molecular, mononuclear $(Btz^{H,H})Cu(PR_3)_n$ complexes, where $n = 1$ or 2 and depends on the steric bulk of the phosphine [21, 22]. Other references describe hydrogen bonding in Btz complexes of divalent metals [16] and Ag complexes of Btz [27, 28]. No sterically bulky Btz derivatives have been described in the literature, and the chemistry of Btz with the rest of the periodic table is rather undeveloped. Our preliminary results suggest that, with Ru, Btz forms discrete complexes (e.g., (η^6-arene)RuCl(Btz)) that are useful as catalysts for hydrogenation reactions [31].

3 Use of Bulky Tris(triazolyl)borate Ligands for Biomimetic Chemistry

Our efforts at formation of biomimetic structures that can perform biologically relevant chemical reactions have centered on Cu and Zn chemistry. As our biomimetic work with copper is still developing and just one paper has been published [60], this review will feature a brief description of biomimetic chemistry with copper, but this is a promising area for future work. This review will provide more in-depth coverage of biomimetic chemistry with zinc, which is more developed.

3.1 Ttz Copper Complexes as Structural and Functional Models of Copper Nitrite Reductase

Bacteria utilize copper nitrite reductase (CuNiR) to convert nitrite into $NO_{(g)}$ as a key step in denitrification, which is part of the global nitrogen cycle [11]. Denitrification includes the breakdown of excess fertilizers (nitrates and nitrites) in soil and water to produce NO. NO generation and reduction processes are relevant to human health and how bacteria evade our immune response [66, 67]. The site of nitrite reduction in CuNiR is a Cu ion ligated by three histidines in a facial arrangement [68]. In the catalytic cycle, it is proposed that a four-coordinate Cu(II)−aqua species binds nitrite and is reduced to Cu(I), though the order of these two events

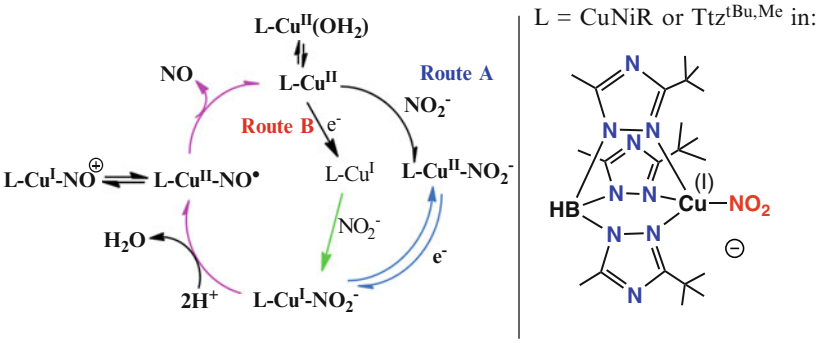

Fig. 31 Key steps in enzymatic nitrite reduction by CuNiR, the *colored arrows* represent steps that were modeled using $[Tz^{tBu,Me}Cu^{I}NO_2]^-$

is still debated (Fig. 31, Routes A and B, L is the enzyme) [69]. The resulting Cu(I) nitrite complex can then reduce nitrite to form NO upon protonation.

As described briefly in Sect. 2.1.6, we synthesized $(Tz^{tBu,Me})Cu(\kappa^2\text{-}O_2N)$ as a model of the Cu^{II} nitrite species postulated as an intermediate in the catalytic cycle of CuNiR [60]. This species can be reduced irreversibly to form $[Tz^{tBu,Me}Cu^{I}NO_2]^-$, which is a model of the reduced, nitrite bound form of the enzyme. $[Tz^{tBu,Me}Cu^{I}NO_2]^-$ $[PPN]^+$ (PPN = bis(triphenylphosphine)iminium) has also been made via synthesis, via first combining $TlTz^{tBuMe}$ with $Cu^{I}Cl$ to produce $[Tz^{tBu,Me}Cu]_n$ in situ, which is then treated with a nitrite source. The product, $[Tz^{tBu,Me}Cu^{I}NO_2]^-$, is very air and moisture sensitive, but it can be used to model the chemistry of nitrite reduction.

Notably, $[Tz^{tBu,Me}Cu^{I}NO_2]^-$ is an accurate functional model for CuNiR [60]. Upon addition of acetic acid to $[Tz^{tBu,Me}Cu^{I}NO_2]^-$ stoichiometric nitrite reduction to $NO_{(g)}$ is observed (Fig. 31). This reaction was followed by UV–vis spectroscopy by trapping $NO_{(g)}$ with a cobalt porphyrin indicator. The copper-containing product ($(Tz^{tBu,Me})CuOAc$) was also isolated and fully characterized. Thus we have characterized the Cu and N containing products of this reaction, and it is clear that copper reduced the nitrite ligand to form NO.

Our study provided the first functional model to use an anionic ligand donor set [60] (while Tp does form several interesting Cu nitrosyl complexes [70], it had not been reported to serve as a functional model until after our work appeared) [71]. The steps (in Fig. 31) marked with the colored arrows were modeled or studied by indirect means. Specifically, (1) the green arrow shows a process similar to how we make $[Tz^{tBu,Me}Cu^{I}NO_2]^-$ (modeled by synthesis); (2) the blue arrows represent a process we observed irreversibly by cyclic voltammetry (Cu^{II} to Cu^{I}); and (3) the magenta arrows correspond to the reduction of nitrite that we observed. We are interested in probing the mechanism of nitrite reduction with Tz complexes, including what role protonation at the exodentate nitrogen may play. The electronic differences between Tp and Tz and the different mechanistic possibilities open up many interesting lines of study.

3.2 Synthesis of ($Ttz^{tBu,Me}$)ZnOH: An Exploration of the Differences Between Ttz and Tp Chemistry

Our work on Zn chemistry began as an effort to model hydroxide-containing active sites, including carbonic anhydrase [11, 72] and phosphotriesterase [73]. These enzymes, which perform hydration of CO_2 and hydrolysis of pesticides, respectively, seemed especially promising for modeling with Ttz. We postulated that any enzyme that uses water in its reaction chemistry could be better modeled by incorporating ligands that promote water solubility. Carbonic anhydrase has in its active site a zinc (II) ion bound by three histidine residues and hydroxide (or water) in a hydrophobic pocket, but there are nearby channels that deliver water to the active site and are lined with hydrogen bonding groups [11]. Phosphotriesterase has two zinc ions in close proximity ligated by histidines, aspartate residues, and bridging ligands, and one zinc is in a hydrophobic pocket but the other is in a hydrophilic environment [73]. In the literature, most ligands for enzyme modeling utilize hydrophobic ligands, and very few ligands are capable of water solubility and modeling hydrophilic pockets, as Ttz can do.

Despite these worthwhile goals, the synthesis of (Ttz)ZnOH complexes has been challenging and this target has been elusive until recently. However, the differences in Tp versus Ttz reactivity are interesting in their own right, as the modest change in electron donor ability has produced a big change in the reactivity of zinc complexes, as described below.

In the Tp literature, (Tp)ZnOH complexes are made by two routes: (1) treatment of TpZnLG (LG = leaving group = OAc, NO_3 or Br) with hydroxide [55] and (2) treatment of $Zn(ClO_4)_2$•$6H_2O$ with KTp and base (Scheme 1) [52, 53]. In our experience, these routes have not produced (Ttz)ZnOH complexes. For example, when ($Ttz^{tBu,Me}$)ZnCl is treated with NaOH (*aq*) in CH_3CN, the isolated organic ligand containing product is ($Ttz^{tBu,Me}$)$NaOH_2$ (Fig. 32a) (Rowe BW, Wells KR, unpublished). This product has been characterized by ^1H and ^{13}C-NMR spectra, IR, and X-ray crystallography. Presumably, the other product is $Zn(OH)_2$ or similar zinc hydroxide complexes, and these insoluble products provide a driving force for the reaction. An initial hypothesis was that increasing the size of the base may prevent formation of $[M]^+[Ttz]^-$ complexes, thus route (1) was attempted with both KOH and $[NMe_4]OH$•$5H_2O$ as hydroxide sources. However, the evidence (^1H, ^{13}C-NMR, IR) shows that the Ttz ligand winds up in [K][$Ttz^{tBu,Me}$] and [NMe_4][$Ttz^{tBu,Me}$], thus formation of zinc hydroxide by-products still determines the course of this chemistry. For [NMe_4]$Ttz^{tBu,Me}$ we were able to obtain a crystal structure (as the • $3H_2O$ and $1CH_2Cl_2$ solvate, Fig. 32b), and this indicates no interaction between the Ttz ligand and the monocation (as expected).

The alternate route, described as route (2) above with $Zn(ClO_4)_2$•$6H_2O$ as the zinc source, was also explored with $KTtz^{tBu,Me}$ and three separate bases (NaOH, KOH and $[NMe_4]OH$•$5H_2O$). In these experiments, the fate of our ligand is less well defined, but with NaOH we again form ($Ttz^{tBu,Me}$)$NaOH_2$ as characterized spectroscopically (and spectra are consistent with ($Ttz^{tBu,Me}$)$NaOH_2$ obtained via route 1). With KOH

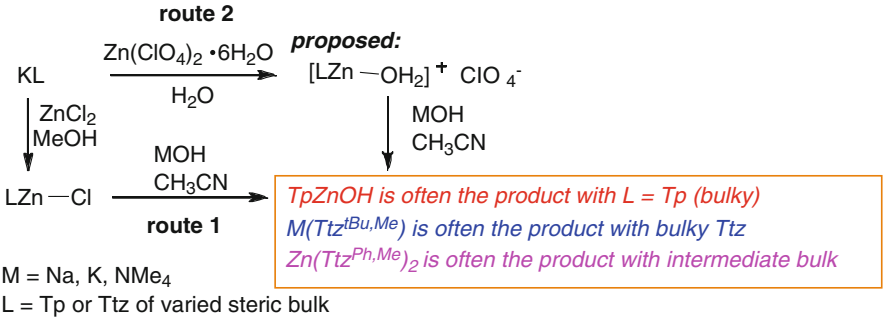

Scheme 1 Synthetic routes to LZnOH

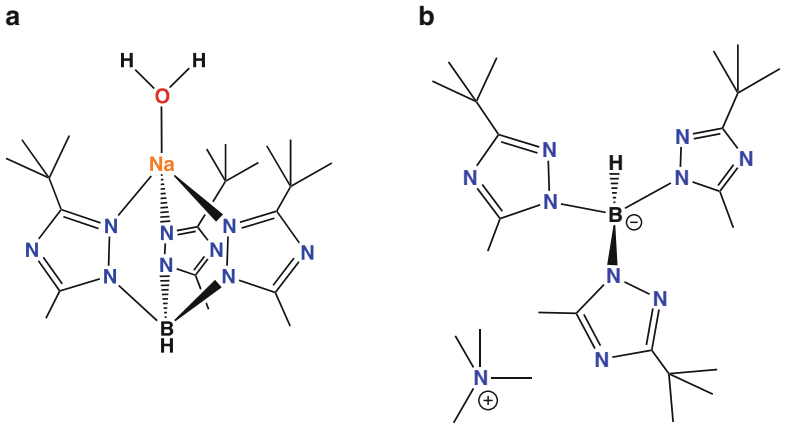

Fig. 32 Products of the reactions shown in Scheme 1 with L = $Ttz^{tBu,Me}$, (**a**) ($Ttz^{tBu,Me}$)$NaOH_2$ (**b**) $[NMe_4]Ttz^{tBu,Me}$ with solvent molecules omitted

and $[NMe_4]OH•5H_2O$, it appears that our ligand partially decomposes via B–N bond cleavage under these conditions. Zinc (II) perchlorate is a powerful Lewis acid and has been shown to cleave B–N bonds in the Tp literature [74].

With L = $Ttz^{Ph,Me}$, both routes shown in Scheme 1 have been attempted with more effort directed towards route 2, and this has led to the isolation of $Zn(Ttz^{Ph,Me})_2$ as the product.

The above experiments have led us to conclude that the Ttz ligands are bound less strongly to zinc than the Tp ligands. It also appears that strong bases, like hydroxide, should be avoided in the synthesis of ($Ttz^{tBu,Me}$)ZnOH. Thus, we imagined that removal of halide from ($Ttz^{tBu,Me}$)ZnCl in aqueous solution could result in $[(Ttz^{tBu,Me})ZnOH_2]^+$ or ($Ttz^{tBu,Me}$)ZnOH. However, treatment of ($Ttz^{tBu,Me}$)ZnCl with $Ag(SbF_6)$ in water gave H($Ttz^{tBu,Me}$) as the only organic product, by ^{1}H-NMR and MS evidence, and similar results were obtained with other silver salts. The protonated Ttz ligand can be made in a more straightforward fashion (and 90% yield) from K[$Ttz^{tBu,Me}$] and HCl in ether (Scheme 2). While these two routes constitute acidic conditions (if $[(Ttz^{tBu,Me})ZnOH_2]^+$ forms as an intermediate it should be quite acidic, based on the pK_a values of similar N_3 zinc aqua complexes),

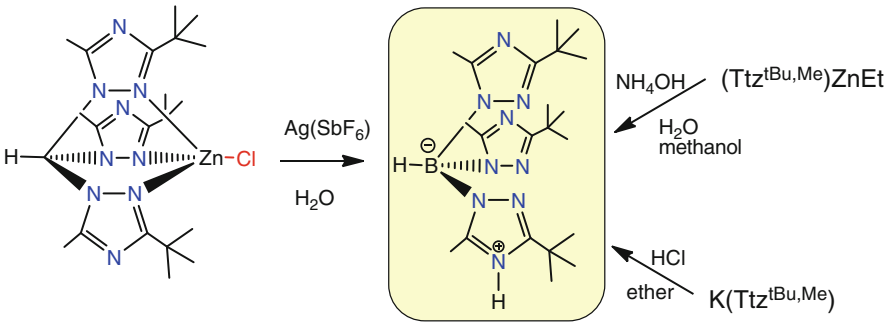

Scheme 2 Three unique routes to H(Ttz^{tBu,Me})

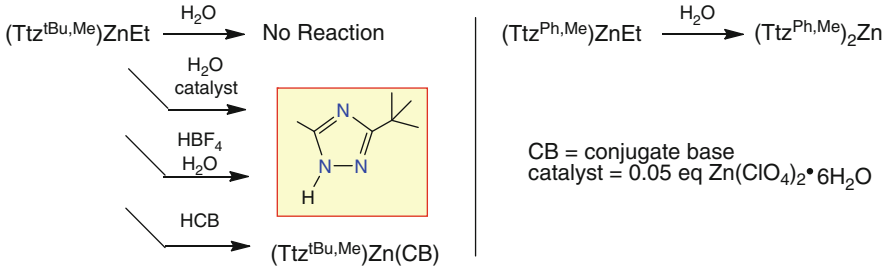

Scheme 3 Attempted hydrolysis of organometallic co-ligands

we have also formed H(Ttz^{tBu,Me}) under basic conditions by treating (Ttz^{tBu,Me})ZnEt with NH_4OH in water and methanol (Scheme 2). This route is reported in our recent paper [50], along with full characterization and crystallography on hydrated H(Ttz^{tBu,Me}) (discussed in Sect. 2.1.6 and shown in Fig. 29b). This suggests exodentate nitrogens in Tz ligands were able to take a proton from ammonium and either zinc hydroxide or zinc amine complexes are the likely side products. The hydrogen bonding network present in H(Ttz^{tBu,Me})•H_2O and the utility of this molecule as a synthetic starting material (see below) indicate that the chemistry of Ttz ligands has unique facets not available with Tp ligands.

The use of a Ttz zinc complex with a readily hydrolysable ligand appeared to be a promising route to (Ttz^{tBu,Me})ZnOH (Scheme 3). However, (Ttz^{tBu,Me})Zn(alkyl) (alkyl = Me, Et) complexes co-crystallized with water (Fig. 29a) and were water stable, even after several weeks in contact with water [49]. This was clearly a kinetic rather than thermodynamic stability, as the steric bulk around the zinc had made the metal inaccessible. Zinc alkyls are known to react violently with water, when they are sterically accessible. (Ttz^{Ph,Me})ZnEt reacts with water to produce (Ttz^{Ph,Me})$_2$Zn, and (Ttz^{Ph,Me})ZnOH is a plausible intermediate that could undergo metathesis to give the observed product (Scheme 3) [50]. Stronger acids (HCB, where CB is the conjugate base) reacted slowly with (Ttz^{R,Me})ZnEt (R = tBu, Ph) complexes to give (Ttz^{R,Me})Zn(CB) products [50]. Thus B–N bonds are generally acid stable, even for slow reactions (occurring over several days) [50]. Only in two

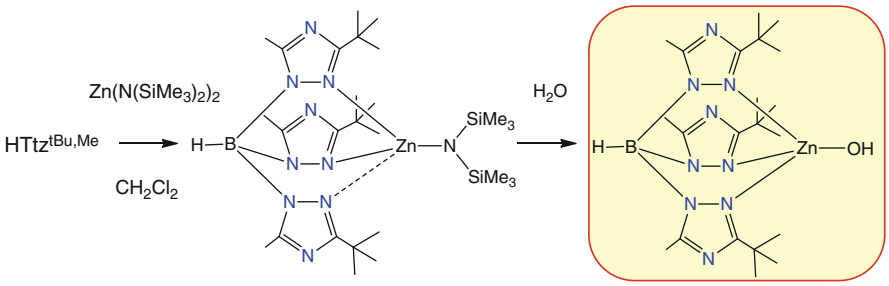

Scheme 4 Successful route to ($Ttz^{tBu,Me}$)ZnOH via Zn amide. Zn amide structure is tentatively assigned as κ^3 or κ^2

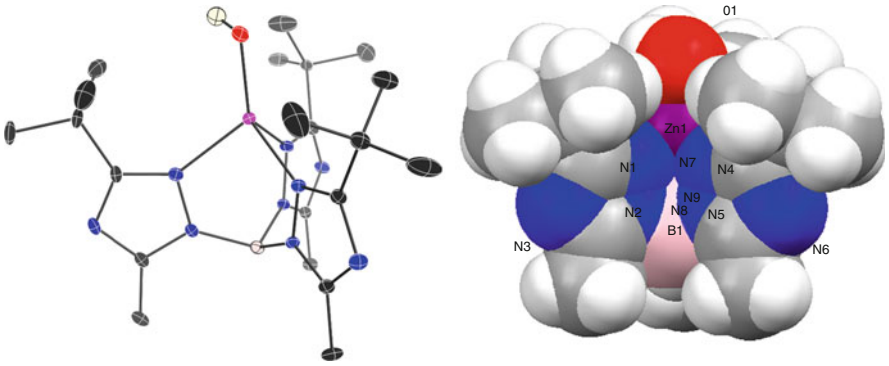

Fig. 33 Crystal structure of ($Ttz^{tBu,Me}$)ZnOH, thermal ellipsoids (*left*) and space-filling (*right*). Zn in *purple*, O in *red*, N in *blue*, B in *pink*, and C in *black* and the hydroxyl hydrogen is shown in *white*

cases were B–N bond cleavage products observed: both (1) treatment of ($Ttz^{tBu,Me}$)ZnEt with HBF_4 and (2) prolonged [or for shorter time periods with an appropriate Lewis acid catalyst (Kumar M, Papish ET, unpublished)] heating of ($Ttz^{tBu,Me}$)ZnEt in the presence of water, produced 3-*t*-butyl-5-methyl-1,2,4-triazole (Scheme 3) [50].

The use of amide as a readily hydrolysable ligand has proven most promising, but this leads to a rather long synthetic route (Scheme 4). Protonated Ttz ligand ($HTtz^{tBu,Me}$, described above) reacts readily with $Zn(N(SiMe_3)_2)_2$ to produce what is tentatively assigned to be ($Ttz^{tBu,Me}$)$Zn(N(SiMe_3)_2)$. However, since we do not have a crystal structure for this molecule, it is possible that this molecule has an unusual geometry or the Ttz bound κ^3 or κ^2, as the latter would relieve steric congestion at the metal center and permit further reactivity. Attempts to recrystallize this zinc amide complex yielded ($Ttz^{tBu,Me}$)ZnOH (Fig. 33), which was formed from the hydrolysis of the Zn amide bond in the presence of adventitious moisture. The crystal structure showed similarities to ($Tp^{tBu,Me}$)ZnOH and the carbonic anhydrase active site. Steric crowding around the zinc and a lack of co-crystallized

solvent molecules resulted in no hydrogen bonds present in the structure. Efforts to scale up this synthesis for further characterization of this molecule and reactivity studies are in progress.

Thus we have spent 6 years trying many different unique routes to ($Ttz^{tBu,Me}$)ZnOH starting from ($Ttz^{tBu,Me}$)ZnCl, ($Ttz^{tBu,Me}$)ZnEt, ($Ttz^{tBu,Me}$)Zn($N(SiMe_3)_2$) or $Zn(OH_2)_6$•ClO_4 and $KTtz^{tBu,Me}$. For our efforts, we have found one successful route and we have learned something about the differences between Tp and Ttz ligands. Ttz ligands seem to readily coordinate to or form salts with monocationic ions, and the H^+ salt of Ttz is quite stable. While we have found a successful route to ($Ttz^{tBu,Me}$)ZnOH, this procedure is lengthy and our studies suggest that ($Ttz^{tBu,Me}$)ZnOH is a sensitive molecule. These results suggest areas of active research: (1) use of other ligands, perhaps of intermediate steric bulk and (2) use of a catalyst that can promote a more efficient route to ($Ttz^{tBu,Me}$)ZnOH. We are working on these problems and exploring the biomimetic chemistry of ($Ttz^{tBu,Me}$)ZnOH, a molecule that accurately represents the active sites of hydrolytic Zn enzymes while offering improved water solubility.

4 Conclusions and Future Directions

Thus Ttz ligand can offer distinct advantages over Tp ligands. They favor larger coordination numbers as they produce a more electropositive metal center. Thus with the right degree of steric bulk, they can produce an electron-deficient metal that is poised to react with various electron sources, including hard to activate covalent bonds. The unique electronic features can also lead to isolation of metalloradicals and unusual or typically unstable metal oxidation states. The water and alcohol solubility makes these ligands suitable for green chemistry applications. An underdeveloped but nonetheless transformative area of research with Ttz ligands is the use of metal or H binding to the exodentate N to tune the donor properties. Binding to this nitrogen can promote a change in Ttz denticity from tridentate to bidentate and promote reactivity, thereby the metal or H^+ can act as a catalyst. Thus bulky Ttz ligands can be considered *orthogonally functionalized scorpionates* that are heteroditopic, tunable ligands.

Acknowledgments This review is dedicated to the memory of Jessica L. Bongiovanni (1987–2012), an undergraduate researcher in the Papish group (B.S. in Chemistry in 2009 from Drexel University) originally from Manchester, NJ who studied chemistry at University of North Carolina, Charlotte (M.S. in 2011) and Princeton University (in Ph.D. program). Jessica was a dedicated scientist who truly enjoyed the scientific process, was not deterred by negative results, and really wanted to understand fundamental reaction chemistry. Jessica worked on the synthesis of biomimetic zinc, copper, and nickel Ttz complexes described herein.

Over the years, our group has been supported by ACS-PRF, NSF CAREER (grant CHE-0846383), Salisbury University and Drexel University. The work described herein would not have been possible without the dedication of many undergraduate, graduate students, and two postdoctoral fellows. These include undergraduates Michael T. Taylor, Finith E. Jernigan III, Bryan D. Klebon, Brittany W. Rowe, Kirsten R. Wells (now Kehl), Patrick T. Fadden, Trisha

M. Donahue (now Darby), Aaron S. Jenkins, Sean R. Gardner, Jessica L. Bongiovanni, Paul R. DeGregory, Shannon N. Oseback, Sarah W. Shim, graduate student Natalie A. Dixon, postdocs Mukesh Kumar, and Ismael Nieto. We are also grateful for the support and camaraderie of other group members who did not contribute to this work. We wish to also thank our collaborators Gregory M. Ferrence, Matthias Zeller, Glenn P. A. Yap, David L. Tierney, and Nicolai Lehnert, and the students in their research groups. We thank Ged Parkin and Tony Addison for helpful discussions.

References

1. Trofimenko S (1999) Scorpionates: polypyrazolylborate ligands and their coordination chemistry. World Scientific Publishing Company, Singapore
2. Pettinari C (2008) Scorpionates II: chelating borate ligands. Imperial College Press, London
3. Trofimenko S (1967) J Am Chem Soc 89:3170
4. Gioia Lobbia G, Bonati F, Cecchi P (1991) Synth React Inorg Met Org Chem 21:1141
5. Janiak C (1994) J Chem Soc Chem Commun 545
6. Janiak C, Scharmann TG, Green JC, Parkin RPG, Kolm MJ, Riedel E, Mickler W, Elguero J, Claramunt RM, Sanz D (1996) Chem Eur J 2:992
7. McGaughy TW, Fung BM (1972) Inorg Chem 11:2728
8. Janiak C, Scharmann TG, Guenther W, Girgsdies F, Hemling H, Hinrichs W, Lentz D (1995) Chem Eur J 1:637
9. Irving EH, Williams RJP (1948) Nature 162:746
10. Janiak C, Scharmann TG, Guenther W, Hinrichs W, Lentz D (1996) Chem Ber 129:991
11. Bertini I, Gray HB, Stiefel EI, Valentine JS (2007) Biological inorganic chemistry. University Science, Sausalito
12. Janiak C (1994) Chem Ber 127:1379
13. Janiak C, Hemling H (1994) J Chem Soc Dalton Trans 2947
14. Janiak C, Scharmann TG, Mason SA (2002) J Am Chem Soc 124:14010
15. Jeffrey GA (2003) Crystallogr Rev 9:135
16. Janiak C, Scharmann TG (2003) Polyhedron 22:1123
17. Xiao Z, Gable RW, Wedd AG, Young CG (1994) J Chem Soc Chem Commun 1295
18. Youm K-T, Kim MG, Ko J, Jun M-J (2006) Angew Chem Int Ed 45:4003
19. Youm K-T, Kim MG, Ko J, Jun M-J (2007) Polyhedron 26:929
20. Ryu DW, Lee WR, Lee JW, Yoon JH, Kim HC, Koh EK, Hong CS (2010) Chem Commun 46:8779
21. Gioia Lobbia G, Pellei M, Pettinari C, Santini C, Skelton BW, Somers N, White AH (2002) J Chem Soc Dalton Trans 2333
22. Santini C, Pellei M, Gioia Lobbia G, Fedeli D, Falcioni G (2003) J Inorg Biochem 94:348
23. Shiu KB, Lee JY, Wang Y, Cheng MC (1993) Inorg Chem 32:3565
24. Shiu K-B, Lee JY, Wang Y, Cheng M-C, Wang S-L, Liao F-L (1993) J Organomet Chem 453:211
25. Janiak C, Temizdemir S, Scharmann TG, Schmalstieg A, Demtschuk J (2000) Z Anorg Allg Chem 626:2053
26. Shiu K-B, Guo W-N, Peng S-M, Cheng M-C (1994) Inorg Chem 33:3010
27. Effendy, Gioia Lobbia G, Marchetti F, Pellei M, Pettinari C, Pettinari R, Santini C, Skelton BW, White AH (2004) Inorg Chim Acta 357:4247
28. Gioia Lobbia G, Pellei M, Pettinari C, Santini C, Skelton BW, White AH (2005) Inorg Chim Acta 358:1162
29. Janiak C, Scharmann TG, Albrecht P, Marlow F, Macdonald R (1996) J Am Chem Soc 118:6307

30. Li J, Djurovich PI, Alleyne BD, Yousufuddin M, Ho NN, Thomas JC, Peters JC, Bau R, Thompson ME (2005) Inorg Chem 44:1713
31. Kumar M, DePasquale J, White NJ, Papish ET, Zeller M (2012) Organometallics (in press). doi:10.1021/om301260j
32. Zeng Z, Twamley B, Shreeve JM (2007) Organometallics 26:1782
33. Xiao Z, Young CG, Enemark JH, Wedd AG (1992) J Am Chem Soc 114:9194
34. Roberts SA, Young CG, Cleland WE, Ortega RB, Enemark JH (1988) Inorg Chem 27:3044
35. Cleland WE, Barnhart KM, Yamanouchi K, Collison D, Mabbs FE, Ortega RB, Enemark JH (1987) Inorg Chem 26:1017
36. Macleod IT, Tiekink ERT, Young CG (1996) J Organomet Chem 506:301
37. Xiao Z, Bruck MA, Doyle C, Enemark JH, Grittini C, Gable RW, Wedd AG, Young CG (1995) Inorg Chem 34:5950
38. Xiao Z, Gable RW, Wedd AG, Young CG (1996) J Am Chem Soc 118:2912
39. Oseback SN, Shim SW, Kumar M, Greer SM, Gardner SR, Lemar KM, DeGregory PR, Papish ET, Tierney DL, Zeller M, Yap GPA (2012) Dalton Trans 41:2774
40. Mairena MA, Urbano J, Carbajo J, Maraver JJ, Álvarez E, Díaz-Requejo MM, Pérez PJ (2007) Inorg Chem 46:7428
41. Mairena MA, Díaz-Requejo MM, Belderraín TR, Nicasio MC, Trofimenko S, Pérez PJ (2004) Organometallics 23:253
42. Díaz-Requejo MM, Pérez PJ (2005) J Organomet Chem 690:5441
43. Caballero A, Despagnet-Ayoub E, Mar Diaz-Requejo M, Diaz-Rodriguez A, Gonzalez-Nunez ME, Mello R, Munoz BK, Ojo WS, Asensio G, Etienne M, Perez PJ (2011) Science 332:835
44. Dias HVR (2010) Pure Appl Chem 82:649
45. Kou X, Wu J, Cundari TR, Dias HVR (2009) Dalton Trans 915
46. Kou X, Dias HVR (2009) Dalton Trans 7529
47. Papish ET, Donahue TM, Wells KR, Yap GPA (2008) Dalton Trans 2923
48. Gardner SR, Papish ET, Monillas WH, Yap GPA (2008) J Inorg Biochem 102:2179
49. Kumar M, Papish ET, Zeller M, Hunter AD (2010) Dalton Trans 39:59
50. Kumar M, Papish ET, Zeller M, Hunter AD (2011) Dalton Trans 40:7517
51. Marts AR, Greer SM, Whitehead DR, Woodruff TM, Breece RM, Shim SW, Oseback SN, Papish ET, Jacobsen FE, Cohen SM, Tierney DL (2011) Appl Magn Reson 40:501
52. Puerta DT, Cohen SM (2002) Inorg Chem 41:5075
53. Alsfasser R, Trofimenko S, Looney A, Parkin G, Vahrenkamp H (1991) Inorg Chem 30:4098
54. Mehn MP, Fujisawa K, Hegg EL, Que L (2003) J Am Chem Soc 125:7828
55. Kitajima N, Hikichi S, Tanaka M, Morooka Y (1993) J Am Chem Soc 115:5496
56. Kitajima N, Fujisawa K, Morooka Y, Toriumi K (1989) J Am Chem Soc 111:8975
57. Kitajima N, Fujisawa K, Fujimoto C, Morooka Y, Hashimoto S, Kitagawa T, Toriumi K, Tatsumi K, Nakamura A (1992) J Am Chem Soc 114:1277
58. Jernigan FE III, Sieracki NA, Taylor MT, Jenkins AS, Engel SE, Rowe BW, Jove FA, Yap GPA, Papish ET, Ferrence GM (2007) Inorg Chem 46:360
59. Bongiovanni JL, Rowe BW, Fadden PT, Taylor MT, Wells KR, Kumar M, Papish ET, Yap GPA, Zeller M (2010) Inorg Chim Acta 363:2163
60. Kumar M, Dixon NA, Merkle AC, Zeller M, Lehnert N, Papish ET (2012) Inorg Chem 51:7004
61. Jones RL, Rees CW (1969) J Chem Soc C 2251
62. Julia S, Del MJM, Avila L, Elguero J (1984) Org Prep Proced Int 16:299
63. Reger DL, Grattan TC, Brown KJ, Little CA, Lamba JJS, Rheingold AL, Sommer RD (2000) J Organomet Chem 607:120
64. Janiak C, Scharmann TG, Hemling H, Lentz D, Pickardt J (1995) Chem Ber 128:235
65. Youm K, Huh S, Kim Y, Park S (2006) Bull Korean Chem Soc 27:1521
66. Averill BA (1996) Chem Rev 96:2951
67. Anjum MF, Stevanin TM, Read RC, Moir JW (2002) J Bacteriol 184:2987
68. Merkle AC, Lehnert N (2012) Dalton Trans 3355

69. Kujime M, Izumi C, Tomura M, Hada M, Fujii H (2008) J Am Chem Soc 130:6088
70. Halfen JA, Mahapatra S, Wilkinson EC, Gengenbach AJ, Young VG, Que L, Tolman WB (1996) J Am Chem Soc 118:763
71. Hsu SCN, Chang Y-L, Chuang W-J, Chen H-Y, Lin IJ, Chiang MY, Kao C-L, Chen H-Y (2012) Inorg Chem. 51(17), pp 9297–9308
72. Parkin G (2004) Chem Rev 104:699
73. Benning MW, Shim H, Raushel FM, Holden HM (2001) Biochemistry 40:2712
74. Alsfasser R, Vahrenkamp H (1993) Chem Ber 126:695

Index